UNIVERSITY OF SOUTHAMPTON

FACULTY OF ENGINEERING, SCIENCE & MATHEMATICS

OPTOELECTRONICS RESEARCH CENTRE

# Novel Power Scaling Architectures for Fibre and Solid-State Sources

Lee Pearson

Thesis submitted for the degree of Doctor of Philosophy

February 2011

UNIVERSITY OF SOUTHAMPTON

## ABSTRACT

FACULTY OF ENGINEERING, SCIENCE AND MATHEMATICS
OPTOELECTRONICS RESEARCH CENTRE

Doctor of Philosophy

# Novel Power Scaling Architectures for Fibre and Solid-State Sources

By Lee Pearson

This thesis explores approaches for scaling the output power of rare-earth ion doped fibre lasers and amplifiers, fibre amplified spontaneous emission sources, and solid-state laser oscillators.

Scaling output power from laser sources has been a topic of interest ever since the first laser was demonstrated. The development of new geometries and novel techniques for reducing effects that limit the maximum output power are particularly important. Three approaches for power scaling are demonstrated here.

The first is an all fibre geometry for producing predominately single-ended operation. By exploiting the high available gain in rare-earth-ion doped fibres, predominately single-ended laser output can be achieved in a high loss cavity with feedback at one end considerably lower than the other. This was demonstrated with an Yb-doped fibre laser using a low loss end termination scheme to produce 29W and 2W in the forward and backward directions, respectively, for launched pump power of 48W. This corresponds to a slope efficiency for the forward direction of $\sim$77%. The single-ended scheme was also applied to a Tm-doped fibre ASE system, producing a maximum output of 11W for 43W of launched pump, with an emission bandwidth of $\sim$36nm centred at 1958nm.

Secondly, a Tm-doped fibre distributed feedback laser with 875mW of single-frequency output at 1943nm was used in a master oscillator power amplifier configuration. Using three amplifier stages, the output was scaled to 100W of output with a final polarisation extinction ratio of $>$94% and a beam propagation factor of $M^2$ $<$1.25.

The last laser architecture was a cryogenically cooled Ho:YAG laser in-band pumped by a diode pumped Tm-doped fibre laser. After determining the absorption bandwidth as a function of temperature at the desired pump wavelength of 1932nm in Ho:YAG, the fibre laser was constructed to have an emission line-width of $<$0.2nm to achieve efficient overlap with the absorption peak. This fibre laser was used to pump two different Ho:YAG laser configurations. The first was a free-running laser based on a simple two-mirror cavity design, which showed a factor of 1.7 increase in the laser slope efficiency and a factor of 10 decrease in threshold pump power when the crystal temperature was reduced from 300K to 77K. The second cavity condition discussed was for low-quantum defect operation, which was demonstrated at 1970nm corresponding to a quantum defect of just 2%.

Lastly, further power scaling and other applications for all three approaches are discussed.

# Contents

# Author's Declaration

I, **Lee Pearson**, declare that this thesis entitled *Novel Power Scaling Architectures for Fibre and Solid-State Sources* and the work presented in it are my own. I confirm that:

- this work was done wholly while in candidature for a Research degree at the University of Southampton;
- where any part of this thesis has been previously submitted for a degree or any other qualification at this University or any other institution, this has been clearly stated;
- where I have consulted the published work of others, this is always clearly attributed;
- where I have quoted from the work of others; the source is always given. With the exception of such quotations, this thesis is entirely my own work;
- I have acknowledged all main sources of help;
- where the thesis is based on work done by myself jointly with others, I have made clear exactly what was done by others and what I have contributed myself;
- parts of this work have been published (see Appendix I for details).

Signed:............................................................ Date: ...........................

# Acknowledgements

I'd like to start by globally thanking all those who have helped me during my PhD. Firstly, thanks to my supervisor Andy for always being honest and upfront with his opinions and insights, and for also keeping me motivated and moving in the right direction. Additionally, thanks to all the ASSS group for the support and advice they've given me over the years. I'd like to thank Pu for helping to teach me the ropes in the early days, and Deyuan for introducing me to working at 2µmand getting things moving in the lab. For all their support in getting the Cryogenic Laser project underway I'd like to say thanks to Jacob and Ji Won, whose experience and advice was invaluable. Additionally, I'd like to thank Wendell Bailey and Yifeng Yang from the Institute of Cryogenics for designing and constructing the Liquid Nitrogen Cryostat. For keeping the lab running smoothly I'd like to thank Simon, Tim, Aide and Chris. Additionally I'd like to thank Simon for all his advice and help in designing and constructing many of my optical components, as well as for being a friendly ear to let off some steam with. Many thanks also to Eve and the admin. staff for keeping the ORC running smoothly, and to Dave and Kevin for maintaining the IT side of things and keeping my work safe. I'd like to also thank my family for all their support over the years both financially and emotionally, without whom I would never have gotten this far. Additionally, for helping keep my sanity thanks to the poker club: Roger, Sam, Katie, Mark, Nelly, Hollie, Melanie and Amos. Finally, a big thankyou to my wife Lorraine for always being by my side and making all the sacrifices worth while.

I would also like to acknowledge financial support from the EPSRC and the ORC.

# Frequently used symbols and abbreviations

| | |
|---|---|
| $P_{out}$ | Output power |
| $\eta_s$ | Slope efficiency |
| $P_{abs}$ | Absorbed pump power |
| $P_{thres}$ | Absorbed threshold pump power |
| $c$ | Speed of light |
| $h$ | Planck's constant |
| $\nu_p$ | Pump frequency |
| $\nu_l$ | Laser frequency |
| $\tau_f$ | Fluorescence lifetime |
| $\eta_q$ | Pump quantum efficiency |
| $\sigma_e$ | Emission cross-section |
| $\sigma_a$ | Absorption cross-section |
| $\alpha$ | Absorption coefficient |
| $\eta_{abs}$ | Pump absorption efficiency |
| $N$ | Total rare-earth-ion density |
| $I_{sat}$ | Signal saturation intensity |
| $P_{sat}$ | Signal saturation power |
| $M^2$ | Beam propagation factor |
| $z_0$ | Rayleigh range |
| $w$ | Gaussian beam radius |
| $w_0$ | Gaussian beam waist |
| $\theta$ | Far-field beam divergence |
| $P_h$ | Heat dissipated per unit length |
| $P_{hT}$ | Total Heat dissipated |
| $k$ | Thermal conductivity |
| $H$ | Heat transfer coefficient |
| $n$ | Refractive index |
| $dn/dT$ | Temperature dependent refractive index |
| $G$ | Effective single pass gain |
| $G_0$ | Total small signal gain for a single pass |
| ASE | Amplified spontaneous emission |
| CW | Continuous-wave |
| MOPA | Master oscillator power amplifier |
| Tm | Thulium |
| Ho | Holmium |
| Yb | Ytterbium |
| Er | Erbium |
| YAG ($Y_3Al_5O_12$) | Yttrium aluminium garnet |
| YLF ($LiYF_4$) | Yttrium lithium fluoride |
| SBS | Stimulated Brillouin Scattering |
| SRS | Stimulated Raman Scattering |
| $LN_2$ | Liquid nitrogen |
| FWHM | Full width half maximum |
| DFB | Distributed feedback |

| | |
|---|---|
| NA | Numerical aperture |
| PM | Polarisation maintaining |
| SFPI | Scanning Fabry Perot Interferometer |
| FSR | Free spectral range |

# Chapter 1

# Introduction

## 1.1 General introduction

Lasers and amplified spontaneous emission (ASE) sources are finding their way into an ever increasing number of applications. Many of these applications require sources with high efficiency, high output power and low cost. In addition, many more make use of the wide range of operational outputs that lasers and ASE sources offer from broadband to single-frequency; multimode to diffraction limited performance; and with the commonly used rare-earth ion doped materials there is a relatively wide range of operational wavelengths. Applications using these sources can be broken down into three main categories: industrial, medical and scientific. The industrial processes include cutting, welding, drilling and marking, where lasers have improved both the product quality and processing speeds. Furthermore, lasers have revolutionised the telecommunications industry where silica fibre technology and rare-earth ion doped amplifiers and lasers have drastically increased the data bandwidth and reduced the cost. In addition to these, lasers are also finding applications in defence and aerospace projects such as light detection and ranging (LIDAR) and remote missile defence. In terms of medicine lasers are used in applications such as microsurgery, dentistry and dermatology. The scientific uses for high power lasers and ASE sources include applications such as fibre-optic gyroscopes, optical coherence tomography, spectroscopy, atom cooling, interferometry, and non-linear frequency conversion. Therefore, the challenge for laser engineers is now to meet the requirements of these applications and to develop sources for applications not previously considered.

As such, the goal of the research described in this thesis is to develop and demonstrate different approaches for power scaling to meet some of the requirements for the above applications. This research covers the fairly wide topic area of power scaling in both fibre and 'bulk' solid state lasers with continuous-wave (CW) output. Although the research develops different laser and ASE sources, each using a different power scaling approach, the overall aim of this thesis is to show the merit of each system and to highlight their future potential.

## 1.2 Background

Since the first laser was demonstrated by Maiman [1] there has been a continued desire to improve the efficiency and output power from rare-earth-ion doped materials. Initially, progress was slow due to the poor optical-to-optical efficiency between the flash lamps and the laser gain medium. This was due to the rare-earth-ions having narrow absorption peaks compared to the broadband emission from the flash lamps, such that a significant proportion of the flash lamps power was not absorbed. A solution to this problem was the construction of the laser diodes in 1962, which were desirable due to their narrow spectral bandwidth compared to flash lamps, allowing for more efficient absorption and therefore much higher optical-to-optical efficiencies. However, it was not until the 1980s that improved fabrication techniques were developed to produce diode lasers with long enough lifetimes and high enough output power for them to become a practical alternative to flash lamps. For example, the first diode laser pumped Ho:YAG laser was not demonstrated until 1986 [2].

For both flash lamp and diode pumping regimes, the laser performance is often limited due to detrimental thermal effects inside the gain medium. These are typically caused by a combination of quantum defect heating, excited-state absorption (ESA), energy transfer upconversion (ETU), and absorption by impurities in the laser medium. The thermal effects include melting, thermally induced stress fracture, thermally induced birefringence and thermal lensing and guiding. As a result, good thermal management is important in order to increase the output power for which these thermal effects begin to limit laser performance. Therefore, many approaches have been developed over the years to combat these detrimental effects, for examples see [3–8]. The approach of importance in this thesis for 'bulk' solid state lasers is the use of cryogenic cooling of the gain medium.

The benefits of cryogenic cooling have been well documented [9,10] and show that as the temperature is reduced, certain materials have beneficial temperature dependent changes to their thermo-optical properties. Aggarwal et al. [10] showed that by reducing the temperature in yttrium aluminium garnet (YAG) from 300K to 100K, there is a 12.5 times reduction in dn/dT and a 4.7 times reduction in the thermal expansion coefficient, whilst the thermal conductivity increases by 6.7 times. The impact of these changes are that they dramatically reduce the impact of thermal effects on laser performance. Therefore, by reducing the laser material's temperature to 100K, the output power achieved will be much higher than that at room temperature before the laser performance is degraded to the same extent. This enhancement has been demonstrated to good effect recently using ytterbium and erbium doped materials for operation at $1\mu m$ and $1.5\mu m$ respectively [11–15]. However, at present there has been little research conducted in the $2\mu m$ regime. Therefore, Chapter 5 demostrates cryogenic cooling of a Ho:YAG rod laser.

An alternative approach for power scaling is to use rare-earth ion doped silica fibres. An optical fibre's large surface area to volume ratio and long device length makes thermal management easier than in conventional 'bulk' laser geometries. Furthermore, the wave-guiding nature of the fibre's core allows relatively simple selection of good output beam quality and immunity from the thermally-induced beam distortion that is a common problem in other types of gain medium geometry. Additionally, the fibre geometry can also be selected to allow them to be end pumped by high power diodes arrays making them ideal for power scaling. The output power from fibre lasers has seen a significant increase in recent years, as can be seen in Figure 1.1 for ytterbium and thulium doped silica. These beneficial properties provide the motivation for the research conducted on fibre based lasers and ASE sources within this thesis.

(a) Yb-doped silica fibre lasers (b) Tm-doped silica fibre lasers

Figure 1.1: Showing the maximum output power of a single stage oscillator with time for (a) Ytterbium doped silica fibres [16–21], and (b) Thulium doped silica fibres [22–26].

## 1.3 Thesis overview

Given the breadth of the power-scaling field for lasers and ASE sources, this thesis will focus only on specific areas. The main interests are in the development of architectures for enhancing the output power from fibre based laser and ASE sources, and enhancing the performance of Ho-doped YAG lasers by cryogenically cooling the crystal. In all of these situations, only CW operation is considered.

The thesis starts in Chapter 2 with discussion of some of the main issues affecting laser performance. Typically, the maximum laser output power is limited by the available pump power, thermally induced effects and/or non-linear processes. To obtain high output powers, most laser systems will use high power laser diodes as a pump source. Typically these diode sources consist of individual diode emitters that are stacked together to form arrays or stacks of arrays to increase the maximum output power. However, as the maximum output power from these diode arrays/stacks is increased, the mechanical constraints in the diode design results in the output beam propagation factor ($M^2$) also increasing with the impact of effectively reducing their usefulness as pump sources. Therefore, techniques for reducing the beam propagation factor to improve the usefulness of these sources are considered.

Even with sufficiently high pump powers, the theoretical maximum laser output power is not always achieved due to thermal effects limiting laser performance. Thermally induced effects impact the laser performance in a number of ways. Of particular interest here are thermal lensing and/or de-polarisation losses in polarised systems that degrade the laser performance, and stress induced fracture and melting thresholds which result in critical failure. Therefore, each of these effects is considered in both fibre and 'bulk' laser rod regimes with suggestions for reducing their impact given.

Another significant limitation on performance can be due to non-linear effects in the laser medium. Non-linear effects are signal intensity dependent processes. As such, the tight beam confinement in a fibre core results in the impact of non-linear effects being more pronounced in fibre systems than bulk for CW operation. Therefore, non-linear processes in bulk systems are not considered. In the case of fibres, the two main non-linear processes that can affect the performance are Stimulated Brillouin Scattering (SBS) and Stimulated Raman Scattering (SRS). For both of these effects, the threshold signal intensity for the onset of these is given with discussion of how to increase this threshold to enable further power scaling.

The first of the experimental chapters starts in Chapter 3 where the work focuses on achieving predominately single-ended output in a fibre based laser and ASE source. Typically, single-ended output would be achieved using an external feedback cavity or in-fibre Bragg grating. However, here we demonstrate an all-fibre approach where the difference in the fibre end facets reflectivities determines the relative output power extracted from each end. The advantage of this are that the fibre does not require modifications to the fibre core composition with photosensitive dopants for writing in-fibre gratings, and similarly reduces the cost required for the optics for an external feedback cavity. Furthermore, the approach is suitable for cladding pumping and is therefore compatible with high power diode pumping.

When this approach was applied to a ytterbium-doped fibre laser, there was a non-negligible ASE background due to the high laser threshold caused by the high cavity losses. The implications of this are discussed and a technique is described for determining the power contained in both the laser and ASE individually. This showed that the ASE signal continued to increase even once the laser threshold was reached, but that it rolled over as the pump power was further increased. An explanation for this is given with future implications discussed.

In the second part of Chapter 3, the all-fibre approach was applied to a thulium-doped fibre ASE source. This showed that in ASE sources operating well above saturation, the relative power extracted from each end of the fibre was dependent on the fibre end facets reflectivities. However, for high power operation, further power scaling was restricted by the onset of parasitic lasing. This result supported the theory suggested for why the ASE rolls-over in the single-ended laser situation outlined above. The result also suggested that no matter how low the fibre facet reflectivities, the laser threshold will always be reached if there is sufficient pump power. This was confirmed by further experiments where the parasitic laser threshold was increased by reducing the fibre end facet reflectivities. Finally, the chapter concludes by discussing methods for further power scaling and the future prospects for the single-ended output approach.

The experimental chapters continue in Chapter 4 where the output from a single-frequency fibre laser is power scaled using a master oscillator power amplifier (MOPA). The chapter begins by considering some common approaches for obtaining single-frequency output with reference to the limitations in each case, before discussing in more detail the distributed feedback approach used. In any amplifier system, knowledge of the expected gain and output power are important. This is discussed for both the small signal gain and saturated gain regimes. The minimum seed power required for efficient amplification was determined by considering the saturated gain and extraction efficiency for each of the fibres used in the amplifier stages. Continuing the discussion on non-linear effects that was started in Chapter 2, the threshold signal power for SBS (as this has a lower threshold power than SRS) in each amplifier stage was estimated. This allowed the determination of the upper limit on the signal power that should be used to avoid the onset of these non-linear effects. Therefore, the amplifier stages were designed so that the expected signal power after each amplifier stage did not exceed this limit. Lastly, the results for each amplifier stage are individually presented, with discussion given to the limitations of this system and approaches that will allow further power scaling in the future.

Chapter 5 moves the discussion of power scaling away from fibres and considers Holmium-doped YAG rods. In most cases, the performance of 'bulk' laser rods is limited by thermal effects as discussed in Chapter 2. Therefore, this chapter considers cryogenic cooling of the laser crystal to reduce the impact of these thermal effects, which therefore allows for further power scaling. The attraction of this approach is that cryogenic cooling YAG beneficially changes the crystal's thermo-optic properties and therefore reduces any thermal effects. The possible enhancements due to cryogenic cooling are considered by estimating the de-polarisation loss and the beam quality degradation due to thermally induced phase abberation for a crystal at room temperature and liquid nitrogen temperature ($LN_2$).

However, cryogenic cooling does not only affect the thermo-optic properties, but also changes the crystal's spectroscopy. This has the impact of placing tighter constraints on the required pumping laser bandwidth. Therefore, an ASE probe source was used in conjunction with a scanning monochromator to measure the temperature dependent absorption spectra, so that a fibre laser could be designed to pump the Ho:YAG laser with the required pump bandwidth. The resulting fibre laser is discussed with its performance given.

For the Ho:YAG laser, two cavity designs are discussed. The first was a 'free-running' laser (i.e. with no wavelength selection), and the second used wavelength selection to force low quantum defect operation. In both cavity designs, it is important to have a good overlap between the pump and laser signals to achieve efficient lasing. Therefore, ray transfer matrixes are briefly introduced for calculating the laser mode size in the Ho:YAG laser cavities. The attraction of operating the Ho:YAG in two cavities was that in the free-running case the enhancement in performance between room temperature and $LN_2$ was highlighted, whilst for the low quantum defect operation further power scaling is explored, due to the enhancement in the laser slope efficiency. The results from these cavity designs are given with suggestions for further power scaling discussed.

Finally, the thesis concludes with a discussion of the major findings and future directions for each power scaling architecture.

## 1.4 References

[1] **Maiman, T. H.**, *Stimulated optical radiation in Ruby*, Nature, Vol. 187, No. 4736, pp. 493–494, August 1960.

[2] **Allen, R., Esterowitz, L., Goldberg, L., Weller, J. F.** and **Storm, M.**, *Diode-pumped 2$\mu$m holmium laser*, Electronics Letters, Vol. 22, No. 18, pp. 947, August 1986.

[3] **Clarkson, W. A.**, *Thermal effects and their mitigation in end-pumped solid-state lasers*, Journal of Physics D: Applied Physics, Vol. 34, No. 16, pp. 2381, August 2001.

[4] **Clarkson, W. A., Felgate, N. S.** and **Hanna, D. C.**, *Simple method for reducing the depolarization loss resulting from thermally induced birefringenece in solid-state lasers*, Optics Letters, Vol. 24, No. 12, pp. 820–822, June 1999.

[5] **Fluck, R., Hermann, M. R.** and **Hackel, L. A.**, *Birefringence compensation in single solid-state rods*, Applied Physics Letters, Vol. 76, No. 12, pp. 1513–1515, March 2000.

[6] **Hua, R., Wada, S.** and **Tashiro, H.**, *Principles and limitations of a quarter-wave plate for reducing the depolarization loss from thermally induced birefringence in Nd:YAG lasers*, Optics Communications, Vol. 175, No. 1-3, pp. 189–200, February 2000.

[7] **Khazanov, E., Potemkin, A.** and **Katin, E.**, *Compensating for birefringence in active elements of solid-state lasers: novel method*, Journal of the Optical Society of America B, Vol. 19, No. 4, pp. 667–671, April 2002.

[8] **Moshe, I.** and **Jackel, S.**, *Correction of birefringence and thermal lensing in nonreciprocal resonators by use of a dynamic imaging mirror*, Applied Optics, Vol. 39, No. 24, pp. 4313–4319, August 2000.

[9] **Brown, D. C.**, *The promise of cyrogenic solid-state lasers*, IEEE Journal of Selected Topics in Quantum Electronics, Vol. 11, No. 3, pp. 587–599, May/June 2005.

[10] **Aggarwal, R. L., Ripin, D. J., Ochoa, J. R.** and **Fan, T. Y.**, *Measurement of thermo-optic properties of* $Y_3Al_5O_12$, $Lu_3Al_5O_12$, $YAlO_3$, $LiYF_4$, $LiLuF_4$, $BaY_2F_8$, $KGd(WO_4)_2$, *and* $KY(WO_4)_2$ *laser crystals in the* 80-300*K temperature range*, Journal of Apllied Physics, Vol. 98, No. 10, pp. 103514–1–103514–14, Novemeber 2005.

[11] **Manni, J. G., Hybl, J. D., Rand, D., Ripin, D. J., Ochoa, J. R.** and **Fan, T. Y.**, *100W Q-switched cryogenically cooled Yb:YAG laser*, IEEE Journal of Quantum Electronics, Vol. 46, No. 1, pp. 95–98, January 2010.

[12] **Ripin, D. J., Ochoa, J. R., Aggarwal, R. L.** and **Fan, T. Y.**, *300-W cryogenically cooled Yb:YAG laser*, IEEE Journal of Quantum Electronics, Vol. 41, No. 10, pp. 1274–1277, October 2005.

[13] **Tokita, S., Kawanaka, J., Fujita, M., Kawashima, T.** and **Izawa, Y.**, *Efficient high-average-power operation of Q-switched cryogenic Yb:YAG laser oscillator*, Japanesse Journal of Applied Physics, Vol. 44, No. 50, pp. 1529–1531, 2005.

[14] **Ter-Gabrielyan, N., Merkle, L. D., Ikesue, A.** and **Dubinskii, M.**, *Ultralow quantum-defect eye-safe Er:*$Sc_2O_3$ *laser*, Optics Letters, Vol. 33, No. 13, pp. 1524–1526, July 2008.

[15] **Ter-Gabrielyan, N., Dubinskii, M., Newburgh, G. A., Michael, A.** and **Merkle, L. D.**, *Temperature dependence of a diode-pumped cryogenic Er:YAG laser*, Optics Express, Vol. 17, No. 9, pp. 7159–7169, April 2009.

[16] **Dominic, V., MacCormack, S., Waarts, R., Sanders, S., Bicknese, S., Dohle, R., Wolak, E., Yeh, P. S.** and **Zucker, E.**, *110W fiber laser*, Electronic Letters, , No. 35, pp. 1158–1159, 1999.

[17] **Plantonov, N. S., Gapontsev, D. V., Gapontsev, V. P.** and **Shumilin, V.**, *135W CW fiber laser with perfect single mode output*, Proceedings of the Conference on Lasers and Electro-Optics, 2002, paper Number CPD3-1 - CPDC3-4.

[18] **Jeong, Y., Sahu, J. K., Payne, D. N.** and **Nilsson, J.**, *Ytterbium-doped large-core fiber laser with 1.36 kW continuous-wave output power*, Optics Express, Vol. 12, pp. 6088–6092, 2004.

[19] **Liem, A., Limpert, J., Zellmer, H., Tnnermann, A., Reichel, V., Mrl, K., Unger, S., Mller, H. R., Kirchhof, J.** and **Harschak, A.**, *1.3 kW Yb-doped fiber laser with excellent beam quality*, Proceedings of the Conference on Lasers and Electro-Optics, 2004, paper Number CPDD2.

[20] **Gapontsev, V., Gapontsev, D., Platonov, N., Shkurikhin, O., Fomin, V., Mashkin, A., Abramov, M.** and **Ferin, S.**, *2 kW CW ytterbium fiber laser*

*with record diffraction-limited brightness*, Proceedings of the Conference on Lasers and Electro-Optics Europe, p. 508, June 2005.

[21] **Fomin, F., Mashkin, A., Abramov, M., Ferin, A.,** and **Gapontsev, V.**, *3 kW Yb fibre lasers with a singlemode output*, International Symposium on High-Power Fiber Lasers and their Applications, 2006.

[22] **Hayward, R. A., Clarkson, W. A., Turner, P. W., Nilsson, J., Grudinin, A. B.** and **Hanna, D.**, *Efficient cladding-pumped Tm-doped silica fibre laser with high power singlemode output at 2pm*, Electronics Letters, Vol. 36, No. 8, pp. 711–712, April 2000.

[23] **Jackson, S. D.**, *Cross relaxation and energy transfer upconversion processes relevant to the functioning of* 2µm*Tm*$^{3+}$*-doped silica fibre lasers*, Optics Communications, Vol. 230, pp. 197–203, 2004.

[24] **Frith, G., Lancaster, D. G.** and **Jackson, S. D.**, *85W Tm*$^{3+}$*-doped silica fibre laser*, Electronics Letters, Vol. 41, No. 12, pp. 687, June 2005.

[25] **Slobodtchikov, E., Moulton, P. F.** and **Frith, G.**, *Efficient, high-power, Tm-doped silica fiber laser*, Proceedings of the Conference on Advanced Solid-State Photonics, 2007, paper Number MF2.

[26] **Moulton, P. F., Rines, G. A., Slobodtchikov, E. V., Wall, K. F., Frith, G., Samson, B.** and **Carter, A. L. G.**, *Tm-doped fiber lasers: Fundamentals and power scaling*, IEEE Journal of Selected Topics in Quantum Electronics, Vol. 15, No. 1, pp. 85–92, January/February 2009.

# Chapter 2

# Power scaling in lasers: fibre vs bulk

## 2.1 Introduction

The requirement for ever higher output powers from lasers for applications ranging from machine processing and welding through to scientific applications, medicine and defence places large demands on approaches for improving laser efficiency and combating performance limiting effects. To meet the demands of these various applications, laser sources have been developed using a wide range of host materials doped (and co-doped) with different rare earth ions (the most common being Nd, Yb, Er, Tm, Ho) for different wavelength operation. These lasers have then been developed to operate with either continuous wave (CW) or pulsed output. As such, the topic of power scaling in laser sources is vast. Of particular interest in this thesis are lasers operating in CW operation in step-index fibre lasers and end pumped laser rods. Therefore, the discussion of power scaling in lasers is restricted to consider only the factors affecting power scaling in these regimes of interest.

In this thesis, lasers based on Thulium doped silica and Holmium doped YAG and YLF are of particular interest because they are commercially available and also have well understood properties given in the literature. This makes any performance calculations easier than if less well understood materials were used, where some of the characteristics would need to be determined. Thulium was used as the rare-earth dopant because of its emission band in the $2\mu m$ spectral region, which is of particular interest in industry and by the military for 'eye safe' applications. Of course at high power levels $2\mu m$ radiation will still result in damage to the eye regardless of it being outside the spectral sensitivity of the eye's photo-receptors. These lasers of interest will be predominantly operated in a 3 level regime, so this chapter begins by giving expressions for the laser slope efficiency and absorbed threshold pump power in a 3 level laser. These are applied more specifically to step index fibre and end pumped rods with discussion of the expected laser performance.

Improvements in diode technology have enabled scaling in laser output power in both fibre and bulk lasers. However, as the number of diode emitters is increased to increase the maximum output power, the brightness is reduced. This is discussed with reference to the impact it has on their use as pump sources for bulk and fibre laser systems. Also summarised are some approaches for beam shaping to enhance the output brightness to make them more useful for pumping rare-earth doped fibres and bulk rods, as they will be used throughout this thesis.

In most laser systems the output performance is limited by detrimental effects of the heat generated due to the energy difference between the pump and signal photons, spectroscopic effects and defects in the material. The impact of thermally induced effects are considered for fibre and bulk systems to highlight the limits at which they begin to degrade laser performance. Similarly, nonlinear effects, which can be significant in cw fibre lasers, are also considered and the limits for power scaling are estimated. For both thermal and nonlinear effects, design considerations are given which should enhance the power scaling capabilities in bulk and fibre lasers.

Lastly, the chapter is summarised, discussing the design considerations required to reduce the impact of thermal and nonlinear effects, and therefore enable the output power to be scaled in the laser geometries of interest (i.e. End-pumped solid-state lasers and cladding pumped fibre lasers).

## 2.2 CW end-pumped laser oscillators

### 2.2.1 Laser efficiency

Lasers are used for a wide range of applications, with each imposing different constraints on the output beam properties and the overall laser performance. For most applications it is desirable to maximise the laser output efficiency, so long as this does not result in an undesirable change in the output beam properties, such as the beam propagation factor, laser linewidth, output stability or output wavelength. A simple approximation for predicting the laser output power is given by $P_{out} \approx \eta_s(P_{abs} - P_{thres})$ [1], where $\eta_s$ is the laser slope efficiency with respect to absorbed pump power, $P_{abs}$ is the absorbed pump power, and $P_{thres}$ is the absorbed threshold pump power (defined as the absorbed pump power required for the round trip gain to equal the round trip cavity losses). Using this approximation, the maximum output power can be calculated for a given pump power, by optimising the laser parameters in equations (2.1) & (2.3) (such as the output coupler transmission, pump and signal beam sizes, the absorption efficiency and the cavity losses). The lasers of interest in this thesis are predominantly quasi 3 level. To simplify the calculation of the threshold, a simplified rate equation approach is used which assumes rapid decay of pump excitation into the upper laser level so that the pump level population can be assumed to be 0. The absorbed threshold pump power can be calculated as being [2]

$$P_{thres} = \frac{h\nu_p A}{2\tau_f \eta_q \eta_{abs}(\sigma_a(\lambda_L) + \sigma_e(\lambda_L))}[-\ln(1-L) - \ln(1-T) + 2\sigma_a(\lambda_L)Nl + 2\alpha_L l] \tag{2.1}$$

where $\nu_p$ is the pump frequency, $\tau_f$ is the fluorescence lifetime of the upper laser level, $\eta_q$ is the pump quantum efficiency (defined as the number of ions excited to the upper laser level per pump photon absorbed), N is the total rare-earth ion density, $l$ is the length of the gain medium, $\eta_{abs}$ is the pump absorption efficiency (such that $\eta_{abs} = 1 - \exp(-\sigma_a(\lambda_P)Nl)$ where $\sigma_a(\lambda_P)$ is the absorption cross-section for the pump wavelength), $\alpha_L$ is the material attenuation coefficient for the laser signal, L is the loss due to the other cavity optics, and T the output coupler transmission, and $\sigma_{a,e}(\lambda_L)$ are the absorption and emission cross-sections for the laser wavelength, respectively. The pumped region A, is equal to $\pi w_p^2$ (or $\pi r_{core}^2$ for fibres) assuming a 'top-hat' pump intensity profile, and for a Gaussian pump intensity profile $A = \pi(w_p^2 + w_l^2)/2$ [3] where $w_p$ is the pump beam radius and $w_l$ is the laser mode radius, where it is assumed that there is negligible beam divergence over the crystal length.

A laser is considered to be operating many times above threshold when the signal intensity is much larger than the saturation intensity, given in a 3-level system as

$$I_{sat} = \frac{h\nu_L}{\tau_f(\sigma_a(\lambda_L) + \sigma_e(\lambda_L))} \tag{2.2}$$

When operating in this regime, and where it is assumed the signal reabsorption and background losses are significantly lower than the loss due to the output coupler and the other cavity optics, the slope efficiency can be approximated to a simpler 4-level approximation [4] given by

$$\eta_s \approx \frac{T\sqrt{1-L}}{T\sqrt{1-L} + L\sqrt{1-T}} \left(\frac{\nu_L}{\nu_p}\right) \eta_q \eta_{abs} \tag{2.3}$$

where for low output coupler transmission and cavity losses this can be simplified to

$$\eta_s \approx \frac{T}{T+L} \left(\frac{\nu_L}{\nu_p}\right) \eta_q \eta_{abs} \tag{2.4}$$

### 2.2.2 Implications for fibre and bulk lasers

This thesis is mainly interested in lasers operating in the 2$\mu m$ spectral region, using holmium and thulium doped materials. Therefore, to highlight the differences in laser performance between end pumped 'bulk' laser rods and fibre lasers the examples of Tm-doped silica, YAG and YLF are compared.

From Table 2.1 it can be seen that the emission cross-section in Tm:silica is comparable to Tm doped-YAG and YLF, suggesting that the laser thresholds will be similar. However, the fluorescence lifetime in silica is approximately 4 times shorter than in YAG or YLF, which would suggest that the threshold will be 4 times higher in silica, but when considering that the pump area in fibres is considerably smaller than typical pump sizes in the bulk media (of the order of 400 times smaller, using a pump beam radius of 500$\mu m$ and 25$\mu m$ in the bulk and fibre respectively). Therefore, the impact of pump area is particularly significant meaning that the absorbed threshold power will typically be lower in Tm:silica. As a result, fibre lasers can operate with much higher cavity losses and output coupler transmission, whilst still having relatively low threshold that is comparable to bulk crystal laser thresholds.

| **Parameter** | **Silica** | **YAG** | **YLF** |
|---|---|---|---|
| $\tau_f$ | 200-600$\mu s$ [5–8] | 2.1ms [9] | 2ms [10] |
| $\lambda_P$ | ~790nm | 785nm | 780-790nm |
| $\lambda_L$ | 1800-2100nm | 2.01$\mu m$ peak | 1.88-1.9$\mu m$ peak (for p-pol and s-pol) |
| $\sigma_a(\lambda_L)$ ($\times 10^{-20}$cm$^2$) | >0.02 $\lambda$ >1880nm [11] | <0.01 | 0.06 & 0.02 (for p-pol and s-pol) |
| $\sigma_e(\lambda_L)$ ($\times 10^{-20}$cm$^2$) | 0.31 $\lambda$=2$\mu m$ [12] | 0.27 [9] | 0.36 & 0.22 (for p-pol and s-pol) |

Table 2.1: Summary of key parameters required for calculating the slope efficiency and threshold condition for diode pumped Tm-doped silica, YAG and YLF.

When the slope efficiency is considered, both bulk and fibre should have slopes given approximately by equation (2.3) for operation well above the saturation intensity. However, for stimulated emission to dominate over spontaneous emission the signal intensity needs to be greater than the saturation intensity over the entire inverted region. This is much easier to achieve in Tm-doped fibre lasers due to the tight signal confinement in the core, even when the larger saturation intensity is considered. As a result, fibres typically have higher slope efficiencies than their bulk counterparts. Furthermore, fibres typically have much higher gain than their bulk counterparts which allows them to be operated with high output coupler transmissions, allowing for higher slope efficiencies as $T/(T+L) \rightarrow 1$, whilst still maintaining a relatively low threshold. Another benefit of fibres is that as the pump power is increased, solid-state lasers become more susceptible to thermally induced effects which limit their performance, as discussed in a later section.

The slope efficiency and threshold in Tm doped materials can be further enhanced due to the advantageous two-for-one cross-relaxation process $^3F_4, ^3H_6 \rightarrow\ ^3H_4, ^3H_4$ (see Figure 2.1). This two-for-one process generates 2 excited ions in the upper laser manifold for each absorbed pump photon at ~790nm. Therefore, the Stokes limit of $\nu_L/\nu_p$ can be theoretically doubled, although performance approaching this limit has not yet been demonstrated. In Tm-doped bulk crystals, this process has been exploited for a number of years, where to obtain a high cross-relaxation efficiency, crystals are typically doped with high $\mathrm{Tm}^{3+}$ concentrations (>2%) [13].

It was only recently that the same two-for-one cross-relaxation was observed in Tm:silica. Since its observation, research has been conducted to optimise the process to obtain higher efficiencies. Jackson et al. [14, 15] show that the $\mathrm{Tm}^{3+}$ doping concentration has a significant impact on the slope efficiency due to the pumping quantum efficiency being enhanced by the two-for-one cross-relaxation process, as is expected from Tm:crytsal results. However, in [14] they report that the increased $\mathrm{Tm}^{3+}$ doping concentration leads to ion clustering and an increase in energy-transfer-upconversion (ETU). To overcome this, the core is required to be co-doped with $\mathrm{Al}^{3+}$ with a ratio ($\mathrm{Al}^{3+}$:$\mathrm{Tm}^{3+}$) of greater than 10. With this core doping arrangement, a fibre laser with a slope efficiency of ~74% was produced [14], highlighting the benefits of the two-for-one process when this value is compared with the Stokes limit of only ~40%.

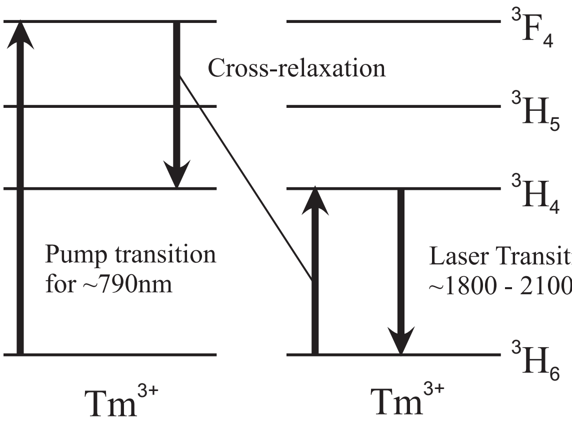

Figure 2.1: Schematic representation of the four lowest Stark levels in $Tm^{3+}$ doped silica showing the cross-relaxation process between neighbouring Tm ions, and the pump and laser transitions [14].

## 2.3 Pumping considerations

### 2.3.1 Power scaling in diode lasers

The development of higher power diode emitters and arrays has enabled significant scaling of the output power in both fibre and bulk laser systems. In addition to their output power, the different diode materials have enabled the emission wavelengths of these sources to be tailored to match the absorption peaks in many rare-earth doped laser hosts. This allowed for simple pumping arrangements to achieve laser output from the rare-earth doped materials over a range of wavelengths, typically concentrated in the 0.9-2.1$\mu m$ region. However, using diode lasers as pump sources is not without its complications. A single mode diode emitter has an output beam propagation factor, $M^2$=1, making it ideal for pumping fibres and bulk lasers, as discussed later, but it has an output power which is limited to <1W due to critical failure of the emitter. Therefore, in order to scale the diode output power, many diode emitters must be combined to form arrays. The emission region in a diode laser is only a fraction of the emitting face area, where the ratio between them is determined by the physical separation of the emitters and the mechanical structure of the semi-conductor. Considering the impact of the heat removal method, it can be seen that for a micro-channel cooled diode, the ratio can be as high as 80% (emitter to 'dead' space) compared to 30% without micro-channels. When individual emitters are combined incoherently to form arrays, the beam divergence from the emitters is unchanged. However, the 'dead' space between the emitters results in the overall beam propagation factor, $M^2$, increasing. This can be seen when considering the beam propagation factor defined as

$$M^2 = \frac{\pi w_0 \theta}{\lambda} \tag{2.5}$$

where $w_0$ is the beam waist, $\theta$ is the far-field beam divergence and $\lambda$ is the laser wavelength. Figure 2.2 shows the effective output beam for a single emitter compared to that for all of the emitters combined. It can be seen that beam divergence of the combined beam is the same as the individual emitters, whereas the effective beam waist increases from $D_E/2$ for a single emitter to a group of emitters being equal to $2w_0 = D_S(N-1) + D_E$ where $D_S$ is the emitter spacing, $D_E$ is the emitter height and $N$ is the number of emitters. Therefore, it follows that beam propagation factor for a single emitter, $M_S^2$, is given by

$$M_S^2 = \frac{\pi D_E \theta}{2\lambda} \tag{2.6}$$

compared to the beam propagation factor for a group of N emitters of

$$M_U^2 = \frac{\pi (D_S(N-1) + D_E)\theta}{2\lambda} \tag{2.7}$$

Given that a typical diode stack has an emitter height of $\sim 1\mu m$ and an emitter separation of 1.9mm [16], the beam propagation factor in the fast axis can be calculated. Only emission in the fast axis is considered here as the beam propagation factor will be largest in this axis due to the beam divergence in the fast axis ($\theta \sim 30°$ (FWHM)) being much higher than for the slow axis (($\theta \sim 7°$ (FWHM)). It can be seen that the beam propagation factor in the fast axis for a

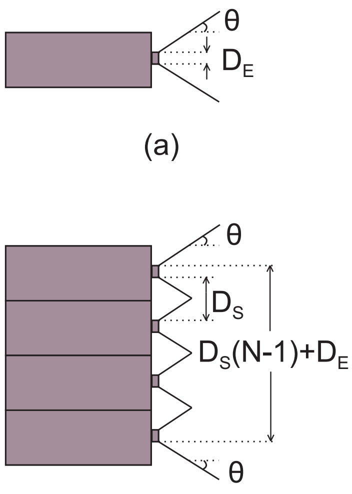

(a)

(b)

Figure 2.2: Schematic representation of (a) a single diode emitter with a far-field beam divergence $\theta$ and beam waist $D_E/2$, compared to (b) an array of the same emitters with an overall far-field beam divergence of $\theta$ and beam waist $0.5[D_S(N-1)+D_E]$.

6 diode bar stack operating at 808nm is $M^2 \approx 9500$, compared to $M^2 \approx 1$ for a single emitter.

This reduction in the output brightness with power in diodes has had a significant impact on how effective and efficient they are as pump sources for both fibre and bulk laser systems. The constraints placed on the pump launching and performance limits due to diode brightness are considered below. For both regimes, having an equal and low beam propagation factor in both the fast and slow axis with a symmetrical beam profile is desirable. As such, to make high power diode lasers more useful as pump sources, many techniques have been developed to try to preserve the emitter brightness. Those applied during this thesis are outlined below.

#### 2.3.1.1 Aperture filling

Diode bars and stacks have a large area of 'dead space' between the emitting regions, which reduces the overall output brightness. A technique for reducing this 'dead space' is known as 'aperture filling'. From equation (2.7) it can be seen that to reduce the beam propagation factor from an array of emitters requires the far-field divergence to be reduced and the beam waist to dead space ratio to be increased. This is achieved with the 'aperture filling' approach by collimating the diode emitters separately in the fast and slow axis. It can be seen in Figure 2.3, that by collimating each emitter separately the output for each emitter has a larger beam waist and a smaller far-field divergence, where the change is given by $\theta_U/\theta_C = D_C/D_E$ (from equation (2.5)) for $\theta_{U,C}$ the un-collimated and collimated far-field divergences, and $D_C$ the collimated beam diameter. It follows then that the beam propagation factor for a collimated array of N diodes is given by

$$M_C^2 = \frac{\pi(D_S(N-1)+D_C)\theta_C}{2\lambda} \tag{2.8}$$

and that the reduction in the beam propagation factor from the un-collimated beam to collimated is given by

$$\frac{M_U^2}{M_C^2} = \frac{\theta_U}{\theta_C}\frac{D_S(N-1)+D_E}{D_S(N-1)+D_C} \tag{2.9}$$

Therefore, achieving the largest reduction in the beam propagation factor requires the space between the individual collimated beams to be minimised, such that the collimating lens for the fast and slow axis are selected so that the collimated beam size is approximately equal to the emitter separation, i.e. $D_C/D_S \approx 1$. Using the approximation that $\theta_U/\theta_C = D_C/D_E$ and assuming that the emitter size is negligible due to $D_E \ll D_S$, allows equation (2.9) to be simplified to

$$\frac{M_U^2}{M_C^2} = \frac{\theta_U}{\theta_C}\frac{(N-1)}{N} \approx \frac{D_C}{D_E}\frac{(N-1)}{N} \tag{2.10}$$

Therefore, using the same example as in the section above for 6 diode bar stack with an emitter size of $\sim 1\mu m$ and a collimated beam size that is approximately equal to the diode spacing of 1.9mm, the beam propagation factor will be re-

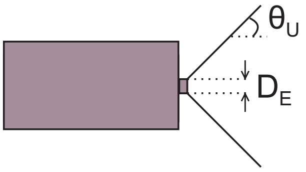

(a) Un-collimated Output

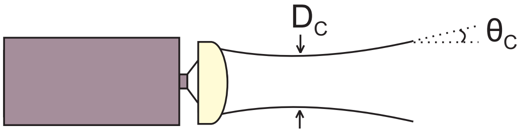

(b) Collimated Output

Figure 2.3: Schematic representation of (a) an un-collimated output beam and (b) a collimated output beam from a diode emitter, highlighting that the far-field beam divergence ($\theta_{U,C}$) is reduced and beam waist ($2w_0 = D_{E,C}$) is increased for the collimated output beam compared to the un-collimated.

duced by a factor of 1580 from an un-collimated output to a collimated one in the fast axis. As such, the output beam propagation factor in the fast axis for the 6 diode-bar stack would be $M^2 \approx 6$.

In practice, collimating the diode emitters requires careful consideration. In the fast axis, there is a very high beam divergence ($\theta \approx 30^\circ$ (FWHM)) which requires the collimating lens to have a high NA and diffraction limited performance, so that the beam quality is not degraded. The fast axis is collimated using a cylindrical lens that is the length of the emitting region of the diode bar, which enables all the emitters in the bar to be collimated simultaneously. For the slow axis, the beam divergence is much less ($\theta \approx 7^\circ$ (FWHM)), so the constraints on the collimating lens are reduced such that an array of micro-lenses can be used to collimate the output. Both the fast and slow axis collimation for a diode-stack can be seen in Figure 2.4.

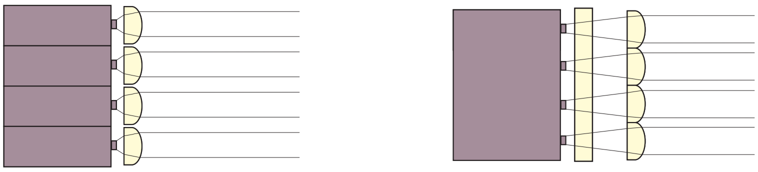

(a) Fast-axis Collimation (b) Slow-axis Collimation

Figure 2.4: Schematic representation of the aperture filling technique applied to a diode-stack laser

#### 2.3.1.2 The two-mirror beam shaper

This technique builds upon the aperture filling approach, and corrects the large difference in beam propagation factors for the slow and fast axis of the diodes bar [17, 18]. The approach, as shown in Figure 2.5, uses two parallel high-reflectivity mirrors that are separated by a small distance. The mirrors are transversely offset from each other so that small sections of each mirror are unobscured and can act as input and output apertures. The diode laser beam is the incident upon the unobscured section of mirror B, with a small proportion of the beam (in Figure 2.5 labelled (1)) passing over the edge of mirror A and therefore emerging with no change in direction. The rest of the beam is reflected by mirror B back towards mirror A, where beam (2) is incident on mirror A just below beam (1). Beam (2) is then reflected past the side of mirror B in the same direction as beam (1), and is thus stacked directly below it. This process is continued until the beams are all stacked in the y axis in the output. The result of the beam shaping is that the output beam width is reduced for the slow axis, with approximately the same beam divergence, thus applying the relationship, $M^2 = \pi\omega_0\theta/\lambda$, the beam propagation factor is reduced. Similarly, the increase in beam size for the fast axis has the effect of increasing the beam propagation factor. By carefully controlling the mirror angle and separation, it is possible to convert the diode output such that $M_x^2 \approx M_y^2$, with limited degradation in brightness. This beam can then be re-proportioned using a combination of cylindrical and spherical lenses to obtain a more symmetrical beam profile, which can be used to directly pump a solid state laser or similarly be focused into a multi-mode delivery fibre. However, if a delivery fibre is used, the power will be reduced due to coupling losses and background attenuation losses in the fibre.

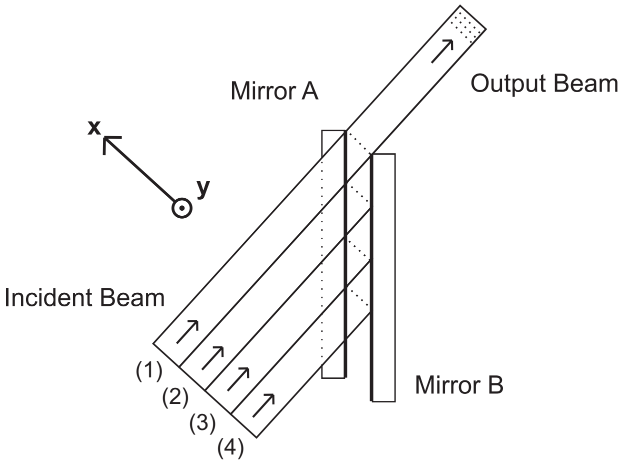

(a) plan view

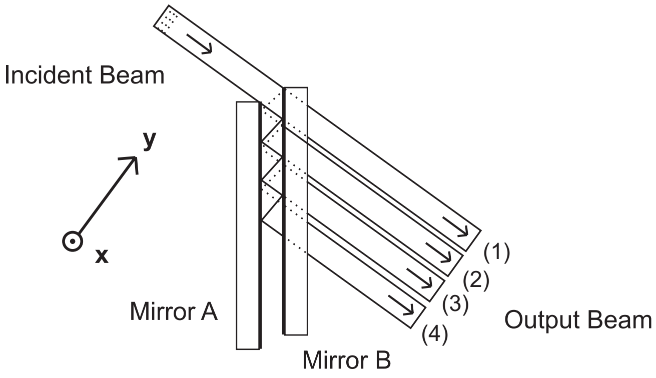

(b) side view

Figure 2.5: Two-mirror beam shaper: (a) plan view (b) side view

#### 2.3.1.3 Polarisation combining

Diode lasers have highly polarised output, which are not always required in their applications. It is therefore possible to exploit this to reduce the beam propagation factor ($M^2$) in the slow axis by up to a factor-of-two. In this approach, shown in Figure 2.6, the beam is halved at the beam waist using a knife-edge mirror to produce two beams of roughly equal beam dimensions and each with a beam propagation factor which is half that of the incident beam. One arm's polarisation is then rotated using a half-wave plate so that it's orthogonal to the other arm. The two beams are then polarisation combined using a polarising beam splitter, with the final output having half the input beam propagation factor in the slow axis, and limited beam quality degradation in the fast axis.

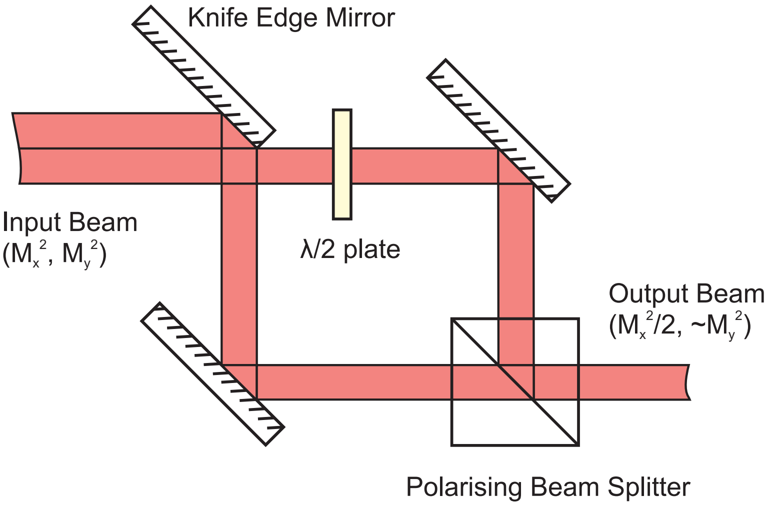

Figure 2.6: Schematic of polarisation recombining using a knife edge mirror, half-wave plate and polarising beam splitter.

### 2.3.2 Fibre lasers

In step-index fibres, pump light is either directly launched into the core or is alternatively launched into the inner cladding, depending on the pump beam parameters, as shown in Figure 2.7. As can be seen, the refractive index profile is different depending on where the pump light is guided. For core pumping, the fibre is typically designed such that $n_{clad} < n_{core} < n_{outer}$ for a step-index fibre, so that only core propagation modes are supported. Core pumping has the advantage of a high absorption compared to cladding pumping due to the strong overlap between the pump and doped region. As a result, much shorter device lengths can be used which is ideal for some applications, such as for Distribute Feedback (DFB) lasers. Furthermore, the output signal wavelength of a fibre laser is dependent on fibre length, where Clarkson et al [19] show that in Tm-doped silica, when the device length is increased the operational wavelength is also increased because of the reduced re-absorption loss for longer wavelengths.

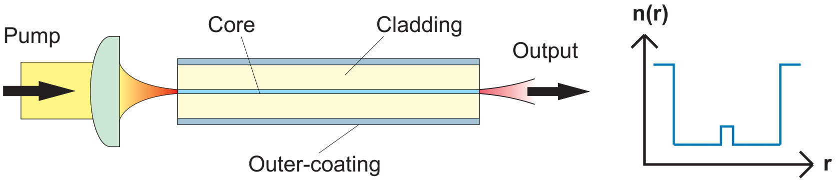

(a) Core Pumping

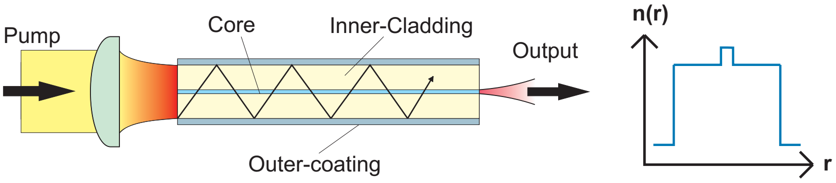

(b) Cladding Pumping

Figure 2.7: Fibre cross-sections and radial refractive index profile for the fibre in a (a) core pumped and (b) cladding pumped fibre geometry

The limitation of core pumping is that when using single-mode fibres, the pump source will typically need to have a low beam propagation factor to obtain a high launch efficiency. A rough estimation of the required beam propagation factor can be calculated from equation (2.5), where the paraxial approximation for small angles is applied such that the far-field divergence is given by $\sin\theta \approx \theta = NA$, the core's numerical aperture. For a fibre to be single-mode it is defined as having a V-value of $V < 2.405$ for a step-index fibre, where the V-value is given by

$$V = \frac{2\pi r_{core}}{\lambda} NA \tag{2.11}$$

For a typical single-mode fibre operating at 2$\mu m$, the core radius is $\sim$5$\mu m$ with an NA of $\sim$0.15. For diode pumping at 790nm (to take advantage of the beneficial two-for-one cross-relaxation), the diode output beam propagation factor will need to be $M^2 < 3$. Therefore, higher pump power arrays can not be used due to their low brightness. As a result, the output from core pumped fibre lasers will typically be limited to lower operational power levels.

To scale the output power in fibre lasers, high power diode lasers must be used. To accommodate these low brightness sources, the fibre design must be altered such that the inner cladding refractive index is changed to allow cladding guiding modes (i.e. $n_{outer} < n_{clad} < n_{core}$). In this case, the restriction on the maximum pump beam propagation factor can be relaxed, as can be seen by equation (2.5) due to an increased spot size and NA. However, light launched into the inner cladding will only partially overlap with the core as it propagates along the fibre and is absorbed. As a result, the device lengths required for efficient pump absorption will be significantly increased compared to core pumping. Many inner-cladding structures have been designed to increase the pump overlap with the core, with some examples shown in Figure 2.8 [19–21]. The conventional inner cladding geometry consists of a circular cladding with a central core due to the simplicity of its manufacture. However, with this geometry, some guided ray trajectories do not pass through the core, thereby hindering effective pump absorption. One approach to overcome this is to offset the fibre core so that these pump trajectories now overlap with the core, as seen in Figure 2.8(b). However, for this to be practical the core has to be offset by a large amount, which makes fabrication more challenging. Alternatively, the inner cladding geometry can be changed such that these guided rays are re-directed to overlap with the core. The choice of the inner cladding geometry is dependent on the fibre's application. For example, if the fibre was going to be spliced to other fibres the only design that is relatively easy to splice (other than circular) is the polygon-shaped inner cladding.

Alternatively, if the diode pump source has not been beam shaped and has an asymmetrical beam, then the rectangular inner cladding may be suitable for aiding the pump launch, as well as pump absorption. For most free space laser systems, increased pump absorption is obtained by using a D-shaped inner cladding due to the flat surface breaking the symmetry, as well as the fibre being relatively easy to fabricate.

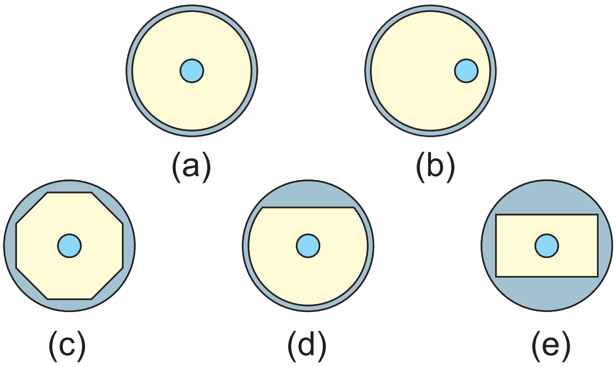

Figure 2.8: Fibre cross-sections for different inner cladding geometries: (a) Circular, (b) Circular with an offset core, (c) Polygon-shaped, (d) D-shaped, and (e) Rectangular.

Applying these cladding geometries enables the fibre to achieve its absorption coefficient. However, for increased absorption, either the doping concentration and/or the core size need to be increased. Increasing the core size is commonly used as the larger core, and resulting increased absorption coefficient, allows shorter device lengths to be used whilst maintaining a high pump absorption efficiency, which has the benefit of reducing the impact of detrimental nonlinear effects, which are discussed in more detail later. In order for this larger core fibre to remain single-mode the core NA must be reduced. However, the minimum NA that is achievable in conventional step-index fibres is $\sim$0.04-0.05. This places an upper limit on the core radius before more advanced fibre designs are required to scale it further. For a fibre operating at 2$\mu m$, this means the largest core radius obtainable that still supports only the fundamental mode is $r_{core}$ $\sim$19$\mu m$.

In addition to pump absorption considerations, the inner-cladding can also be modified to induce a birefringence in the fibre, enabling the core propagation to be polarisation-maintaining (PM). This is desirable for polarised laser cavities and polarised master oscillator power amplifier configurations. The two commonly used approaches are the bow-tie design and the Panda design, aptly named after the cross section patterns as seen in Figure 2.9.

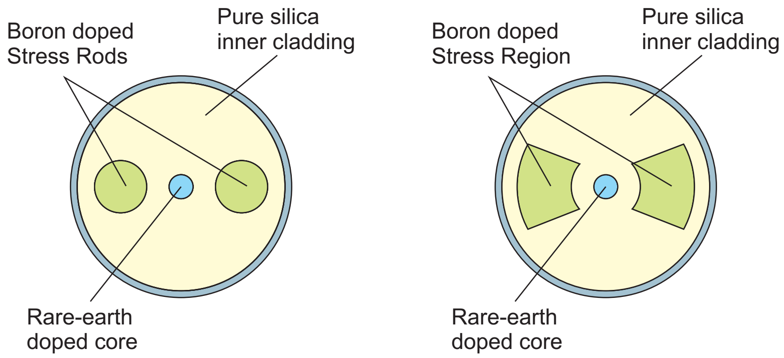

(a) Panda (b) Bow-Tie

Figure 2.9: Fibre cross-sections for polarisation-maintaining fibres using (a) the Panda and (b) the Bow-tie approach.

### 2.3.3 End-pumped laser rods

The advantage of end-pumping over other schemes, such as side-pumping, is that it ensures a good spatial overlap between the pump beam and the laser cavity mode and therefore a high inversion density only in this region. Additionally, closely matching the pump beam and fundamental laser mode helps to reduce the gain available to higher order modes outside the fundamental mode region, which reduces wasted pump energy implying a greater overall efficiency, as well as avoiding multi-mode operation. This is desirable as in the absence of any beam quality degradation, the output for the laser will be approximately diffraction limited ($M^2 \sim 1$).

To obtain a reasonable threshold condition, such that $P_{thres} \ll P_{p\,max}$, requires the pump beam and laser mode to be small in the pumped region of the crystal. The constraint for this is often determined by the pump source's beam propagation factor. For a given crystal length the minimum pumped volume can be calculated from the beam size as a function of position through the beam focus, given by

$$\omega(z) = \omega_0 \left[1 + \left(\frac{z}{z_0}\right)^2\right]^{\frac{1}{2}} \tag{2.12}$$

where $\omega(z)$ is the beam size at position $z$, $\omega_0$ is the beam waist, and $z_0$ is the Rayleigh range defined as the distance from the beam waist position to where the beam radius has expanded to $\sqrt{2}w_0$. The Rayleigh range is given by

$$z_0 = \frac{n\pi w_0^2}{M^2\lambda} \tag{2.13}$$

where $\lambda$ is the laser wavelength, n is the refractive index of the material and $M^2$ is the beam propagation factor. The beam waist is defined as

$$w_0 = \frac{M^2\lambda}{n\pi\theta} \tag{2.14}$$

for the far field divergence $\theta$. These parameters are shown in Figure 2.10. The minimum pump volume can be calculated from equation (2.12) by setting the beam waist half way along the crystal and by assuming a circular symmetrical beam. By squaring both sides and multiplying by $\pi$, the beam area as a function of position is given by

$$\pi\omega^2(z) = \pi\omega_0^2 \left[1 + \left(\frac{z}{z_0}\right)^2\right] \tag{2.15}$$

Now integrating equation (2.15) between $0$ and $l/2$ gives the volume of half the crystal as

$$\frac{V_{pump}}{2} = \frac{\pi\omega_0^2}{2}\left(l + \frac{l^3}{12z_0^2}\right) \tag{2.16}$$

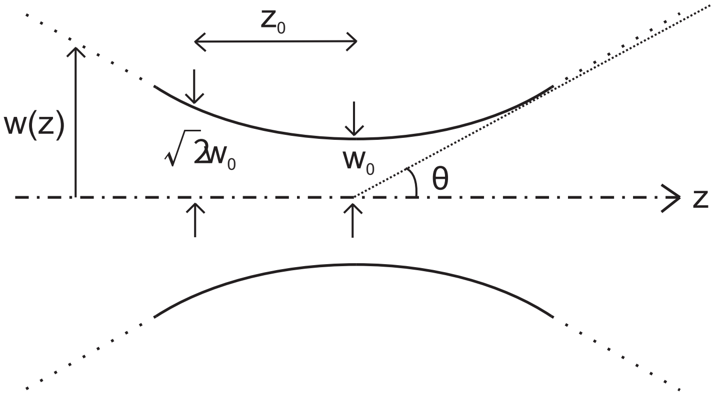

Figure 2.10: Schematic showing the beam size as it propagates through a beam waist ($w_0$).

The minimum volume is calculated by differentiating this with respect to $l$ and setting it to 0, such that

$$\frac{dV_{pump}}{dl} = \pi\omega_0^2\left(1+\frac{l^2}{4z_0^2}\right) = 0 \tag{2.17}$$

therefore the minimum volume is achieved when $l = 2z_0$, where twice the Rayleigh range is known as the confocal parameter. For this reason, this pumping configuration is called confocal pumping. If the rod length is longer than the length over which most of the absorption occurs, then as a rough guide the confocal parameter can be reduced to three absorption lengths, $l_\alpha = 1/\alpha_P$, which corresponds to 95% absorption of the incident pump light. Adjusting the confocal parameter to this shorter length will reduce the beam waist size and therefore reduce the threshold condition.

## 2.4 Thermal effects

In any laser system, power scaling is limited due to thermally induced effects caused by pump energy converted to heat. This section highlights some of the main sources of heat generation in laser systems and the main effects it has on laser performance. The limits imposed by thermal effects are considered below for silica step-index fibres and 'bulk' lasers based on cylindrical YAG rods. Understanding these limits and the factors that contribute to them enables laser systems to be designed such that thermally induced limits on performance can be reduced, with the result that higher output powers can be obtained, as discussed below.

### 2.4.1 Sources of unwanted heat

Thermal management in laser systems has an important role for obtaining efficient laser operation. Heat generation in laser systems has many origins including: quantum defect heating, excited-state absorption (ESA), energy-transfer upconversion (ETU), as well as absorption by impurities. Quantum defect heating, shown in Figure 2.11(a), is caused by the net difference in energy between the pump and laser signal photons (ie $\Delta E = h\nu_p - h\nu_L$), such that the excess energy is converted to heat, increasing the laser material's temperature. ESA, shown in Figure 2.11(b), is where an ion in the upper laser level absorbs a pump or signal photon and is excited to a higher energy level. From this higher level the ion decays back to the upper laser level via non-radiative transitions, therefore increasing the material temperature. Similarly, ETU is a process, shown in Figure 2.11(c), where two excited ions in close proximity exchange energy such that one ion is de-excited to a lower energy level and the other excited to a higher one. The excited ion can then decay back to the upper laser level via non-radiative decay, with the energy difference between the levels converted to heat. This ETU process is strongly dependent on the rare-earth ion concentration and excitation density, with it becoming more significant when both are high.

### 2.4.2 Critical failure limits

An edge mounted laser rod or fibre laser with its outer cladding heat sunk or convection cooled can be considered as a cylindrical geometry with periphery

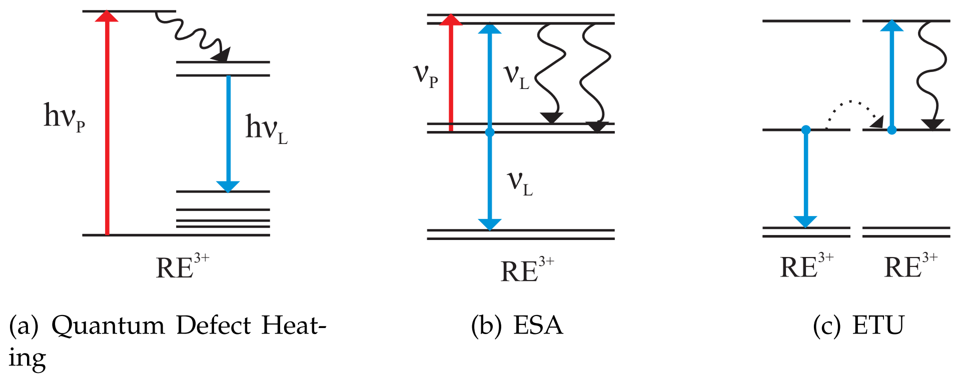

(a) Quantum Defect Heating (b) ESA (c) ETU

Figure 2.11: Energy level representation for (a) Quantum defect heating, (b) ESA, and (c) ETU.

at a fixed temperature. Under steady state conditions the heat flux $\underline{h}(r,z)$ must satisfy the equation [22]:

$$\underline{\nabla}.\underline{h}(r,z) = Q(r,z) \tag{2.18}$$

where $Q(r,z)$ is the heat deposition density, $Q(r,z) = dP(r,z)/dV$, and P(r,z) is power converted to heat. From Fourier's Law, the heat flux results in a temperature distribution $T(r,z)$ given by [22]

$$\underline{h}(r,z) = -k\underline{\nabla}T(r,z) \tag{2.19}$$

By making the simplifying approximation that the axial heat flow is negligible and therefore that the heat flow is purely radial, then the total radial heat flow from a volume bounded by $z$ and $\Delta z$ is equal to the net heat generated in the region [22]

$$2\pi r\Delta z h(r,z) = \int_{z}^{z+\Delta z}\int_{0}^{r} 2\pi r' Q(r',z)dr'dz' \tag{2.20}$$

For a constant heat deposition density within the pumped region (ie $r < r_p$) and no heat load outside this region, the heat flux is given by

$$h(r,z) = \frac{P_p(z)\alpha_p\gamma_h r}{2\pi {r_p}^2} \qquad for\ (r \leq r_p) \tag{2.21}$$

$$h(r,z) = \frac{P_p(z)\alpha_p\gamma_h}{2\pi r} \qquad for\ (r > r_p) \tag{2.22}$$

where $P_p(z) = P_p(0)\exp(-\alpha z)$ is the pump power at position $z$, $\gamma_h$ is the fraction of the pump power converted to heat, $\alpha_p$ is the absorption coefficient for pump light, and $r_p$ is the pump beam radius (where $r_p$ is the core radius in fibres).

Applying the boundary conditions that $h(r,z)$ and $T(r,z)$ are continuous at the boundaries between layers, the temperature distribution can be obtained from equation (2.19) as being

$$\Delta T(r,z) = T(r,z) - T(0,z) = -\frac{1}{k}\int_0^r h(r',z)dr' \tag{2.23}$$

In the case of a rod, the temperature distribution is given by

$$T(0,z) - T_s = \frac{P_h(z)}{4\pi}\left[\frac{1}{k_1} + \frac{2}{k_1}\ln\left(\frac{r_1}{r_p}\right) + \frac{2}{r_1 H_1}\right] \tag{2.24}$$

and for a double clad fibre is given by

$$T(0,z) - T_s = \frac{P_h(z)}{4\pi}\left[\frac{1}{k_1} + \frac{2}{k_1}\ln\left(\frac{r_1}{r_p}\right) + \frac{2}{k_2}\ln\left(\frac{r_2}{r_1}\right) + \frac{2}{r_2 H_2}\right] \tag{2.25}$$

where $P_h(z) = P_p(z)\alpha_p\gamma_h$ is the heat generated per unit length, $T_s$ is the ambient temperature of the surroundings, $T(0,z)$ is the temperature in the centre of the material (and pumped region), $r_1$ is the rod/inner cladding radius, $r_2$ is the outer polymer coating radius, $k_1$ is the thermal conductivity of the laser rod or the core and inner cladding of the fibre, $k_2$ is the thermal conductivity of the outer polymer coating of a double clad fibre, and $H_{1,2}$ are the heat transfer coefficients for laser rod and the outer polymer coating, respectively.

Using these equations, the heat deposition per unit length required to soften, melt or damage the material can be calculated, thus yielding a critical failure value for a laser rod as being

$$P_{h\ max} = 4\pi(T_m - T_s)\left[\frac{1}{k_1} + \frac{2}{k_1}\ln\left(\frac{r_1}{r_p}\right) + \frac{2}{r_1 H_1}\right]^{-1} \tag{2.26}$$

and for a double clad fibre as

$$P_{h\ max} = 4\pi(T_m - T_s)\left[\frac{1}{k_1} + \frac{2}{k_1}\ln\left(\frac{r_1}{r_p}\right) + \frac{2}{k_2}\ln\left(\frac{r_2}{r_1}\right) + \frac{2}{r_2 H_2}\right]^{-1} \tag{2.27}$$

where $T_m$ is the softening, melting or damage temperature of the material.

If silica fibres are considered, the thermal load required to melt the silica can be seen in Figure 2.12, where it is plotted for a 25$\mu m$ core fibre with inner cladding diameters of 200$\mu m$, 400$\mu m$ and 600$\mu m$, and a 50$\mu m$ thick outer polymer cladding. These inner claddings were chosen due to them typically being used and to highlight the increase in the required thermal load to melt silica for a given heat transfer coefficient. Figure 2.12 shows that for low power systems, convection cooling (ie. $H$ ~10Wm$^{-2}$K$^{-1}$ [23]) is sufficient for keeping a fibre below its melting point. However, for high power lasers, the pump power available from commercially available diodes can be of the order of several kW's, meaning that there is an inherently higher thermal load in the laser rod which requires the heat transfer coefficient to be in excess of 1000Wm$^{-2}$K$^{-1}$ to remain below the melting temperature of silica.

However, considering only the melting point of silica is not the whole story as the outer polymer coating has a much lower damage threshold of typically $T_d \approx 150°C$, which can be reached before the core temperature reaches silica's melting point. The heat deposition per unit length required for the outer polymer coating to reach its damage limit can be calculated from

$$P_{h\ max} = 4\pi(T_d - T_s)\left[\frac{2}{k_2}\ln\left(\frac{r_2}{r_1}\right) + \frac{2}{r_2 H_2}\right]^{-1} \tag{2.28}$$

Figure 2.13 shows the heat deposition per unit length required to melt/soften the outer polymer coating as a function of the heat transfer coefficient for the same fibre dimension used in Figure 2.12. It can clearly be seen that the outer polymer coating damage threshold will be reached well before that of silica. Therefore, from equation (2.28) and the Figure, it can be seen that the strategy required for scaling to higher power levels is to increase the inner cladding

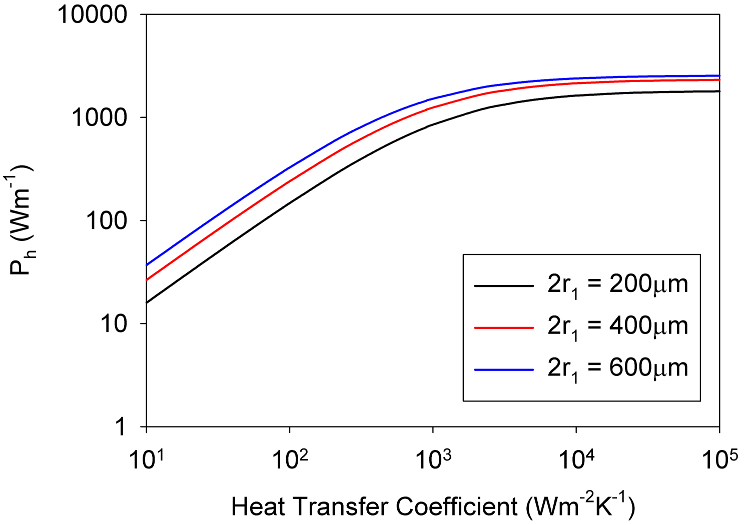

Figure 2.12: The maximum heat deposition required to reach the melting point in the core as a function of the heat transfer coefficient for a 25$\mu m$ diameter core fibre and an inner cladding diameter of 200$\mu m$, 400$\mu m$ and 600$\mu m$, and an outer polymer coating thickness of 50$\mu m$. The melting point of silica is used as $T_m \approx 2000^\circ K$, the surrounding temperature $T_s = 293^\circ K$, and the thermal conductivity for silica and the outer polymer coating of 1.38W/mK [24] and 0.1W/mK, respectively.

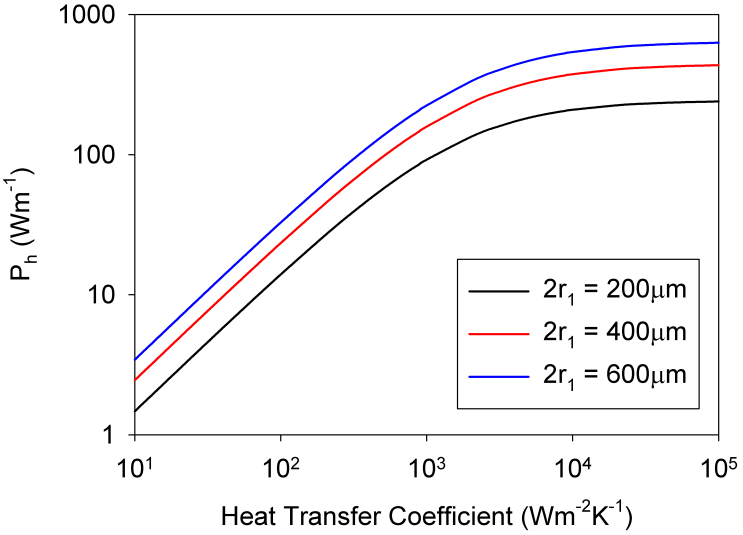

Figure 2.13: The maximum heat deposition required to reach the damage limit of the outer polymer coating as a function of the heat transfer coefficient for a $25\mu m$ diameter core fibre and an inner cladding diameter of $200\mu m$, $400\mu m$ and $600\mu m$, and an outer polymer coating thickness of $50\mu m$. Using the damage limit of coating as $T_d \approx 450^{\circ}K$, the surrounding temperature $T_s = 293^{\circ}K$, and the thermal conductivity of the outer polymer coating is ∼0.1W/mK.

diameter whilst reducing the outer polymer coating thickness. Additionally, employing a good thermal management system around the fibre will enable higher heat transfer coefficients to be obtained. For example, mounting the fibre in a v-groove heat sink with water cooling will improve the heat transfer coefficient over that from convection cooling, as the thermal conductivity is increased due to the mount having a higher thermal conductivity than air combined with active removal of the heat to an external water cooler allowing the temperature of the block to remain constant. Furthermore, for a cladding pumped laser, increasing the inner cladding radius will reduce the absorption coefficient for a fixed core radius, which means that a longer device length is required to obtain efficient pump absorption. As a result, the power dissipated as heat per unit length is reduced, thereby increasing the total power converted to heat required to reach the damage limit for a given coating and heat transfer coefficient.

The melting threshold in bulk laser rods is now considered. Using the example of a 5mm diameter YAG laser rod (as this is of interest in this thesis), the thermal load required to melt it, as a function of the pump beam diameter and the heat transfer coefficient, can be seen in Figure 2.14. The pump beam sizes of 200$\mu m$, 500$\mu m$ and 1mm in diameter were chosen to highlight the difference beam size has in the typical range used in bulk laser systems. Figure 2.14 shows that the heat deposition density per unit length required to reach this limit is very high for heat transfer coefficients $H$ >10Wm$^{-2}$K$^{-1}$. However, given the short crystal lengths used in solid-state lasers, typically less than a few centimetres, the heat deposition density is much higher than in a fibre laser system. As a result, very small thermal loads can cause crystal damage without adequate cooling. This is highlighted if we use the example rod in Figure 2.14 which is convectively cooled ($H$ ~10Wm$^{-2}$K$^{-1}$ [23]), in which case the required power dissipated as heat to melt a 3cm long YAG rod is only ~10W. Thus, for high power operation the rod requires active cooling, which is achieved with a water cooled heat sink with a good thermal contact along the shaft of the rod. In this case, for the same 3cm long rod, from Figure 2.14 it can be seen that for a given pump spot size the power dissipated as heat would need to be greater than 450W for $H$ >1000Wm$^{-2}$K$^{-1}$, which is achievable with water cooling using a air cooled heat exchanger (where the heat transfer coefficient for the exchanger varies from between 600-750Wm$^{-2}$K$^{-1}$ [25]), and for $P_h$ >1kW requires $H$=10$^5$Wm$^{-2}$K$^{-1}$ which is not practically achievable. It needs to be acknowledged that different bulk materials will have a different melting point, so the thermal loads required for melting will differ. However, in general they are all the same in that they will all require active cooling for high power operation.

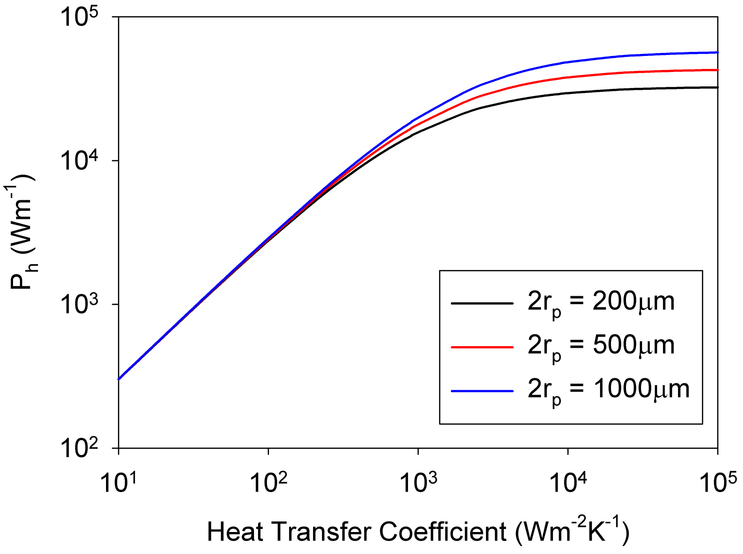

Figure 2.14: The maximum heat deposition required to reach the melting point in YAG as a function of the heat transfer coefficient for a 5mm diameter rod and pump beam diameters of 200$\mu m$, 500$\mu m$ and 1mm. The melting point of YAG was used as $T_m \approx 2220°K$, the surrounding temperature $T_s = 293°K$, and the thermal conductivity of YAG as ~10W/mK [26].

In addition to thermal damage, the radial variation in temperature will result in induced stresses due to the differential expansion with temperature across the material, which can lead to fractures in the material. Bulk crystalline solids and some glassy materials are stronger in compression than in tension, making surfaces susceptible to fracture due to the tangential and $z$ direction tensile forces [23]. This critical fracture limit can be calculated in terms of the heat deposition per unit length as being [23]

$$P_{h\ max} = \frac{4\pi R_t}{1 - \left(\frac{r_p^2}{2r_1^2}\right)} \tag{2.29}$$

where

$$R_t = \frac{k_1 \sigma_{max}(1-\nu)}{\alpha E} \tag{2.30}$$

is the Thermal shock parameter. For $r_p^2/r_1^2 \ll 1$ this simplifies such that

$$P_{h\ max} \approx 4\pi R_t \tag{2.31}$$

It is worth noting that these calculations for the stress-fracture limit are only a guide, as the actual fracture point is very dependent on the material quality and the surface finish [13,23].

The stress fracture limit in silica can be estimated using the values of $k_{silica} = 1.38W/mK$ [24], $\alpha = 0.55 \times 10^{-6} K^{-1}$ [24], $\sigma_{max} = 150MPa$ [24], $E = 73GPa$ [23], and $\nu = 0.16$ [23]. Using these values gives a thermal shock parameter of $R_t = 4330W/m$. Using the fibre dimensions from the melting point calculations, the maximum heat deposition per unit length at which stress fracture occurs is ∼45.4kW/m. This is clearly well above the heat deposition density achievable with available laser diode technology. Furthermore, the required power is far in excess of the damage point of the outer polymer cladding which will limit power scaling well before the thermal load for stress fracture is achieved.

This is not the case for the stress induced fracture limit in YAG. Using the values $\nu = 0.25$ [27], $k = 10W/mK$ [26], $\sigma_{max} = 280MPa$ [28], $E = 282GPa$ [28], $\alpha = 6.65 \times 10^{-6} K^{-1}$ (calculated for 293K using [28]), the thermal shock parameter is $R_t = 1120W/m$. Therefore, using equation (2.31) the maximum heat deposition is 14kW/m. In YLF $R_t = 180W/m$ [29], so the heat deposition to fracture the crystal is 2.25kW/m, which is a factor of 7 lower than for YAG.

Given that solid state laser crystals are typically of the order of a few centimetres, this means that the power converted to heat to reach the stress fracture point can be of the order of a few hundred watts. So, for high power systems with a high quantum defect, plus other sources of heat, this can pose a serious constraint on performance. This is especially true when the surface quality of the rod is considered as this can reduce the stress limit significantly [24].

### 2.4.3 Performance degrading effects

Before the critical failure limits discussed above are reached, the temperature distribution in the material will result in stress induced birefringence, thermal lensing in bulk materials, and thermal guiding in fibres, which can all seriously degrade the laser performance. The induced stresses in the radial and tangential directions are different such that the resulting refractive index in each direction is also different, causing an induced birefringence in the material. In a polarised cavity configuration, the induced birefringence will result in an additional cavity loss. This de-polarisation loss is given by [30]

$$L_d = \frac{\int_0^{2\pi}\int_0^{w_l}[I_{in}(r,\phi)f_d(r,\phi)]rdrd\phi}{\int_0^{2\pi}\int_0^{w_l}I_{in}(r,\phi)rdrd\phi} \tag{2.32}$$

where $I_{in}(r,\phi)$ is the intensity beam profile and $f_d(r,\phi)$ is the de-polarisation loss, with both being functions of the radius $r$ and the angle $\phi$. For a pump beam with a 'top-hat' intensity function, such that the intensity is 0 for beam radii greater than the beam radius $w_p$, and that the pump absorption is uniform along the rod, the de-polarisation function for a round-trip in the cavity is given by [30]

$$f_d(r,\phi) = [\sin(C_T P_{hT}(r/w_p)^2)]^2[\sin(2\phi)]^2 \tag{2.33}$$

where $P_{hT} = \int_0^z P_h(z)dz = P_p(0)(1-\exp(-\alpha_p z))\gamma_h$, and $C_T = \frac{2n_0^2\alpha C_B}{\lambda k}$ where $C_B$ defined by Koecher [13] is a function of the material's elasto-optical coefficients. Making the simplifying assumption that the laser beam radius, $w_l$, is less than the pump beam radius, the de-polarisation loss is given by [30]

$$L_d = \frac{1}{4}\left[1 - \frac{\sin\left(2C_T P_{hT}\left(\frac{w_l}{w_p}\right)^2\right)}{2C_T P_{hT}\left(\frac{w_l}{w_p}\right)^2}\right] \tag{2.34}$$

The significance of this additional cavity loss becomes apparent when the laser performance is considered, with an increased loss resulting in a increased threshold pump power and a decreased slope efficiency.

In polarised solid-state laser cavities, the depolarisation loss can significantly affect the laser performance. Figure 2.15 shows the de-polarisation loss as a function of the dissipated heat, as well as its impact in a loss-less cavity with a 10% transmitting output mirror. This was calculated assuming that $w_l/w_p = 1$ and using the values of $\nu = 0.25$ [27], $E = 2.84 \times 10^6\ kg.m/cm^2$ [27], $k = 10W/mK$ [26], $\alpha = 6.65 \times 10^{-6}K^{-1}$ calculated for 293K using [28], $C_B = -0.00474$ (calculated using $C_B$ defined in Koecher [13] and the values $p_{11} = -0.07145$, $p_{12} = 0.02325$ and $p_{14} = -0.0332$ [31]) and therefore $C_T = -9.77 \times 10^{-3}W^{-1}$. It shows that above ~10W of total dissipated heat the slope efficiency begins to reduce. This fall off continues such that by 80W of total heat load, the slope efficiency will be reduced by 50%. This heat load is well within practical pumping loads so would need to be addressed for further power scaling. In addition to the decrease in slope efficiency, the threshold will increase as the de-polarisation loss increases, further reducing the output performance of the laser. Various approaches for overcoming the de-polarisation loss have been developed (for examples see [13,30,32,33]). However, these are not described further, as the method employed in Chapter 5 for counteracting the de-polarisation loss in YAG uses cryogenic cooling to beneficially change the thermo-optic properties in YAG, such that the de-polarisation loss is significantly reduced. Therefore, the methods employed in the examples above for reducing the de-polarisation loss are not required.

In fibre lasers, thermally induced stress birefringence would not normally be considered, given that fibres are not polarisation maintaining (PM), without

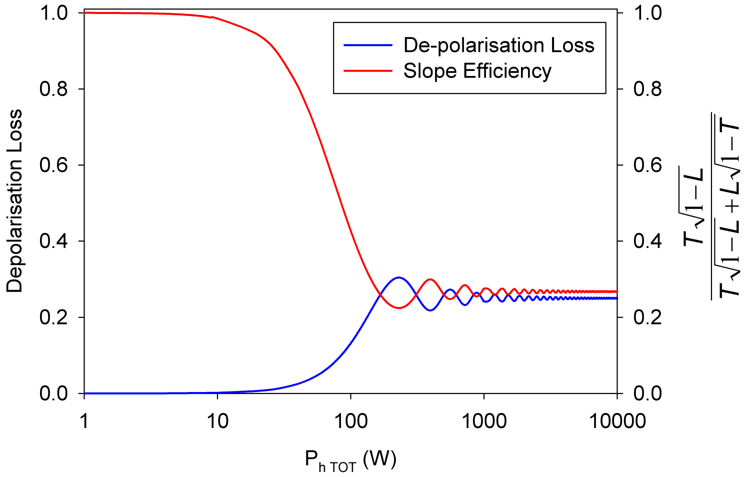

Figure 2.15: Showing the impact of the de-polarisation loss in a YAG laser rod as a function of total dissipated heat and the impact of this loss on the slope efficiency due to the $\frac{T\sqrt{1-L}}{T\sqrt{1-L}+L\sqrt{1-T}}$ component, for a cavity with a 10% transmitting output coupler and no additional cavity losses.

the use of specially designed fibres, as previously discussed. In the case of these PM fibres, the induced birefringence caused by the stress rods should exceed any caused by thermally induced stresses. This can be seen when one compares the stress induced birefringence in a PM fibre which is of the order of $\Delta n_r - \Delta n_\phi \sim 10^{-4}$ [34] to those thermally induced of $10^{-6}$ for reasonable heat loads. Therefore, thermally induced birefringence should not be a limitation for fibre lasers.

For end-pumped solid state lasers in a rod geometry, the radial variation in refractive index with temperature results in a thermal lens. There are three main components that determine the strength of this thermal lens, which are the temperature dependent refractive index (dn/dT), stress induced changes in refractive index, and end face curvature. In YAG, the dominant factor is the dependence on dn/dT which in the case of Nd:YAG was reported to account for 80% of the thermal lensing focal length [13]. The relative contributions do however vary between laser hosts depending on the particular material's thermo-mechanical and thermo-optical properties. Clarkson [33] derived expressions for the thermal lens of a 'top-hat' and Gaussian pump intensity profile, with the simplifying assumptions that the axial heat flow is negligible and the only contribution to thermal lensing is from the temperature dependent refractive index. From these assumptions, the thermal lens focal length for an arbitrary intensity profile $I_P(r)$ was expressed as [33]

$$f_{th}(r) = \frac{2\pi k r^2}{P_p \gamma_h \eta_{abs} \frac{dn}{dT} s(r)} = \frac{2\pi k r^2}{P_{hT} \frac{dn}{dT} s(r)} \tag{2.35}$$

where $s(r)$ is the fraction of the pump power contained within a disc of radius $r$ given by

$$s(r) = \frac{2\pi}{P_p} \int_0^r r' I_p(r') dr' \tag{2.36}$$

In general, equation (2.35) predicts a thermal lens with a radially varying focal length for a pump beam that has a radially varying intensity. For most practical pump beam profiles, which have a strong radial intensity variation, this implies a highly aberrated thermal lens that will severely degrade the beam quality. To highlight the impact of the pump beam intensity profile on the thermal lens, the special cases of a 'top-hat' and Gaussian profile are considered.

For 'top-hat' pumping, the intensity profile is uniform across the pump beam radius $w_p$, such that $I_p = P_p/\pi w_p^2$ for $r \leq w_p$ and $I_p = 0$ for $r > w_p$. Therefore, the thermal lens focal length of a 'top-hat' intensity profile is [33]

$$f_{th}(r) = \frac{2\pi k w_p^2}{P_{hT} \frac{dn}{dT}} \qquad for\ (r \leq w_p) \tag{2.37}$$

$$f_{th}(r) = \frac{2\pi k r^2}{P_{hT} \frac{dn}{dT}} \qquad for\ (r > w_p) \tag{2.38}$$

From equations (2.37) and (2.38) it can be seen that for $r \leq w_p$ the thermal lens is independent of the radius, and as such for $w_l < w_p$ the beam is not aberrated. However, for $w_l > w_p$ the focal length varies with $r^2$ suggesting that the beam will become highly aberrated for high thermal loads.

For a Gaussian pump profile with $I_p(r) = \frac{2P_p}{\pi w_p} \exp\left(\frac{-2r^2}{w_p^2}\right)$ the thermal lens focal length is [33]

$$f_{th}(r) = \frac{2r^2 f_{th}(0)}{w_p^2[1 - \exp(-2r^2/w_p^2)]} \tag{2.39}$$

where $f_{th}(0)$ is the focal length on axis given by

$$f_{th}(0) = \frac{\pi k w_p^2}{P_{hT} \frac{dn}{dT}} \tag{2.40}$$

This implies that for a Gaussian pump profile, the thermal lens on axis is a factor of two stronger than the 'top-hat' profile, and is highly aberrated for both $r \leq w_p$ and $r > w_p$. The significance of this is that although the Gaussian pump beam will have a better spatial overlap with the fundamental mode and therefore a lower threshold and higher slope efficiency than for a 'top-hat' pump beam profile, it does however suffer from a more pronounced beam distortion and degradation in the laser beam quality.

Siegman [35] used a quartic approximation of the phase aberration of a spherical lens to express the degradation in beam quality for a Gaussian laser signal for a plano-convex lens. For an input beam propagation factor $M_i^2$, the final beam propagation factor $M_f^2$ after passing through the medium, is given by

$$M_f^2 = \sqrt{(M_i^2)^2 + (M_q^2)^2} \tag{2.41}$$

where $M_q^2$ is the degradation to the beam propagation factor for a quartic phase aberration. Using this approximation for the phase aberration caused by a thermal lens, Clarkson [33] showed that for a thermal lens generated by an arbitrary pump intensity profile $I_p(r)$ and with the simplifying assumption that $w_l < w_p$, so that higher order aberrations can be neglected, the beam propagation degradation factor is given by

$$M_q^2 = \frac{\gamma_h \eta_{abs} \pi w_l^4}{4k\lambda\sqrt{2}} \frac{dn}{dT} \frac{d^2 I_p(r)}{dr^2} \qquad at\ r = 0 \tag{2.42}$$

For a 'top-hat' pump intensity profile $d^2I_p(r)/dr^2 = 0$ implying that there is no degradation in beam quality, supporting equation (2.37). However, for a Gaussian pump intensity profile, $d^2I_p(r)/dr^2 = 8P_p/\pi w_p^4$ for $r = 0$, which implies that

$$M_q^2 = \frac{dn}{dT}\frac{2P_{hT}}{k\lambda\sqrt{2}}\left(\frac{w_l}{w_p}\right)^4 \tag{2.43}$$

This indicates that the beam quality degradation is not only dependent on the power dissipated as heat, $dn/dT$ and the thermal conductivity, but also very strongly on the signal to pump overlap. It can be seen that choosing $w_l < w_p$ helps to reduce the beam quality degradation, but does have the disadvantage that the laser intensity in the wings may be too low to saturate the gain in the outer sections of the pumped region, leading to a reduction in efficiency, as well as higher order mode lasing resulting in reduced beam quality.

Using equation (2.43) for a Gaussian pump beam, the power dissipated as heat required for the beam quality to be significantly degraded can be calculated. For example, if the beam propagation factor was $M^2$=1, and a final beam propagation factor of $M_f^2 \leq$1.2 was acceptable (i.e. $M_q^2$=0.66), the maximum heat dissipated would be

$$P_{hT} = \frac{0.47k\lambda}{\frac{dn}{dT}}\left(\frac{w_p}{w_l}\right)^4 \tag{2.44}$$

For an edge cooled Tm:YAG rod operating at 2$\mu m$, where $dn/dT = 10 \times 10^{-6}$ [23], $k = 10Wm^{-1}K^{-1}$ [26] and with a $w_p/w_l \sim 1$, then the maximum power dissipated as heat for the beam propagation factor to be increased to $M_f^2 \leq$1.2 is $P_{hT} \leq 1.2$W. This implies an absorbed pump power of ~6W (assuming $\gamma_h$=0.2, i.e. that there is perfect two-for-one cross-relaxation), which means that the beam quality degradation will become observable at low power levels. It is worth noting that Clarkson's [33] work above is only strictly valid for a single pass of a pump laser rod. However, even considering this, the analysis still suggests that laser performance will become degraded for thermal loads of a few tens of watts, and therefore will be a major problem for power scaling.

For step-index fibres, the temperature increase, due to the power dissipated as heat, leads to changes in the core's refractive index. The radial variation in the refractive index is given by [36]

$$n(r) = n_0 - \frac{dn}{dT}\frac{P_h}{4\pi r_{core}^2 k}r^2 \tag{2.45}$$

where $n_0$ is the on axis refractive index and P$_h$ is the power dissipated as heat per unit length. The refractive index has a quadratic profile, so acts like a quadratic waveguide which has a guided Gaussian beam of constant radius, called the thermal guiding radius, given by [36]

$$w_{th} = \left(\frac{2k\lambda^2 r_{core}^2}{\pi n_0 P_h \frac{dn}{dT}}\right)^{1/4} \tag{2.46}$$

In fibre's this thermally guided mode can significantly impact the performance if it is less than the fundamental mode radius of the un-pumped step-index fibre. In silica fibres, the thermal guiding results in tighter mode confinement, resulting in a reduced overlap with the inversion at the edge of the core and therefore a decrease in efficiency for the fundamental mode. Additionally, the unsaturated gain around the edge of the core can allow higher order modes to oscillate or similarly ASE to see gain, which in both cases would reduce the output beam quality. The fundamental mode radius $w_0$ in a step-index fibre is given by [37] $w_0 = r_{core}/\sqrt{\ln V}$ where $V = 2\pi r_{core} NA/\lambda$ [38] and the fibre $NA$ is given by $NA = \sqrt{n_{core}^2 - n_{clad}^2}$ (for $NA \ll 1$). Thermal guiding will impact on the laser performance when $w_{th} \leq w_0$, meaning that it is a problem when

$$P_{h\ max} \geq \frac{2k\lambda^2(\ln V)^2}{\pi r_{core}^2 n_0 \frac{dn}{dT}} \tag{2.47}$$

For a step-index fibre to be single transverse mode the V-value has to be <2.405. Figure 2.16 shows the required dissipated heat for a single-mode fibre to become degraded due to thermal guiding as a function of the core radius. It can be seen that thermal guiding will have a greater effect on guiding and hence performance in larger cored fibres. Therefore, careful selection of the fibre geometry is required to balance the performance degradation limits from thermal guiding with the benefits gained by an increased core radius which increases the non-linear threshold signal intensity, as discussed in the next section. However, the Figure shows that the power dissipated as heat for thermal guiding to begin to degrade the performance is >450W/m for a 20$\mu m$ radius core fibre with a signal wavelength at 2$\mu m$, which would imply an absorbed pump power in excess of 750W/m (assuming $\gamma_h$=0.6). As such damage to the outer coating will limit the laser performance before thermal guiding becomes significant.

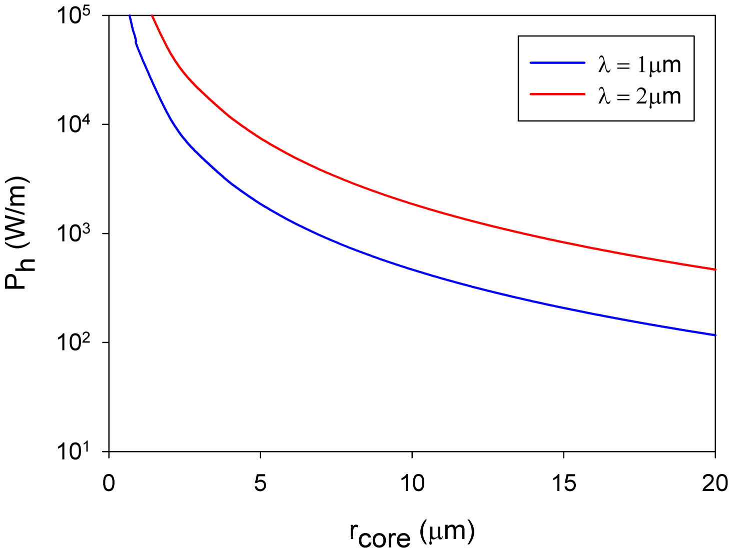

Figure 2.16: Showing the power dissipated per unit length for the thermal guiding mode size to equal the fundamental mode size in a step-index fibre with a V-value of 2.405 as a function of the core radius for a laser operating at 1$\mu m$ and 2$\mu m$. Calculated using $k_{silica} = 1.38W/mK$ [24], $dn/dT = 10 \times 10^{-6}$K$^{-1}$ [23] and $n_0 = 1.45$ [23].

However, this is not always necessarily the case when considering a laser operating at 1$\mu m$. It can be seen from Figure 2.16 that in a single mode fibre the required dissipated heat for thermal guiding to degrade performance at 1$\mu m$

is much lower than for the same radius single mode fibre at 2$\mu m$. For example, for a 20$\mu m$ core fibre the power dissipated as heat for thermal guiding to degrade the performance is $>$120W/m. This is 4 times lower than the required power at 2$\mu m$ for the same core radius and V-value. The reason for this difference is due to the core's NA at 2$\mu m$ being twice that of the core at 1$\mu m$ at a fixed core radius and V-value, as can be seen by the definition of the V-value, $V = 2\pi r_{core} NA/\lambda$ [38]. The significance of this is that fibre lasers operating at 2$\mu m$ are much less susceptible to thermal guiding than at 1$\mu m$, thus highlighting a potential benefit of operating fibre lasers at longer wavelengths. It is worth noting though that even at 1$\mu m$ the power required for thermal guiding to degrade the performance is still higher than the thermal load required to damage the outer polymer coating. But, depending on the fibre's thermal management approach, the thermal guiding at 1$\mu m$ could still impact on laser performance. This can be seen when a 200$\mu m$ radius inner cladding fibre with a 50$\mu m$ thick coating is considered (as used previously in Figure 2.13), where the heat transfer coefficient is 1000Wm$^{-2}$K$^{-1}$, the power dissipated as heat to damage the coating is only $\sim$160W/m. Therefore, it is possible at these thermal loads that thermal guiding is beginning to degrade laser performance before coating damage occurs.

In addition to the critical damage limits and the degradation in performance discussed in this section, the thermo-optical and thermo-mechanical properties of the material are also temperature dependent. These properties can significantly change the impact of induced stresses, thermal lensing and guiding, as well as the critical damage limits. The temperature dependence of these parameters is discussed more in Chapter 5, where their impact is more significant.

The changes in the material temperature also changes the spectroscopy. The most significant change is in the populations of the energy levels governed by the Boltzmann distribution. The significance of this is that the emission and absorption cross-sections are directly proportional to the thermal occupancies of the levels. These occupancies are given by

$$f_i = \frac{\exp(-\varepsilon_i/k_B T)}{\Sigma_i \exp(-\varepsilon_i/k_B T)} \quad (2.48)$$

where $\varepsilon_i$ is the energy of the $i^{th}$ level above the lowest energy in the manifold. If energy splitting of the sub-levels is $\sim k_B T$, then it can be seen that an increase in temperature will increase the laser signal's absorption cross-section and therefore increase absorbed threshold pump power.

In addition to the energy level populations, the temperature also affects the spacing of the energy levels (and therefore the transition wavelengths), as well as changing the transition linewidths. Both of these effects are explored in more detail in Chapter 5 where their impact is more relevant.

## 2.5 Nonlinear effects

It is well known (e.g. [13, 39]) that the response to light in dielectric materials becomes increasingly non-linear as the intensity grows. In the context of this thesis, non-linear response in solid-state lasers is not considered as the operational intensities presented are low. Furthermore, as has been previously discussed, for low thermal loads thermal lensing and stress induced birefringence significantly impact on laser performance, thereby keeping the maximum signal intensity low. However, in fibre lasers the non-linear effects have to be considered due to the tight signal confinement in the core, resulting in much higher intensities than typical in a solid-state laser with the same signal power. This tight confinement coupled with the typical long device lengths means that non-linear effects can begin to limit power scaling. In silica fibres the $\chi^{(3)}$ is the lowest order nonlinear susceptibility, so that the non-linear effects of interest are the Kerr effect, Stimulated Brillouin Scattering (SBS) and Stimulated Raman Scattering (SRS).

The Kerr effect can be described as the refractive index change with signal intensity, such that $\Delta n = n_2 I$ where $n_2$ is the nonlinear refractive index and $I$ the signal intensity. The impact of this is that it results in a radially varying refractive index change due to the Gaussian intensity profile of the signal. As such, this radial refractive index variation in fibres causes guiding of the signal in the same way as thermal guiding. However, in fused silica $n_2 \sim 3 \times 10^{-20} m^2 W^{-1}$ [40], so for a single mode fibre with a core radius of $5\mu m$ with a 1kW signal, the change in refractive index would be $\sim 4 \times 10^{-7}$. This is much smaller than the change in refractive index with temperature, so the Kerr effect can be neglected. Therefore, the effects of interest for optical fibres are SBS and SRS.

SBS is an effect where the signal electric field generates acoustic vibrations in the medium via electrostriction causing variations in the refractive index. These variations act as a travelling grating from which the pump signal is scattered by Bragg reflection. The back reflected Stokes wave, $\nu_s$, is down-shifted in frequency due to the Doppler shift caused by the grating moving at the acoustic velocity, $v_A$. The Stokes wave frequency is give by $\nu_s = \nu_p - \frac{2nv_A}{\lambda_P}$ where $v_A$ for silica is $v_A \approx 6km/s$. The threshold for SBS is approximately given by [41]

$$P^{SBS}_{thres} = \frac{21 A_{eff} K}{g_B l_{eff}} \frac{\Delta\nu_p + \Delta\nu_B}{\Delta\nu_B} \tag{2.49}$$

where $A_{eff}$ is the effective core area and $l_{eff}$ the effective fibre length, and $g_B$ is the Brillouin gain coefficient equal to $g_B \sim 5 \times 10^{-11} m/W$ in silica [42]. The effective fibre length is defined as $l_{eff} = \frac{1}{\alpha_P}(1 - \exp{(-\alpha_P l)})$, where $l$ is the fibre length and $\alpha_P$ is the loss coefficient for the pump signal. Additionally, $K$ is a factor that accounts for the polarisation of the pump (for polarised light $K = 1$ and for unpolarised light $K = 2$) [43], and $\Delta\nu_p$ and $\Delta\nu_B$ are the Lorentzian linewidths of the pump and of the SBS gain, respectively. In bulk silica $\Delta\nu_B$ ~33MHz at 1.06$\mu m$ [44]. The pump wavelength dependence on $\Delta\nu_B$ is $\Delta\nu_B \propto 1/\lambda^2$ [44], so for light at 2$\mu m$ $\Delta\nu_B$ ~10MHz. It can be seen then that the SBS is more prone in narrow linewidth sources, where $\Delta\nu_B \gg \Delta\nu_p$. In this situation, equation (2.49) simplifies to

$$P_{thres}^{SBS} = \frac{21 A_{eff} K}{g_B l_{eff}} \tag{2.50}$$

SRS is similar to SBS except scattering in this case occurs due to high energy optical phonon vibration modes in the medium. The pump radiation is scattered by these optical phonons and is down shifted to a lower energy Stokes wave, with the amount determined by the optical phonon of the medium. The energy difference $E_v = h\nu_p - h\nu_s$, is dissipated as heat [45]. Due to the wave-guiding nature of fibres, a proportion of the scattered Stokes wave will be guided along the core in both propagation directions. Given the potentially long interaction lengths available in fibres, these forward and backward propagating Stokes waves can see significant gain by stimulating further emission.

Due to the high intensities required for Stimulated Raman Scattering the process can be given a threshold power [46]. The threshold is defined as the input pump power required such that the unseeded Stokes power equals the pump power at the fibre output. This threshold for the forward and backward Stokes waves is approximately [46]

Forward SRS:

$$P_{thres}^{SRS\,+} = \frac{16 A_{eff} K}{g_R l_{eff}} \tag{2.51}$$

Backward SRS:

$$P_{thres}^{SRS\,-} = \frac{20 A_{eff} K}{g_R l_{eff}} \tag{2.52}$$

where $g_R$ is the Raman gain coefficient which has a maximum value in silica of $g_R \sim 1.5 \times 10^{-13} m/W$ [47, 48]. These equations are only strictly valid for narrow linewidth signals, but due to the broad Raman bandwidth they still roughly predict the SRS threshold for much broader linewidth sources [46].

Determining whether the threshold for SBS or SRS will be reached first is dependent on the signal linewidth. For single-frequency sources, SBS will be the dominant effect limiting power scaling as the threshold signal power is two orders of magnitude lower than SRS's. However, as the signal linewidth increases the SBS threshold increases, as shown by equation (2.49), whilst the

SRS threshold remains approximately constant. Therefore, once the signal linewidth is greater than two orders of magnitude larger than the SBS gain linewidth, then SRS becomes the dominant effect limiting the laser performance.

Equations (2.50) and (2.51) show that to scale the laser power requires that the core area is increased and the fibre length decreased. For a cladding pumped fibre laser, assuming the cladding diameter is fixed, scaling the core radius should increase the pump absorption and therefore allow a much reduced device length to be used, whilst maintaining a high pump absorption efficiency. The scaling of the core area does however have a limit if single mode operation is to be maintained due to the practical limits on the fibre's $NA$, as was discussed in Section 2.3. It is worth noting that the calculated thresholds above are in practice a lower limit with the measured values being generally much higher. For SBS, the threshold is increased due to temperature changes along the fibre as this changes the refractive index non-uniformly across the effective grating via the thermo-optic effect. Furthermore, in practice, a natural temperature gradient along the fibre is established in laser oscillators and amplifiers due to the exponential reduction in the pump power along the fibre length, resulting in differing levels of heat generation and therefore changing the core temperature as a function of propagation distance.

## 2.6 Discussion and summary

For CW operation of step-index fibres and end pumped cylindrical rods, there are many factors that can degrade laser performance. These limiting effects have a different impact on the two geometries, and therefore are summarised below separately.

In step-index fibres, the two main limits on performance are due to thermally induced effects and a non-linear material response. Thermally induced effects typically have a larger impact on laser performance, except in the situation whereby the laser signal has a narrow linewidth and then nonlinear effects become dominant. Of the thermal effects reviewed, thermally induced damage to the fibres outer polymer coating was found to significantly limit power scaling. It was shown that the coating can become degraded for thermal loads as low as a few watts, depending on the fibres inner cladding radius, coating thickness and the heat transfer coefficient of the fibre's cooling mechanism. Therefore, aggressive cooling of the fibre is required to increase the damage threshold for the coating due to more efficient heat removal. This allows a higher pump power to be used before damage occurs, meaning that the laser output power will also be increased. Furthermore, if the core area is not increased, this has the advantage that the absorption coefficient for cladding pumping will be reduced such that a longer device length is required for efficient pump absorption. This has the additional benefit of reducing the heat deposition density in the fibre, allowing even higher pump powers to be used before the outer polymer coating begins to degrade. Another benefit for scaling the cladding size is that a lower brightness pump source can be used whilst still obtaining a high launching efficiency.

However, this is not the only consideration because as the signal power increases, it can approach the threshold for nonlinear effects, in particular SBS and SRS, causing propagation losses for the signal as well as a reduction in the available gain. For broadband laser signals, SRS is the dominant of the two effects, but as the laser linewidth is reduced and eventually becomes single-frequency, SBS will become the dominant process. The threshold signal power at which both effects become significant is linearly proportional to the $A_{core}/l_{fibre}$. Therefore, to increase their respective thresholds, the use of large core fibres with short device lengths is required. This can readily be achieved by increasing the core to cladding ratio as the pump absorption coefficients will be increased due to a stronger pump overlap with the core, which will allow a shorter device length to be used to obtain a high absorption efficiency.

There is however an upper limit on the core radius if single transverse mode of operation is to be maintained. This is imposed by fabrication restraints. In step-index fibres, the lower limit on the NA is ~0.04, which means that the largest core that will support only the single transverse mode as determined by the fibres V-value is $r_{core} \approx 9.5\lambda$. As such, for a step-index fibre operating at 2$\mu m$, the largest single mode core radius is ~20$\mu m$.

Another problem in step-index fibres is that the radial temperature profile causes a radial variation in the refractive index. As a result, the fibre begins to behave like a quadratic waveguide with a guide mode size that is not determined by the step-index profile. When the thermal load is increased, the guided mode size can be decreased such that it becomes less than the fundamental mode of the fibre, which will degrade the laser beam quality and efficiency. The power dissipated as heat required for the guided mode to equal the fundamental mode is inversely proportional to the core area. Although increasing the core area is advantageous for increasing the SBS and SRS thresholds, it does however decrease the threshold at which thermal guiding become significant. Therefore, in large core fibres, thermal guiding can form the upper limit for power scaling.

To extend the operational power levels of lasers, a balance is required between the advantages and disadvantages of scaling the core area. For narrow linewidth lasers with suitable heat sinking (such that the heat transfer coefficient is high) then the major concern for power scaling is SBS, which has a threshold signal power even for a 20$\mu m$ radius core fibre of ~530Wm, so assuming a typical device length of a few metres then $P_{thres}^{SBS} \sim 130W$ (for a 4m fibre). This is much smaller than the coating damage point for a 600$\mu m$ diameter inner clad fibre with a 50$\mu m$ thick polymer coating and $H = 10^5\ Wm^{-2}K^{-1}$ of P$_{h\ max}$ >2kW. Furthermore, the thermal guiding threshold in a 20$\mu m$ core fibre corresponds to an absorbed pump power in excess of 750W (assuming $\gamma_h$=0.6). Therefore, the laser slope efficiency is ~40%, so it follows that the signal power would be above the SBS threshold, making SBS limit the performance.

On the contrary, in broadband lasers with large core fibres, the nonlinear thresholds become very large, such that thermal guiding becomes the limiting factor on laser performance. Therefore, by reducing the core area, the threshold for thermal guiding will be increased, allowing the pump power and thus laser power to be further increased. Reducing the core radius will eventually make the signal power reach the SRS threshold, but this should not become an issue for signal powers below 1kW (assuming a minimum core radius of $\sim 5\mu m$) for device lengths of less than 10m.

In end-pumped rods, the upper limit for power scaling is imposed by the stress fracture limit, which for YAG was calculated to be 14kW/m. For typical rod lengths of a few centimetres this corresponds to a few hundred watts of dissipated heat. However, before this critical failure limit is reduced, stress induced birefringence and most importantly thermal lensing can seriously degrade laser performance to the point that the stress fracture limit cannot be achieved. In the case of thermal lensing it was shown that, based on work by Clarkson [33], the radial temperature distribution results in an highly aberrated thermal lens that can severely degrade the laser beam quality. It was shown that to reduce the impact of the thermal lensing, it is advantageous to have a smaller signal beam size than pump beam size. In the idealised case of a 'top-hat' pump profile, it was shown that for $w_l < w_p$ there was no beam degradation and the thermal lens focal length did not vary radially within the pumped region. However, for a Gaussian pump beam, the thermal lens was highly aberrated even for $w_l < w_p$. Using Siegman [35] Clarkson [33] showed that the beam quality degradation for a Gaussian pump profile was proportional to $w_l/w_p$, such that decreasing the laser beam size reduced the beam quality degradation. However, decreasing the laser beam size too far can result in unsaturated gain in the wings, which will allow higher order modes to oscillate and thus reduce the output beam quality. It was estimated that the thermal lensing for a Gaussian pump profile can increase the beam propagation factor from $M^2$=1 to $M^2$=1.2 with as little as 6W of absorbed pump power, highlighting the detrimental impact thermal lensing can have in bulk laser systems.

In addition to thermal lensing, for bulk lasers operating in a polarised cavity configuration, the depolarisation losses due to induced stress can also significantly limit the laser performance. The calculations presented showed that in YAG, the depolarisation losses begin to increase for a total dissipated heat of ∼10W. The increase in the cavity losses above this power level causes the slope efficiency to decrease and the absorbed threshold pump power to increase, thereby reducing the output performance of the laser. There are many approaches for reducing the impact of depolarisation losses, such as in a two rod configuration (where both rods are pumped identically) inserting a half-wave plate between the rods [13], and in a single rod configuration using a Porro prism and quarter-wave plate [33], or similarly inserting only a quarter-wave plate between the rod and a cavity mirror [32].

For both fibre and bulk lasers, it is clear that in order to scale the output power, the detrimental impact of thermal effects must be reduced. An advantageous route for both geometries is to reduce the sources of heat in the first instance by operating in a lower quantum defect state as well as by selecting the doping concentration to reduce clustering and up-conversion losses that lead to heat generation. Furthermore, ensuring adequate heat sinking for heat removal will considerably extend the thermal induced limits. Additionally, another solution, as is considered for Ho:YAG in Chapter 5, is to reduce the crystal's temperature as this can positively scale the thermo-optic and thermo-mechanical properties of a material, which reduces the impact of thermal effects and therefore allows a significant increase in the output power.

## 2.7 References

[1] **Honea, E. C., Beach, R. J., Sutton, S. B., Speth, J. A., Mitchell, S. C., Skidmore, J. A., Emanuel, M. A.** and **Payne, S. A.**, *115W Tm:YAG Diode-pumped solid-state laser*, IEEE Journal of Quantum Electronics, Vol. 33, No. 9, pp. 1592–1600, September 1997.

[2] **Taira, T., Tulloch, W. M.** and **Byer, R. L.**, *Modeling of quasi-three-level lasers and operation of cw Yb:YAG lasers*, Applied Optics, Vol. 36, No. 9, pp. 1867–1874, March 1997.

[3] **Clarkson, W. A.** and **Hanna, D. C.**, *Effects of transverse-mode profile on slope efficiency and relaxation oscillations in a longitunidinally-pumped laser*, Journal of Modern Optics, Vol. 36, No. 4, pp. 483–498, April 1989.

[4] **Clarkson, W. A.**, *High power fiber lasers and amplifiers*, CLEO Short Course, 2008.

[5] **Hanna, D. C., Percival, R. M., Smart, R. G.** and **Tropper, A. C.**, *Efficient and tunable operation of a Tm-doped fibre laser*, Optics Communications, Vol. 75, No. 3.4, pp. 203–206, March 1990.

[6] **Hanna, D. C., Jauncey, I. M., Percival, R. M., Perry, I. R., Smart, R. G., Suni, P. J., Townsend, J. E.** and **Tropper, A. C.**, *Continuous-wave oscillation of a monomode thulium-doped fibre laser*, Electronics Letters, Vol. 24, No. 19, pp. 1222–1223, September 1988.

[7] **Boj, S., Delevaque, E., Allain, J. Y., Bayon, J. F., Niay, P.** and **Bernage, P.**, *High efficiency diode pumped thulium-doped silica fibre lasers with intracore Bragg gratings in the 1.9-2.1*µ*mband*, Electronics Letters, Vol. 30, No. 13, pp. 1019–1020, June 1994.

[8] **Barnes, W. L.** and **Townsend, J. E.**, *Highly tunable and efficient diode pumped operation of* $Tm^{3+}$ *doped fibre lasers*, Electronics Letters, Vol. 26, No. 11, pp. 746–747, May 1990.

[9] **Mackenzie, J. I., Li, C., Shepherd, D. P., Beach, R. J.** and **Mitchell, S. C.**, *Modeling of high-power continuous-wave Tm:YAG side-pumped double-clad waveguide lasers*, IEEE Journal of Quantum Electronics, Vol. 38, No. 2, pp. 222–230, February 2002.

[10] **Walsh, B. M., Barnes, N. P., Petros, M., Yu, J.** and **Singh, U. N.**, *Spectroscopy and modeling of solid state lanthanide lasers: Application to trivalent* $Tm^{3+}$ *and* $Ho^{3+}$ *in* $YLiF_4$ *and* $LuLiF_4$, Journal of Applied Physics, Vol. 95, No. 7, pp. 3255–3271, April 2004.

[11] **Engelbrecht, M., Haxsen, F., Wandt, D.** and **Kracht, D.**, *Wavelength resolved intracavity measurement of the cross sections of a Tm-doped fiber*, Optics Express, Vol. 16, No. 3, pp. 1610–1615, February 2008.

[12] **Jackson, S. D.** and **King, T. A.**, *Theoretical modeling of tm-doped silica fiber lasers*, Journal of Lightwave Technology, Vol. 17, No. 5, pp. 948–956, May 1999.

[13] **Koechner, W.**, Solid-State Laser Engineering, Springer, New York, 6th edn., 2006.

[14] **Jackson, S. D.**, *Cross relaxation and energy transfer upconversion processes relevant to the functioning of 2µmTm$^{3+}$-doped silica fibre lasers*, Optics Communications, Vol. 230, pp. 197–203, 2004.

[15] **Jackson, S. D.** and **Mossman, S.**, *Efficiency dependence on the Tm$^{3}+$ and Al$^{3}+$ concentrations for Tm$^{3}+$-doped silica double-clad fiber lasers*, Applied Optics, Vol. 42, No. 15, pp. 2702–2707, 2003.

[16] *DILAS the laser diode company*, Website:`http://www.dilas.com`.

[17] **Clarkson, W. A.** and **Hanna, D. C.**, *Two-mirror beam-shaping technique for high-power diode bars*, Optics Letters, Vol. 21, No. 6, pp. 375–377, March 1996.

[18] **Clarkson, W. A., Neilson, A. B.** and **Hanna, D. C.**, *UK Patent Application 9324589.2*, 1993.

[19] **Clarkson, W. A., Barnes, N. P., Turner, P. W., Nilsson, J.** and **Hanna, D. C.**, *High-power cladding-pumped Tm-doped silica fiber laser with wavelength tuning from 1860 to 2090nm*, Optics Letters, Vol. 27, No. 22, pp. 1989–1991, November 2002.

[20] **Liu, A.** and **Ueda, K.**, *The absorption characteristics of circular, offset, and rectangular double-clad fibers*, Optics Communications, Vol. 132, pp. 511–518, December 1996.

[21] **Jackson, S. D.** and **King, T. A.**, *High-power diode-cladding-pumped Tm-doped silica fiber laser*, Optics Letters, Vol. 23, No. 18, pp. 1462–1464, Septemeber 1998.

[22] **Innocenzi, M. E., Yura, H. T., Fincher, C. L.** and **Fields, R. A.**, *Thermal modeling of continuous-wave end-pumped solid-state lasers*, Applied Physics Letters, Vol. 56, No. 19, pp. 1831–1833, May 1990.

[23] **Brown, D. C.** and **Hoffman, H. J.**, *Thermal, stress, and thermo-optic effects in high average power double-clad silica fiber lasers*, IEEE Journal of Quantum Electronics, Vol. 37, No. 2, pp. 207–217, February 2001.

[24] **Krupke, W. F., Shinn, M. D., Marion, J. E., Caird, J. A.** and **Stokowski, S. E.**, *Spectroscopic, optical, and thermomechanical properties of neodymium- and chromium-doped gadolinium scandium gallium garnet*, Journal of the Optical Society of America B, Vol. 3, No. 1, pp. 102–114, January 1986.

[25] *U in heat exchangers*, Website:`http://www.cheresources.com/uexchangers.shtml`.

[26] **Slack, G. A.** and **Oliver, D. W.**, *Thermal conductivity of garnets and phonon scattering by rare-earth ions*, Physical Review B, Vol. 4, No. 2, pp. 592–609, July 1971.

[27] **Brown, D. C.**, *Ultrahigh-average-power diode-pumped Nd:YAG and Yb:YAG lasers*, IEEE Journal of Quantum Electronics, Vol. 33, No. 5, pp. 861–873, May 1997.

[28] **Wynne, R., Daneu, J. L.** and **Fan, T. Y.**, *Thermal coefficients of expansion and refractive index in YAG*, Applied Optics, Vol. 38, No. 15, pp. 3282–3284, May 1999.

[29] **Webb, C. E.** and **Jones, J. D. C.**, Handbook of Laser Technology and Applications: Laser design and laser systems, IoP, 2004.

[30] **Fluck, R., Hermann, M. R.** and **Hackel, L. A.**, *Birefringence compensation in single solid-state rods*, Applied Physics Letters, Vol. 76, No. 12, pp. 1513–1515, March 2000.

[31] **Brown, D. C.**, *Nonlinear thermal distortion in YAG rod amplifiers*, IEEE Journal of Quantum Electronics, Vol. 34, No. 12, pp. 2383–2392, December 1998.

[32] **Clarkson, W. A., Felgate, N. S.** and **Hanna, D. C.**, *Simple method for reducing the depolarization loss resulting from thermally induced birefringenece in solid-state lasers*, Optics Letters, Vol. 24, No. 12, pp. 820–822, June 1999.

[33] **Clarkson, W. A.**, *Thermal effects and their mitigation in end-pumped solid-state lasers*, Journal of Physics D: Applied Physics, Vol. 34, No. 16, pp. 2381, August 2001.

[34] **Guan, R., Zhu, F., Gan, Z., Huang, D.** and **Liu, S.**, *Stress birefringence analysis of polarization maintaining optical fibers*, Optical Fiber Technology, Vol. 11, No. 3, pp. 240–254, July 2005.

[35] **Siegman, A. E.**, *Analysis of laser beam quality degradation caused by quartic phase aberrations*, Applied Optics, Vol. 32, No. 30, pp. 5893–5901, October 1993.

[36] **Gong, W., Gong, M., Liu, Q.** and **Lu, F.**, *Analysis of transverse mode formation in quasi-three-level microchip lasers*, Optical and Quantum Electronics, Vol. 37, pp. 1109–1120, 2005.

[37] **Jeunhomme, L. B.**, Single-mode fiber optics, Marcel Dekker, New York, 1990.

[38] **Digonnet, M. J. F.** and **Gaeta, C. J.**, *Theoretical analysis of optical fiber laser amplifiers and oscillators*, Applied Optics, Vol. 24, No. 3, pp. 333–342, February 1985.

[39] **Pedrotti, F. L.** and **Pedrotti, L. S.**, Introduction to Optics, Prentice-Hall, 2nd edn., 1993.

[40] **Boling, N. L., Glass, A. J.** and **Owyoung, A.**, *Empirical relationships for predicting nonlinear refracive index changes in optical solids*, IEEE Journal of Quantum Electronics, Vol. QE-14, No. 8, pp. 601–608, August 1978.

[41] **Denariez, M.** and **Bret, G.**, *Investigation of Rayleigh wings and Brillouin-Stimulated Scattering in liquids*, Physical Review, Vol. 171, No. 1, pp. 160–167, July 1968.

[42] **Aoki, Y., Tajima, K.** and **Mito, I.**, *Input power limits of single-mode optical fibers due to Stimulated Brillouin Scattering in optical communication systems*, Journal of Lightwave Technology, Vol. 6, No. 5, pp. 710–719, May 1988.

[43] **Stolen, R. H.**, *Polarization effects in fiber Raman and Brillouin lasers*, IEEE Journal of Quantum Electronics, Vol. QE-15, No. 10, pp. 1157–1160, October 1979.

[44] **Yu, D., Lu, W.** and **Harrison, R. G.**, *Physical origin of dynamical Stimulated Brillouin Scattering in optical fibers with feedback*, Physical Review A, Vol. 51, No. 1, pp. 669–672, January 1995.

[45] **Hecht, E.**, Optics, Addison Wesley, 4th edn., 2002.

[46] **Smith, R. G.**, *Optical power handling capacity of low loss optical fibers as determined by Stimulated Raman and Brillouin Scattering*, Applied Optics, Vol. 11, No. 11, pp. 2489–2494, 1972.

[47] **Hellwarth, R., Cherlow, J.** and **Yang, T.-T.**, *Origin and frequency dependence of nonlinear optical susceptibilities of glasses*, Physical Review B, Vol. 11, No. 2, pp. 964–967, January 1975.

[48] **Stolen, R. H.** and **Ippen, E. P.**, *Raman gain in glass optical waveguides*, Applied Physics Letters, Vol. 22, No. 6, pp. 276–278, March 1973.

# Chapter 3

# Single-ended operation in an all fibre geometry

## 3.1 Introduction

In this chapter, work conducted into operating fibre sources in a single-ended output regime is discussed. The motivation for this is that single-ended operation increases the useful power that can be extracted from a source, thereby increasing its output efficiency. For a laser operating in a saturated regime (i.e. well above the laser threshold), with a standard resonator design consisting of a laser medium and two cavity mirrors with feedback reflectivities $R_1$ and $R_2$, the ratio of the output power coupled from each mirror can be calculated using Rigrod's analysis [1].

For a cavity where the cavity mirrors have no scattering or absorption losses such that $R = 1 - T$, the signal growth after one pass in the cavity is given by the signal power times the effective single pass gain, $G$. The signal powers at each mirror are shown in Figure 3.1, where it can be seen that after one round-trip the signal power incident on cavity mirror 1 is given by

$$\frac{P_1}{1-R_1} = \frac{P_1 R_1 R_2 G^+ G^-}{1-R_1} \tag{3.1}$$

where $P_1$ is the output power from mirror 1, and $G^+$ and $G^-$ are the effective

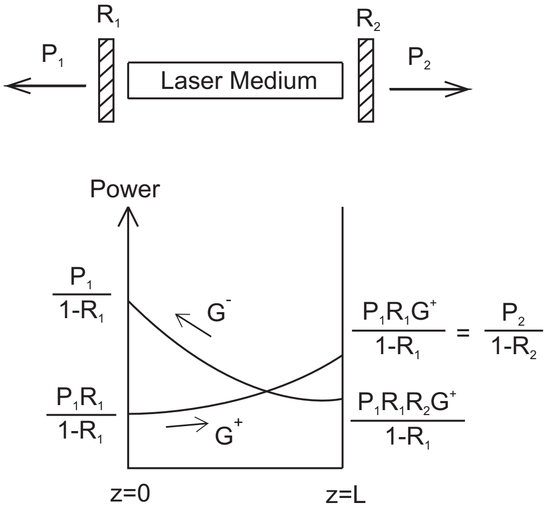

Figure 3.1: Schematic of a laser cavity showing the signal power in each direction for an effective single pass gain $G$ (accounting for core propagation losses) and cavity mirror reflectivities $R_{1,2}$ for mirrors 1 and 2 respectively. It is assumed that there are no absorption or scattering losses at the cavity mirrors.

single pass gain (taking into account the core propagation loss) in the forward and backward directions respectively. Under steady state operation, the signal power at a given position in the cavity has to be the same as after one round-trip, so from equation (3.1) it can be seen that

$$R_1 R_2 G^+ G^- = 1 \tag{3.2}$$

Therefore, if the signal power at the second cavity mirror is considered it can be seen from Figure 3.1 that

$$\frac{P_2}{1-R_2} = \frac{P_1 R_1 G^+}{1-R_1} \tag{3.3}$$

where $P_2$ is the output power coupled from mirror 2. Given that the single-pass signal gain is the same in both directions (i.e. $G^+ = G^- = G$), substituting $G$ from equation (3.2) into equation (3.3) gives the ratio of the output power coupled from each end of the cavity as

$$\frac{P_1}{P_2} = \frac{1 - R_1}{1 - R_2}\sqrt{\frac{R_2}{R_1}} \tag{3.4}$$

From this it can be seen that predominantly single-ended output is obtained from end 1 by selecting $R_1 \ll R_2$. The high gains obtainable in RE-doped fibres allow for laser oscillation even in the presence of very high cavity losses where $R_{1,2} \ll 1$. In this high loss regime, single-ended output can still be achieved, for example, by using a perpendicularly cleaved facet to provide a 3.5% Fresnel reflection, and at the other end of the fibre using an angle polished/cleaved facet which has a much lower feedback efficiency. In this situation, the output power ratio can be approximated to

$$\frac{P_1}{P_2} \approx \sqrt{\frac{R_2}{R_1}} \tag{3.5}$$

In addition to single-ended operation, this all-fibre geometry has the advantage that it is compatible with cladding pumping, therefore enabling scaling to high output powers. The use of this high loss, cladding pumped, all-fibre approach is discussed in the following sections for a laser oscillator and an ASE source.

## 3.2 Yb-doped laser oscillator

### 3.2.1 Introduction

In this section, work on obtaining single-ended operation of fibre lasers is discussed. Commonly, this is achieved by having a high reflectivity at one end of the fibre and a low reflectivity (often provided by a 3.5% Fresnel reflection from a perpendicularly cleaved end facet) at the other. The high reflectivity end can take many forms including: an external feedback cavity consisting of a collimating lens and mirror [2–4], a butted mirror or coated end-facet [5], or an in-fibre Bragg grating [6]. Table 3.1 briefly summarises the main considerations for each feedback approach. It shows that for operation at high power

| **Feedback Method** | **Strengths** | **Limitations** |
|---|---|---|
| Butted Mirror / Coated End Facets | Simplicity in obtaining single-ended operation | The main limitation to this approach is the damage threshold of the optical coatings, which can be reached even at low powers due to the small incident beam size and thus high intensity. Furthermore, the coatings are also susceptible to thermal damage from heat generated in the fibre. |
| In-Fibre Bragg Gratings | Suitable for high power operation, but has less flexibility than external feedback cavities. | The requirement for photosensitive dopants to be added to the fibre to increase the fibre photosensitivity and therefore the strength of any written grating has the associated limitation of increased photo-darkening. Therefore, to limit photo-darkening the grating region can be spliced to the gain medium, but this results in splice losses and an increased system complexity. |
| External Feedback Cavities (i.e. Collimating lens and Mirror) | Suitable for high power operation and allows greater operational flexibility as optical components can be inserted into the cavity to give, for example: wavelength tuning, Q-switched output, mode-selection, etc. | Requires components with appropriate anti/high reflection coatings as well as the added cost and complexity of the system. Furthermore, the cavity requires careful alignment, otherwise significant re-coupling losses will occur, degrading laser performance. However, this can be easily remedied. |

Table 3.1: Summary of Strengths and Limitations of some commonly used methods for obtaining high reflectivity feedback.

levels, the most suitable approach is using an external feedback cavity. However, our approach has the benefit that it is suitable for power scaling to high power levels, whilst maintaining a simple geometry which does not require additional components, splicing or place additional constraints on the fibre core design.

In a proof-of-principle experiment, predominantly single-ended operation of a fibre laser in a simple all-fibre geometry is discussed. In this experiment, the low feedback reflectivity was provided by using a twisted end facet termination (discussed in more detail in the next section). This approach uses a helical core trajectory at the low feedback fibre end, which is perpendicularly cleaved in the helical region, such that the core direction is angled with respect to the facet and therefore suffers a reduced feedback efficiency. This has the advantage over angle polishing, as perpendicularly cleaved facets have a higher quality surface finish than is typically obtained by angle polishing. The only constraint to this approach is the requirement for the core to be offset from the fibre centre. As such, this work was conducted using a Yb-doped fibre with an offset core which was developed for other applications using the twisted-end termination [7–9]. In addition to the availability of suitable fibre, operating in the $1\mu m$ spectral region has the benefit of there being a larger range of commercially available optical components and diagnostic equipment, when compared to the $2\mu m$ region which is used throughout the rest of this thesis.

### 3.2.2 Experimental procedure

The fibre used in these proof-of-principle experiments was produced in house by modified chemical vapour deposition and solution doping. The fibre produced had a $28\mu m$ diameter Yb-doped alumino-silicate core with an Yb concentration of $\sim$7000ppm (by weight) and a numerical aperture of $\sim$0.1. Surrounding the core was a pure silica inner cladding of diameter $380\mu m$. The outer coating on the fibre was a UV-cured polymer with a low refractive index (n = 1.375), giving the inner cladding a calculated NA of 0.49. In this fibre the core was laterally offset to allow the fibre to be used in conjunction with a twisted end termination method [7], as well as to aid pump absorption (as described in Chapter 2).

The twisted end facet was produced by heating the end section of the fibre and twisting it to form a helical path for the core in that region. This causes the core to be angled with respect to the central longitudinal axis of the fibre, with an angle given by $\theta_{core} = P/(2\pi r_0)$, where $P$ is the period and $r_0$ is the core offset [10]. The fibre was then perpendicularly cleaved in the twisted region to produce a high quality surface finish with low scattering loss. The helical core path now has an angled path with respect to the facet normal, causing light fed-back by the Fresnel reflection to incur an increased loss, which is dependent on the angle [11]. Using this approach, the core angle can be selected by designing the appropriate core offset during fabrication combined with the number of rotations per unit length induced in the twisting process.

Helical core trajectories can result in significant bend losses. This is not a problem in this case, as the helical region in the fibre is short (typically only a few millimetres) so does not induce significant bend losses and therefore allows a low threshold pump power to be maintained. However, one concern with helical core trajectories is that there is pump loss due to reflection. This can be overcome by only using the twisted end facet termination at the un-pumped end of the fibre.

Another potential advantage to this approach is that, if required, the helical region can be tailored to help suppress higher order mode propagation via tighter coiling of the fibre core, therefore increasing the bend loss incurred for the higher order modes compared to the fundamental mode. This was shown by Wang et al. [10] when comparing the output beam propagation factors for a helical core fibre laser with that of the same fibre with a straight core trajectory, whereby the output beam propagation factor was improved from $M^2$=5.5 for the straight core to $M^2$=1.1 for the helical core trajectory. In this case the bend loss also significantly reduced the laser efficiency. It was suggested that reducing the core angle so that the $LP_{01}$ mode loss is reduced, whilst still having a comparatively higher loss for the next higher order mode $LP_{11}$, will increase the laser slope efficiency [10]. Mode suppression using a helical core could be applied to the twisted end facet approach to improve the output beam propagation factor by increasing the length of the helical region and thus increasing the propagation loss for higher order modes. However, the impact of this is likely to be small as the helical region will need to be kept small so that the laser efficiency is not affected, and therefore the loss for higher order modes will be limited.

For our fibre, the twisted end facet was configured for a core angle with respect to the longitudinal axis of the fibre of $\sim 2.4^\circ$. The angle was chosen so that a feedback reflectivity lower than 3.5% was obtained, therefore meeting the requirements for predominantly single-ended output (i.e. $R_1 \ll R_2$). However, the angle was also chosen to be small, so that the resulting reflectivity was not too low as this would have drastically increased the laser threshold pump power.

Pump power for the laser was provided by a high power diode source operating at 976nm, with a maximum output power of 76W. This was coupled into the perpendicular facet (non-twisted end) by a 30mm focal length aspheric lens, with a launching efficiency measured to be 66%. Before the 30mm lens, a dichroic with a high transmission (>95%) for the pump and high reflectivity (>99.5%) over the wavelength range of 1020-1200nm was placed in the collimated beam. This mirror was angled to approximately 10° to facilitate extraction of the signal light from this end of the fibre for monitoring. The absorption efficiency for the fibre in a cladding pumped configuration was measured using a cut-back technique to be ~1dB/m, so a device length of 16m was used. The fibre was mounted in a water-cooled V-groove heat-sink to facilitate heat removal due to stray pump light and quantum defect heating in the fibre core. To analyse the output from the twisted end of the fibre, the beam was collimated with a lens orientated perpendicularly to the beam direction, which by Snell's Law forms an angle with the longitudinal axis of the fibre $\theta = \arcsin\left(n_{core} \sin\left(\theta_{core}\right)\right)$, as shown in Figure 3.2.

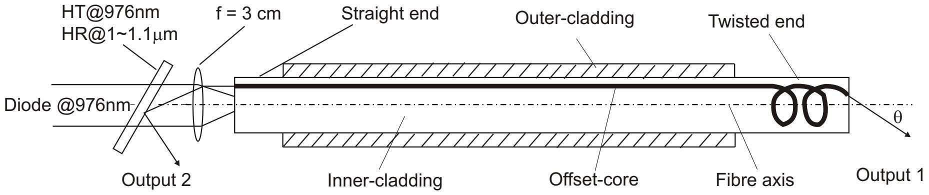

Figure 3.2: Schematic of the cladding pumped Yb-doped fibre laser used in these experiments

### 3.2.3 Results and analysis

Figure 3.3 shows the laser output power from both the twisted and straight ends of the fibre, as a function of the launched pump power. It shows that the output power from the twisted end facet was significantly higher than the straight end, reaching a maximum power of 29.1W, limited only by the available pump power. By comparison, the output from the straight end was only 1.98W at the maximum power, and hence a factor of 15 lower. This suggests that the reflectivity of the twisted end facet is $\sim 1.6 \times 10^{-4}$. The output beam propagation factor from the twisted end facet was $M^2 \approx 2.3$, which is better than expected for this fibre given its V-value of 8.2 (which from $V = 2M^2$ would roughly suggest a maximum output beam propagation factor of $M^2 \approx 4$). This beam quality could be improved further by optimising the design and length of the twisted end section as discussed in the previous section, due to tighter coiling of the fibre core increasing the propagation loss for higher order modes.

The output slope efficiency for the laser above 24W of launched pump power was measured to be 77% (or 79% with respect to absorbed pump power). This was compared to the theoretical maximum slope efficiency calculated using equation (2.3). Assuming the cavity losses were given by $L = 1 - R_2$ and that the output coupler reflectivity was $R_1 = 1.62 \times 10^{-4}$, $\eta_{abs} = 0.975$ and $\eta_q = 1$, then the maximum slope efficiency was calculated to be $\eta_s \approx 83\%$. It can be seen that the measured value is only slightly less than the theoretical maximum, which suggests that the fibre is operating close to its optimal

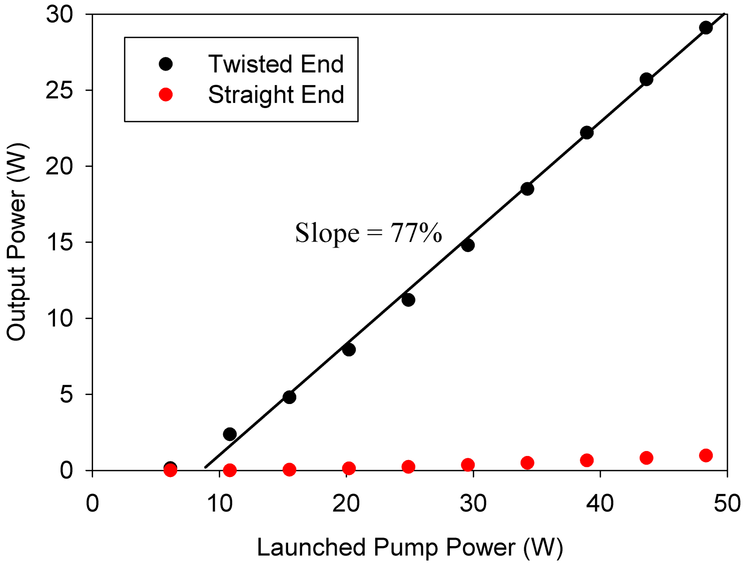

Figure 3.3: Output power from the twisted and straight ends as a function of launched pump power

performance.

The theoretical laser threshold pump power was calculated to be $P_{thres} = 2.94W$ using equation (2.1) and the values given above, and $\sigma_e(\lambda \approx 1080nm) \approx 3 \times 10^{-25}m^2$ and $\sigma_e(\lambda \approx 1080nm) \approx 0$ [12]. This is significantly lower than the measured value of ~10W of absorbed pump power. This discrepancy is due to the assumption of no amplified spontaneous emission (ASE) in the theory, whilst in practice there is ASE which depletes the inversion so that more pump power is required to reach the laser threshold. The ASE background can be seen in Figure 3.4. The figure shows that the laser emission bandwidth of this source was 14nm, which was centred around 1080nm, whilst the ASE bandwidth is ~70nm (Full-width). The impact of the ASE background on the threshold raises the question of how much of the output power is ASE and how much the laser signal. Therefore, to determine this, the approach discussed below was used.

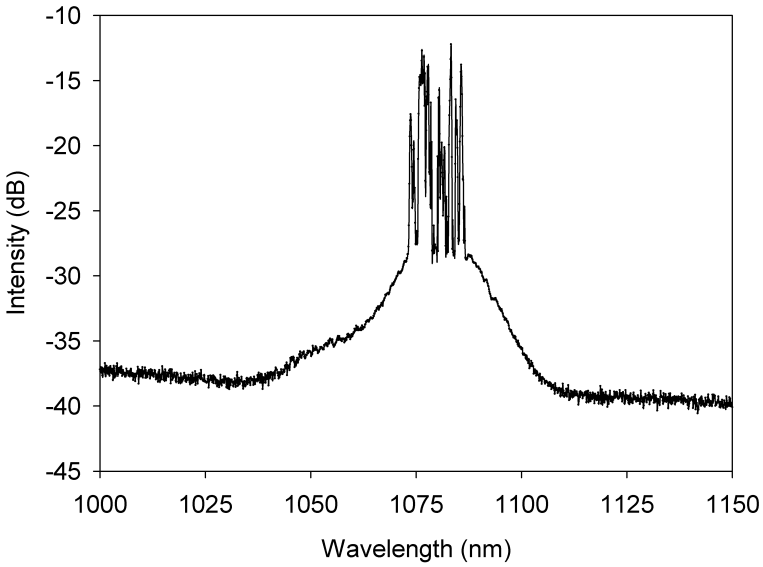

Figure 3.4: Emission Spectrum for the output from the twisted end facet at maximum pump power.

### 3.2.4 Measuring the Amplified Spontaneous Emission in a laser signal

The high output coupler loss used in this approach for single-ended operation has the implication that the laser threshold is significantly higher than for conventional Yb-doped fibre laser configurations. Below threshold, any inversion due to pumping is depleted predominately by spontaneous emission and amplified spontaneous emission (ASE). Therefore, below the laser threshold, the ASE power will increase with increased pump power. For lasers with low thresholds, the ASE power that builds up will be small, however, as the threshold is increased the ASE power builds up considerably. This is apparent from Figure 3.4 where there is a significant ASE component in the output. It is often considered that the ASE power is negligible if it is 20-30dB below the laser emission peak. However, given that the laser emission typically has a very small bandwidth, whilst the ASE can be very broad, this means that the relative contribution to the power from the ASE component could be larger than is assumed. Therefore, an approach for estimating the ASE power was required. Our approach used a Scanning Fabry Perot Interferometer (SFPI) to distinguish between the ASE and laser signal.

The basic principle behind this approach is that the transmitted frequency spectrum from the SFPI is different for the laser and ASE, allowing them to be distinguished from each other. For a laser, the SFPI under ideal conditions will have a transmitted signal identical to the laser output frequency spectrum (shown in Figure 3.5). In the case of ASE, the SFPI can, under certain conditions, have a constant transmitted intensity as a function of the signal frequency (shown in Figure 3.6). When both the ASE and laser signal are present, the SFPI can be configured so that the transmitted signal will have the laser mode structure, but with it offset by a constant amount due to the ASE (shown in Figure 3.7). By calibrating this ASE offset to the incident ASE power below the laser threshold (i.e. so there is only ASE present), the relative ASE and laser power can be determined above the laser threshold. In practice, selecting the ideal SFPI arrangement to achieve this requires careful consideration.

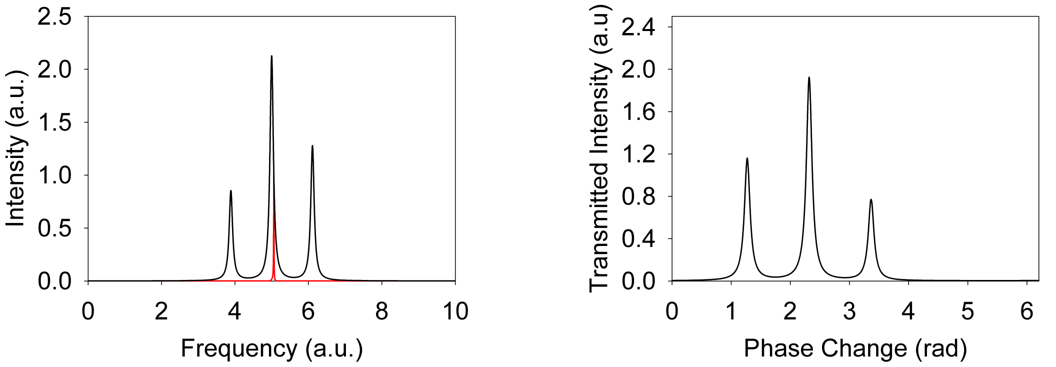

(a) Example laser frequency spectrum

(b) Transmitted signal as a function of the phase change

Figure 3.5: Showing (a) an example laser signal (black) and the SFPI Airy function (red) , and (b) the transmitted signal intensity from the SFPI, as a function of the phase change.

The transmitted intensity through the SFPI is dependent on the mirror reflectivity, mirror separation and the incident signal frequency spectrum. The ratio of the transmitted to incident intensity is given by the Airy function [13],

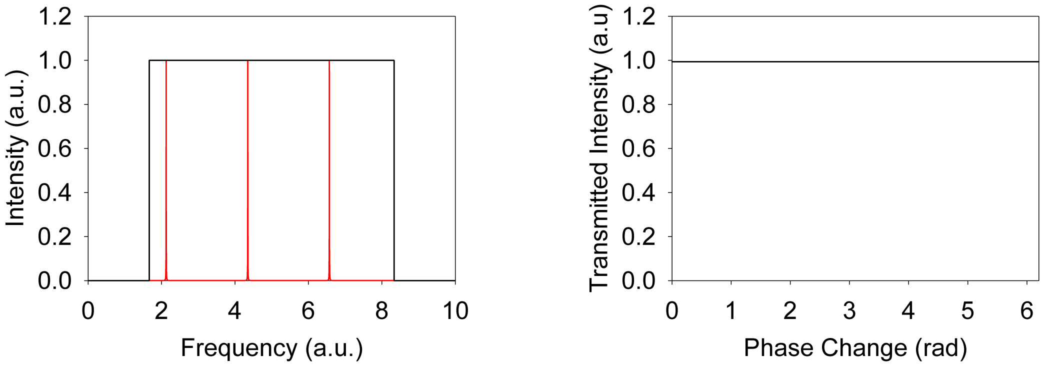

(a) Example ASE frequency spectrum

(b) Transmitted signal as a function of the phase change

Figure 3.6: Showing (a) an ASE signal with a 'top-hat' frequency distribution (black) and the SFPI Airy function (red) , and (b) the transmitted signal intensity from the SFPI as a function of the phase change.

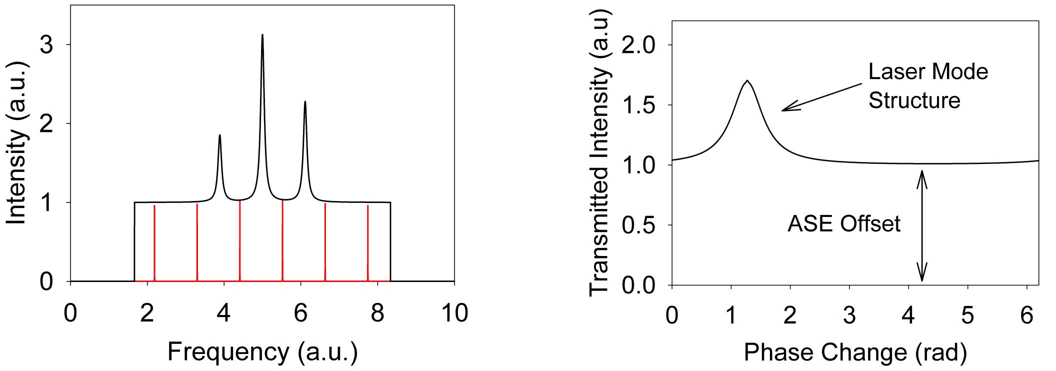

(a) Combined Laser and ASE frequency spectrum

(b) Transmitted signal as a function of the phase change

Figure 3.7: Showing (a) the combined laser and ASE frequency spectrum (black) with the SFPI Airy function (red), and (b) the transmitted signal intensity from the SFPI with the ASE offset and laser mode structure labelled.

$$\mathscr{A}(\theta) = \frac{I_t}{I_i} = \frac{1}{1 + F\sin^2(\delta/2)} \tag{3.6}$$

where $\delta = 4\pi n\nu_0 d/c$ is the phase difference between two successive transmitted waves with frequency $\nu_0$, for a mirror separation $d$ in a medium with a refractive index $n$. When the phase difference corresponds to an integer of $2\pi$, the maximum signal intensity is transmitted. The frequency spacing between two successive transmission maxima is called the Free Spectral Range (FSR) given by [14]

$$\Delta\nu_{FSR} = c/2nd \tag{3.7}$$

The coefficient of Finesse, $F$, for the cavity is determined by the etalon mirror reflectivities which, when equal, is given by [14]

$$F = \frac{4R}{(1-R)^2} \tag{3.8}$$

To distinguish between the ASE and the laser signal, the SFPI's Airy function has to be selected so that it only overlaps with the ASE for certain mirror separations. This is achieved by selecting the SFPI FSR to equal an integer number of the laser mode spacing. At these mirror positions, the Airy function peaks overlap between the laser modes (i.e. at the minimum intensity between successive modes, as shown in 3.7(a)) and therefore the transmitted frequencies from the SFPI are only due to ASE. As such, for these mirror positions, the transmitted intensity from the SFPI is constant and dependent on the incident ASE power. As previously discussed, by measuring this offset, both the ASE and laser power can be determined.

However, there is another factor to be considered so that a constant transmitted intensity is obtained from the SFPI when the Airy function only overlaps with the ASE. In the example used in Figure 3.6 where the ASE has a 'top-hat' intensity distribution, a constant transmission is achieved when the SFPI FSR is less than the total ASE bandwidth. However, in practice the ASE has a more complicated intensity distribution, so this is no longer strictly valid. For a real ASE signal, there are tighter constraints on selecting an appropriate SFPI FSR so that a constant transmitted signal is maintained as a function of the SFPI mirror separation. To demonstrate this, an approximation of the measured ASE, shown in Figure 3.4, was approximated using quadratically varying intensity profiles, shown in Figure 3.8(a), with an intensity distribution given by

$$I_s(\nu) = I_{max} - \frac{(\nu - \nu_0)^2}{2\Delta\nu} \quad for\ \nu = \nu_0 \pm \sqrt{2\Delta\nu}\ and\ I_s(\nu) = 0\ everywhere\ else \tag{3.9}$$

where $I_{max}$ is the peak intensity, $\nu_0$ the central frequency and $\Delta\nu$ is the FWHM bandwidth. Using this approximation of the ASE, the transmitted signal intensity from the SFPI was calculated as a function of the mirror separation (with a maximum mirror displacement of $c/(2\nu)$) for a range of SFPI FSR's. This is shown in Figure 3.8 where the percentage change in the signal intensity from that at the initial mirror position is shown as a function of the change in mirror position. The figure highlights that when the FSR is decreased to less than approximately one fifteenth of the ASE bandwidth (full-width (FW)), the transmitted signal intensity variation is less than 1% of the transmitted intensity at the initial mirror position. As such, for FSR less than this, the transmitted ASE can be considered constant. This is significant for determining the ASE offset when both the laser and ASE are present. For the ASE background in the signal observed (shown in Figure 3.4), the FW$\sim$70nm, and therefore the FSR would need to be $\nu_{FSR}$ <620GHz, which corresponds to a mirror separation of $d$ >0.25mm. From this it can be seen that for all practical mirror separations the transmitted intensity for the ASE will be effectively constant.

### 3.2.5 Laser vs ASE output power

To determine the ASE component in the signal, a FPI-25 plane-plane Scanning Fabry-Perot Interferometer was used in conjunction with a FP-3-RG ramp gen-

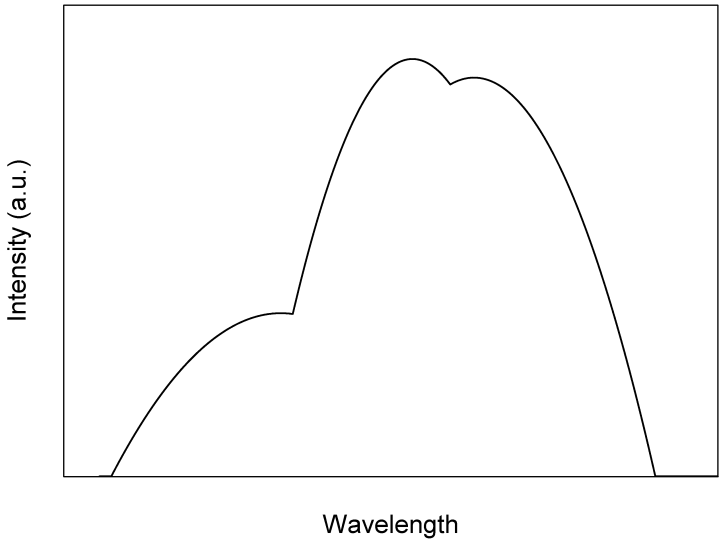

(a) ASE Spectrum Approximation

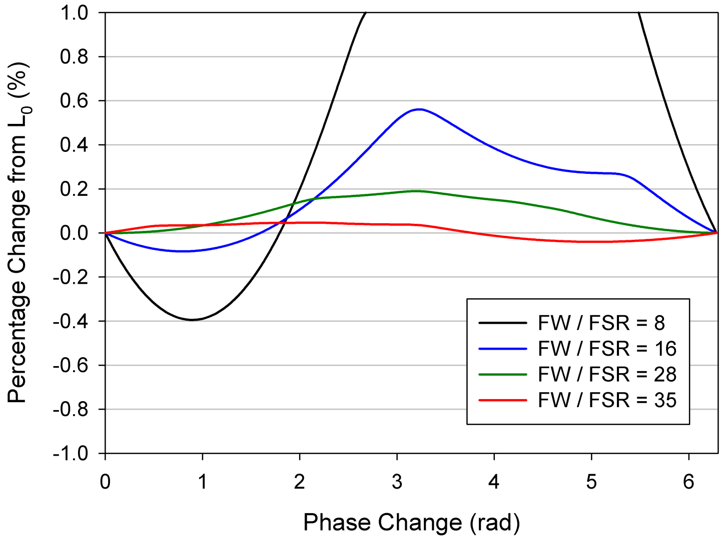

(b) Percentage Change in Transmitted Intensity as a function of the phase change

Figure 3.8: Showing (a) an approximation of the ASE spectrum with wavelength, and (b) the percentage change in transmitted intensity as the etalon mirror separation varies by half the central wavelength ($2\pi$) as a function of the FW of the ASE signal to FSR of the etalon.

erator to allow the mirror separation to be controlled electronically. Alignment of the SFPI was conducted in the regime where both ASE and laser signals were present in the fibre laser's output (i.e. operation above the laser threshold). Using an oscilloscope showing the transmitted intensity as a function of mirror separation, the Fabry-Perot's mirrors parallelism was aligned. The optimum alignment was obtained when the laser mode structure was sharply defined. This was achieved by initially adjusting the coarse mechanical adjusters on the back mirror for a rough alignment, before making fine corrections with the applied voltage and offset to each of the three piezos on the front mirror. The calibration of the ASE power per unit offset is achieved using the method outlined above.

The mirror separation used in the experiment was 1.56mm, so that the FSR would correspond to an integer number of cavity modes. This mirror separation gave a FSR of 96GHz. Both mirrors had a 90% reflectivity over a broad wavelength range in the $1\mu m$ region, which gave a cavity a coefficient of finesse of $F = 360$, and therefore a calculated finesse of 30 and an Airy function fringe linewidth (FWHM) of 3.2GHz. Due to its good response at $1\mu m$, a germanium detector was used to measure the transmitted signal intensity for observation on an oscilloscope.

After calibrating the intensity offset as a function of ASE power, the ASE content was measured for both the straight and twisted end outputs, as shown in Figure 3.9. It can be seen that the ASE power, from both the twisted end and straight end, increases with pump power well beyond the laser threshold pump power, with both eventually rolling over at pump powers approaching 50W. This is interesting as it is often thought that the ASE power clamps when the laser threshold is reached, whilst this shows that the laser intensity is not high enough to completely deplete the inversion until well above the threshold.

A possible explanation for the roll-over in the ASE power with increasing pump power can be seen when considering the cavity as an etalon containing a gain medium. Figure 3.10 shows how the electric field amplitude changes

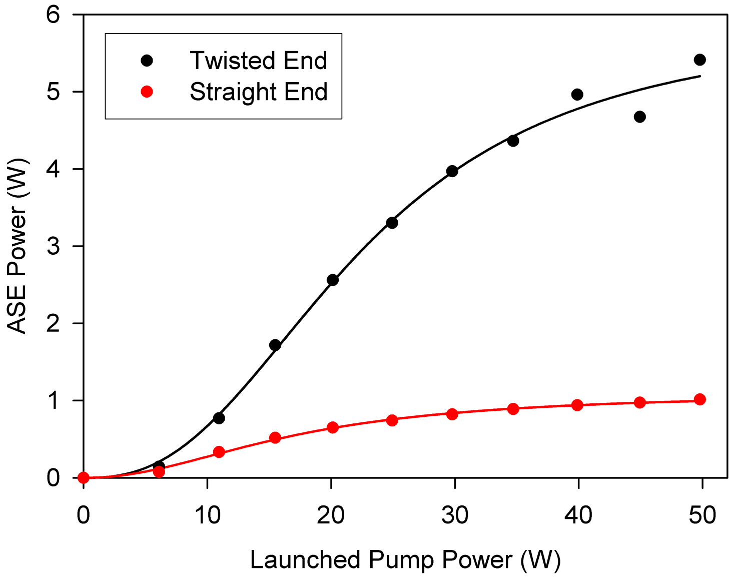

Figure 3.9: Measured ASE power from the twisted and straight ends as a function of launched pump power

during multiple passes through the gain medium inside the etalon mirrors. Of particular interest here is how the transmitted electric field is affected by the etalon. The total transmitted amplitude is determined by all of the transmitted electric fields after each round-trip added together. As such, the total transmitted electric field amplitude is given by

$$E_t = E_0Gt_2 + E_0r_1r_2G^3t_2e^{\imath\delta} + E_0r_1^2r_2^2G^5t_2e^{2\imath\delta} + ... + E_0Gt_2(r_1r_2G^2e^{\imath\delta})^{n-1} \quad (3.10)$$

which simplifies to

$$E_t = E_0Gt_2[1 + r_1r_2G^2e^{\imath\delta}(1 + r_1r_2G^2e^{\imath\delta} + ... + (r_1r_2G^2e^{\imath\delta})^{n-2}] \quad (3.11)$$

where $r_{1,2}$ are the reflection coefficients for mirrors 1 and 2 respectively, $t_2$ is the transmission coefficient for mirror 2, $G$ is the effective single pass gain and $\delta$ is the phase difference between two successively transmitted beams. If $|r_1r_2G^2e^{\imath\delta}| < 1$, then equation (3.11) converges using

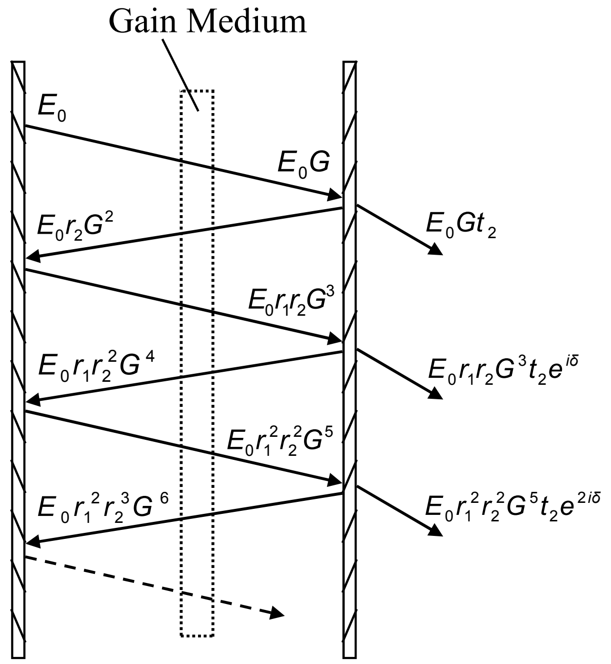

Figure 3.10: Showing the signal electric field amplitude as a function of position in the etalon and the transmitted electric field amplitude per round-trip.

$$\sum_{n=0}^{n=\infty} (X)^n = \frac{1}{1-X} \tag{3.12}$$

and therefore

$$E_t = E_0 G t_2 \left[ 1 + \frac{r_1 r_2 G^2 e^{\imath\delta}}{1 - r_1 r_2 G^2 e^{\imath\delta}} \right] \tag{3.13}$$

which simplifies to

$$E_t = \frac{E_0 G t_2}{1 - r_1 r_2 G^2 e^{\imath\delta}} \tag{3.14}$$

Given that the intensity is given by $I = EE^*/2$, the total transmitted intensity is then given by

$$\frac{I_2}{I_0} = \frac{t_2^2 G^2}{(1 - r_1 r_2 G^2 e^{\imath\delta})(1 - r_1 r_2 G^2 e^{-\imath\delta})} \tag{3.15}$$

where $e^{\imath\delta} + e^{-\imath\delta} = 2\cos\delta$, $R = r^2$ and $T = t^2$, such that the transmitted intensity is simplified to

$$\frac{I_2}{I_0} = \frac{T_2 G^2}{1 + R_1 R_2 G^4 - 2\sqrt{R_1 R_2} G^2 \cos\delta} \tag{3.16}$$

where $R_{1,2}$ are the feedback reflectivities for mirrors 1 and 2 respectively and $T_2$ is the transmission of mirror 2. For beams at normal incidence to the mirrors, as is the case here, $\delta$ is given by

$$\delta = \frac{4\pi n d}{\lambda} \tag{3.17}$$

where $n$ is the refractive index of the material between the mirrors, $d$ is the mirror separation and $\lambda$ is the wavelength of the beam.

Below the laser threshold, ASE depletes a proportion of the inversion, such that the ASE power grows with increased pump power. For simplicity, if the gain is assumed to be constant over the range $\Delta\lambda$, centred around $\lambda_0$ and zero for all other wavelengths, then the ASE spectrum transmitted from the etalon can be calculated from equation (3.16), as a function of the effective single pass gain. This is shown in Figure 3.11 where it can be seen that for small signal gains the output intensity as a function of the wavelength is effectively constant. However, as the gain increases, the signal intensity for the wavelengths that resonate becomes much larger than for those that are non-resonating. As such, these resonating wavelengths use a larger proportion of the available inversion and begin to dominate. Eventually the resonating wavelengths round-trip gain reaches unity and the gain is clamped. However, as there is considerable ASE power in the non-resonant wavelengths, there is competition between the ASE and laser. From the rate equations it can be seen that the rate of change in the population of the upper laser manifold is

$$\frac{dN_2}{dt} \propto \frac{\sigma_p I_p}{h\nu_p} N_1 - \left( \frac{\sigma_e(\nu_l) I_l}{h\nu_l} + \frac{\sigma_e(\nu_a) I_a}{h\nu_a} \right) N_2 \tag{3.18}$$

where $\sigma_p$ is the absorption cross-section at the pump frequency, $\nu_p$, $\sigma_e(\nu_l)$ is the emission cross-section at the laser frequency, $\nu_l$, $\sigma_e(\nu_a)$ is the emission cross-section at the ASE frequency, $\nu_a$, $I_p$ is the pump intensity, $I_l$ is the laser intensity and $I_a$ is the ASE intensity. It can be seen therefore that as the pump rate is increased, the relative increase in the laser signal and ASE is dependent on their intensities. Therefore, as the laser intensity is higher than the ASE intensity at threshold, the laser intensity grows more quickly. As the pump power is increased, the laser intensity continues to grow, whilst the relative increase in the ASE intensity reduces. Eventually, as the pump power is further increased, the laser intensity will begin to dominate the inversion and therefore the ASE intensity will roll-over.

At the maximum pump power, the ASE power emitted was 5.4W and $\sim$1W from the twisted and straight ends respectively. The implications of this are that the actual laser power for 50W of pump power are 23.7W and 0.97W from the twisted and straight ends respectively (see Figure 3.12). Therefore, the laser slope efficiency is 67% (69% with respect to absorbed pump power). Using

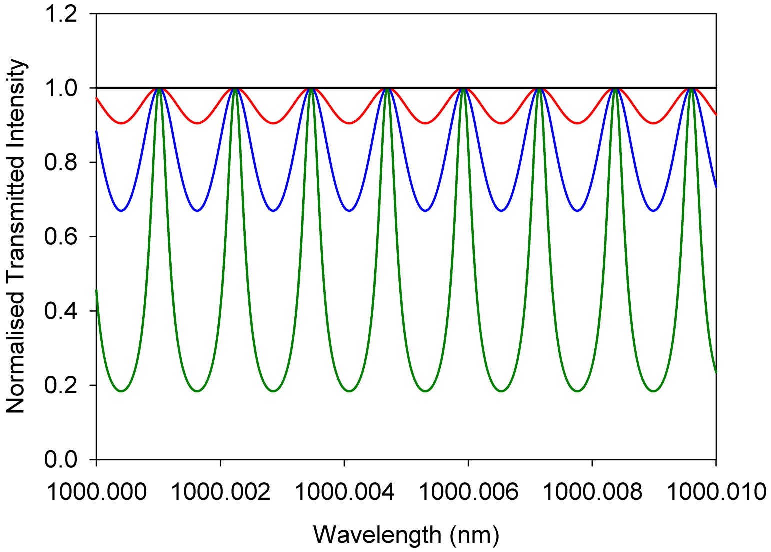

Figure 3.11: Showing the normalised signal intensity transmitted from the etalon, as a function of the wavelength for a single pass gain of G=1 (black), G=50 (red), G=100 (blue), G=200 (green). This highlights that below threshold, the ASE intensity is non-uniform due to resonant cavity modes. As the pump power (and therefore single pass gain) is increased, eventually these axial modes have a round-trip gain equal to the loss and therefore begin to lase.

these values for the laser power, the output power ratio can be calculated to give $P_1/P_2 = 24.6$, which gives the reflectivity of the twisted end facet as being $\sim 5.8 \times 10^{-5}$. The output power ratio can be further improved by increasing the core angle to further reduce the reflectivity. However, this comes with the disadvantage of increasing the laser threshold and increasing the ASE component of the output power. In the current setup, this would prove detrimental due to the limited pump power available. However, with some higher power diodes, the relative ASE contribution to the output would become negligible due to the ASE rolling over.

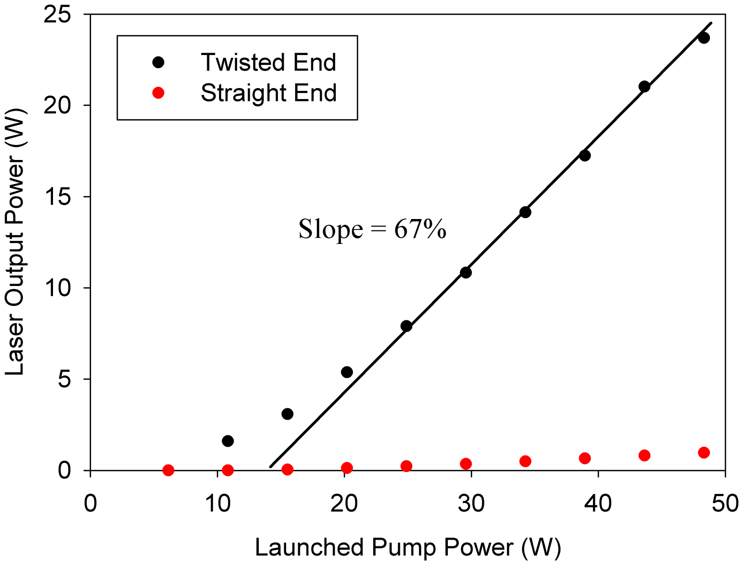

Figure 3.12: Measured laser power from the twisted and straight ends, as a function of launched pump power

### 3.2.6 Conclusion

It has been shown that single-ended operation of a Yb-doped fibre laser is achievable using an all fibre cavity, consisting of a 3.5% Fresnel reflection and a low reflectivity end termination (twisted end facet). Using this configuration, maximum output powers of 29.1W and 1.98W from the twisted end and straight end, respectively, were obtained for a launched pump power of 48.3W.

This corresponded to the slope efficiency for the twisted end of 77% with respect to launched power.

The output spectrum had a significant ASE background. The ASE power was determined using a Scanning Fabry-Perot Interferometer technique that filtered the ASE and laser components in the output. This showed that the ASE content was non-negligible, but that it rolled over at higher pump powers. This implies that increasing the available pump power will have a positive impact on the laser power to ASE ratio and should, at much higher powers, lead to a negligible ASE component, as well as an increased laser efficiency.

The simplicity in this approach, combined with the cladding pumped geometry, should allow for significant scaling in the fibre output power using higher power diodes. Additionally, modifying the fibre end termination to increase the core angle relative to the facet normal will reduce the output beam propagation factor due to the increased propagation losses for higher order modes. Equally, replacing the twisted end facet with a conventional angle polished end should yield equivalent results, although the twisted end facet has a better surface finish due to cleaving generally being better than polishing. A significant limitation to this low feedback approach is its susceptibility to external feedback. This can be a serious problem, as any feedback will increase the effective output coupler reflectivity and as such, will cause the output power ratio to reduce and therefore will also reduce the effective laser efficiency. Furthermore, an increase in the effective feedback will reduce both the threshold and the slope, which also reduces the maximum obtainable output power for operation many times above threshold. To deal with unwanted feedback, careful management of optics downstream from the laser is required and potentially the use of an optical isolator.

## 3.3 Tm-doped Amplified Spontaneous Emission source

### 3.3.1 Introduction

In this section, single-ended output from an all-fibre Tm-doped fibre ASE source is described. This work continued the approach of a high loss cavity with one end facet having a significantly lower reflectivity than the other, resulting in an output power ratio given by equation (3.5) and thus predominantly single-ended output. This equation is only strictly true for a laser oscillator, but in the regime where an ASE source is operated well above the signal saturation intensity given by

$$I_{sat} = \frac{h\nu_s}{(\sigma_a(\nu_s) + \sigma_e(\nu_s))\tau_f} \tag{3.19}$$

where $\nu_s$ the central frequency of the ASE spectrum, the stimulated emission dominates the inversion in the same way as in a laser oscillator, suggesting that this equation will serve as a good approximation for an ASE source as well. Using this high loss fibre feedback arrangement offers the capability for scaling the broadband emission to high output powers with careful control of feedback from both the cavity and external optics downstream of the source, so as to effectively suppress parasitic lasing.

A motivation for this work was that high power broadband sources operating in the 2$\mu m$ spectral range are of particular interest for applications such as gas sensing [15], spectroscopy, and optical coherence tomography [16]. Additionally, at the time this work was conducted, the published work on 2$\mu m$ broadband sources showed limited bandwidth and particularly limited output powers. For example, a Tm doped fibre based superfluorescence source at 1.91$\mu m$ was demonstrated with $\sim$1mW of output and a bandwidth of 77nm [17], and two sources based on Tm:Ho- [18] and Tm-doped [19] fibres had output powers of 40mW and $\sim$100mW, with slope efficiencies from the output end of $\sim$7% and 3%, respectively. Therefore, we believed our approach, applied to this operational wavelength region, could significantly improve the output power obtainable.

This all fibre single-ended output approach was applied to a thulium doped fibre that was cladding pumped by 790nm beam shaped diodes. The ASE output achieved was over 11W for a launched pump power of 40.3W. This was limited by the onset of parasitic lasing. The slope efficiency with respect to the launched pump power was 38%. The emission bandwidth (FWHM) was ~280nm at an output power of 8mW and ~36nm at the highest output power of 11W.

### 3.3.2 Theory

Kalman et al. [20] have developed a model for calculating numerically the ASE signal power in Er-doped silica fibres. This model can be modified to suit the requirements here for a Tm-doped silica fibre pumped at 790nm.

To simplify the calculations, it is advantageous to use the approximation that all pump absorption leads to inversion in the upper laser level, such that the gain medium can be considered as having only two Stark manifolds. These manifolds have the ion densities $N_1$ and $N_2$ for the lower and upper manifolds respectively, such that the total ion density $N$ is given by $N_1 + N_2 = N$. Under steady state conditions, the rate equations for the upper and lower manifolds are given by

$$\frac{dN_2}{dt} = (R_{12} + W_{12})N_1 - (W_{21} + A)N_2 = 0 \tag{3.20}$$

$$\frac{dN_1}{dt} = (W_{21} + A)N_2 - (R_{12} + W_{12})N_1 = 0 \tag{3.21}$$

for the transition rates

$R_{12} = \frac{\sigma_p P_p}{A_{cl} h\nu_p}\eta_q$, $W_{12} = \frac{\sigma_a P_s}{A_{co} h\nu_s}$, $W_{21} = \frac{\sigma_e P_s}{A_{co} h\nu_s}$, and $A = 1/\tau_f$

where $\sigma_p$ is the absorption cross-section at the pump frequency $\nu_p$, $\sigma_a$ is the absorption cross-section and $\sigma_e$ is the emission cross-section both at the signal frequency $\nu_s$, $P_p$ is the pump power, $P_s$ is the signal power, $\eta_q$ is the pump quantum efficiency (defined as the number of ions excited to the upper level per pump photon absorbed), $\tau_f$ is the fluorescence lifetime of the upper level, and $A_{co}$ and $A_{cl}$ are the core and cladding areas respectively.

Using $N_1 + N_2 = N$ and substituting for $N_1$ into equation (3.20), the fraction of the ions in the upper manifold is given by

$$a(z) = \frac{N_2}{N} = \left(\frac{P_p(z)\eta_q}{A_{cl}I_{psat}} + \frac{P_s(z)}{A_{co}I_{ssat}}\right)\left(1 + \frac{P_p(z)\eta_q}{A_{cl}I_{psat}} + \frac{P_s(z)}{A_{co}I_{sat}}\right)^{-1} \tag{3.22}$$

where $P_p(z)$ is the pump power at position $z$, $P_s(z)$ is the total signal power at position $z$, which is given by $P_s(z) = P_s^+(z) + P_s^-(z)$. The saturation intensities are given by

$$I_{psat} = \frac{h\nu_p}{\tau_f \sigma_p} \tag{3.23}$$

$$I_{ssat} = \frac{h\nu_s}{\tau_f \sigma_a} \tag{3.24}$$

$$I_{sat} = \frac{h\nu_s}{\tau_f (\sigma_a + \sigma_e)} \tag{3.25}$$

The pump power at position $z$ is calculated using the pump loss along the fibre given by [21]

$$\frac{dP_p}{dz} = -\frac{A_{co}}{A_{cl}}\sigma_p N[1 - a(z)]P_p(z) \tag{3.26}$$

In the case of the ASE signal, calculating the signal power at a given position is more complex than the pump due to their broadband nature. Typically, the ASE is considered to be made up of $n$ narrow bandwidth frequency components, which have a frequency spacing $(ASE\ Bandwidth)/n$. With this approach, solving for the total signal power requires calculating the signal growth for each frequency component simultaneously with all others. As such, this is both complex and time consuming. To simplify the calculations, the 'mean' wavelength approach can be used. With this approach, the model considers only three optical waves propagating along the fibre: a unidirectional pump wave with power $P_p(z)$, and the two counter-propagating signals with a power in the forward direction of $P_s^+(z)$ and in the backward direction of $P_s^-(z)$. The ASE signals have a central frequency $\nu_s$ and a bandwidth $\Delta\nu_s$. Under this approximation, the signal growth along the fibre is given by [20]

$$\frac{dP_s^\pm}{dz} = \pm N\left([(\sigma_e + \sigma_a)a(z) - \sigma_a]P_s^\pm \pm P_0\sigma_e a(z)\right) \tag{3.27}$$

where $\sigma_a$ and $\sigma_e$ are the absorption and emission cross-sections of the mean signal frequency, and $P_0$ is the spontaneous emission power given by

$$P_0 = 2h\nu_s\Delta\nu_s \tag{3.28}$$

By solving equations (3.26), (3.27) and (3.22) numerically, the extracted output power from each end of the fibre can be determined.

### 3.3.3 Experimental procedure

The experimental setup for our high power ASE source can be seen in Figure 3.13(b). The Tm-doped fibre used was fabricated in-house using standard modified chemical vapour deposition and the solution doping technique. The resulting fibre had a 25$\mu m$ diameter Tm-doped alumino-silicate core with a $Tm^{3+}$ concentration of ~1.5wt.% and an $Al^{3+}$:$Tm^{3+}$ concentration ratio of 10:1. The core $NA$ was 0.18. The core was surrounded by a 300$\mu m$ diameter D-shaped pure silica inner-cladding with a nominal $NA$ of 0.49. The inner-cladding was then coated by a low refractive index polymer outer coating.

This fibre was operated in a cladding pumped configuration using two beam shaped diode bars at 790nm. Each had an output power of ~30W. The two diodes were arranged to facilitate independent pumping of each fibre end facet, allowing the measurement of the output power performance as a function of pump direction. The beam propagation factor for both diode bar mod-

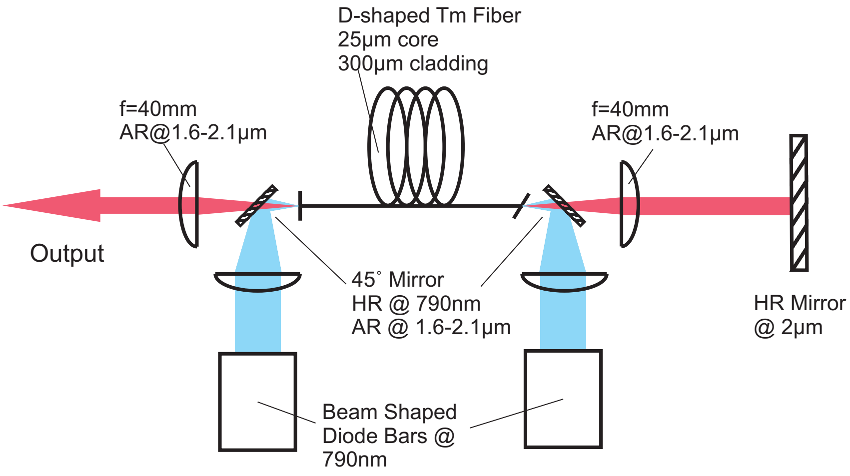

(a) Laser Cavity

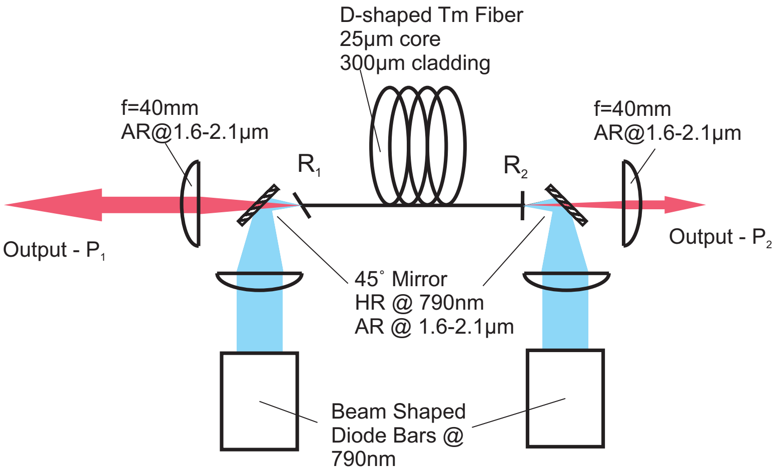

(b) ASE Cavity

Figure 3.13: The cavity setup for (a) the laser with an external feedback cavity consisting of a f=40mm collimating lens and HR mirror, (b) ASE cavity with feedback is provided from the end facets labelled $R_1$ and $R_2$.

ules, after using a 2 mirror beam shaper, was $M^2$ <70 in both the fast and slow axis. Pump light was launched into the inner cladding of the fibre via an AR coated 30mm focal length lens and a dichroic mirror with a HR (>98%) at 785-795nm and HT (>97%) at 1600-2100nm at 45°. The dichroic mirror was used to allow extraction of 2$\mu m$ ASE emission. In this configuration, the launch efficiency into the fibre was ~87%. The absorption efficiency for 790nm light in the cladding pumped regime was estimated using a cut-back measurement to be ~3.4dB/m. Therefore, a fibre length of 5m was chosen for efficient pump absorption.

The fibre was operated in two regimes. The first was as a laser with a cavity formed from a perpendicularly cleaved end facet to provide a Fresnel reflection (with a reflectivity of ~0.035) and an external feedback cavity on the other end of the fibre, as shown in Figure 3.13(a). The external feedback cavity consisted of an AR coated (1600-2100nm) 40mm focal length lens and a plane mirror with high reflectivity. With this set-up, the fibre operated single-ended, as governed by equation (3.4). In the second regime, the fibre was operated as an ASE source and had a cavity formed from a perpendicularly cleaved facet one end and the other end angle polished to ~14° to suppress parasitic lasing, whilst maintaining predominantly single-ended output. For both regimes, the fibre ends were mounted in water-cooled V-groove heat sinks to prevent fibre damage due to scattered pump light and quantum defect heating in the fibre core.

### 3.3.4 Results and analysis

The first experiment conducted was in a laser configuration as outlined above, as this formed a benchmark for the fibre performance for comparison with the fibre operated as an ASE source. At the maximum launched pump power of 50.3W, the fibre laser produced 18.2W of output with a slope efficiency of 41%, as seen in Figure 3.14. The laser threshold (estimated by extrapolation) was ~5W of launched pump power.

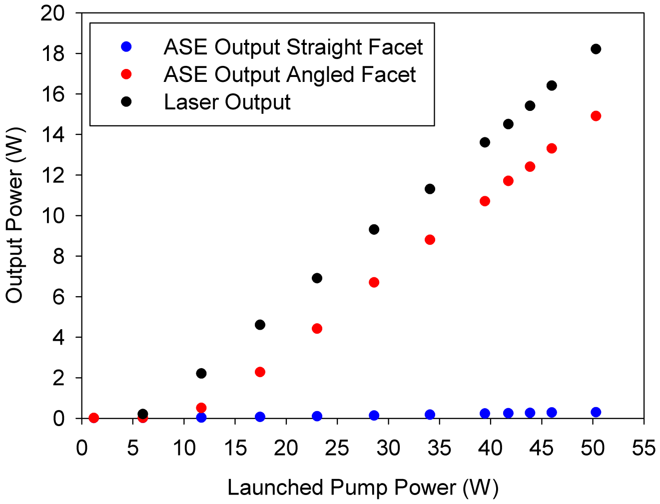

Figure 3.14: Showing the output power from the straight and angled facets, as a function of launched pump power when both fibre ends are pumped. Additionally, the laser output power for the same fibre with a perpendicularly cleaved facet and external feedback cavity is shown for comparison.

Using the expressions from Chapter 2, the theoretical slope and threshold were calculated. The value of the pumping quantum efficiency needed for the calculations is not known for this fibre, so the measured slope efficiency was compared to the literature. Jackson [22] reported that for a 9:1 $Al^{3+}$:$Tm^{3+}$ ratio, they measured a slope efficiency of 47% (but did not mention the cavity losses used to estimate $\eta_q$). However, in [23] Jackson and Mossman report a 20-25$\mu m$ core 300$\mu m$ cladding fibre with a 10:1 doping ratio that has a slope of ~46% for single-ended operation. The cavity was formed from a HR mirror butted at one end and a fresnel reflection at the other. This suggests that our laser is operating around its maximum theoretical efficiency, given the same $Al^{3+}$:$Tm^{3+}$ concentration ratio and similar fibre geometry. Due to the similarity with the reported data, it seems reasonable to use our slope to estimate the pump quantum efficiency.

To calculate the expected laser threshold and slope efficiency, the following values for the fluorescence lifetime and cross-sections were taken from the literature to be $\tau_f = 360\mu s$ [24], and $\sigma_e(\lambda = 1960nm) = 4.2 \times 10^{-25}m^2$ and

$\sigma_a(\lambda = 1960nm) = 5 \times 10^{-27}m^2$ [25]. By assuming that the loss in the external feedback cavity is ∼5% and using the measured absorption efficiency of $\eta_{abs} = 98\%$, the theoretical slope efficiency is given by $\eta_s = 0.368\eta_q$. Therefore, assuming our measured slope is optimum, the pump quantum efficiency is $\eta_q \approx 1.11$. Using this value, the threshold pump power can be estimated as being $P_{thres} = 0.99W$. This is considerably less than what we observed, which is understandable given that in practice the laser signal grows gradually just above threshold, it is only once the signal intensity is greater than the signal saturation intensity that the true slope is realised and the output power grows linearly with increased pump power. As such, the actual threshold will always be much lower than the extrapolated measurement would suggest.

For the situation whereby the fibre was operated as a single-ended ASE source with one end facet angle polished to 14° and the other perpendicularly cleaved, a maximum output power of 14.9W was obtained for a total launched pump power of 50.2W (both ends pumped). However, as can be seen from the emission spectrum in Figure 3.16, at the highest output power, there is evidence of the onset of lasing. This is due to residual feedback from the fibre end facets, although it could also potentially be from imperfections along the fibre. It is worth noting that even with the onset of lasing, the signal is still predominantly ASE. The highest output power obtained before the onset of parasitic lasing was measured to be 11W from the angled end facet, for a launched pump power of 40.3W. This corresponds to a slope efficiency of 38%, which is comparable to that for the laser oscillator previously tested. The slight decrease in slope does suggest that the ASE signal is not completely saturating all of the inversion, allowing the inversion to build up until the laser threshold condition is reached, as was shown in this case. It is then expected that as the pump power is increased, the proportion of laser to ASE in the output will increase, as shown in the single-ended Yb doped laser previously. This does raise an interesting question as to why the laser signal can begin to dominate over the ASE, even though the ASE signal is much stronger. At present, there is not an answer to this in the literature. However, the theory presented in Section 3.2.5 offers a potential explanation. It describes how as the pump power increases, the wavelengths that resonate in the cavity see a favourable increase in intensity over non-resonant ones. Therefore, these resonant wavelengths can eventually dominate the inversion so that their round-trip gain equals the cavity losses and therefore can begin to lase. The proposed theory suggests that reducing the feedback efficiency for each fibre end will increase the laser threshold, but that the laser threshold will always eventually be reached. The interesting point here is to what extent the ASE power can be scaled before lasing occurs.

The ASE output power from the angled facet was calculated as a function of the launched pump power using the theory in Section 3.3.2. This is shown in Figure 3.15, where the following values were used in the calculations: $N = 5.14 \times 10^{25} m^{-3}$, $\sigma_p = 8.59 \times 10^{-25} m^2$ [26], $\sigma_a = 5.01 \times 10^{-27} m^2$ [25], $\sigma_e = 4.16 \times 10^{-25} m^2$ [25], $\nu_s = 1.53 \times 10^{14} Hz$ ($\lambda_s = 1960 nm$), $\Delta\nu = 2.81 \times 10^{12} Hz$, $\tau_f = 360 \mu s$ [24] and $\eta_q = 1.11$ (calculated from the laser slope for the same fibre). From the Figure, it can be seen that the theory is a good fit for the data, but slightly over-estimates the output power.

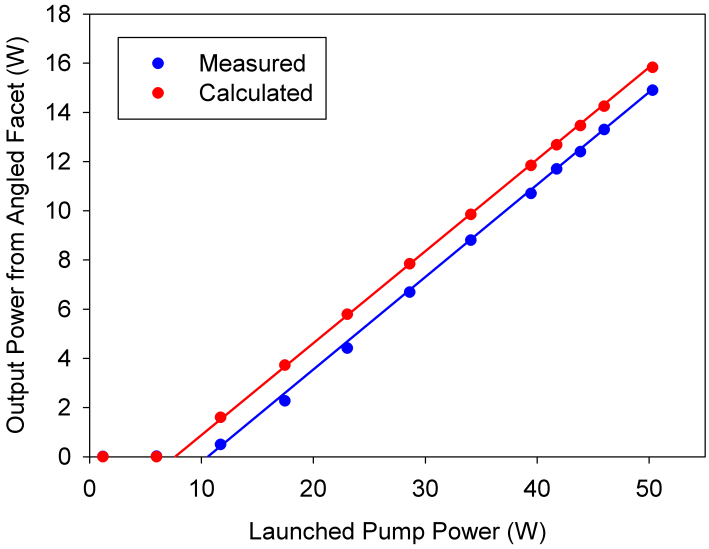

Figure 3.15: The theoretical ASE output power from the angled facet compared to the measured value for both ends of the fibre pumped as a function of the launched pump power.

The output beam propagation factor was measured to be $M^2$ <2.8, which given the fibres V-value of 7.2 (at the central wavelength of 1958nm) is reasonably good. This is especially true given that the measurement technique will record a worse beam quality for a broadband source than for a narrow linewidth one, due to multimode interference. Both the beam quality and slope efficiency can be improved by modifying the fibre design so that it has a smaller V-value (and therefore by the rough guide where $V \approx 2M^2$, a smaller output beam propagation factor) and by modifying the core composition such that the $Al^{3+}$:$Tm^{3+}$ ratio is further optimised to favour two-for-one cross-relaxation [22, 23].

The emission spectrum for output power above ~300mW had a central wavelength of ~1958nm and a bandwidth (FWHM) of ~36nm, as seen in Figure 3.16. The line shape in this power range is nearly a perfect Gaussian, suggesting that Tm-doped ASE sources should be ideal where a Gaussian intensity profile are desired, such as in Fibre-optic gyroscopes [27] and in optical coherence tomography [28]. Furthermore, for optical coherence tomography, the spectral bandwidth and power of the source is important because the broader the emission bandwidth, the better the resolution and contrast achievable, whilst the high spectral power density is required to improve the signal to noise ratio in the system [28].

For low power operation (<20mW), the emission spectrum was very broad, spanning a wavelength range of ~1650$\mu m$ to ~2100$\mu m$, as seen in Figure 3.17. For the 8mW emission spectrum, the structure seen in the range of 1800nm to 1950nm is caused by absorption from water vapour in the air (more details on water absorption in ASE sources is given in Chapter 5, Section 5.2.3). As the output power increases, the emission bandwidth narrows so that for the output powers of 8mW, 51mW and 300mW, the FWHM bandwidths are 280nm, 80nm and 42nm respectively. This is to be expected due to the wavelengths that experience the highest gain beginning to saturate the inversion with increased pump power, resulting in an ever reducing gain for wavelengths in the wings. This can be seen by the fact that above the signal saturation intensity of $P_{sat} \approx 340mW$, the bandwidth is nearly constant.

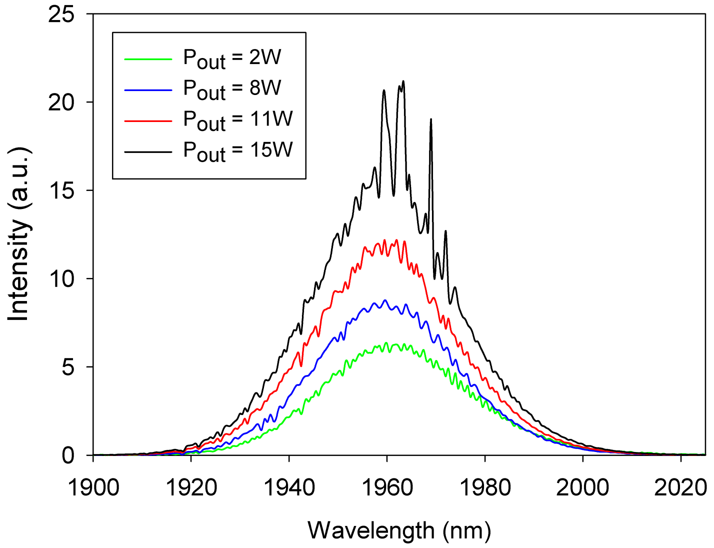

Figure 3.16: The output emission spectrum for the angle polished fibre end as a function of the output power for high powers.

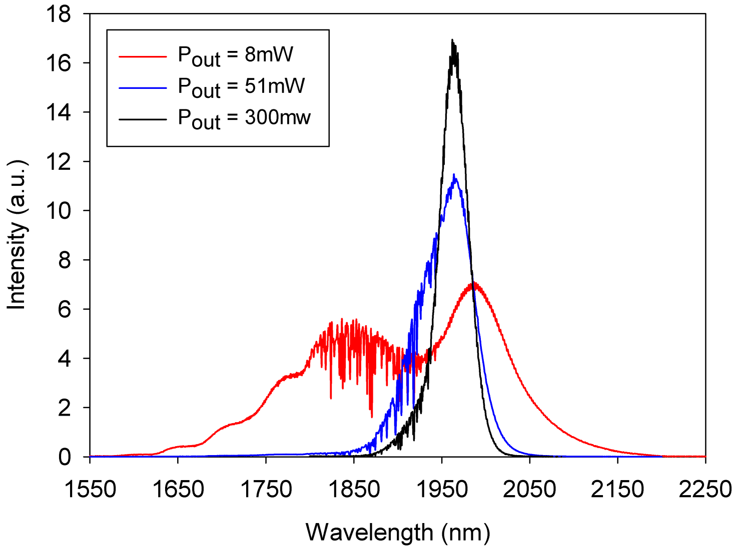

Figure 3.17: The output emission spectrum for the angle polished fibre end as a function of the output power for low powers.

To investigate the effect of pumping direction on the output performance, each end of the fibre was pumped individually by a 30W diode bar. The output power as a function of launched pump power measured is shown in Figure 3.18. In both cases, the output spectrum from the angled end was monitored using the DongWoo Monochromator Model DM500i. In the case where the angled end was pumped (counter-propagating pump) with 25W of launched pump power, the maximum output power was 4.9W and 0.12W for the angled and straight ends respectively, resulting in a $P_{angle}/P_{straight}$ of 42. The slope efficiency from the angle end was 36%. This is slightly less than for both end pumping, due to the increased re-absorption of the signal in the un-pumped end of the fibre. The output spectrum was centred at 1960nm, with a bandwidth (FWHM) of 36nm. For the situation where the straight end was pumped (co-propagating pump), the output powers at 25W of launched power were 3.8W and 0.16W for the angled and straight ends respectively, resulting in a power ratio of $P_{angle}/P_{straight} = 23$. This corresponded to a slope efficiency from the angle end of 28%. The decreased slope and output power compared to the counter-propagating regime is attributed to reabsorption loss at the output end of the fibre, and thus the gain in the two pumping directions is different. The emission spectrum from the angled facet was very similar to that for the counter-propagating pump, with a central wavelength of 1960nm and bandwidth (FWHM) of 39nm. For both pumping directions, the maximum output powers were limited only by the available pump power, but in the current cavity configuration, the onset of lasing (as shown in the case where both ends were pumped) will be a limiting factor. Comparing the output power with that predicted by the theory, it can be seen that as was the case before, the theory predicts a higher output power. A comparison of the theoretical output power with the measured value is shown in Figure 3.19, where the values used in the calculations were the same as those used above. In both cases, the theoretical power is much higher than the measured value. The reason for this is that the theory assumes that there is no energy transfer up-conversion (ETU) or excited state absorption (ESA) from the $^3F_4$ manifold. In practice, this is not the case as fluorescence through the fibre cladding can be observed in the blue spectral region, where the emission must originate from much higher energy levels. This is shown by Moulton et al. [29], where they show that pumping at 790nm can lead to inversion in the $^1G_4$ manifold whose energy level is 21277cm$^{-1}$, corresponding to an emission wavelength of 470nm. The impact of this is that there is a higher inversion in the model than there is in practice and as such, the theoretical ASE power is higher. Therefore, accounting for ESA and ETU in the modelling should improve its accuracy.

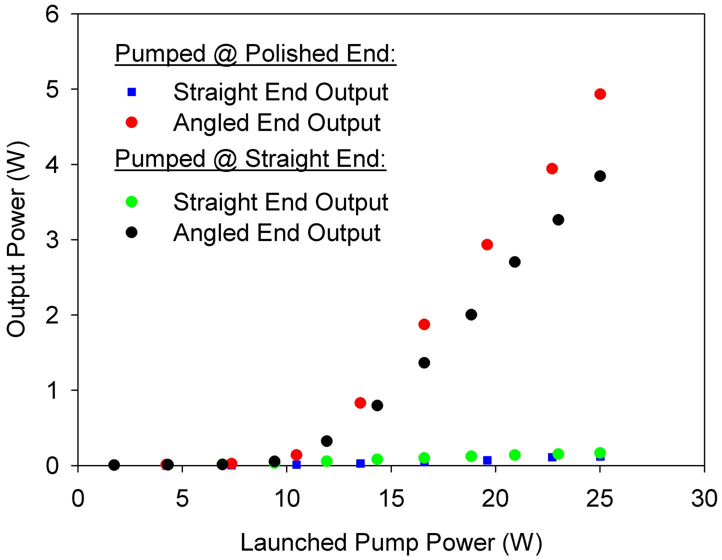

Figure 3.18: ASE output power from the straight and angled facets, as a function of launched pump power and the pumping direction.

To explore if the ASE output power in a predominantly single-ended all fibre approach can be scaled further before the onset of lasing, the same fibre was angle polished to 14° at both ends. This fibre was firstly pumped at only one end with an output power of 2.3W from the pumped end compared to 1W from the un-pumped one. This further shows the significance of pump direction on output power. With both ends of the fibre pumped, the maximum output power achieved was 8.2W and 6.8W (from the pumped and un-pumped ends respectively) for a launched pump power of 50.3W, with no presence of parasitic lasing. The combined ASE output of 15W was achieved with a slope efficiency of 42.5% with respect to launched pump powers for out-

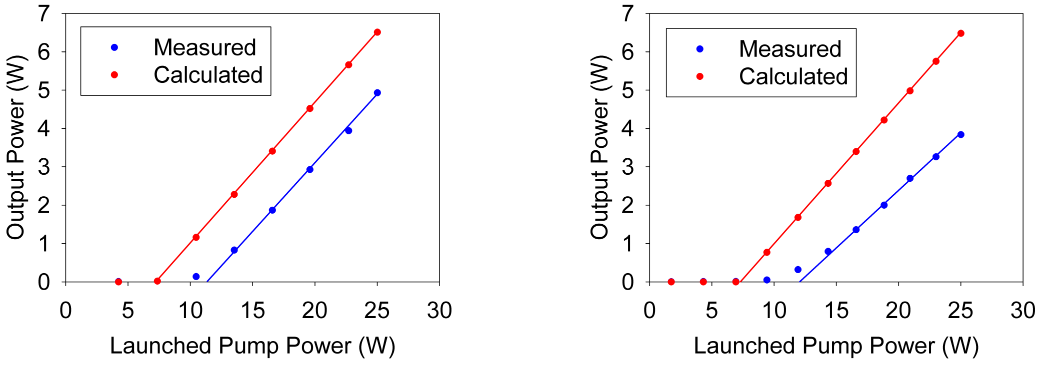

(a) Angled Facet Pumped (b) Straight Facet Pumped

Figure 3.19: The ASE output power from the angled facet as a function of pump direction, comparing the theoretical output with measured values, as a function of the launched pump power for (a) the angled facet pumped and (b) the perpendicularly cleaved facet pumped.

put powers above 10W. This suggests that further power scaling in the single-ended regime is still achievable by slightly angling the straight facet to reduce the feedback reflectivity, whilst still maintaining a large reflectivity difference between the facets so that a predominantly single-ended output is obtained. However, although reducing the fibre's end facet's reflectivity will increase the laser threshold, it cannot stop lasing altogether. Therefore, as previously discussed, the onset of lasing will ultimately limit the maximum obtainable ASE power.

### 3.3.5 Conclusion

In conclusion, a single-ended ASE source has been demonstrated based on a Tm-doped silica fibre, which was operated in a high cavity loss configuration, such that one fibre end facet had a much lower feedback reflectivity than the other. This approach produced predominantly single-ended ASE output of 11W for 40.3W of launched pump power. The emission bandwidth at this power level was ∼36nm, with a central wavelength of ∼1958nm. With the cavity design used, the output power was limited by the onset of parasitic lasing. The laser threshold can be increased by further reducing the feedback reflectivity of the end facets. To maintain single-ended operation, the output coupler reflectivity would still need to be significantly lower than the other end facet. This could be achieved by angle polishing both ends, but with the output coupler polished to a larger angle. Alternatively, by changing the fibre geometry, the twisted end facet [7] approach used previously could be applied to this system. The benefit of this approach is that it has been shown that the feedback reflectivity can be as low as $\sim 10^{-7}$, compared to the typical lowest reflectivity of an angle polished surface of $\sim 10^{-5}$ [30].

A point of interest to further this research would be to explore the limits of reducing the fibre feedback, whilst maintaining single-ended output, before the laser threshold is reached. It would seem that even when operating well above the saturation intensity and achieving a slope efficiency comparable to a laser oscillator with the same fibre, the ASE cannot completely dominate the inversion. In Section 3.2.5, a theory was proposed to explain why lasing will occur. This showed that resonant wavelengths inside the fibre see a favourable increase in intensity compared to non-resonant ones, as the pump power is increased. As a result, these resonant wavelengths begin to dominate the inversion at higher pump powers, such that eventually their round-trip loss equals the gain and they begin to lase. It would seem therefore that no matter what the fibre end facet reflectivities, lasing will always eventually occur with high enough pump powers. Therefore, reducing the fibre reflectivities whilst maintaining $R_1 \ll R_2$, for predominately single ended output, will scale the maximum ASE power, but this will still be limited by the onset of lasing. Another potential limit on the maximum ASE power is due to Rayleigh scattering from microscopic inhomogeneities along the fibre [13]. Rayleigh scattering causes unwanted feedback inside the fibre core, which could result in parasitic lasing and therefore limit the ASE power.

A solution to parasitic lasing could be to use an amplifier system to further power scale the ASE signal. This approach was successfully applied by Wang et al. [9] in Yb-doped silica fibres, where they showed that for their single stage gain element, the onset of lasing limited the performance to 40W of ASE power, but that by using an amplifier, this power could be scaled to 122W, limited only by the available pump power. However, using an amplifier system will add to the system complexity and require the use of high power optical isolators. In the $1\mu m$ regime this would not be a problem, but at $2\mu m$, commercially available isolators are limited to particular wavelengths and currently have very low damage thresholds, which in turn limit the maximum ASE powers launched into the amplifier and therefore the maximum amplified power.

## 3.4 Summary

It has been shown that an all fibre approach using low reflectivity feedback fibre end facets with $R_1 \ll R_2$ and $R_{1,2} \ll 1$, can achieve predominantly single-ended operation in both a laser oscillator and ASE source. The laser oscillator was based on a cladding pumped Yb-doped silica fibre with a twisted-end termination method [7] to obtain a very low feedback reflectivity ($\sim 6 \times 10^{-5}$) one end and a perpendicular cleave the other. The maximum output power obtained was 29.1W, which was limited by the available pump power. Due to the large cavity losses, the laser threshold was higher than a typical Yb-doped fibre laser, and as a result, the output spectrum had a significant ASE component. The relative power contained in the ASE was determined using a Scanning Fabry Perot Interferometer to filter the laser and ASE signals. This showed that the contribution to the output was ~18% ASE at the maximum power. However, this analysis showed that at high pump powers, the ASE power rolled over, suggesting that with additional pump power, the laser emission could be further scaled and the relative ASE component in the output reduced.

For the ASE source, a cladding pumped Tm-doped fibre with a perpendicularly cleaved facet (3.5% Fresnel Reflection) and an angle polished end facet were used to form the single-ended output cavity. The source produced 11W of ASE power for a total launched pump power of 40W (pumped equally from both ends), which with the current cavity design was limited by the onset of parasitic lasing. The slope efficiency of the source was 38% to launched pump power, which was comparable to that for a laser using the same fibre but with an external feedback cavity to yield single-ended operation ($\eta_{laser\ slope} = 41\%$). The impact of pumping direction on output performance was measured and showed that a counter-propagating pump gave a higher output power and slope efficiency than the co-propagating pump, as expected. Furthermore, to explore the limits imposed by the onset of lasing, the fibre was angle polished to 14° at both ends. The total output power extracted was 15W for a launched pump power of 50.3W. At this highest available pump power, there was no evidence of parasitic lasing. This suggests that further scaling in the output power of this all fibre single-ended approach should be possible if the perpendicularly cleaved facet was angle polished slightly to reduce its feedback reflectivity (and therefore increase the laser threshold), whilst still maintaining $R_1 \ll R_2$ and thus predominantly single-ended output. It has been shown, since this work was conducted, that the ASE output in an Yb-doped fibre using the twisted end termination can be scaled to 62W of single-ended output [9] before the onset of lasing. Furthermore, Chan et al. [30] showed that by applying a low reflectivity at both ends, the output could be scaled to ~110W of double ended ASE power. This is similar to our 2$\mu m$ results, emphasising that with additional pump power and a further reduction in total cavity feedback will result in significant scaling in the output power. However, it would seem from our calculations that the onset of lasing will always occur and that reducing the reflectivity will only increase the laser threshold, not stop lasing altogether. A solution to this problem is to use an amplifier system. Wang et al. [9] demonstrated this approach in Yb-doped silica where they showed that the output power of a single gain element was limited to 40W by parasitic lasing, but that by using a second gain element the output power could be scaled to >120W, limited only by the available pump power. Therefore, using an amplifier system based on Tm doped fibre would appear to be the best strategy for further power scaling. The only potential limit to an amplifier system is the availability of high power optical isolators. In the 1$\mu m$ regime this is not a problem, but as was found in the next chapter, commercially available isolators at 2$\mu m$ are very limited in both their power handling and in the range operational wavelengths.

A further limitation to both of these low feedback regimes is their susceptibility to external feedback. This can be a serious problem, as in the case of a laser any feedback will change the laser dynamics, and if the effective feedback reflectivity for the output coupler is increased, it will cause the output power ratio to reduce and therefore also reduce the effective laser efficiency. In the case of the ASE source, the impact of external feedback is even more pronounced as any feedback could cause parasitic lasing and potentially damage the fibre. Therefore, in both cases, controlling sources of feedback is a high priority.

## 3.5 References

[1] **Rigrod, W. W.**, *Saturation Effects in High-Gain Lasers*, Journal of Apllied Physics, Vol. 36, No. 8, pp. 2487–2490, August 1965.

[2] **Liem, A., Limpert, J., Zellmer, H., Tnnermann, A., Reichel, V., Mrl, K., Unger, S., Mller, H. R., Kirchhof, J.** and **Harschak, A.**, *1.3 kW Yb-doped fiber laser with excellent beam quality*, Proceedings of the Conference on Lasers and Electro-Optics, 2004, paper Number CPDD2.

[3] **Jeong, Y., Sahu, J. K., Payne, D. N.** and **Nilsson, J.**, *Ytterbium-doped large-core fiber laser with 1.36 kW continuous-wave output power*, Optics Express, Vol. 12, pp. 6088–6092, 2004.

[4] **Shen, D. Y., Sahu, J. K.** and **Clarkson, W. A.**, *Highly efficient Er,Yb-doped fiber laser with 188W free-running and $>$ 100W tunable output power*, Optics Express, Vol. 13, No. 13, pp. 4916–4921, 2005.

[5] **Frith, G., Lancaster, D. G.** and **Jackson, S. D.**, *85W $Tm^{3+}$-doped silica fibre laser*, Electronics Letters, Vol. 41, No. 12, pp. 687, June 2005.

[6] **Plantonov, N. S., Gapontsev, D. V., Gapontsev, V. P.** and **Shumilin, V.**, *135W CW fiber laser with perfect single mode output*, Proceedings of the

Conference on Lasers and Electro-Optics, 2002, paper Number CPD3-1 - CPDC3-4.

[7] **Clarkson, W. A.** and **Wang, P.**, *UK Patent Application "Optical fiber device", Application Number 0600179.6*, Jan 2006.

[8] **Wang, P., Sahu, J. K.** and **Clarkson, W. A.**, *110W double-ended ytterbium-doped fiber superfluorescent source with* $M^2$*=1.6*, Optics Letters, Vol. 31, No. 21, pp. 3116–3118, 2006.

[9] **Wang, P., Sahu, J. K.** and **Clarkson, W. A.**, *Power scaling of ytterbium-doped fiber superfluorescent sources*, IEEE Journal of Selected Topics in Quantum Electronics, Vol. 13, No. 3, pp. 580–587, 2007.

[10] **Wang, P., Cooper, L. J., Williams, R. B., Sahu, J. K.** and **Clarkson, W. A.**, *Helical-core ytterbium-doped fibre laser*, Electronics Letters, Vol. 40, No. 21, pp. 1325–1326, October 2004.

[11] **Marcuse, D.**, *Reflection losses from imperfectly broken fiber ends*, Applied Optics, Vol. 14, No. 12, pp. 3016–3020, December 1975.

[12] **Pask, H. M., Carman, R. J., Hanna, D. C., Tropper, A. C., Mackechnie, C. J., Barber, P. R.** and **Dawes, J. M.**, *Ytterbium-doped silica fiber lasers: Versatile sources for the 1-1.2µmregion*, IEEE Journal of Selected Topics in Quantum Electronics, Vol. 1, No. 1, pp. 453–464, April 1995.

[13] **Pedrotti, F. L.** and **Pedrotti, L. S.**, Introduction to Optics, Prentice-Hall, 2nd edn., 1993.

[14] **Hecht, E.**, Optics, Addison Wesley, 4th edn., 2002.

[15] **Morse, T. F., Oh, K.** and **Reinhart, L. J.**, *Carbon dioxide detection using co-doped Tm-Ho optical fiber*, Proceeding of SPIE, Vol. 2510, pp. 158–164, 1995.

[16] **Bouma, B. E., Nelson, L. E., Tearney, G. J., Jones, D. J., Brezinski, M. E.** and **Fujimoto, J. G.**, *Optical coherence tomographic imaging of human tissue at 1.55µmand 1.81µmusing Er- and Tm-doped fiber sources*, Journal of Biomedical Optics, Vol. 3, pp. 76–79, 1998.

[17] **Oh, K., Kilian, A., Reinhart, L., Zhang, Q., Morse, T. F.** and **Weber, P. M.**, *Broadband superfluorescent emission of the* $^3H_4 \rightarrow ^3 H_6$ *transition in a Tm-doped multicomponent silicate fiber*, Optics Letters, Vol. 19, pp. 1131–1133, 1994.

[18] **Tsang, Y. H., El-Sherif, A. F.** and **King, T. A.**, *Broadband amplified spontaneous emission fibre sources near 2µmusing resonant in-band pumping*, Journal of Modern Optics, Vol. 52, pp. 109–118, 2004.

[19] **Tsang, Y. H., King, T. A., Ko, D. K.** and **Lee, J.**, *Broadband amplified spontaneous emission double-clad fibre sources with central wavelengths near 2µm*, Journal of Modern Optics, Vol. 53, pp. 991–1001, 2006.

[20] **Kalman, R. F., Wysocki, P. F.** and **Digonnet, M. J. F.**, *Large signal three-level superfluorescent fiber sources*, Feb 1993.

[21] **Paschotta, R., Nilsson, J., Tropper, A. C.** and **Hanna, D. C.**, *Ytterbium-doped fiber amplifiers*, IEEE Journal of Qunatum Electronics, Vol. 33, No. 7, pp. 1049–1056, July 1997.

[22] **Jackson, S. D.**, *Cross relaxation and energy transfer upconversion processes relevant to the functioning of 2µm*$Tm^{3+}$*-doped silica fibre lasers*, Optics Communications, Vol. 230, pp. 197–203, 2004.

[23] **Jackson, S. D.** and **Mossman, S.**, *Efficiency dependence on the* $Tm^3+$ *and* $Al^3+$ *concentrations for* $Tm^3+$*-doped silica double-clad fiber lasers*, Applied Optics, Vol. 42, No. 15, pp. 2702–2707, 2003.

[24] **Agger, S., Povlsen, J. H.** and **Varming, P.**, *Single-frequency thulium-doped distributed-feedback fiber laser*, Optics Letters, Vol. 29, No. 13, pp. 1503–1505, July 2004.

[25] **Engelbrecht, M., Haxsen, F., Wandt, D.** and **Kracht, D.**, *Wavelength resolved intracavity measurement of the cross sections of a Tm-doped fiber*, Optics Express, Vol. 16, No. 3, pp. 1610–1615, February 2008.

[26] **Jackson, S. D.** and **King, T. A.**, *Theoretical modeling of tm-doped silica fiber lasers*, Journal of Lightwave Technology, Vol. 17, No. 5, pp. 948–956, May 1999.

[27] **Burns, W. K., Chen, C. L.** and **Moeller, R. P.**, *Fiber-optic gyroscopes with broad-band sources*, Journal of Lightwave Technology, Vol. LT-1, No. 1, pp. 98–105, March 1983.

[28] **Schmitt, J. M.**, *Optical coherence tomography (OCT): A Review*, IEEE Journal of Selected Topics in Quantum Electronics, Vol. 5, No. 4, pp. 1205–1215, July/August 1999.

[29] **Moulton, P. F., Rines, G. A., Slobodtchikov, E. V., Wall, K. F., Frith, G., Samson, B.** and **Carter, A. L. G.**, *Tm-doped fiber lasers: Fundamentals and power scaling*, IEEE Journal of Selected Topics in Quantum Electronics, Vol. 15, No. 1, pp. 85–92, January/February 2009.

[30] **Chan, J. S. P., Wang, P., Sahu, J. K.** and **Clarkson, W. A.**, *Ultra-low feedback fibre end termination geometry for high power fibre source applications*, CLEOE-IQEC, 2007.

# Chapter 4

# Single frequency Tm-doped fibre master oscillator power amplifier

## 4.1 Introduction

This chapter focuses on work conducted on a high power single-frequency source operating in the $2\mu m$ spectral region. These sources are of particular interest for spectroscopy, gas sensing and nonlinear frequency conversion to the mid-infrared. After reviewing common approaches for obtaining single-frequency oscillation, it was apparent that a single-stage oscillator would not be able to operate at high power levels. Therefore, a master oscillator power amplifier configuration was employed, whereby a low power laser with stable, narrow linewidth output and an excellent beam quality, is power scaled using a series of amplifier stages without degrading the signal stability or increasing beam propagation factor. The master oscillator approach chosen was based on a Tm-doped silica fibre with a distributed feedback (DFB) grating UV written into the core, as this approach allows for wavelength selection and will enforce robust single-frequency operation [1–3]. This master-oscillator was then power scaled using three amplifier stages.

As was discussed in Chapter 2, in fibre based oscillators and amplifiers the tight beam confinement in the core can result in high peak intensities, which induce non-linear effects in the fibres. Therefore, the impact of non-linear effects on the performance is discussed, with limits given in terms of the signal power required before the onset of each non-linear effect.

To aid the design and production of an efficient amplifier system, the amplifier performance was modelled to predict the system gain and power extraction efficiency with the incident signal power available. This model showed that the small signal gain in the fibres used in the amplifier stages is very high, such that operating in a saturated regime can be achieved for moderate seed power levels ($\sim$1W). Furthermore, using the model, the output signal intensity from an amplifier stage can be estimated so that the design can be modified to ensure that the onset of non-linear effects, in particular Stimulated Brillouin Scattering, does not occur.

Lastly, the results for the MOPA configuration are discussed, with the potential for further power scaling given. In this chapter, the single-frequency DFB laser and intermediate amplifier were constructed by Dr. Zhaowei Zhang with the DFB grating written by Dr. Morten Ibsen. The power amplifier stage construction and the subsequent results and analysis were conducted by myself.

## 4.2 Single-frequency oscillator

### 4.2.1 Approaches

By definition, a single frequency oscillator only operates on a single-axial mode. There are many approaches for achieving this, which are briefly discussed. One approach is to select the cavity length such that the mode spacing $\Delta\nu$ is large compared to the transition linewidth, where $\Delta\nu$ is given by

$$\Delta\nu = \frac{c}{2nl} \tag{4.1}$$

where $n$ is the fibre refractive index and $l$ the cavity length. However, depending on the laser transition and gain medium, this can require a small cavity length, such that for efficient lasing, the doping concentration in the region would have to be very high, which is not always practical. Another approach is to insert mode selecting elements into the cavity, such as etalons, which will suppress modes that are adjacent to the laser mode. This means that longer cavity designs can be used with lower doping concentrations. The drawbacks to this are that the system has limited flexibility for wavelength tuning, added to the requirement for polarisation selecting elements (and in the case of fibres, using polarisation maintaining fibre). Furthermore, these additional cavity elements add to the system complexity and cost.

The problem for both of these standing wave configurations is the build up of gain at the nodes of the stand-wave, due to spatial hole-burning. This can result in a reduction in the overall efficiency due to a reduced effective gain, with these areas not being used. To overcome this, a travelling wave cavity can be used in the form of an unidirectional ring laser geometry. However, these cavities are not without their limitations. To achieve unidirectional oscillation requires that the loss in one direction is greater than in the other. This is typically achieved using an optical isolator. Therefore, it is required that the transmission for through direction in the isolator is high so that the cavity losses are kept low for higher performance (i.e. a lower threshold pump power and higher slope efficiency). In the 2$\mu m$ spectral region, low loss optical isolators are not always available for the desired operational wavelength, whereas for lasers operating in the 1-1.5$\mu m$ regime, there is considerably greater choice. However, unidirectional operation does not always need an isolator, it only requires the loss in each direction to differ. Shen et al. [4] demonstrated this at 2.1$\mu m$, using a Ho:YAG laser where an acousto-optic modulator (AOM) was used to enforce unidirectional operation by increasing the loss in the lasing direction by just 0.5% (due to diffraction). Another requirement for single-mode operation is that it is linearly polarised, requiring a cavity to have some form of polarisation control. For fibres, the fibre will need to be polarisation maintaining, which makes the splicing more complicated as the fast and slow axis have to be correctly aligned, whilst maintaining minimal coupling losses. Additionally, 'mode-hopping' is also a problem in ring-cavity lasers. Given the typical longer length in the ring laser, many axial modes are present and closely spaced to the laser mode. Therefore, changes in path length due to temperature and pressure fluctuations can cause the mode frequencies to shift, whilst the gain maximum remains fixed, resulting in the mode ’hopping’ to one that now has a higher gain with the effect that the output frequency will change [5,6]. One solution for this is to actively control the cavity length using, for example, a piezoelectric transducer fibre stretcher, which compensates for the undesired changes in cavity length by automatically adjusting its length to maintain the desired output frequency. However, using active controls such as this increases the system complexity and cost.

Given the limitations in these approaches, it was decided that a DFB laser would be used as the single-frequency master oscillator, due to the monolithic structure of the grating making it resistant to mode hopping and that it offers wavelength tuning by stretching and compressing the grating (although in silica fibres compression is used, as the fibre can withstand much larger compressive stress than tensile [7]), which changes the grating pitch and therefore the Bragg wavelength [7]. Furthermore, DFB gratings are desirable as their construction and operation is simpler than the ring laser or external cavity laser. These benefits have been demonstrated for other rare earth doped fibres, for example in an Er/Yb DFB fibre laser Mokhtar et al. [8] achieved a tuning range of 110nm whilst maintaining single mode operation. The basic theory for DFB fibre lasers and their operation and fabrication is outlined below.

### 4.2.2 Distributed feedback laser

Modelling distributed feedback lasers has been well documented in the literature, such as by Kogelnik and Shank [9]. The analysis is based on two counter propagating waves that are coupled via Bragg scattering for a periodic variation in the material’s refractive index. Figure 4.1 shows a simplified illustration of the operation of a DFB structure with two counter propagating waves at a wavelength $\lambda$. As each wave propagates through the periodic structure, it receives light scattered via Bragg scattering from light travelling in the opposite direction. Therefore, the feedback is effectively distributed throughout the grating region. In the presence of gain, the signal intensity increases as expected, with energy coupled into the waves in both directions via the Bragg scattering.

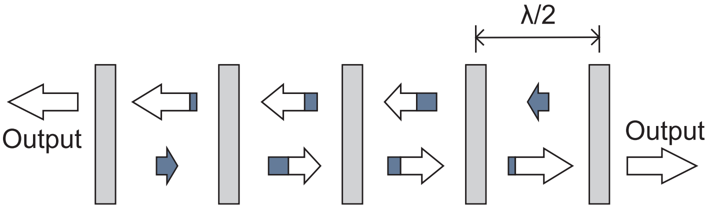

Figure 4.1: Illustration demonstrating laser oscillation in a periodic structure [9].

The coupling of light into the forward and backward directions is strongly dependent on the Bragg condition being satisfied, where the spatial period of the grating, $\Lambda$, satisfies

$$\Lambda = \frac{\lambda_B}{2n_{eff}} \tag{4.2}$$

where $\lambda_B$ is the Bragg wavelength and $n_{eff}$ is the effective refractive index. Therefore, by controlling the period of the grating, the operational wavelength can be selected. The reflectivity of a distributed feedback grating can be calculated using

$$R = \tanh(\kappa L) \tag{4.3}$$

where $L$ is the grating length, and $\kappa$ is the coupling coefficient given by

$$\kappa = \frac{\pi \Delta n}{\lambda_B} \tag{4.4}$$

where $\Delta n$ is the refractive index modulation. By inducing a permanent $\pi$ phase shift in the cavity, the feedback in the cavity in each direction can be modified, depending on the phase change position [10]. The region of the grating with the shortest length after the phase change will see more output due to the reduced effective reflectivity, given by equation (4.3). As was discussed in Chapter 3, the ratio of these reflectivities will determine the output power ratio well above threshold, such that for predominantly single ended output, one reflectivity needs to be smaller than the other. Due to the typically short cavity lengths used in DFB lasers, typically <10cm, the reflectivities need to be high so that the optimum output power is achieved for a given pump power (i.e. the threshold is low and that the slope efficiency is high).

In fibres, these periodic changes in refractive index in the core are created when photosensitive dopants, such as germanium, absorb ultra-violet light in the form of an intense optical interference pattern. The refractive index change is dependent on the intensity of the UV light, the duration of exposure and the photosensitivity of the medium. The two commonly used techniques for writing Bragg gratings into fibres are the transverse holographic technique, and the phase mask technique [11].

The Transverse Holographic Technique uses two overlapping UV light beams that interfere to produce a periodic interference pattern that is subsequently written into the core. For this technique, the fibre cladding has to be transparent to the UV light. With this technique, the grating period is determined by the angle between the two coherent UV beams and the wavelength.

Alternatively, the Phase Mask Technique uses a phase mask made from a flat slab of silica glass, which is transparent at UV. On one surface, a one dimensional periodic surface relief structure is etched using photolithographic techniques, such that the profile of the pattern approximates a square wave. The fibre is placed in close proximity to the mask and a UV beam projected onto it. The UV beam is then diffracted by the periodic corrugations of the mask to form an interference pattern inside the fibre via the ±1 diffracted orders. By careful control of the phase mask design, the zero order diffracted mode is reduced to <5% and the ±1 modes have roughly equal intensity. If the period of the phase mask grating is $\Lambda_{mask}$ then the period of the DFB grating is $\Lambda = \Lambda_{mask}/2$. For this technique, the grating period is independent of the writing wavelength, so, by careful mask design, can be written for any operational wavelength regime. This technique has the advantage over others due to it being easier to implement, with less constraints on alignment and coherence of the source, which enable cheaper excimer lasers to be used. A potential drawback to this approach is that a separate phase mask is needed for every Bragg wavelength. However, the usefulness of each phase mask can be extended by adjusting the written grating pitch (and therefore the Bragg wavelength) using different techniques during the writing process. One approach is to angle the fibre in relation to the phase mask, such that one end of the fibre is in contact with the phase mask and the other is a distance $d$ away. In this case the grating's central wavelength can be shifted by [12]

$$\lambda_B = 2n\Lambda\sqrt{1+\frac{d^2}{l^2}} \tag{4.5}$$

where $n$ is the refractive index of the fibre, $\Lambda$ is the fibre grating period and $l$ is the length of the phase mask. With this approach, Othonos and Lee [12] demonstrated 2nm of tuning for a Bragg wavelength centred at 1558nm. However, the limitation to this approach is that the written grating was blazed at a small angle (in this case $<$0.05 radians), which results in a propagation loss [13].

Alternatively, by changing the radius of curvature of the UV beam incident on the phase mask, it is possible to magnify the image written into the fibre and thus change the grating pitch and therefore the Bragg wavelength [14]. Prohaska et. al. [14] demonstrate this using a positive lens to focus the UV beam through the phase mask. By adjusting the distance between the lens and the phase mask, and the phase mask and the fibre, they tuned the Bragg wavelength by 1.7nm from the central wavelength at 1.3$\mu m$. They predict that the tuning range of the grating period using this method is limited to a few percent.

However, if greater flexibility in operational wavelength is required from a given phase mask, it is worth noting that the Bragg wavelength can be tuned by compressing the grating, for example [7,8]. Therefore, the usefulness of the phase mask can be extended just by operating the written fibre grating under compression for wavelength selection.

The simplest approach for writing the permanent phase change into the grating is to expose the phase change position for longer, such that the refractive index change will be increased [15]. Alternatively, using the moving fibre-scanning beam technique and phase masks, the phase change can be incorporated by simply moving the fibre by the appropriate distance at the desired position, while the UV beam is scanning [16].

In a typical germanium doped fibre, the refractive index change produced in the writing process is $\delta n = 10^{-5} - 10^{-3}$. This refractive index change can be further enhanced using techniques such as hydrogen loading, whereby the refractive index change can be as high as $10^{-2}$ [17]. This technique involves exposing the fibre to high pressure $H_2$ gas for a prolonged period of time, of the order of a days. The result is that the $H_2$ diffuses into the core and increases the core photosensitivity, such that when the dissolved $H_2$ is exposed to UV light, it reacts with the silica, typically at the Ge sites, causing a large permanent change in refractive index. This is significant as an increase in the refractive index difference will increase the coupling coefficient and therefore reduce the required grating length to achieve the same effective reflectivity. Therefore, as a result of the shorter cavity length, the mode spacing is increased, making single-frequency operation in the cavity easier to achieve.

## 4.3 Amplifier considerations

### 4.3.1 Small signal gain operation

In the simple case of a single-pass amplifier, where the signal passes through the inverted gain medium, the small signal gain can be predicted analytically. By assuming that the input signal is small, such that it does not significantly deplete the inversion, the total available small signal gain, $G_0$, for a single pass is given by

$$G_0 = \exp\left(\int_0^l g_0(z)dz - \alpha_L l\right) \tag{4.6}$$

where $g_0(z)$ is the small signal gain coefficient at position $z$ in the fibre, $\alpha_L$ is the background fibre attenuation coefficient at the signal wavelength and $l$ is the fibre length. The small signal gain coefficient is given by

$$g_0(z) = N_2(z)\sigma_e(\lambda_L) - N_1(z)\sigma_a(\lambda_L) \tag{4.7}$$

where $N_2$ is the upper laser level, $N_1$ is the lower laser level, and $\sigma_e(\lambda_L)$ and $\sigma_a(\lambda_L)$ are the absorption and emission cross-sections at the signal wavelength. For a three-level system, it can be assumed that the pump excitation rapidly decays to the upper signal level, such that $N_1 = N_2 - N$ for a total ion density $N$. In this case, the small signal gain is

$$g_0(z) = N_2(z)(\sigma_e(\lambda_L) + \sigma_a(\lambda_L)) - \sigma_a(\lambda_L)N \tag{4.8}$$

Assuming that there is no ASE or signal, the rate at which the pump power is depleted as a function of $z$ due to the spontaneous emission power is given by [18]

$$\frac{dP_P(z)}{dz} = -\frac{A_{core}h\nu_p N_2(z)}{\eta_q \tau_f} \tag{4.9}$$

where $A_{core}$ is the core area, $\nu_p$ the pump frequency, $\tau_f$ is the fluorescence lifetime of the upper laser level, $\eta_q$ is the pump quantum efficiency (defined as the fraction of absorbed pump photons that result in excited ions in the upper laser level). Substituting equations (4.9) and (4.8) into equation (4.6), and integrating gives a total small signal gain of

$$G_0 = \exp\left(\frac{(\sigma_e(\lambda_L) + \sigma_a(\lambda_L))\eta_q \tau_f P_{abs}}{A_{core}h\nu_p} - \sigma_a(\lambda_L)Nl - \alpha_L l\right) \tag{4.10}$$

for $P_{abs} = P_P(0) - P_P(l) = P_P(0)\eta_{abs}$ where for negligible ground state depletion $\eta_{abs} = 1 - \exp(-\sigma(\lambda_P)Nl))$.

### 4.3.2 Saturated gain operation

In the small signal gain regime, the signal power grows exponentially as it propagates through the medium, if the inversion is uniform. However, for large signals, more of the ions are depleted and therefore the gain is reduced, so that the amplifier is said to be saturated. In the highly saturated regime and for a uniform inversion along the medium, the signal power will grow linearly as it propagates as all the inversion is stimulated. In practice it is never possible to completely saturate the amplifier, such that the total gain is unity, as this would require an infinite signal power. The basic differential equation governing the growth rate of a signal with power $P(z)$ along a lossless amplifier is given by [19]

$$\frac{1}{P(z)}\frac{dP}{dz} = \frac{g_0}{1 + \frac{P(z)}{P_{sat}}} \tag{4.11}$$

where $P_{sat}$ is the saturation power defined as the signal power which reduces the gain to half the small-signal value. This saturation power is given by

$$P_{sat} = \frac{h\nu_L A_{core}}{(\sigma_a(\lambda_L) + \sigma_e(\lambda_L))\tau_f} \tag{4.12}$$

Since the gain coefficient varies with signal power and distance along the amplifier, it is not possible to simply relate the gain, $G$, to the total small signal gain and the input signal power $P_{in}$. Instead equation (4.11) can be rearranged and integrated over the length of the fibre and the input and output powers

$$\int_{P_{in}}^{P_{out}} \frac{1}{P(z)} + \frac{1}{P_{sat}} dP = \int_0^l g_0(z)dz \tag{4.13}$$

which can be solved to give

$$\ln\left(\frac{P_{out}}{P_{in}}\right)+\frac{P_{out}-P_{in}}{P_{sat}}=\ln G_0 \tag{4.14}$$

By definition the total gain is given by $G = P_{out}/P_{in}$, so equation (4.14) can be rearranged into the more useful

$$\frac{P_{in}}{P_{sat}}=\frac{1}{G-1}\ln\left(\frac{G_0}{G}\right) \tag{4.15}$$

Given that the maximum available gain is $G_0$, the amplifier gain can be expressed as a function of the input signal power for $1 < G < G_0$.

It is normally desirable to operate an amplifier in the saturated regime so that maximum power is extracted from the amplifier. This implies that higher input signal powers will be required. The power extracted from an amplifier is given by

$$P_{ext}=P_{out}-P_{in}=P_{sat}\ln\left(\frac{G_0}{G}\right) \tag{4.16}$$

In the highly saturated regime, the gain approaches unity, which allows the maximum available gain to be calculated from equation (4.16) as being

$$P_{avail}=\lim_{G\to 1}P_{sat}\ln\left(\frac{G_0}{G}\right)=P_{sat}\ln(G_0) \tag{4.17}$$

From equations (4.16) and (4.17), the extraction efficiency of the amplifier can be calculated as

$$\eta_{ext}=\frac{P_{ext}}{P_{avail}}=1-\frac{\ln G}{\ln G_0} \tag{4.18}$$

Using equations (4.15) and (4.18), the total gain and extraction efficiency can be predicted as a function of the incident signal power for the amplifier stages discussed below. This is shown in Figure 4.2, where they are calculated using the values $\sigma_e(\lambda = 1943nm) = 4.5 \times 10^{-25}m^2$ and $\sigma_a(\lambda = 1943nm) = 6.33 \times 10^{-27}m^2$ [20], and $\tau_f = 360\mu s$ [21]. The following fibre dependent values used are based on the actual fibres used in the experiments. For the preamplifier and intermediate amplifier a 60cm long fibre with a 10$\mu m$ diameter core was used, where $\eta_q = 1$, $\sigma_a(\lambda = 1565nm) = 2.2 \times 10^{-25} m^2$ [22] and $N \approx 1.05 \times 10^{26} m^3$. Likewise, for the power amplifier stage, a 4m long fibre with a 25$\mu m$ diameter core was used, where $\sigma_a(\lambda = 790nm) = 8.2 \times 10^{-25} m^2$ [22], $N \approx 3.2 \times 10^{26} m^3$ and $\eta_q = 1.51$ (calculated from the laser slope efficiency in Chapter 5 using the same 25$\mu m$ fibre). The figure shows that for input signal powers greater than 1mW, the extraction efficiency in both amplifier stages will be >96%.

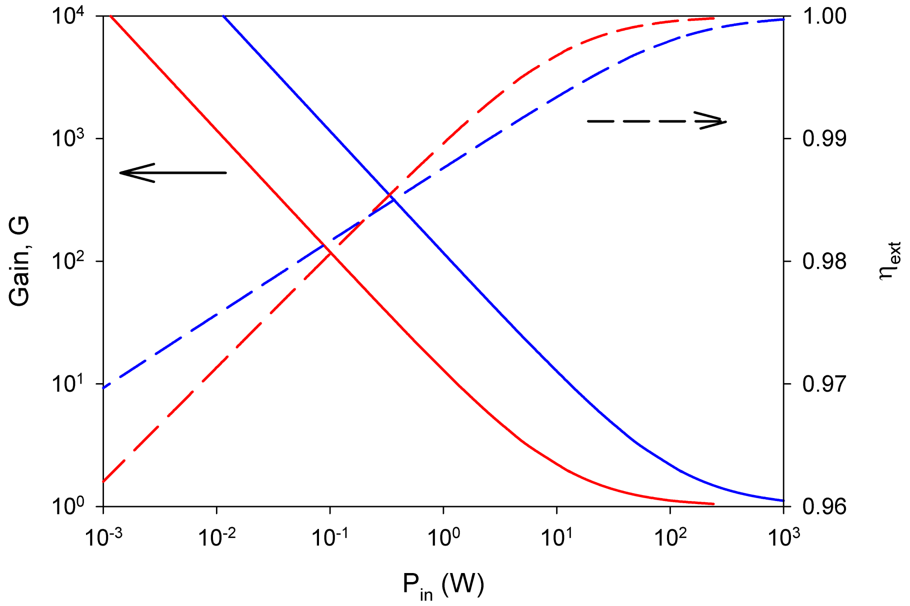

Figure 4.2: Showing the dependence of the Total Gain (solid lines) and the extraction efficiency of the amplifier (dashed lines) as a function of incident signal power. Shown are a 10$\mu m$ diameter Tm-doped fibre with 15W of absorbed pump power (red), and a 25$\mu m$ diameter Tm-doped fibre with 190W absorbed pump power (blue).

### 4.3.3 Nonlinear effects

The onset of nonlinear effects can significantly limit the output power that can be extracted from an amplifier. The impact of nonlinear effects was discussed in Chapter 2, where it was noted that Stimulated Raman Scattering (SRS) and

Stimulated Brillouin Scattering (SBS) can in certain regimes be two of the main limits of power scaling for fibre amplifiers. However, using equations (2.49) and (2.51), it can be seen that SBS will limit the performance before SRS when the lorentzian signal linewidth, $\Delta\nu_p$, is

$$\Delta\nu_p < \Delta\nu_B \left( \frac{g_B}{g_R} - 1 \right) \tag{4.19}$$

where $g_B$ is the Brillouin gain coefficient equal to $g_B \sim 5 \times 10^{-11} m/W$ in silica [23], $g_R$ is the Raman gain coefficient, which has a maximum value in silica of $g_R \sim 1.5 \times 10^{-13} m/W$ [24, 25], and $\Delta\nu_B$ is the Lorentzian linewidth of the SBS gain which is ~9.8MHz at 1943nm (calculated using the fact that the pump wavelength dependence on $\Delta\nu_B$ is $\Delta\nu_B \propto 1/\lambda^2$ [26] and that in bulk silica $\Delta\nu_B$ ~33MHz at 1.06$\mu m$ [26]). Therefore, for signal linewidths less than 3.2GHz at 1943nm, the SBS threshold will be reached first, where for $\Delta\nu_p << \Delta\nu_B$ this signal power threshold is given by [27]

$$P_{thres}^{SBS} = \frac{21 A_{eff} K}{g_B l_{eff}} \tag{4.20}$$

where $A_{eff}$ is the effective core area, $l_{eff}$ is the effective fibre length, and $K$ is a factor that accounts for the polarisation of the pump. For polarised light $K = 1$ and for unpolarised light $K = 2$. The effective fibre length is defined as $l_{eff} = \frac{1}{\alpha_P}(1 - \exp(-\alpha_P l))$, where $l$ is the fibre length and $\alpha_P$ the loss coefficient for the pump signal. This equation gives the maximum theoretical signal power in the fibre before the onset of SBS. Therefore, the impact of SBS on the amplifier system can be controlled by designing the fibres such that the signal power does not exceed the SBS threshold. The SBS threshold signal power has been calculated for the fibres used in this MOPA system. For the pre-amplifier and intermediate amplifier stages, a 60cm long fibre with an $A_{eff} = 7.85 \times 10^{-11} m^2$ was used, and the final power amplifier stage used a 4m long fibre with an $A_{eff} = 4.9 \times 10^{-10} m^2$. Both fibres are discussed in more detail later. Using these values gives a $P_{thres}^{SBS}$=55W for the pre-amplifier and intermediate amplifier stages, and a $P_{thres}^{SBS}$=52W for the power amplifier stage. Given that the pre-amplifier and intermediate amplifier stages are limited to 10W and 20W of pump power at 1565nm respectively (experimental setup discussed below in more detail), it is not possible for the SBS threshold to be reached. In the power amplifier stage, the launched diode pump power available is 380W, which implies a potential signal power of 150W, which is well above the SBS threshold, suggesting that SBS will become a problem at high pump powers. However, as was noted in Chapter 2, the SBS threshold power is only a lower estimate of the signal power, and in practice the actual threshold will be much higher due to temperature variations along the fibre causing the refractive index to vary non-uniformly due to the thermo-optic effect. This temperature variation is predominately caused by the decrease in absorbed pump power along the fibre, which results in differing levels of heat generation as a function of propagation distance along the fibre.

## 4.4 Set-up

The MOPA discussed in this chapter consisted of four stages: a low power thulium doped DFB fibre laser as the master-oscillator; a simple pre-amplifier spliced to the DFB laser and pumped by the residual pump power from the DFB laser; an intermediate amplifier stage; and, a final power amplifier stage, as seen in Figure 4.3. For the DFB laser, the key factor for efficient performance was to obtain a high absorption efficiency in the fibre, as the laser cavity length formed by the DFB grating is very short, typically only a few centimetres, and therefore the available gain for oscillation can be severely limited. To achieve the required levels of absorption, the DFB fibre laser must have a high Tm doping concentration and be operated in a core-pumped configuration. The common approach of pumping Tm-doped fibres using high power diode emitters operating around 790nm cannot be applied to core pumping because of the low brightness output obtained from the diodes. Therefore, the pump source of choice was a commercially available (SPI lasers) Er, Yb fibre lasers operating at 1565nm, which have very good output beam quality and therefore enabled a high coupling efficiency into the core of a single-mode fibre. Single-mode fibre was chosen for single spatial mode operation and therefore allows single-frequency operation, as well as that the output beam quality of the DFB laser would be near-diffraction limited. For the power amplifier stage however, no such constraints are required, allowing a more conventional cladding pumped scheme using diode emitters operating at 795nm to be employed. The motivation for this is the two-for-one cross-relaxation process that occurs in Tm-silica as discussed in Chapter 2. A further motivation is that high power diode sources are commercially available with output powers in excess of several hundreds of Watts.

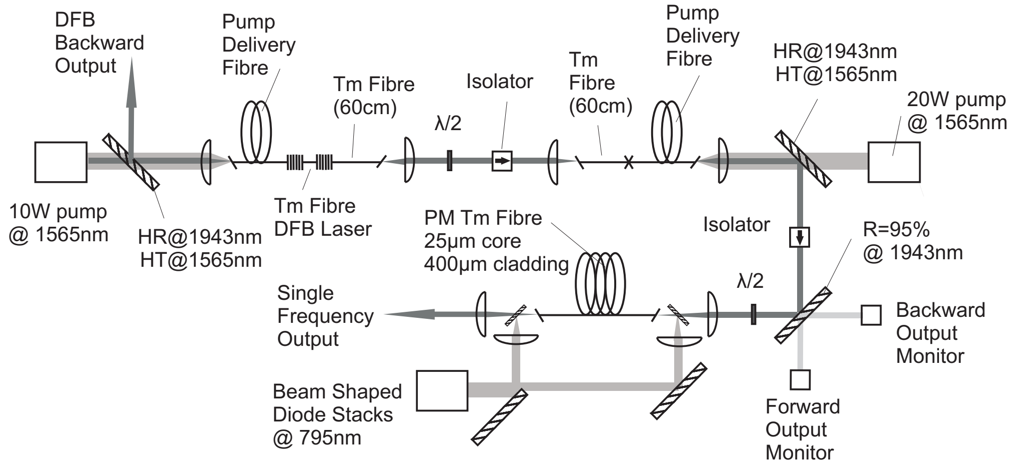

Figure 4.3: Schematic of the single frequency MOPA configuration.

The Tm-doped fibre used for the DFB master oscillator was fabricated in-house via modified chemical vapor deposition (MCVD) and solution doping. The resulting fibre had a thulium, germanium co-doped alumino-silicate core with a diameter of $\sim 10\mu m$ and a numerical aperture (NA) of 0.17, surrounded by a pure silica circular cladding with a diameter of $125\mu m$. The small signal absorption coefficient in the core was measured to be ∼100dB/m at 1565nm. To facilitate writing a high reflectivity grating, the core photosensitivity was enhanced by hydrogen-loading. The grating was written using the phase mask technique. An 8cm long grating was fabricated with a $\pi$-phase shift 6mm from the grating's mid-point in order to produce a predominantly single ended output when operated as a DFB oscillator. The grating pitch was selected for laser operation at 1943nm and had a grating coupling coefficient $\kappa$ of $\sim$100m$^{-1}$. This output wavelength was selected as it was required for an EU funded project for which the single frequency source was being developed.

The pump power for the DFB laser was provided by a 10W Er,Yb doped fibre laser, which had an operating wavelength selected to be 1565nm, with a <2nm linewidth (FWHM), to allow for efficient in-band pumping of the $^3H_6$-$^3F_4$ transition in thulium-doped silica glass. The output beam propagation factor of the pump sources was measured to be $M^2$ <1.1. The excellent beam quality allowed the pump to be coupled into a standard telecom fibre (core diameter 9$\mu m$ and NA of 0.14) which was spliced directly to the DFB laser, with a launch efficiency of 80%.

The forward output end of the DFB laser was spliced to a 60cm long piece of the Tm-doped fibre (10$\mu m$ core), which was pumped by the residual (unabsorbed) pump from the DFB, and used to amplify the forward output. Both the input facet of the pump delivery fibre and output facet from the pre-amplifier were angle-polished to $\sim$10° to reduce broadband feedback and thus suppress parasitic oscillation. The backward propagating output from the DFB laser was extracted from the pump beam with a dichroic mirror (DM) with a high transmission at 1565nm and a high reflectivity at 1943nm. This backward output was used to monitor the performance of the DFB laser during the experiments.

The amplified output from the pre-amplifier was collimated and passed through a half-wave plate and isolator with a measured isolation of 16.9dB at 1943nm. The signal was then launched into the intermediate amplifier stage consisting of a 60cm long piece of the Tm-doped fibre, the same as used for the DFB laser, which was spliced to a short length of pump delivery fibre. A 20W Er, Yb fibre laser pump source, with the same output properties as discussed previously, was coupled into the delivery fibre with a launch efficiency of 80%. Both end facets of the fibre were again angle polished to $\sim$10° to suppress lasing of the amplifier.

The collimated output signal passed through a pair of beam steering mirrors, an isolator and a half-wave plate. The latter was used to align the polarization of the signal parallel to the slow axis of the PM Tm-doped fibre. One of the beam steering mirrors had a transmission of 5%, which allowed us to monitor not only the seed signal but also any backward propagating output due to parasitic lasing or SBS. The signal was coupled into the power amplifier stage via a DM, with a high transmission at 1943nm (T>97%) and a high reflectivity at the pump wavelength of 795nm (R>98%) at 45°. Both end sections of the fibre were mounted in water-cooled V-groove heat sinks to prevent possible thermal damage to the fibre coating due to a small fraction of un-launched pump power. Also, the fibre was air-cooled by the fans to avoid thermal damage due to quantum defect heating in the fibre. Both end facets were angle polished to ∼10° to suppress lasing due to broadband feedback from the facets. The output from the amplifier was extracted through the DM on the output side and collimated for analysis.

The pump source for the power amplifier stage was provided by two 6-bar diode stacks. The output beam propagation factor from the stacks was too large for them to be efficiently launched into the power amplifier fibre. Therefore, the diode output was beam shaped and the beam propagation factor reduced, as shown in Figure 4.4. The beam propagation factor was initially reduced using the aperture filling technique, whereby the output was collimated in the fast and slow axis using micro-lens arrays to remove some of the 'dead space' between the emitters. The collimated beams from each stack were then spatially combined using slotted mirrors to further reduce the 'dead space'. The combined beam had an output beam propagation factor of $M^2_{slow}$ ∼600 and $M^2_{fast}$ ∼50 and a maximum power of 500W. By exploiting the highly polarised output from the diode stacks (polarisation extinction ratio >98%), the beam propagation factor was further reduced in the slow axis by polarisation re-combining the diode output. The resulting beam had a beam propagation factor of $M^2_{slow}$ ∼280 and had a slight degradation in the fast axis beam propagation factor. The beam propagation factor was then further reduced by cutting the beam in half at the beam waist to produce two beams for pumping each end of the power amplifier fibre, each with beam propagation factors of

$M^2_{slow}$ ~175 and $M^2_{fast}$ ~65, and a combined maximum power of 475W. The measured launch efficiency for the 400$\mu m$ diameter inner-cladding fibre was ~80% for both end facets.

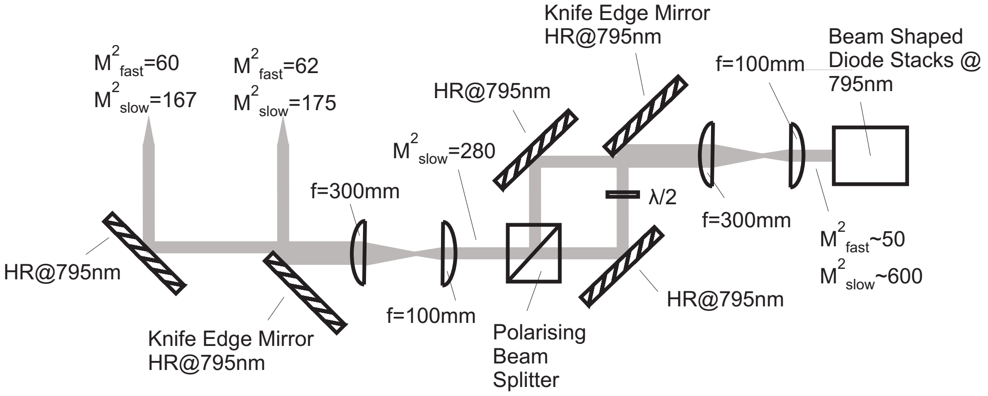

Figure 4.4: Schematic of the beam shaping used on the diode laser output.

The fibre used for the power amplifier stage was a commercially available (PLMA-TDF-25F/400) thulium-doped polarization-maintaining (PM) fibre in a Panda configuration, with a core diameter of 25$\mu m$ and NA of 0.1, and an inner-cladding diameter of 400$\mu m$. The small signal absorption at 795nm, in a cladding pumped configuration, was measured via the cut-back technique to be ~4.5dB/m, so an ~4m long piece of the PM Tm-doped fibre was used in the power amplifier. Both ends of the fibre were mounted in water-cooled V-groove heat sinks to aid heat extraction. Furthermore, the remaining unmounted central portion of the fibre was fan-cooled to aid to heat removal in the fibre.

## 4.5 Results and analysis

### 4.5.1 Master oscillator and preamplifier

The DFB laser used as a master oscillator in this MOPA had a forward output power of 875mW and a backward output power of 70mW at 1943nm, for a launched pump power of 8.1W, corresponding to 3.1W of absorbed power. The residual pump power was transmitted into a 60cm pre-amplifier, which yielded an output power of 3.15W, with a beam propagation factor of $M^2$ <1.06. Figure 4.5 shows the output power as a function of the absorbed/launched pump power, for both the DFB laser and pre-amplifier. The output from the DFB master oscillator consisted of two frequencies operating on orthogonal polarizations [2]. One polarization state was selected using the half-wave plate and a polarizer. Single frequency operation from the output was confirmed by a Scanning Fabry Perot Interferometer (SFPI), with a Free-Spectral-Range (FSR) of 6GHz and a Finesse of 100 [2].

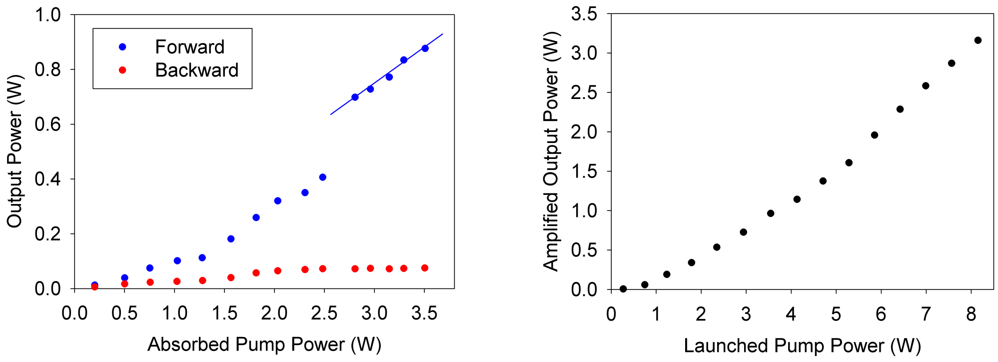

(a) DFB laser oscillator

(b) Pre-Amplifier

Figure 4.5: Showing (a) the output performance for the DFB laser in the forward (blue) and backward (red) directions, and (b) the amplified output power from the pre-amplifier fibre [2].

### 4.5.2 Intermediate amplifier

The signal from the pre-amplifier was launched into the intermediate amplifier stage via an isolator, with a launched efficiency of 75% corresponding to ~1W of launched signal power. The launched power was much lower than would be expected due to the removal of the orthogonal polarization state and losses in the isolator optics, with a total loss measured to be 55%. The maximum output power obtained was 10W for a launched pump power of 15W, corresponding to a slope efficiency of ~63% (see Figure 4.6) [2].

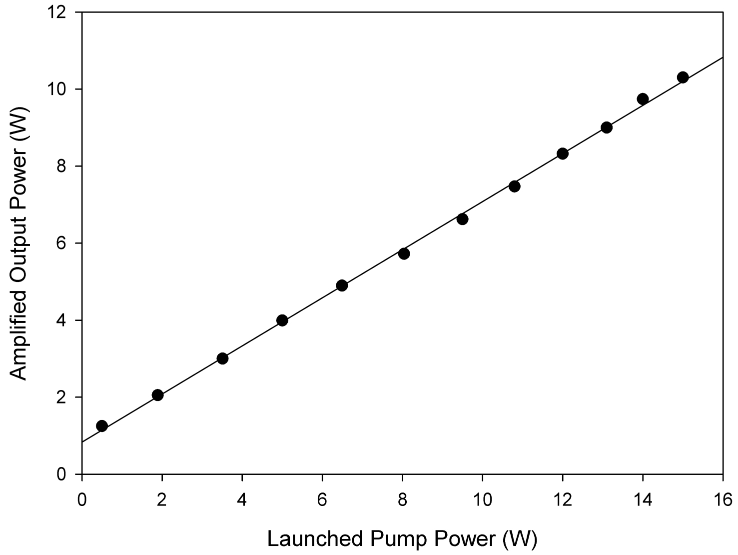

Figure 4.6: Amplified output power as a function of launched pump power for the intermediate amplifier, for a seed power of ∼1W.

### 4.5.3 Power amplifier

For seeding the power amplifier stage, the output of the intermediate amplifier output was passed through another isolator. The isolator had a transmission loss of ∼15% due to absorption in the isolator optics. As a result, the output power from the intermediate amplifier stage was limited to <5W for a beam size of 2mm diameter to avoid beam quality degradation due to thermal lensing. Furthermore, to avoid damaging the isolator, the signal power had to be less than the CW damage threshold of 200W/cm$^2$. The launch efficiency into the power amplifier was measured to be 75%, which when combined with the isolator losses, resulted in a total launched signal power of ∼3W. The transmitted signal beam propagation factor was measured to be $M^2$ <1.07, so was not degraded by thermal aberrations.

Under these conditions, 100W of single frequency output was obtained for a total launched pump power of 190W, which corresponds to a slope efficiency of 59% (see Figure 4.7). Over this power range, there was negligible power (<20mW for 190W of pump power) in the backward propagating beam, confirming that there was no parasitic lasing or SBS present. Using the measured slope efficiency and equation (4.14), the pumping quantum efficiency for the fibre was calculated to be $\eta_q$=1.46. This was in good agreement with the value calculated for the same fibre when operated as an oscillator in Chapter 5 as $\eta_q$=1.51. Therefore, this suggests that the amplifier stage was operating near its maximum efficiency. At the maximum output power, the beam propagation factor was measured to be $M^2$=1.25 and the polarisation extinction ratio was >94%. Single frequency operation was confirmed at full power using the SFPI (see the inset in Figure 4.7).

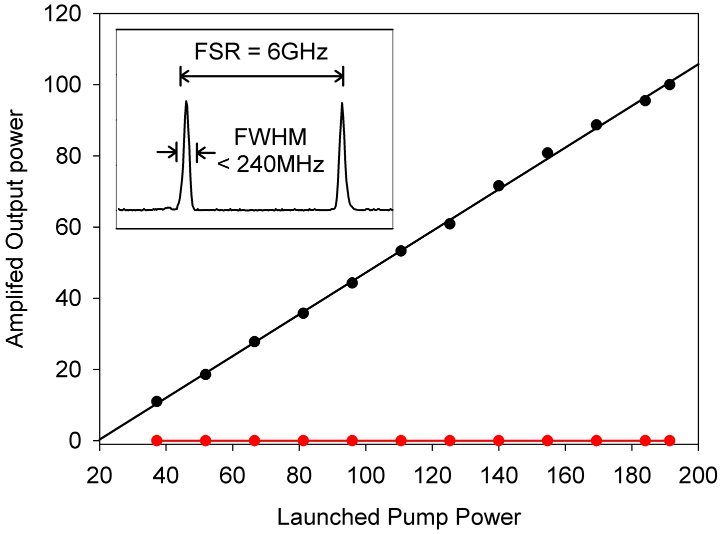

Figure 4.7: Amplified output power as a function of launched pump power for a seed power of ~3W. Shown is the forward direction (black) and the backward direction (red). Inset: Oscilloscope trace for Scanning Fabry-Perot Interferometer.

The main factor limiting the output power was thermally-induced degradation to the fibre's outer polymer coating, resulting in damage to the fibre itself. The impact of coating damage for limiting power scaling in fibre sources was highlighted in Chapter 2. There, the power dissipated as heat per unit length required to reach the coating's damage limit, $P_{h\ max}$, was given by

$$P_{h\ max} = 4\pi(T_d - T_s)\left[\frac{2}{k_2}\ln\left(\frac{r_2}{r_1}\right) + \frac{2}{r_2 H_2}\right]^{-1} \tag{4.21}$$

where $T_s$ is the ambient temperature of the surroundings, $T_d$ is the temperature required to damage the polymer coating of ∼150°C, $r_1$ is the inner-cladding radius, $r_2$ is the outer-polymer coating radius, $k_2$ is the thermal conductivity of the outer polymer coating of 0.1W/mK, and $H_2$ is the heat transfer coefficient for the outer polymer coating. Considering the slope efficiency of 59% and that therefore the pump power converted to heat is approximately 40%, means that the upper-limit at which the damage threshold is reached occurs for a thermal load of ∼80W. Using this power, the heat transfer coefficient for the fibre is estimated to be ∼110Wm$^{-2}$K$^{-1}$. There are several options for increasing the heat deposition density required to damage the polymer coating. One approach would be to use a fibre with a lower doping concentration, requiring a longer device length for the same absorption, as this would mean that the heat deposition density would be decreased. However, the main attraction for pumping at 795nm is the beneficial two-for-one cross relaxation process that results in two excited ions in the upper laser level for one absorbed pump photon. This two-for-one process is dependent on the doping concentration, such that high output efficiencies are achieved for high doping concentrations, as was discussed in Chapter 2. Therefore, there is a limit to how much the doping concentration can be reduced if high efficiency amplification is to be achieved.

Another approach is to increase the heat transfer coefficient by employing better thermal management. This could be achieved by water cooling the entire fibre, instead of only just the first 20cm at each end of the fibre, with fans cooling the rest of the fibre. Additionally, the heat transfer coefficient for our setup would be improved if the mount had better thermal contact with the fibre, i.e. by changing the shape of the fibre groove or using a thermal conduction paste between the fibre and mount (although with this there is the concern of keeping the end facet clean).

Similarly, decreasing the coating thickness also increases the heat deposition density required to damage the polymer coating, as can be seen in Figure 4.8. The graph shows that for heat transfer coefficients greater than ∼600Wm$^{-2}$K$^{-1}$, decreasing the coating thickness significantly increases the heat deposition density required to damage the coating. For example, reducing the coating thickness from 100$\mu m$ to 50$\mu m$ will increase the required heat deposition density from 130Wm$^{-1}$ to 210Wm$^{-1}$ when the heat transfer coefficient is 10000Wm$^{-2}$K$^{-1}$. Reducing the coating thickness beyond 50$\mu m$ will result in an even larger required heat deposition density. However, there is a limit to how thin the coating can be before pump loss becomes a significant problem due to evanescent wave coupling. The coating thickness can be easily selected during the pulling process, making the modification to the fibre potential straight forward.

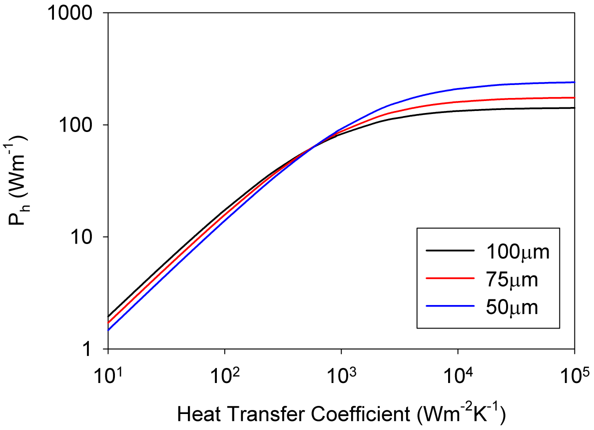

Figure 4.8: The maximum heat deposition required to reach the damage limit of the polymer outer coating as a function of the heat transfer coefficient for a 25$\mu m$ diameter core fibre and an inner cladding diameter of 200$\mu m$, and a polymer outer coating thickness of 100$\mu m$, 75$\mu m$ and 50$\mu m$. Calculated using the damage limit of coating as $T_d \approx 450°K$, the surrounding temperature $T_s = 293°K$, and the thermal conductivity of the polymer coating outer is ∼0.1W/mK.

In addition to the approaches above, changing the outer polymer material to one with a higher damage threshold and/or with a higher thermal conductivity will increase the heat deposition density required to damage the coating. Figure 4.9 shows the heat deposition required to damage the polymer outer coating as a function of its thermal conductivity for the fibre used in power amplifier stage. It can be seen that increasing the coating thermal conductivity for heat transfer coefficients above ~500Wm$^{-2}$K$^{-1}$ increases the heat deposition density required for coating damage significantly as would be expected. Significantly, Figures 4.8 and 4.9 both show that to increase the heat deposition density required for coating damage, the heat transfer coefficient must be first improved before the enhancements due to the coating thickness and thermal conductivity begin to have a significant impact. This suggests that output power in the current setup can be increased simply by better thermal management of the fibre through more effective cooling, and that beyond this to further scale the power requires a new fibre with modifications to the fibre coating thickness and material.

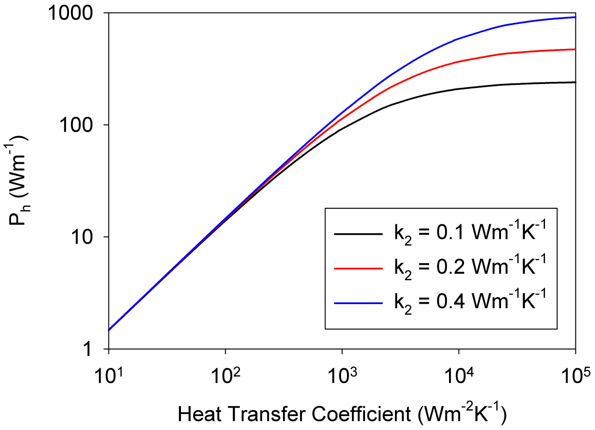

Figure 4.9: The maximum heat deposition required to reach the damage limit of the polymer outer coating as a function of the heat transfer coefficient for a 25$\mu m$ diameter core fibre and an inner cladding diameter of 200$\mu m$, and a polymer outer coating thickness of 50$\mu m$ for a thermal conductivity of the polymer outer coating of 0.1W/mK, 0.2W/mK and 0.4W/mK. Calculated using the damage limit of coating as $T_d \approx 450°K$, the surrounding temperature as $T_s = 293°K$.

## 4.6 Conclusions

In this chapter, power scaling a single frequency laser using a master oscillator power amplifier was demonstrated. The advantage of this approach is that it is not possible to have a high power single frequency laser based on a single stage oscillator. The MOPA configuration allowed a lower power DFB single frequency laser with an excellent beam propagation factor to be power scaled to 100W of output, whilst only slightly increasing the beam propagation factor from $M^2$ <1.06 to $M^2$=1.25, with an output polarisation extinction ratio of >94%.

The output power in the final amplifier stage was limited by thermal degradation of the outer polymer coating of the fibre. This can be improved by employing a better thermal management of the fibre by, for example, water cooling the entire fibre, not just the first portion at each end of the fibre. This improvement is shown above in Figures 4.8 and 4.9, where the heat deposition density required to damage the polymer outer coating is plotted as a function of the heat transfer coefficient for various fibre coating thicknesses and coating thermal conductivities. They showed for the fibre used in the power amplifier stage that doubling the present heat extraction coefficient, calculated to be $\sim$110Wm$^{-2}$K$^{-1}$, would double the tolerable heat deposition density. The coating damage limit can be further increased once the heat extraction coefficient is >600Wm$^{-2}$K$^{-1}$, by changing the coating material to one with a higher thermal conductivity and by reducing the coating thickness. Below this heat transfer coefficient, the gain from these changes is minimal compared to improving the heat transfer coefficient itself. Obviously another way to improve the damage limit is to change the coating to one with a higher damage threshold.

On a more general point, to improve the power scaling for any high power amplifier operating in the 2$\mu m$ region requires increased commercial availability of high power handling optical isolators for this region. At present, those available are limited to damage thresholds of $\sim$200W/cm$^2$. This ultimately limits the maximum seed power available for the last power amplifier stage and thus the maximum extraction efficiency. Furthermore, most amplifier applications require an isolated output to prevent damage to the amplifier via feedback. Therefore, the limited damage thresholds of currently available $2\mu m$ isolators further limit the output power from $2\mu m$ amplifiers, unless feedback to the amplifier is controlled so that an isolator is not required.

## 4.7 References

[1] **Geng, J., Wu, J., Jiang, S.** and **Yu, J.**, *Efficient operation of diode-pumped single-frequency thulium-doped fiber lasers near 2µm*, Optics Letters, Vol. 32, No. 4, pp. 355–357, February 2007.

[2] **Zhang, Z., Shen, D. Y., Boyland, A. J., Sahu, J. K., Clarkson, W. A.** and **Ibsen, M.**, *High-power Tm-doped fiber distributed-feedback laser at 1943nm*, Optics Letters, Vol. 33, No. 18, pp. 2059–, September 2008.

[3] **N.Y. Voo, J. S.** and **Ibsen, M.**, *345mW 1836nm single frequency DFB fiber laser MOPA*, IEEE Photonics Technology Letters, Vol. 17, No. 12, pp. 2550–2552, Decemeber 2005.

[4] **Shen, D. Y., Clarkson, W. A., Cooper, L. J.** and **Williams, R. B.**, *Efficient single-axial-mode operation of a Ho:YAG ring laser pumped by a Tm-doped silica fiber laser*, Optics Letters, Vol. 29, No. 20, pp. 2396–2398, 2004.

[5] **Cowle, G. J., Payne, D. N.** and **Ried, D.**, *Single-frequency travelling-wave Erbium-doped fibre loop laser*, Electronics Letters, Vol. 27, No. 3, pp. 229–230, January 1991.

[6] **Park, N., J. W. Dawson, K. J. V.** and **Miller, C.**, *All fiber, low threshold, widely tunable single-frequency, erbium-doped fiber ring laser with a tandum fiber Fabry-Perot filter*, Applied Physics Letters, Vol. 19, No. 4, pp. 2369–2379, November 1991.

[7] **Ball, G. A.** and **Morey, W. W.**, *Compression-tuned single-frequency Bragg grating fiber laser*, Optics Letters, Vol. 19, No. 23, pp. 1979–1981, December 1994.

[8] **Mokhtar, M. R., Goh, C. S., Butler, S. A., Set, S. Y., Kikuchi, K., Richardson, D. J.** and **Ibsen, M.**, *Fibre Bragg grating compression-tuned over 110nm*, Electronics Letters, Vol. 39, No. 6, pp. 509–511, March 2003.

[9] **Kogelnik, H.** and **Shank, C. V.**, *Coupled-wave theory of distributed feedback lasers*, Journal of Applied Physics, Vol. 43, No. 5, pp. 2327–2335, September 1972.

[10] **Ibsen, M., Ronnekleiv, E., Cowle, G. J., Berendt, M. O., Hadeler, O., Zervas, M. N.** and **Laming, R. I.**, *Robust high power (>20mW) all-fibre DFB lasers with unidirectional and truly single polarisation outputs*, Proceedings of the Conference on Lasers and Electro-Optics Europe, p. CWE4, 1999.

[11] **Hill, K. O.** and **Meltz, G.**, *Fiber Bragg grating technology fundamentals and overview*, Journal of Lightwave Technology, Vol. 15, No. 8, pp. 1263–1276, August 1997, (Invited Paper).

[12] **Othonos, A.** and **Lee, X.**, *Novel and improved methods of writing Bragg Gratings with phase masks*, IEEE Photonics Technology Letters, Vol. 7, No. 10, pp. 1183–1185, October 1995.

[13] **Othonos, A.**, *Fiber Bragg gratings*, Review of Scientific Instruments, Vol. 68, No. 12, pp. 4309–4341, December 1997.

[14] **Prohaska, J. D., Snitzer, E., Rishton, S.** and **Boegli, V.**, *Magnification of mask fabricated fibre Bragg gratings*, Electronics Letters, Vol. 29, No. 18, pp. 1614–1615, September 1993.

[15] **Sejka, M., Varming, P., H$\ddot{u}$bner, J.** and **Kristensen, M.**, *Distributed feedback Er$^{3+}$-doped fibre laser*, Electronics Letters, Vol. 31, No. 17, pp. 1445–1446, August 1995.

[16] **Loh, W. H.** and **Laming, R. I.**, *1.55µmphase-shifted disributed feedback fibre laser*, Electronics Letters, Vol. 31, No. 17, pp. 1440–1441, August 1995.

[17] **Lemaire, P. J., Atkins, R. M., Mizrahi, V.** and **Reed, W. A.**, *High Pressure $H_2$ loading technique for achieving ultrahigh UV photosensitivity and thermal sensitivity in $GeO_2$ doped optical fibers*, Electronics Letters, Vol. 29, No. 13, pp. 1191–1193, June 1993.

[18] **Pask, H. M., Carman, R. J., Hanna, D. C., Tropper, A. C., Mackechnie, C. J., Barber, P. R.** and **Dawes, J. M.**, *Ytterbium-doped silica fiber lasers: Versatile sources for the 1-1.2µmregion*, IEEE Journal of Selected Topics in Quantum Electronics, Vol. 1, No. 1, pp. 453–464, April 1995.

[19] **Koechner, W.**, Solid-State Laser Engineering, Springer, New York, 6th edn., 2006.

[20] **Engelbrecht, M., Haxsen, F., Wandt, D.** and **Kracht, D.**, *Wavelength resolved intracavity measurement of the cross sections of a Tm-doped fiber*, Optics Express, Vol. 16, No. 3, pp. 1610–1615, February 2008.

[21] **Agger, S., Povlsen, J. H.** and **Varming, P.**, *Single-frequency thulium-doped distributed-feedback fiber laser*, Optics Letters, Vol. 29, No. 13, pp. 1503–1505, July 2004.

[22] **Jackson, S. D.** and **King, T. A.**, *Theoretical modeling of tm-doped silica fiber lasers*, Journal of Lightwave Technology, Vol. 17, No. 5, pp. 948–956, May 1999.

[23] **Aoki, Y., Tajima, K.** and **Mito, I.**, *Input power limits of single-mode optical fibers due to Stimulated Brillouin Scattering in optical communication systems*, Journal of Lightwave Technology, Vol. 6, No. 5, pp. 710–719, May 1988.

[24] **Hellwarth, R., Cherlow, J.** and **Yang, T.-T.**, *Origin and frequency dependence of nonlinear optical susceptibilities of glasses*, Physical Review B, Vol. 11, No. 2, pp. 964–967, January 1975.

[25] **Stolen, R. H.** and **Ippen, E. P.**, *Raman gain in glass optical waveguides*, Applied Physics Letters, Vol. 22, No. 6, pp. 276–278, March 1973.

[26] **Yu, D., Lu, W.** and **Harrison, R. G.**, *Physical origin of dynamical Stimulated Brillouin Scattering in optical fibers with feedback*, Physical Review A, Vol. 51, No. 1, pp. 669–672, January 1995.

[27] **Denariez, M.** and **Bret, G.**, *Investigation of Rayleigh wings and Brillouin-Stimulated Scattering in liquids*, Physical Review, Vol. 171, No. 1, pp. 160–167, July 1968.

# Chapter 5

# Cryogenically cooled hybrid laser system

## 5.1 Introduction

One of the limits for power scaling of solid state laser systems is determined by the onset of thermal effects, such as thermal lensing and thermally induced birefringence, that can lead to beam quality degradation, depolarisation losses (in the case of cavities with polarising elements, although this is not a problem for birefringent materials), and eventual crystal damage. These effects were discussed in Chapter 2. There, it is shown that the strength of these thermal effects is dependent on the thermal load inside the material, and the material's thermo-optic properties, i.e. $dn/dT$, thermal conductivity and the thermal expansion coefficient. Therefore, any enhancement of these parameters to reduce the thermal effects will positively impact further power scaling in the solid state laser system.

It has been shown that the thermo-optic properties of a material are temperature dependent, for example [1–4]. Therefore, the approach discussed in this chapter is based on operating solid-state lasers at cryogenic temperatures to favourably scale the thermo-optic properties of the material and to thus reduce the impact of thermal effects. However, the scaling of the thermo-optic properties with temperature is very material dependent, and therefore, as this chapter is concerned predominately with Holmium doped YAG, only the thermo-optic properties of YAG will be considered. The dependence of $dn/dT$, the thermal conductivity and thermal expansion coefficient with temperature in YAG is shown in Figure 5.1. It shows that a temperature change from 300K to 100K results in a 12.5 times reduction in $dn/dT$ and a 4.7 times reduction in the thermal expansion coefficient. Similarly, the thermal conductivity increases by 6.7 times from 300K to 100K. The increase in thermal conductivity allows for rapid dissipation of any heat generated, reducing the thermal gradient, which combined with the reduction in $dn/dT$ and the expansion coefficient will lead to a reduction in the thermal lens strength and induced stresses. This reduction is highlighted by the example where the beam quality degradation and depolarisation loss are considered for 100W of dissipated heat in YAG at room temperature and liquid nitrogen temperature (LN$_2$). The single pass beam quality degradation for a Gaussian pump beam in a cylindrical rod, as discussed in Chapter 2, is given by [5]

$$M_f^2 = \sqrt{(M_i^2)^2 + (M_q^2)^2} \tag{5.1}$$

where $M_f^2$ and $M_i^2$ are the final and initial beam propagation factors and the degradation to the beam propagation factor $M_q^2$ is given by [6]

$$M_q^2 = \frac{dn}{dT}\frac{2P_{hT}}{k\lambda\sqrt{2}}\left(\frac{w_l}{w_p}\right)^4 \tag{5.2}$$

where $P_{hT}$ is the total power dissipated as heat, $\lambda$ is the signal wavelength and $w_{l,p}$ are the laser signal and pump beam radii. At room temperature (300°K), using $dn/dT = 7.65 \times 10^{-6}$K$^{-1}$ [1], $k = 11.2$Wm$^{-1}$K$^{-1}$ [1], and assuming for simplicity that $w_l = w_p$, $\lambda$=2.1$\mu m$ and $M_i^2 = 1$, the final beam propagation factor is $M_f^2 = 46$. However, at LN$_2$ temperature (77°K) $dn/dT = 0.65\times10^{-6}$K$^{-1}$ [1], $k = 75.3$Wm$^{-1}$K$^{-1}$ [1], the final beam propagation factor is $M_f^2 = 1.16$. This is a factor of 50 smaller than the result for room temperature and shows a considerable improvement in beam quality from a highly degraded output at 300°K to near diffraction limited performance at 77°K. Although Clarkson

[6] suggests that in a resonator the degradation will be less severe than the above predicts, this still serves as a reasonable approximation to the scale of the reduction in the beam propagation factor achievable due to reducing the crystal temperature to $LN_2$ temperature.

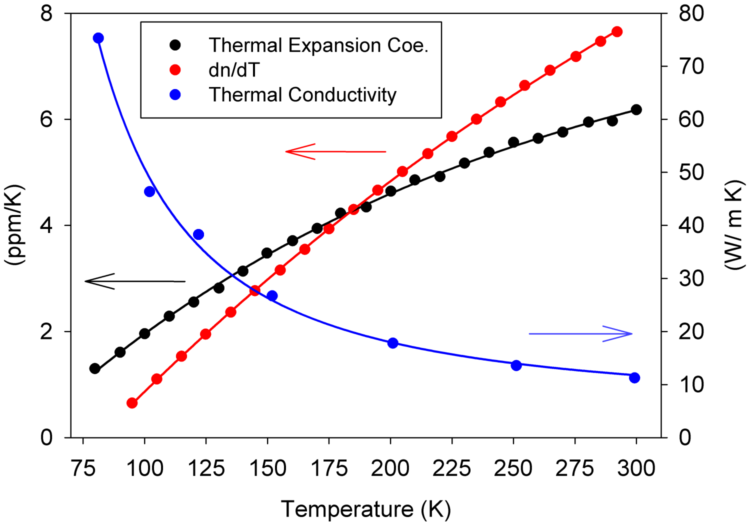

Figure 5.1: Summary of the dependence of the thermo-optic properties affecting thermal lensing and stress induced birefringence as a function of temperature in YAG [1].

Similarly, the improvement in the de-polarisation loss can also be calculated when assuming that the rod is uniformly pumped by a 'top-hat' beam profile with a beam radius $w_p$ and that the Gaussian laser signal with a $1/e^2$ beam radius of $w_l$ is less than the pump beam radius ($w_l < w_p$), the round-trip de-polarisation loss is given by [7]

$$L_d = \frac{1}{4}\left[1 - \frac{\sin\left(2C_T P_{hT}\left(\frac{w_l}{w_p}\right)^2\right)}{2C_T P_{hT}\left(\frac{w_l}{w_p}\right)^2}\right] \tag{5.3}$$

where $P_{hT} = \int_0^z P_h(z)dz = P_p(0)(1 - \exp(-\alpha_p z))\gamma_h$, and $C_T = \frac{2n_0^2 \alpha C_B}{\lambda k}$ where $C_B$ defined by Koecher [8] is a function of the material's elasto-optical coefficients. Using $w_l/w_p = 1$, $\alpha$(T=300°K)=6.18×$10^{-6}$W$m^{-1}$$K^{-1}$ [1],

$\alpha$(T=77°K)=1.3×10$^{-6}$K$^{-1}$ [1], $n_0$ = 1.833, and $C_B$ = -0.0099 (for Nd:YAG) [8], the de-polarisation loss is $L_d(T = 300°K)$ =27.5% and $L_d(T = 77°K)$ =0.05%. This shows that reducing the YAG crystal temperature has significantly reduced the de-polarisation loss. Therefore, combining this with the reduced beam quality degradation with temperatures means that at low temperatures the YAG crystal can be pumped to much higher powers before the heat generated will cause the thermal effects to limit the performance. Therefore, the output power from these cold lasers can be scaled to much higher powers before thermal effects limit the performance, when compared to a room temperature crystal in the same laser configuration.

In addition to the temperature dependence of the thermo-optic properties, reducing the thermal load itself will significantly reduce the impact of thermal effects. As such, to reach the same thermal limits would require much higher pump powers and thus due to the higher pump power will result in an increased output power. In conjunction with cryogenic cooling, the approach used in this chapter was to operate a Ho:YAG laser in a low quantum defect mode of operation by in-band pumping the $^5$I$_8$ $\rightarrow^5$I$_7$ transition in holmium at 1932nm with a high power fibre laser. The benefit of this, over diode pumping at 790nm, is that the quantum defect ($\eta_{qd} = 1 - \lambda_P/\lambda_L$) is significantly reduced. With the Ho:YAG pumped at 1932nm, the quantum defect for laser emission at 2.1$\mu m$ is $\eta_{qd}$ ≈8%, compared to $\eta_{qd}$ ≈62% for diode pumping. This means that by in-band pumping, the thermal load due to quantum defect heating is reduced by a factor of 7, suggesting that the pump power can be increased by the same factor before thermal effects being to limit the laser performance. However, operating in a lower quantum defect regime is not without complications as it also impacts the laser threshold and slope efficiency, and therefore the overall laser performance.

To consider the impact of the quantum defect on laser performance, the slope efficiency and absorbed threshold pump power, given by equations (2.1) and (2.3) in Chapter 2, must be considered. The slope efficiency is directly proportional to $1 - \eta_{qd}$, suggesting that a low quantum defect will yield a higher slope efficiency. However, the slope efficiency is also proportional to the pump absorption efficiency, which can be significantly reduced when operating in a low quantum defect state, due to ground state bleaching. This reduction in the absorption efficiency for low quantum defects also causes the threshold to increase due to $P_{thres} \propto 1/\eta_{abs}$. As a result, the overall laser performance for a given pump power can be reduced for lower quantum defect operation, but ultimately there is a balance required between the benefits of low quantum defect operation and the reduction in performance due to a reduced absorption efficiency. Furthermore, as the threshold is also dependent on the signal emission and absorption cross-sections, their contribution must also be accounted for as the separation in pump and signal wavelength is changed.

In addition to the enhancement of the thermo-optic properties in YAG with decreased temperature, there are also beneficial changes to the energy level populations governed by the Boltzmann distribution. This can be seen from the thermal occupancy of each energy level given by

$$f_i = \frac{\exp(-\varepsilon_i/k_B T)}{\Sigma_i \exp(-\varepsilon_i/k_B T)} \tag{5.4}$$

where $\varepsilon_i$ is the energy of the $i^{th}$ level above the lowest energy in the Stark manifold. The occupancy of the $^5$I$_8$ and $^5$I$_7$ manifolds in Ho:YAG at 300°K and 77°K can be seen in Figure 5.2. It can be seen that at room temperature (300°K), the laser transition is 3 level. However, at 77°K the occupancy of the $^5$I$_7$ level changes, so that 75% of the inversion results in excitation of only the lowest 4 levels of the manifold. Additionally, at 77°K, the energy levels between 400-600cm$^{-1}$ each contain <0.01% of the total population of the $^5$I$_8$ manifold. As the emission and absorption cross sections are directly proportional to the occupancy of the initial energy level, such that $\sigma_a \propto f_i(^5I_8)$ and $\sigma_e \propto f_i(^5I_7)$, the small population in termination level at 2097nm means that the signal reabsorption at 77°K will be very small, and that the laser operates in a quasi 4-level regime. The impact of this is that the threshold condition will be reduced at 77°K, compared to 300°K.

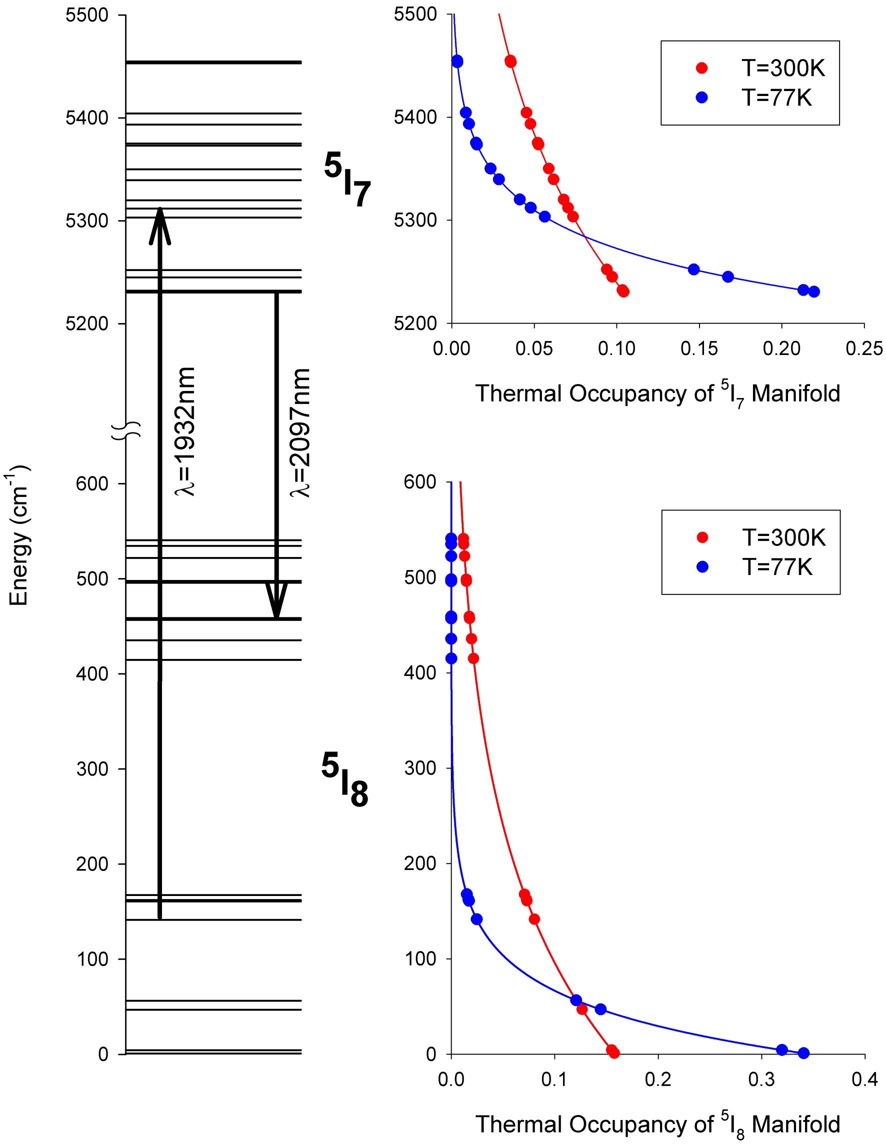

Figure 5.2: Showing the Energy levels for the $^5I_8$ and $^5I_7$ manifolds (left) in Ho:YAG with the 1932nm and 2097nm transitions of interest labelled (energy levels taken from Walsh et al's paper [9] for Ho:YAG at 8K). Additionally, the thermal occupancy of each level at room temperature (300°K) and liquid nitrogen temperature (77°K) are plotted (right) for both manifolds. This highlights that for pumping at 1932nm with laser oscillation at 2097nm, the laser moves from a 3-level system at 300K to a quasi-4 level one at 77K, which will reduce the threshold and increase slope efficiency, and thus improve the overall laser performance.

Another advantage to laser operation at cryogenic temperatures is that the thermal occupancies at this temperature allow for efficient operation in a very low quantum defect state ($\sim$2%), by pumping at 1932nm with emission at 1970nm. This very low quantum defect operation is not achievable at room temperature due to an impractically high threshold, so is only possible due to cryogenic cooling. The potential of this very low quantum defect laser operation is discussed in Section 5.4.4, based on the work of Dr Ji Won Kim.

Although reducing the crystal temperature has the benefits outlined above, it does also cause some less desirable properties. The most significant to achieving efficient lasing are the temperature dependent changes in the absorption linewidths and positions with temperature, for example [10–12]. When reviewing the absorption spectra for Ho:YAG from Walsh et al. [9], it suggests that there are negligible changes in the absorption linewidths with temperature. However, to enable efficient absorption requires a good overlap between the pump and absorption linewidth. Therefore, to ascertain the actual linewidth and peak position, a detailed spectroscopic measurement of Ho:YAG and Ho:YLF (as this was another commercially available laser material which is frequently used for $2\mu m$ laser operation) were conducted in both crystals for the wavelength range of interest for in-band pumping. This data was then used in the design of the fibre laser pump source for an in-band pumped Ho:YAG laser.

## 5.2 Temperature dependent spectroscopy $Ho^{3+}$-doped YAG and YLF

### 5.2.1 Introduction

In this section, work on determining the absorption spectra in Holmium doped YAG and YLF are discussed. The motivation for this is that although there are significant benefits of reducing the crystal temperature, as discussed in the chapter introduction, there are also the less desirable changes in the absorption spectrum. These temperature dependent changes result in a given transition's linewidth narrowing with reduced temperature, as well as a shift in the central wavelength of a given absorption peak [10–13]. This is due to a reduction in energy level broadening, and shifts in the energy levels within the upper and lower manifolds. These changes become significant when considering that the pump absorption efficiency is dependent on the overlap between the pump linewidth and the absorption peak linewidth. Therefore, in order to achieve efficient pump absorption, the pump linewidth needs to be equal to or less than the linewidth of the absorption peak. For this to be achieved in practice, the actual absorption linewidth at liquid nitrogen temperature was measured so that the pump source could be designed such that the laser linewidth would fulfil this requirement.

The absorption spectrum in Ho-doped YAG has been previously measured as a function of temperature by Walsh et al. [9]. However, the changes in linewidth in their data do not support the theory presented in the literature (for example [10–13]), whereby the linewidth should decrease with temperature, suggesting that their measurements would have given a false impression of the required pump laser linewidth.

Typically, absorption spectra are measured using a white light source and suitable spectrophotometer. However, the problem with this approach is that white light sources have a low spectral intensity in the $2\mu m$ region, which means that high sensitivity detectors are required to avoid measurement errors. A potential solution to this is to use a high power amplified spontaneous emission source with a bandwidth in the absorption region of interest. Naturally, this approach is not possible for many wavelengths due to the limits imposed by the emission spectra of rare-earth doped ASE sources. However, in the case of Holmium doped YAG and YLF, the absorption band for in-band pumping between the $^5I_8 \rightarrow ^5I_7$ Stark manifolds is in the range of 1850-1980nm. This conveniently overlaps with the emission bandwidth of Tm doped silica which emits in the range of 1800-2100nm, depending on the fibre configuration. Therefore, a Tm-doped fibre ASE source was designed to coincide with

Holmium absorption band, which was then measured as a function of the crystal temperature in a purpose made cryostat and a spectrophotometer with a resolution of 0.2nm.

### 5.2.2 Methodology

The method for determining the absorption spectrum of each crystal of interest is the same as that using a white light source, whereby the signal intensity as a function of wavelength is compared for radiation propagating through air to that through the crystal with all other conditions the same. Using these wavelength dependent intensities, the absorption cross section, $\sigma_a(\lambda)$, was calculated using

$$\sigma_a(\lambda) = \frac{1}{Nl}\ln\left(\frac{T_b(\lambda)}{T_s(\lambda)}\right) \tag{5.5}$$

where $N$ is the doping concentration, $l$ is the crystal length, and $T_{b,s}(\lambda)$ is the transmitted spectrum as a function of wavelength for the background and sample, respectively.

To measure the temperature dependent absorption spectra, the crystal was housed in a specially designed dewar cryostat for operation at liquid nitrogen temperature. The cryostat was designed to be able to dissipate $>$100W of heat through the interface between the crystal mount and the LN$_2$ dewar. The dewar can hold $\sim$10L of LN$_2$ which would enable several hours of operation at these power levels, or significantly more for a reduced thermal loading. The dewar and crystal housing were thermally isolated using super-insulation and a high vacuum, which was provided by a turbo-molecular vacuum pump. The crystal was optically accessed via two 25.4mm diameter, 6mm thick Calcium Fluoride (CaF$_2$) windows that were AR coated from 1.8-2.2$\mu m$. The crystal housing itself consisted of a copper heat sink, which was attached directly to the base of the LN$_2$ dewar, with a suitable recess for holding a 5mm diameter rod, which could be up to 60mm long. The crystal was fixed in position with a spring loaded stress-relieved copper clamp. The crystal was wrapped in 125$\mu m$ thick Indium foil to facilitate a good thermal contact between the rod and heat sink when fixed in position. The temperature of the crystal was monitored using 2 K-type thermo-couples, which were attached to the top and bottom half of the heat sink. For taking the temperature dependent absorption measurements, the crystal temperature was controlled by pouring $LN_2$ into the dewar and allowing the crystal temperature to stabilise. With this approach, the crystal temperature had a variation during the absorption measurement of less than 5°K due to the crystal reaching thermal equilibrium between the heat generated in the crystal and the $LN_2$ dewar temperature.

### 5.2.3 ASE probe source

#### 5.2.3.1 Experimental set-up

The ASE source used in these spectroscopy experiments consisted of a $Tm^{3+}$-doped fibre, which was made in-house using the standard modified chemical vapour deposition and solution doping technique. The fibre produced had a 20$\mu m$ diameter aluminosilicate core doped with approximately 1.2% $Tm_2O_3$ and 2.8% $Al_2O_3$ with an NA of 0.12. The cladding was formed from pure silica with a 200$\mu m$ diameter (maximum) double D-shaped inner cladding to aid pump absorption, whereby the circular fibre has two segments removed as shown in Figure 5.3.

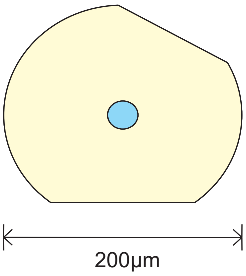

Figure 5.3: Cross-section of the double D-shaped fibre used for the ASE source

The fibre end facets were perpendicularly cleaved on the pump input side, providing a reflectivity of 3.5%, and the other fibre facet was angle polished, as shown in Figure 5.4. The angled facet was polished to ∼12° to suppress parasitic lasing, whilst also ensuring predominately single-ended operation, as discussed in Chapter 3.

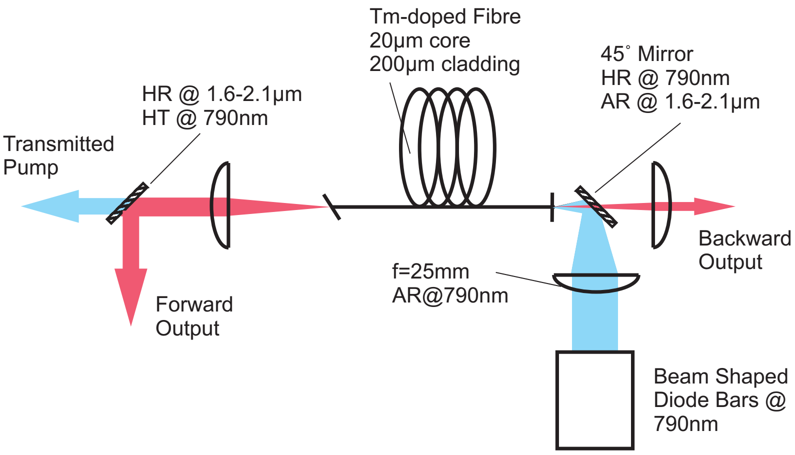

Figure 5.4: Schematic of the ASE fibre setup

This fibre was cladding-pumped by a diode-bar operating at 790nm. The diode-bar was collimated in the fast and slow axis, and a two-mirror beam shaper was used to equalise the beam quality in both directions, such that the output had a final beam propagation factor of $M^2 < 70$ in orthogonal directions with 30.5W of power. The pump launch efficiency into the perpendicular facet was estimated to be 87%. The absorption in this cladding pumped configuration was measured via the cut-back technique to be 4.4dB/m, so a 3m device length of fibre was used for efficient pump absorption, whilst minimising signal reabsorption losses at the output end of the fibre. Both end facets were mounted in V-groove heat sinks and the rest of the fibre was loosely coiled and fan-cooled to aid heat extraction from the fibre.

#### 5.2.3.2 Performance

As can be seen in Figure 5.5, the maximum output power obtained was 3.8W for a launched pump power of 27W, with a slope efficiency for the forward direction of 27% for launched pump powers over 16W. The total output power slope is 28%.

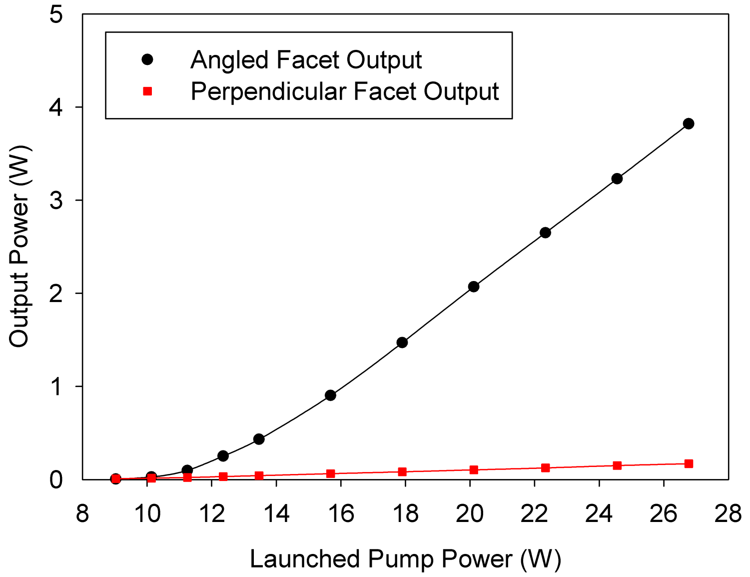

Figure 5.5: ASE output power as a function of launched pump power from both end facets of the tm doped fibre

The ASE output beam propagation factor was measured to be $M^2 < 3$. For the same fibre, Clarkson et al. [14] measured a laser beam propagation factor of $M^2 < 1.3$. This discrepancy is reasonable given that the ASE excites higher order modes, which in a laser configuration do not see gain.

The output ASE spectrum was measured as a function of launched pump power using a DongWoo Monochromator Model DM500i, as shown in Figure 5.6. This shows that the spectral bandwidth of 50nm FWHM (and 120nm full bandwidth) is unchanged as a function of pump power. Furthermore, the emission wavelength range coincides with the absorption bands of both Holmium doped YAG and YLF as required.

The fine structure in the ASE spectrum, that can be seen in Figure 5.6, is predominantly caused by water absorption in the air. Additionally, the sharp peaks for the highest pump power suggested that the laser threshold had been reached. However, for the spectroscopic measurements, the ASE source

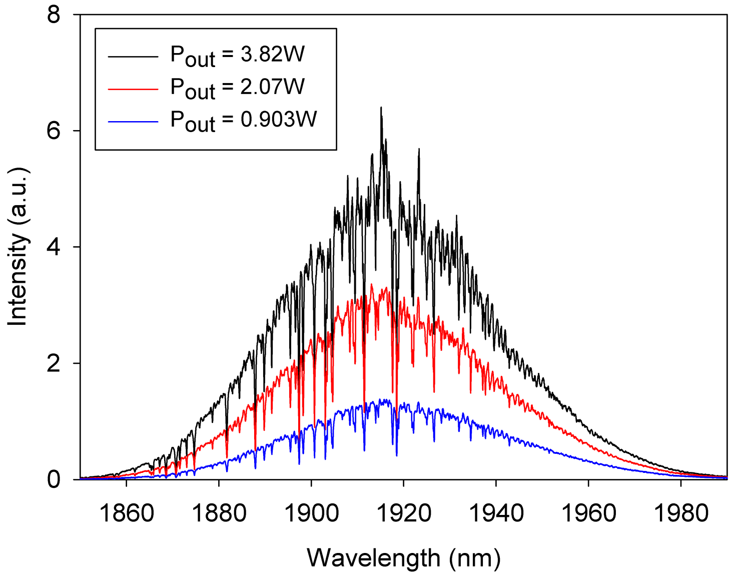

Figure 5.6: ASE output spectrum as a function of the output power

will be operated at a lower power level and so it will be well below the laser threshold. The fine structure due to water absorption can be clearly seen when the ASE spectrum is compared to water vapour absorption from the HITRAN database [15], as shown in Figure 5.7.

The presence of the water absorption structure in the ASE signal is not ideal, but by itself will make little impact on the crystal absorption measurements. However, fluctuations in the ASE output intensity and detector noise will be significant for wavelengths where the signal intensity is low, such as, at strong water absorption wavelengths and the edges of the ASE spectrum. To observe the impact of this background noise, back to back ASE output spectrum scans at various points in a day were taken. Comparing the individual measurements showed that the maximum percentage difference in signal intensity, as a function of the wavelength from the mean, was $<5\%$ for wavelengths between 1870-1990nm. Outside this region, the error rises up to $\sim$10% at the edges of the spectrum as suggested, due to the small signal intensity when compared to the background noise.

The water absorption structure in the ASE did have the benefit that it en-

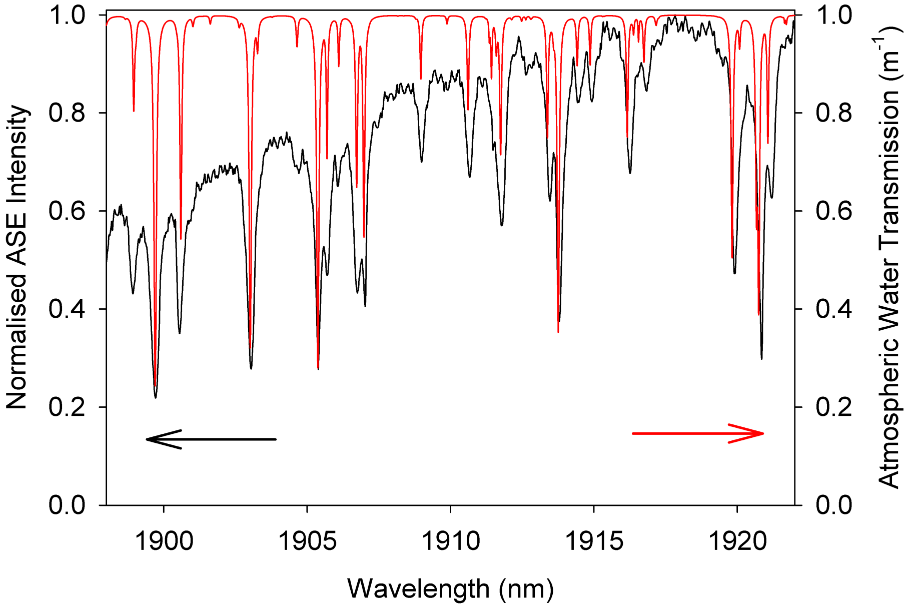

Figure 5.7: Showing the overlap between the atmospheric water transmission per unit length [15] and the normalised ASE intensity spectrum. This shows that the structure observed in the ASE is predominately caused by water vapour in the air along a 2m path length between the fibre output and the detector in the monochromator.

abled the practical resolution of the monochromator to be defined. This was achieved by using the known water absorption peak separations from the HITRAN data [15] and comparing it to the smallest resolvable separations in fine structure of ASE spectrum. This was measured to be ∼0.2nm, which is in keeping with the quoted resolution from the manufacturer.

### 5.2.4 The absorption spectrum for Ho$^{3+}$:YAG as a function of temperature

For measuring the small signal absorption spectrum in Ho:YAG, the ASE probe was operated at 1W of output corresponding to a spectral power density of ∼10mW/nm. Using the method previously outlined, the absorption cross-section was measured over the entire ASE bandwidth (1860nm-1980nm). The crystal used for these measurements was a 5mm diameter by 30mm long 0.5at% Ho:YAG crystal. Figures 5.8 and 5.9 show the absorption cross-section as a function of temperature in the two regions of interest for in-band pumping (i.e. 1900-1915nm and 1928-1932nm). Additionally, in Figure 5.10, the full-scale measurement is given at room temperature and LN$_2$ temperature.

As can be seen in Figures 5.8 - 5.10, as the crystal temperature is decreased, the absorption structure begins to narrow. As the the temperature is decreased below ∼180K, strong absorption transitions between the $^5I_8 \rightarrow ^5I_7$ begin to become resolveable. However, due to the close overlap in energy between the individual transitions, it is not possible to distinguish individual transitions themselves as the energy difference between them is much smaller than the resolution limit of the monochromator. However, as previously discussed, this information is not important here as the main interest is the overall absorption bandwidth for a given wavelength. In the literature, this absorption structure has not been shown [9]. The difference in the spectroscopy compared to the published data is shown in Figure 5.11, showing that our measurements have narrower absorption transitions with higher peak cross-sections, compared to the published data. This is highlighted in the regions of interest for in-band pumping (i.e. 1900-1915nm and 1928-1932nm) where the published

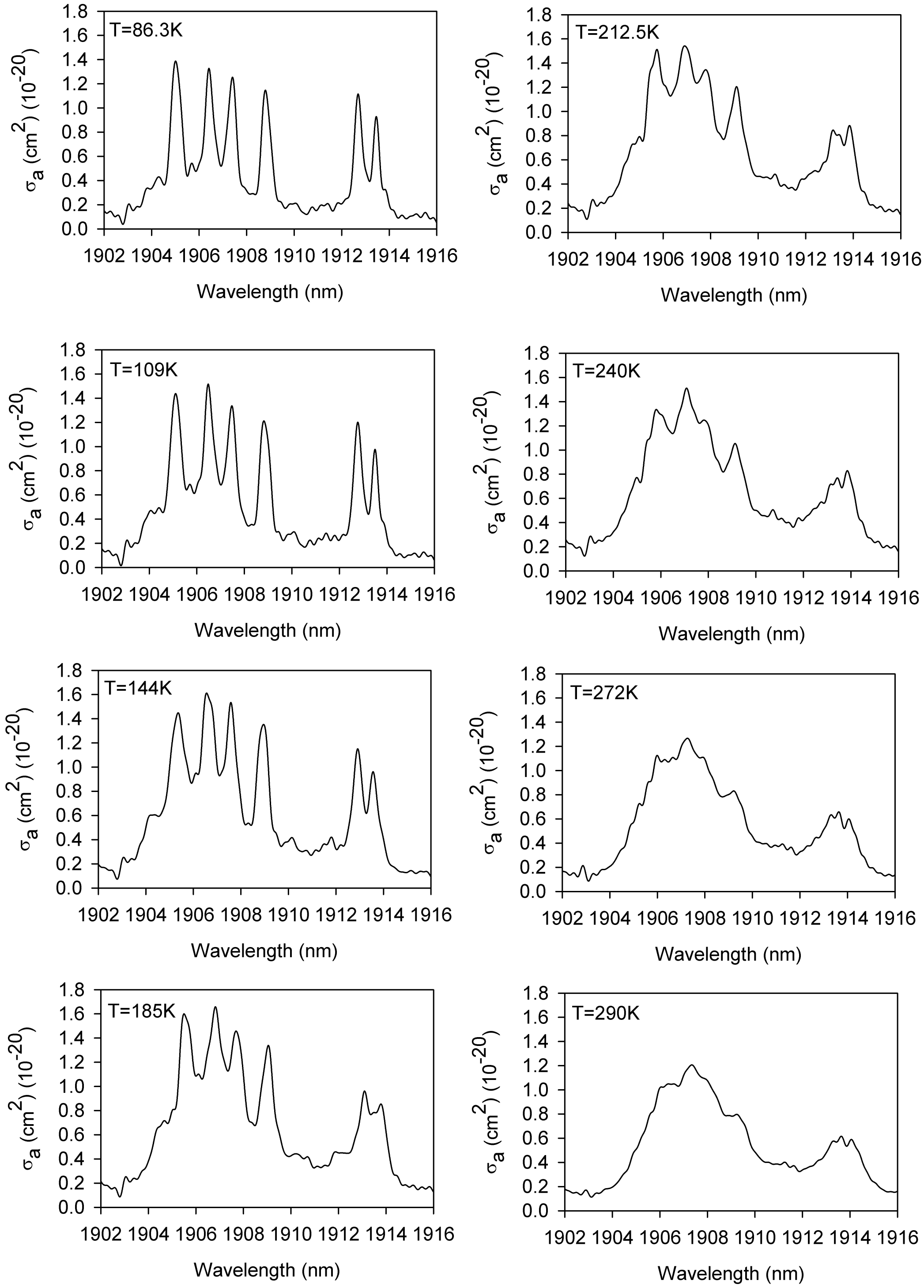

Figure 5.8: Graphs showing the temperature dependent absorption cross-sections for Ho$^{3+}$:YAG for the wavelength range of $1902 - 1916nm$.

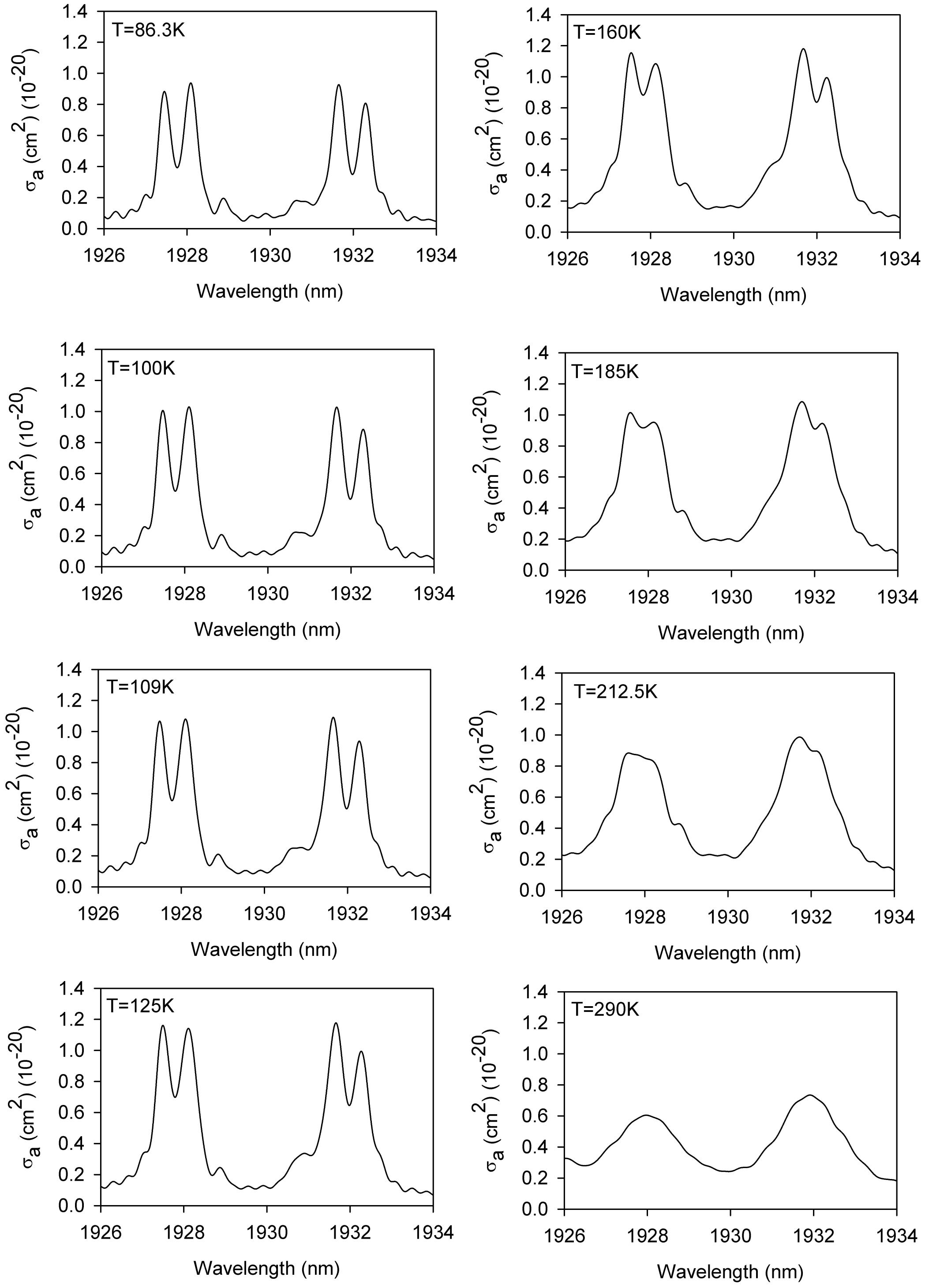

Figure 5.9: Graphs showing the temperature dependent absorption cross-sections for Ho$^{3+}$:YAG for the wavelength range of $1926 - 1934nm$.

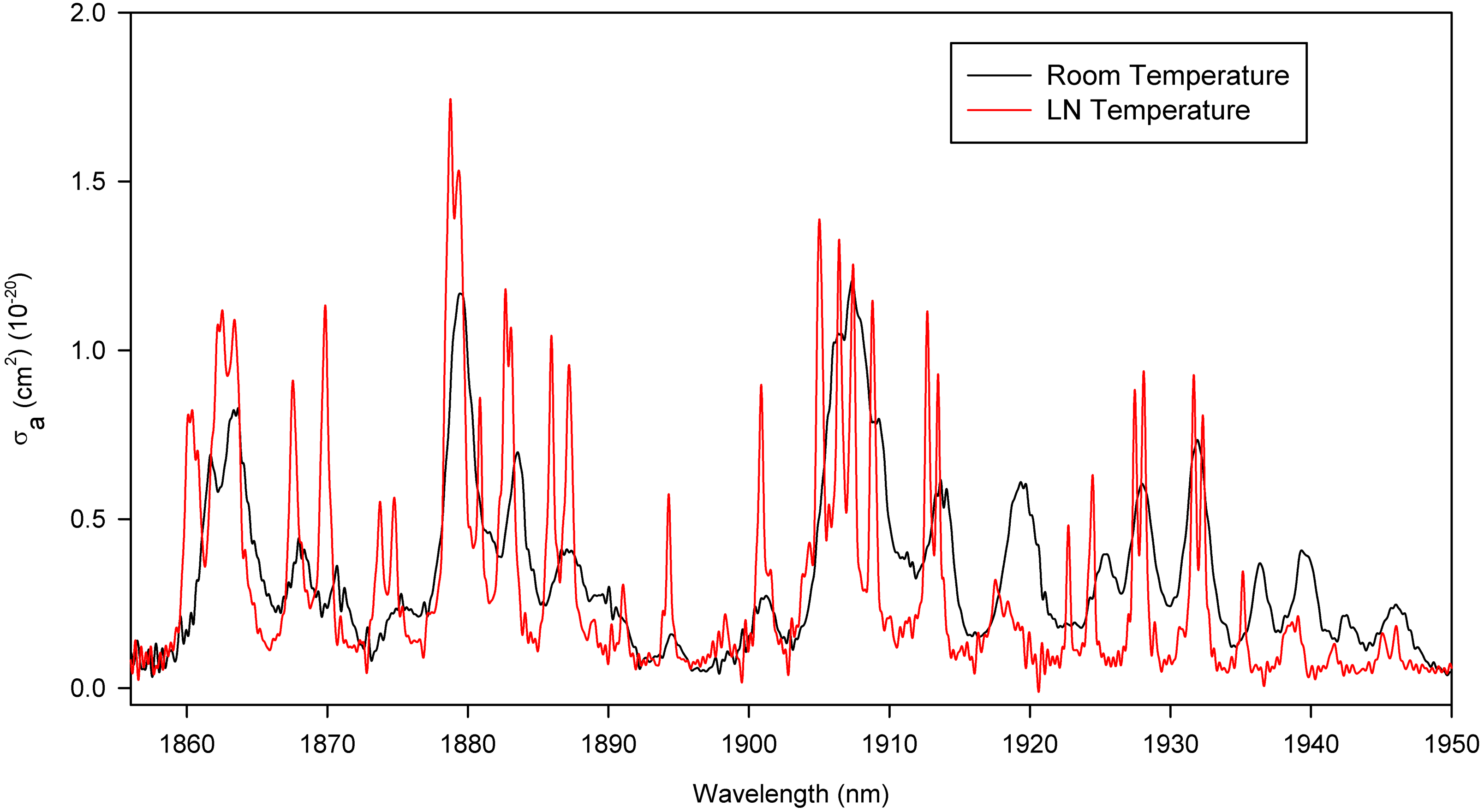

Figure 5.10: Shows the absorption cross section for $Ho^{3+}$:YAG at $LN_2$ and room temperature.

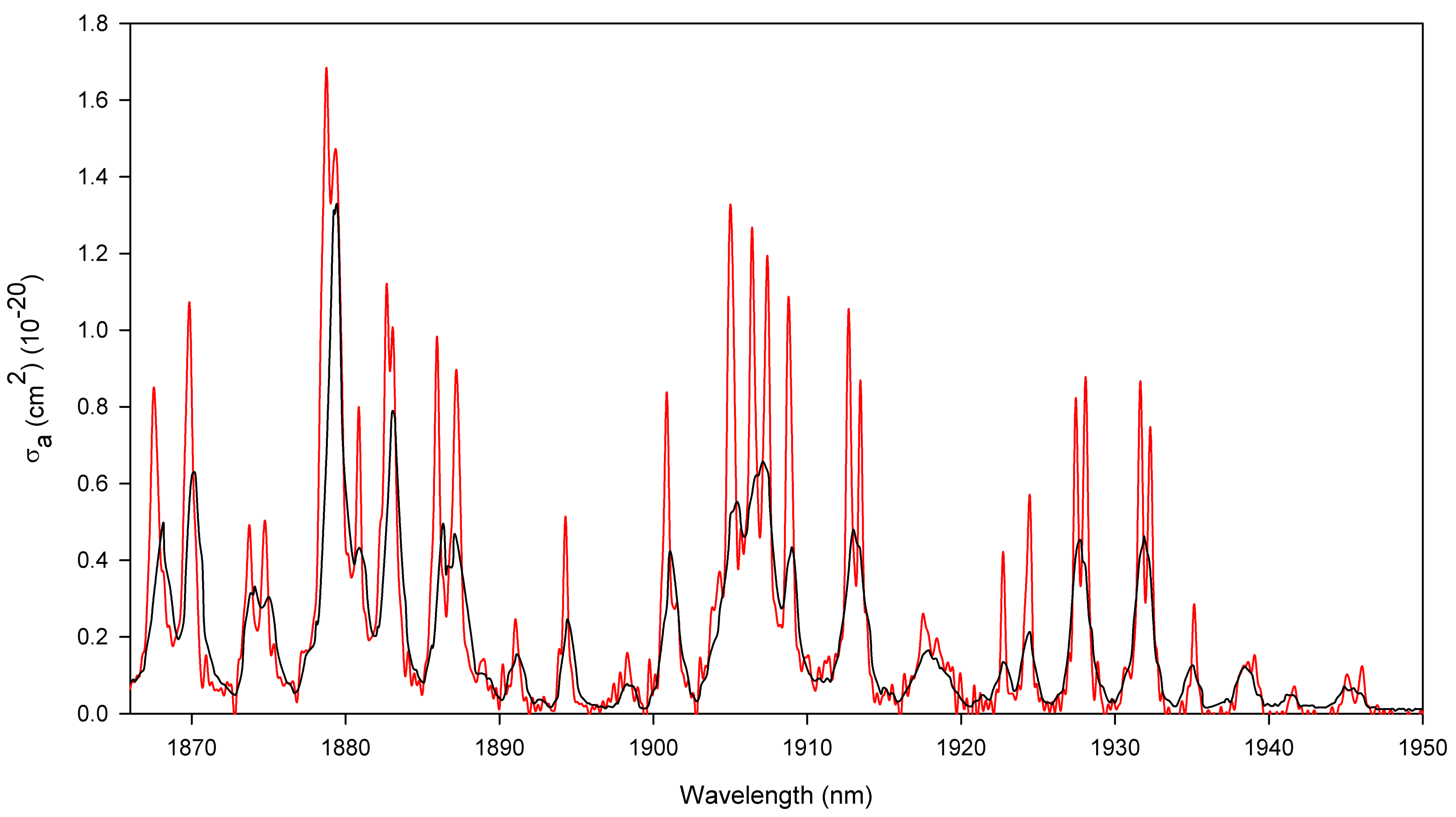

Figure 5.11: Comparing the absorption cross-section for the $^5I_8 \rightarrow ^5I_7$ transition in Ho:YAG at 77K for our measured values (red) with those of the published values in Walsh et al. [9] (black).

data shows a much broader absorption bandwidth (∼5nm for 1900-1910nm and ∼1.2nm for the 1928nm and 1932nm peaks), whereas our data shows there to be multiple narrow absorption peaks within each region, with individual bandwidths (FWHM) of <0.6nm each and peak absorption cross-section twice that of the published data. The significance of this higher resolution is that for efficient absorption, a pump source will need a linewidth narrower than these peaks, suggesting that the published literature gives a false impression that a broader pump linewidth will suffice.

### 5.2.5 The absorption spectrum for Ho$^{3+}$:YLF as a function of temperature

Another laser crystal of interest for use in a cyrogenic laser is Ho:YLF. In preparation for designing a pump source for Ho:YLF, its absorption spectrum was also measured at cryogenic temperatures. For these spectroscopic measurements, a 5mm diameter by 15mm long 1.5at% Ho:YLF crystal was used. Because the crystal is uniaxial, the absorption in the two orthogonal axes were measured independently. This was achieved by using a Glan-Taylor polariser before the sample, and matching the linearly-polarised transmitted light to the axes of interest inside the crystal. The temperature dependence on the absorption spectrum in both axis for wavelengths of interest for in-band pumping can be seen in Figures 5.12 and5.13. Similar to the case of Ho:YAG, the figures show that as the temperature is reduced, the absorption structure begins to narrow with more defined absorption structure shown. As was the case in Ho:YAG, the peaks observed do not correspond to individual transitions due to the close spacing of the energy levels in Holmium. However, in Ho:YLF, the narrowing of the absorption peaks is not as pronounced as was the case for Ho:YAG, with the minimium absorption linewidth of ∼0.8nm (FWHM) and with a minimum bandwidth of >1nm in the 1930-1940nm region of interest for in-band pumping. This will relax the tolerances on any pump source linewidth for laser operation using this material.

For completeness, the full scale absorption coefficient for both polarisations is

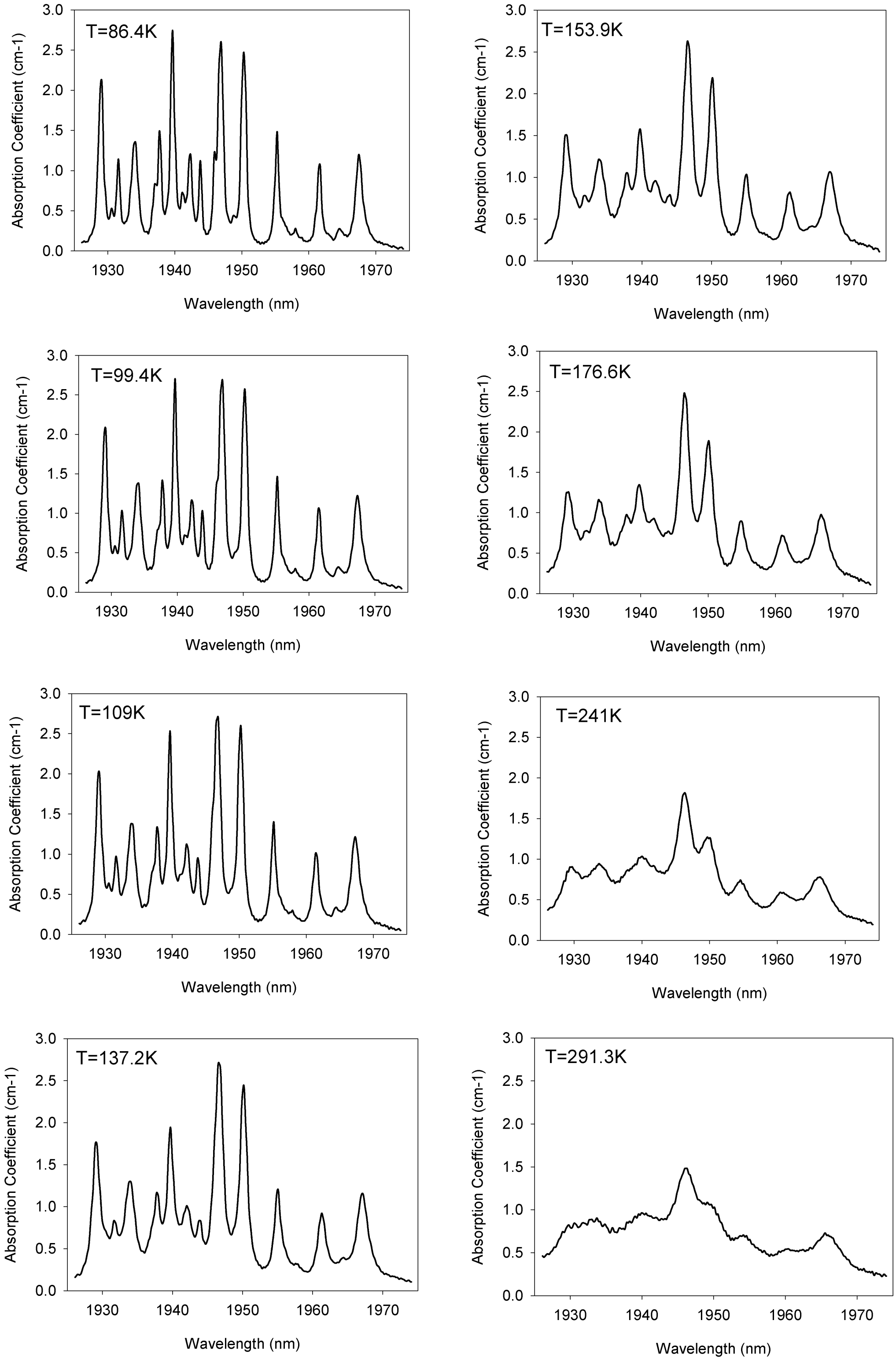

Figure 5.12: Graphs showing the temperature dependent absorption coefficient in the s-polarisation for $Ho^{3+}$:YLF with Lorentzian curve fitting.

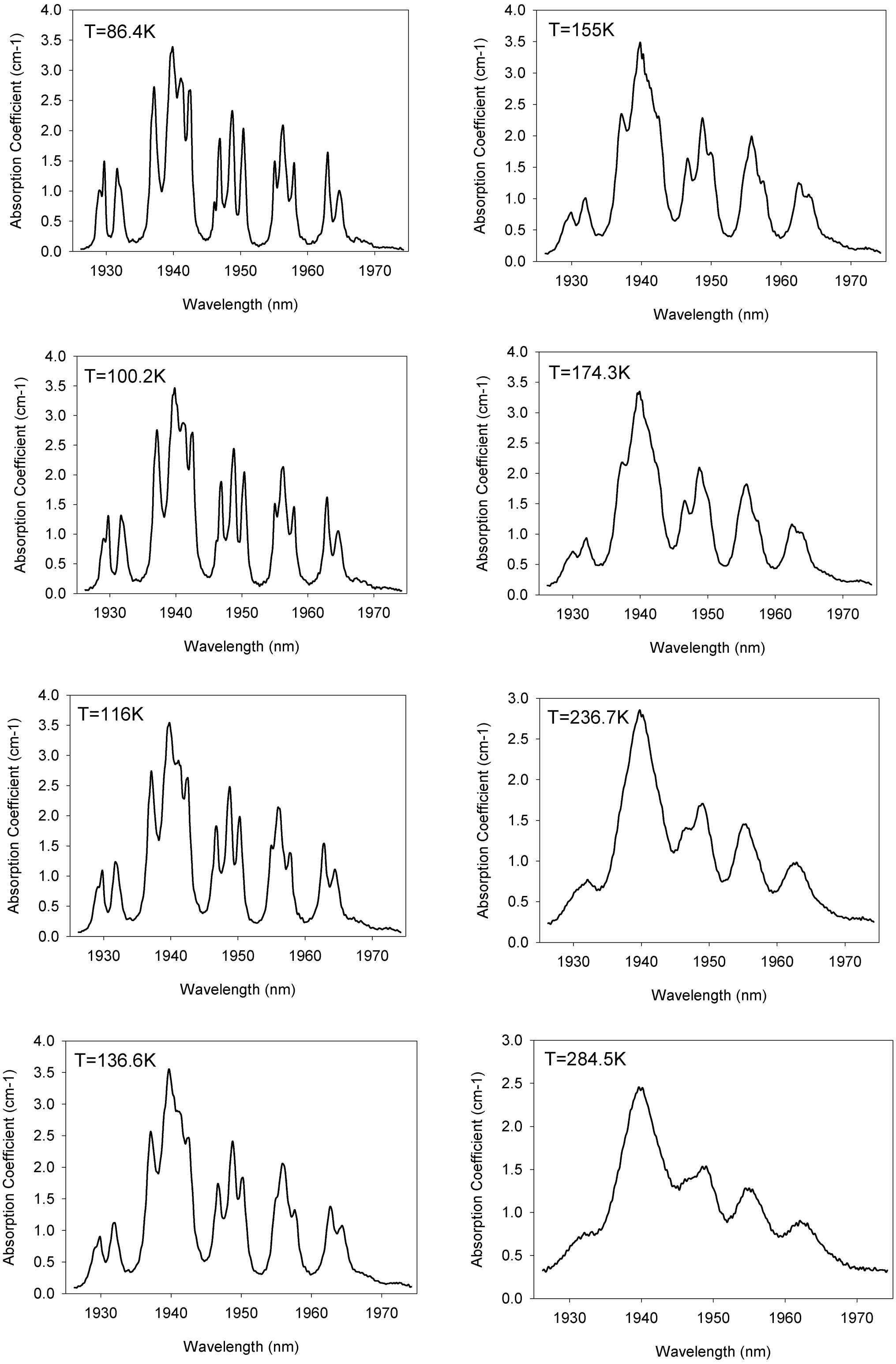

Figure 5.13: Graphs showing the temperature dependent absorption coefficient in the p-polarisation for $Ho^{3+}$:YLF with Lorentzian curve fitting.

shown in Figure 5.14. The figure highlights the increased absorption, as well as the narrowing of individual transitions at $LN_2$ temperatures.

From past experiments with this crystal, it was suspected that it is a co-doped crystal with $Tm^{3+}$ ions. This is not ideal for measuring the absorption cross-section due to Holmium in YLF. However, considering the energy levels for Tm:YLF [16], shown in Figure 5.15, it can be seen from the thermal occupancies in each manifold, that as the temperature is reduced, the changes in thermal occupancy with temperature leads to the absorption cross-section for wavelengths longer than 1880nm becoming effectively zero at $LN_2$ temperatures, due to a thermal occupancy in the transition termination level and a low thermal occupancy in the initial energy level. Therefore, measurement of the absorption cross-sections at $LN_2$ temperature will be due solely to the Holmium ions in the YLF crystal.

### 5.2.6 Conclusions

In this section, a simple approach for measuring high resolution absorption spectra was applied. Using an ASE source and a monochromator with a resolution of $\sim$0.2nm, detailed absorption spectra for Ho:YAG and Ho:YLF were taken. These showed that as the crystal temperature is decreased, individual transitions start to become resolved due to the transition linewidth's narrowing, as was predicted by the published theory [10–13]. This result shows much finer absorption structure than has been previously published [9], due to a higher resolution monochromator being used.

The limitation to this measurement approach is the requirement for the absorption band of interest to fall within the emission bandwidth of a rare-earth doped silica fibre. Therefore, this approach is severely limited due to the limited overlap of other rare-earth ions emission and absorption spectra.

After reviewing the measured absorption spectrum in Ho:YAG, it was decided that for in-band pumping, the 1932nm peak would be ideal due to it being the longest wavelength that still had a reasonably high cross-section. This, in turn,

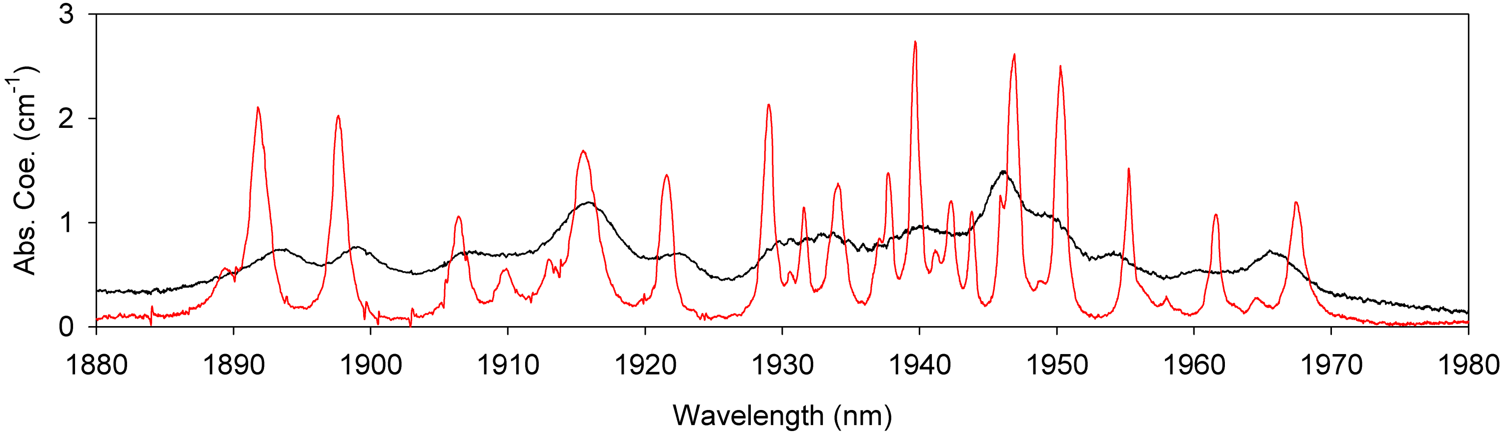

(a) s-pol

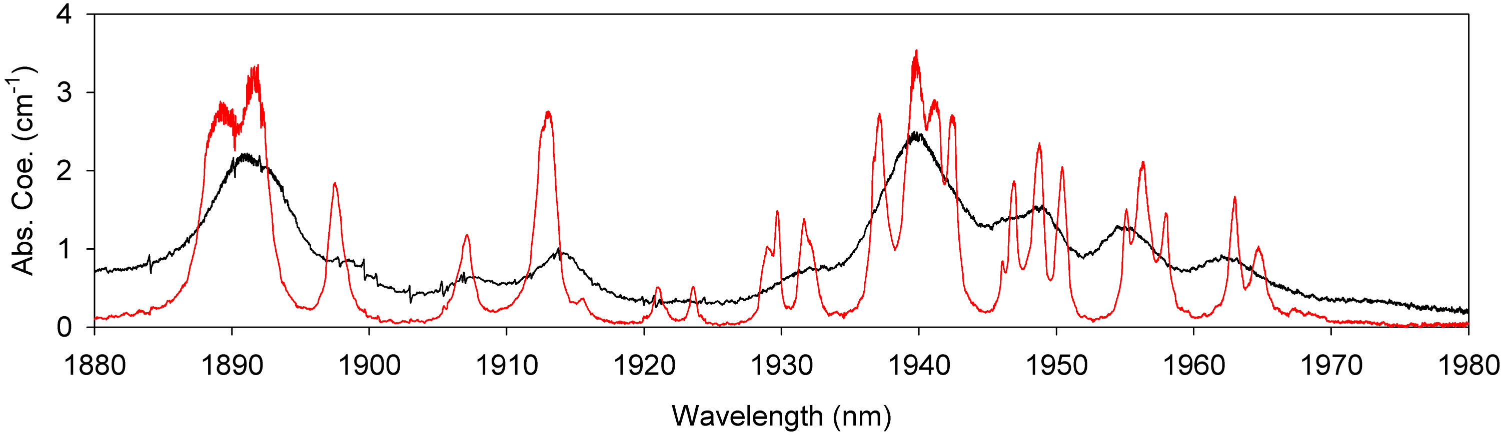

(b) p-pol

Figure 5.14: Showing the absorption spectrum at room temperature (black) and $LN_2$ temperature (red) for (a) s-polarised, and (b) p-polarised, light.

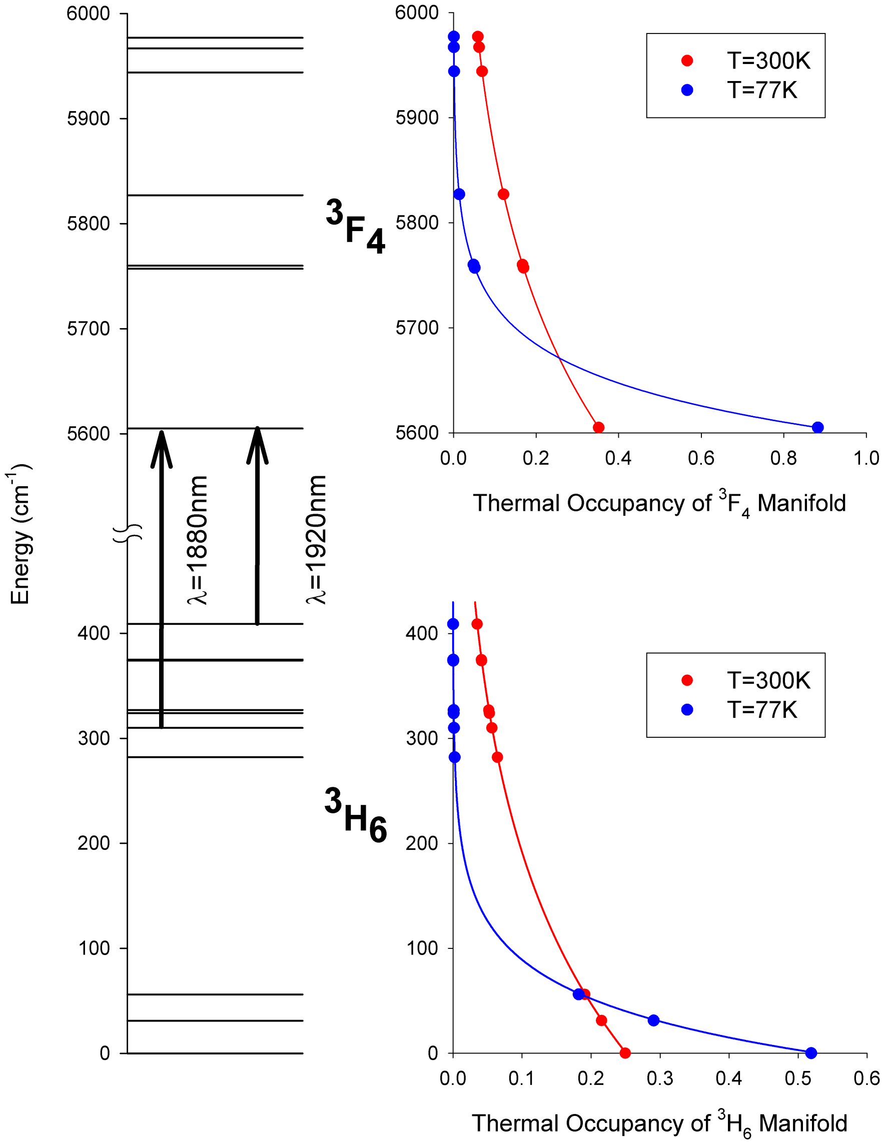

Figure 5.15: Showing the energy levels for the $^3H_6$ and $^3F_4$ manifolds (left) in Tm:YLF with the 1880nm and 1920nm transitions labelled (energy levels taken from Jenssen et al's paper [16] for Tm:YLF). Additionally, the thermal occupancy of each level at room temperature (300°K) and liquid nitrogen temperature (77°K) are plotted (right) for both manifolds. This highlights that absorption cross-section for wavelengths longer than 1880nm is reduced to negligible levels at liquid nitrogen temperature due to the low thermal occupancy for energies above 300cm$^{-1}$ in the $^3H_6$ manifold and a high thermal occupancy in the transition termination level in the $^3F_4$ manifold.

is important as this will allow low quantum defect modes of operation, whilst still maintaining a high absorption efficiency, without the need for particularly long crystals, as would be the case if a longer pump wavelength were used. This is important as low quantum defect operation will reduce the heat deposited into the crystal for a given incident pump power. Furthermore, operating in a low quantum defect will increase the slope efficiency, but will also increase the threshold. Therefore, by carefully selecting the quantum defect, the threshold and slope can be optimised to give much higher output for a given pump power than is possible for a larger quantum defect mode of operation.

The linewidth of the peak at 1932nm was measured to be ∼0.4nm. This is important as the pump source will require an output linewidth less than this to obtain efficient absorption. This highlights the importance of more detailed absorption measurements as the literature suggests that a much larger linewidth would suffice with the impact of a reduced pump absorption efficiency, which would have reduced the Ho:YAG laser performance.

## 5.3 Line-narrowed Tm-doped silica fibre laser

### 5.3.1 Introduction

After analysing the spectrum of Ho:YAG at liquid nitrogen temperatures, it became apparent that to efficiently pump the $^5I_8 \rightarrow ^5I_7$ transition at 1932nm would require a laser source with a linewidth of less than 0.4nm, in order to obtain a high absorption efficiency. As was briefly discussed in the chapter introduction, the approach for pumping the Ho:YAG at 1932nm was to use a diode pumped thulium doped fibre laser in a cladding pumped configuration. The main motivation in using a fibre system, as opposed to a solid state one, is that the fibre's inherent high surface area to volume ratio makes thermal management significantly easier, which when scaling the output powers, can fast become a limiting factor for solid state laser systems, as discussed in Chapter 2. Additionally, the doped region being confined to the wave-guiding core means that the output beam propagation factor can be selected by controlling the core NA during fabrication. This is ideal, as a good pump beam quality facilitates a better overlap between the pump and the fundamental laser mode and therefore will reduce the gain for higher order modes.

It is important for the pump source to have wavelength tuning around 1932nm so that the emission wavelength can be adjusted to overlap with the absorption peak in the Ho:YAG. There are several options for achieving this, including: using a Volume Bragg Grating (VBG) (for wavelength selection) with an etalon to control the linewidth, or using a MOPA configuration consisting of a narrow linewidth (potentially single frequency) master oscillator, or alternatively, a bulk replica diffraction grating feedback cavity. The bulk replica diffraction grating was used here as this offered the simpliest approach and still provided the narrow linewidth feedback required for efficient pump absorption in the Ho:YAG.

### 5.3.2 Impact of a diffraction grating on laser linewidth

In order for the desired linewidth to be obtained, the impact of the diffraction grating on the feedback linewidth needs to be calculated. Starting from the fundamental grating equation [17]

$$\sin\alpha + \sin\beta = kn\lambda \tag{5.6}$$

where $n$ is the number of lines per metre, and $k$ is the diffraction order, and $\alpha$ and $\beta$ are the angles of incidence and diffraction from the grating normal (in degrees). By defining the resolving power of the grating as [18]

$$R = \frac{M^2\lambda}{d\lambda} \tag{5.7}$$

for a beam propagation factor $M^2$ at the central wavelength $\lambda$ and with a difference in wavelength between two spectral lines of equal intensity $d\lambda$. In this case the two peaks are deemed resolved if they follow the Rayleigh Criteria. It can be shown that the resolving power can be defined as [18]:

$$R = \frac{M^2\lambda}{d\lambda} = knW_g \tag{5.8}$$

for a beam size on the grating of $W_g$.

In the Littrow configuration, the grating is blazed at a wavelength $\lambda_b$. In this configuration, the incident angle for $\lambda_b$ is equal to the diffracted angle ($\omega = \alpha = \beta$), so the diffracted beam is retro-reflected along the incident beam path. In this case, equation (5.6) simplifies to

$$2\sin\omega = kn\lambda_b \tag{5.9}$$

From Figure 5.16, it can be seen that the beam width, $W_g$ on the grating can be calculated as $W_g = D/cos\omega$, where $D = 2f\tan\theta$ and $f$ is the focal length of the collimating lens and $\theta$ is the far field divergence angle, which can be approximated to the NA of the fibre core. Using the small angle approximation, such that $\tan\theta \approx \theta$, gives:

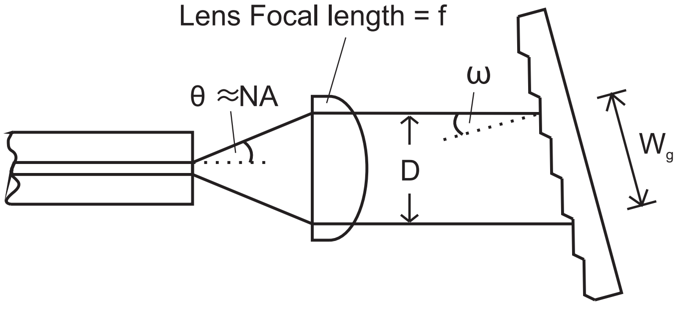

Figure 5.16: Schematic representation of a feedback cavity in Littrow configuration, consisting of a collimating lens focal length f and a diffraction grating.

$$W_g = \frac{2f\theta}{\cos\omega} \tag{5.10}$$

By applying the trigonometric relation $\sin^2\omega + \cos^2\omega = 1$ and substituting for $\sin\omega \approx \omega$ into equation (5.9) gives:

$$W_g \approx \frac{2f\theta}{\sqrt{1-\left(\frac{kn\lambda}{2}\right)^2}} \tag{5.11}$$

Therefore, substituting equation (5.11) into equation (5.8), gives the linewidth of a tunable laser in a Littrow configuration:

$$d\lambda \approx \frac{M^2\lambda}{2f\theta nk}\left(1-\left(\frac{kn\lambda}{2}\right)^2\right)^{\frac{1}{2}} \tag{5.12}$$

### 5.3.3 Set-up

The experimental setup used for the line narrowed thulium doped fibre laser can be seen in Figure 5.17. The fibre used was a commercially available polarisation maintaining (PM) fibre from Nufern (PLMA-TDF-25F/400), with a core diameter of 25$\mu m$ with a 0.1 NA and inner cladding diameter of 400$\mu m$, as used in the final stage amplifier in Chapter 4.

The pump power for this fibre was provided by the same spatially combined diode stacks as used in Chapter 4 for the final stage amplifier. Therefore, the launch into the cladding of the fibre was the same, measured to be 80% into both facets. This was estimated by measuring the transmitted power through an un-doped PM fibre with the same dimensions as the doped fibre. For measuring the launch efficiency into the angle facet the un-doped fibre was polished to the same angle as used in the doped fibre of $12°$. The absorption coefficient in this cladding pumped configuration was measured using a cut-back technique to be $\sim$4.5dB/m, so a device length of 3.5m was used. This length was selected to provide efficient pump absorption ($>$97% of the launched pump light) whilst also favouring emission at shorter wavelengths by reducing the signal reabsorption path length in the fibre. Both ends of the fibre were mounted in water-cooled V-groove heat sinks to aid heat extrac-

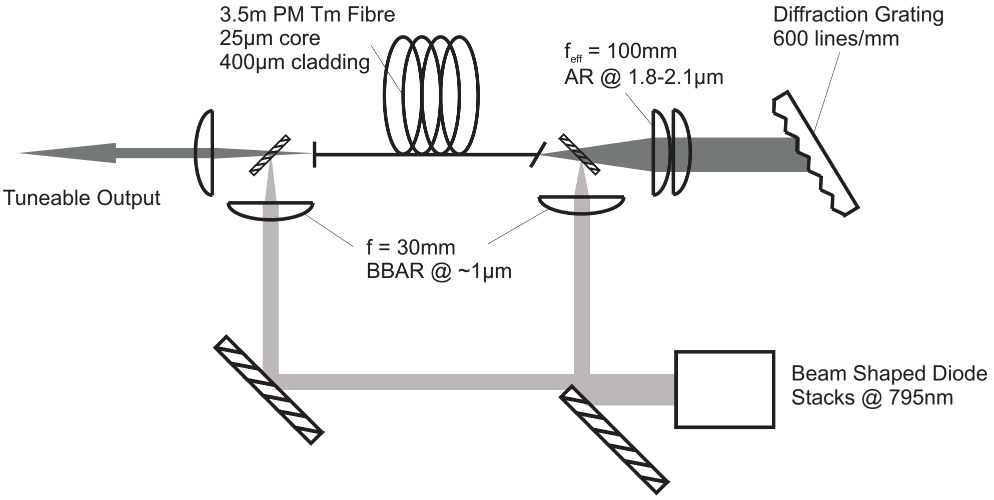

Figure 5.17: Experimental Setup for Tm-doped silica fibre laser.

tion. Furthermore, the remaining unmounted central portion of the fibre was fan-cooled to aid heat removal in the fibre.

The fibre laser cavity was formed by a 3.5% Fresnel reflection from a perpendicularly cleaved end facet and an external feedback cavity with a replica diffraction grating in the Littrow configuration. The fibre end facet adjacent to the external feedback cavity was angle polished to approximately $12^\circ$ to suppress parasitic lasing from the facet. The beam in the external cavity was collimated using a lens combination consisting of a pair of f=200mm $CaF_2$ plano-convex lenses, mounted in close proximity to give an effective focal length of 100mm. The replica grating used had 600 lines/mm and was blazed at a $1.9\mu m$, with a measured reflectivity of 90% (polarised perpendicular to the grooves) and 70% (polarised parallel to the grooves) at $2\mu m$. To increase the grating damage threshold due to inefficient reflection of the incident light, the grating was mounted on a copper heat-sink. For feedback at 1932nm, the grating was angled to approximately 35.4° relative to the incident beam direction. With this arrangement, the laser linewidth at 1932nm was calculated to be ∼0.25nm using equation (5.12) and assuming a beam propagation factor of $M^2$=2 based on the fibres V-value of 4.06.

### 5.3.4 Results and analysis

Figure 5.18 shows the output power as a function of launched pump power for this system. The pump power was limited to these power levels to limit the chance of coating damage, as was experienced in the power amplifier stage in Chapter 4, which would delay progress. As can be seen from Figure 5.18, a slope efficiency of 52% was achieved with an output power of 50W for a launched pump power of 114W. This is reasonable as it is only slightly less than the slope achieved for the power amplifier stage in Chapter 4. Assuming the maximum slope efficiency is ~59% (as achieved in the amplifier) and that there are negligible fibre losses for the signal, the pumping quantum efficiency can be estimated as being $\eta_q = 1.51$. Using this value, and $\tau_f = 360\mu s$ [19], $\sigma_e(\lambda = 1932nm) = 4.6\times10^{-25}m^2$ [20] and $\sigma_a(\lambda = 1932nm) = 0.08\times10^{-25}m^2$ [21], the threshold pump power can be estimated to be $P_{thres} = 0.9W$. This is much lower than the extrapolated value of 15W from Figure 5.18. This is reasonable given how the competition between stimulated and spontaneous emission changes as the pump power is increased beyond threshold. At threshold, the emission is predominately spontaneous, but as the pump power is increased, stimulated emission increases. For signal intensities greater than the signal saturation intensity, the stimulated emission dominates over spontaneous emission and the true slope efficiency is realised. Therefore, extrapolating to determine the threshold using the linear part of the slope will always give a much higher threshold than actually present.

The output beam propagation factor obtained for this fibre was measured to be $M^2 < 1.6$. This is better than the expected beam propagation factor estimated from the fibre's V-value of 4.06, which corresponds to an $M^2 \approx 2$. This means that the calculated laser linewidth should be less than ~0.2nm.

Figure 5.19 shows that with this feedback configuration, it is possible to operate the laser over a 190nm range between 1920-2110nm. The linewidth of the source was not directly confirmed, but was estimated to be $\leq 0.2nm$ as it could not be resolved using the DongWoo Monochromator whose resolution limit is

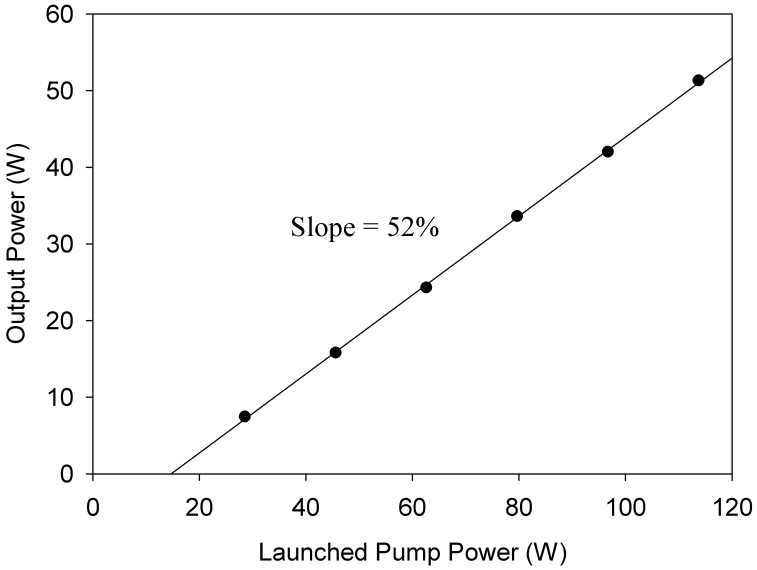

Figure 5.18: Output power at 1932nm as a function of launched pump power.

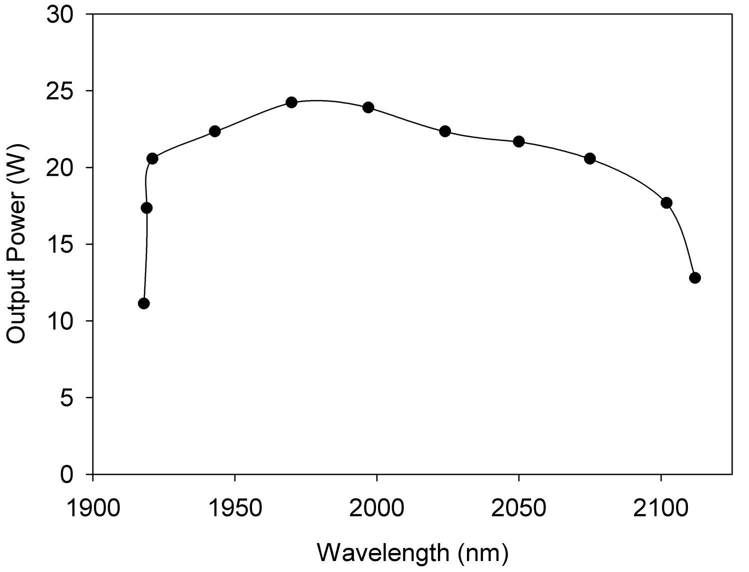

Figure 5.19: Output Power as a function of tuning wavelength for a launched pump power of 60W.

$\sim$0.2nm. This estimation supports the theoretical linewidth calculated using equation (5.12) of $\sim$0.2nm.

The output from this source was slightly astigmatic due to the $45^\circ$ mirror placed between the fibre and output collimating lens. This astigmatism can pose a problem for certain applications, but can be fairly easily resolved by either changing the pumping/collimating configuration (which was not an option in our case due to the lack in the availability of suitable optics) or, as is the case here, by optically correcting the astigmatism using an off axis spherical mirror [22]. This is achieved by rotating the spherical lens in the vertical axis so that the beam hits the mirror off axis, resulting in the horizontal focal length decreasing and the vertical focal length increasing with an increased mirror angle with respect to the input beam direction. Then by adjusting the angle of the mirror, the focal position for each axis can be selected so that with a single spherical lens the collimated beam is no longer astigmatic.

## 5.4 Cryogenically cooled Ho$^{3+}$:YAG laser oscillators

### 5.4.1 Introduction

As was outlined in Section 5.1, operating a solid-state laser at cryogenic temperatures has numerous benefits. These benefits increase the absorbed pump power required for thermal and stress induced effects to limit the output performance of the laser. As a result, cryogenic operation combined with a simple cavity design allows the output power of a laser system to be scaled beyond that achieveable at room temperature whilst maintaining an excellent output beam quality. This approach has been demonstrated in Yb$^{3+}$:YAG with a reported laser with a slope efficiency of 64%, resulting in over 300W of output power and an output beam propagation factor of $\sim$1.2 [23]. This section explores the potential for scaling the output powers of Ho:YAG via cryogenic cooling. This takes two routes. The first is for a free-running laser (i.e. with no wavelength selective cavity components, such that lasing occurs at the wavelength with the highest gain) with a simple 2 mirror cavity, highlighting the enhancements in slope efficiency and threshold conditions by reducing the crystal temperature from 300K to 77K. The second considers low quantum defect operation of a Ho:YAG laser, which is only achieveable at $LN_2$ temperature due to the changes in the temperature dependent Boltzmann distribution of the upper and lower laser manifolds, which results is a quasi 4-level mode of operation. This work on the low quantum defect laser was conducted by Dr Ji Won Kim and is only reviewed here to demonstrate this laser's potential for enhanced performance and further power scaling.

### 5.4.2 Cavity design

In this section, the design of laser resonators based on Gaussian beam optics is considered. A laser resonator mode is determined from the propagating radiation's interaction with any intra-cavity optics, and the boundary conditions established by the cavity mirrors. By considering the propagation of a Gaussian beam and its interaction with the cavity elements, the supported resonator modes can be predicted. The basic theory for these predictions are summarised by Kogelnik et al. [24]. The basic theory uses the description of a Gaussian beam given by the complex beam parameter $q$, such that $q$ is related to the two real beam parameters by

$$\frac{1}{q} = \frac{1}{R} - j\frac{\lambda}{\pi w^2} \tag{5.13}$$

where $w$ is the beam radius and $R$ is the radius of curvature of the wave front. Using the following standard ray transfer matrices for a thin lens of focal length $f$, and free-space propagation over distance $d$ through a medium with a refractive index of $n_d$, given by [24]

$$M_{lens} = \begin{pmatrix} 1 & 0 \\ -\frac{1}{f} & 1 \end{pmatrix}, M_{space} = \begin{pmatrix} 1 & \frac{d}{n_d} \\ 0 & 1 \end{pmatrix}, \tag{5.14}$$

the ABCD matrix for one cavity round trip can be calculated. By setting the boundary conditions such that the initial complex beam parameter is the same after one round trip, i.e.

$$\begin{pmatrix} A & B \\ C & D \end{pmatrix}_{cavity} \begin{pmatrix} w_i \\ w_i' \end{pmatrix} = \begin{pmatrix} w_i \\ w_i' \end{pmatrix}, \tag{5.15}$$

where the initial radius $w_i$ and initial slope $w_i' = w_i/R_i$, it can be shown that the complex parameter is given by

$$\frac{1}{q_i} = \frac{D-A}{2B}(\mp)j\frac{\sqrt{4-(A+D)^2}}{2B} \tag{5.16}$$

Therefore from equation (5.13), the initial values for $w$ and $R$ are given by

$$w_i{}^2 = \left(\frac{2\lambda B}{\pi}\right)\left(\sqrt{4-(A+D)^2}\right)^{-1} \tag{5.17}$$

and

$$R_i = \frac{2B}{D-A}. \tag{5.18}$$

An optical cavity can be considered as a periodic sequence of elements, and as such, it will be either stable or unstable. If the cavity is stable, the radiation is periodically refocused and contained. However, for an unstable cavity, the light will become more dispersed with every successive round trip. The impact of this is that an unstable cavity is very difficult to achieve lasing due to these dispersive losses. A cavity is deemed stable if it obeys

$$|(A+D)| < 2 \tag{5.19}$$

### 5.4.3 Free-running laser operation at 2097nm

#### 5.4.3.1 Set-up

These experiments used the same 5mm diameter by 30mm long 0.5at% Ho:YAG crystal used in the absorption measurements. The two mirror cavity used in these experiments can be seen in Figure 5.20. Due to the availability of suitably coated optics, and to allow for greater flexibility in selecting the output coupler reflectivity, a cavity consisting of two plane mirrors and a suitably AR coated lens was chosen. The two mirror cavity was folded using an additional input coupler (IC) mirror to facilitate the removal of any unabsorbed pump light, enabling the absorption efficiency to be calculated. As can be seen in the figure, a large part of the cavity design was dependent on the cryostat dimensions. For a low threshold condition, it is beneficial for the laser mode size to be small over the crystal length, and this is achieved by designing the cavity such that the crystal is within the Rayleigh range of the waist. Therefore, the IC mirror should be in close proximity to the crystal. To further reduce the threshold, the pump beam size should overlap with laser mode size. This has the added benefit that, as the pump power available is limited to low power, the small pump beam size in the crystal will reduce the pump power required before thermal effects begin to degrade the laser performance, therefore allowing the enhancements due to cryogenic cooling to be more easily demonstrated. With these requirements on the IC mirror and cryostat optics set, the only two adjustable parameters were the lens focal length and the spacings between the lens and the cryostat window ($d_1$) and the output coupler (OC) mirror ($d_2$). In order to keep the cavity length short and therefore more easy to align, the lens was selected to have a focal length of 100mm. For this cavity, the ABCD ray transfer matrix was calculated to enable the cavity stability condition to be determined, and therefore establish the limits on the values of $d_1$ and $d_2$.

As can be seen in Figure 5.21, the values of $d_1$ and $d_2$ in order to have a stable resonator are not particularly restrictive. Therefore, as previously discussed for a low threshold, the mode size in the crystal needs to be small, which is achieved by having the crystal within the Rayleigh range from the beam waist on the IC mirror. Furthermore, to make alignment easier it is advantageous to keep both lengths short, whilst maintaining a spacing that is practical in terms of the space required between the optics and their mounting especially considering the folded cavity. To fulfil these requirements, $d_1$ and $d_2$ were selected to be 40mm and 160mm respectively.

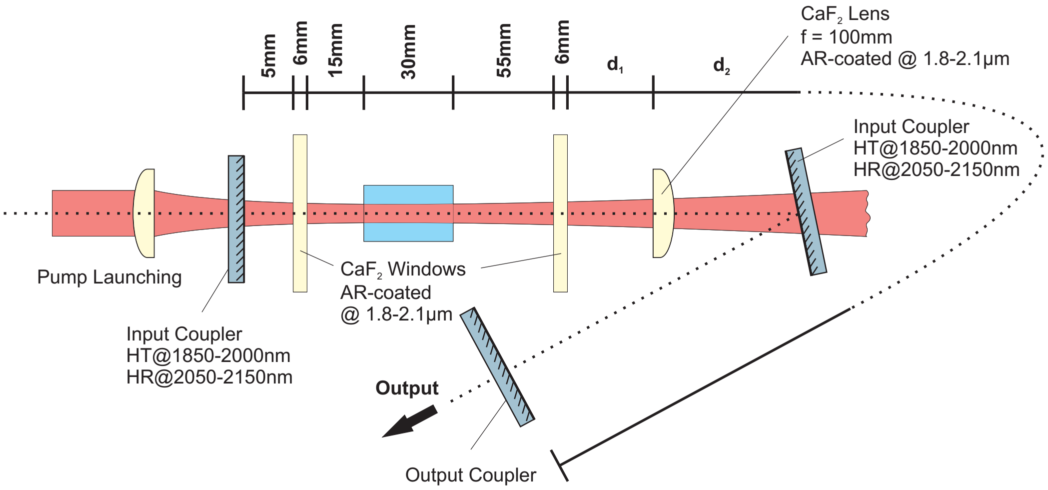

Figure 5.20: Schematic for the 2 mirror $Ho^{3+}$:YAG laser cavity used.

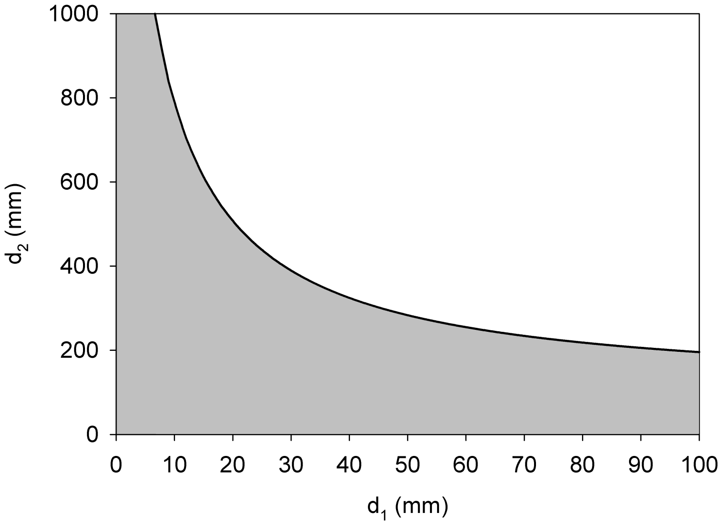

Figure 5.21: Stable cavity requirements for $d_1$ and $d_2$ where the shaded region represents a stable cavity condition.

To estimate the beam size inside the laser crystal, it was calculated using the round trip cavity ray transfer matrix at each position inside the cavity and inserting A,B,C and D into equation (5.17). The beam radius as a function of position in the cavity is shown in Figure 5.22.

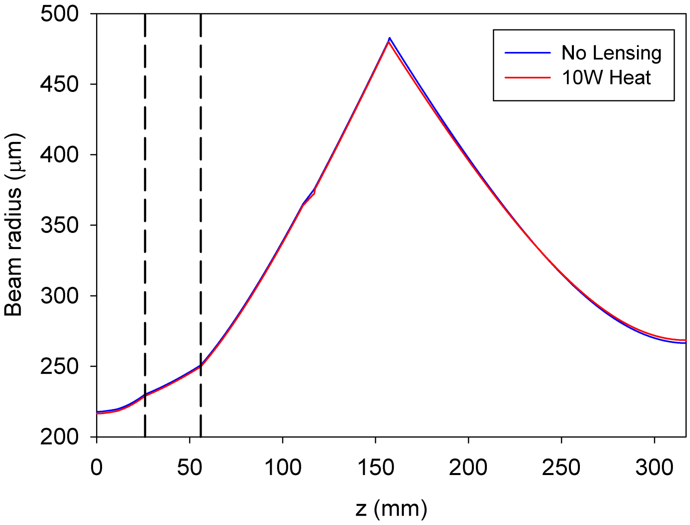

Figure 5.22: Showing the beam radius of the fundamental laser mode, as a function of position in the cavity from the input coupler mirror, where the hashed lines represent the end facets of the $Ho^{3+}$:YAG laser rod.

To observe the impact of thermal lensing, the beam radius inside the cavity was re-calculated to account for thermal lensing in the laser rod. By assuming the crystal is uniformly pumped and that the refractive index varies radially from the axis, such that

$$n = n_0 - \frac{1}{2}\eta r^2 \tag{5.20}$$

then the ray transfer matrix for the laser rod is given by [24,25]

$$M = \begin{pmatrix} \cos b & (\sqrt{n_0\eta})^{-1}\sin b \\ -\sqrt{n_0\eta}\sin b & \cos b \end{pmatrix} \tag{5.21}$$

where $b = L\sqrt{\eta/n_0}$ and $\eta$ is given by

$$\eta = \frac{dn}{dT}\frac{P_{hT}}{2\pi r_0^2 Lk} \tag{5.22}$$

where $P_{hT}$ is the total heat dissipated in the rod, $r_0$ is the rod radius and $L$ is the rod length. Using this ray transfer matrix, the beam radius as a function of position inside the laser cavity was calculated as shown in Figure 5.22. For this calculation, the rod dimensions were $r_0$=2.5mm and $L$=30mm, and the values for the thermal properties of YAG at room temperature were taken as $k$=11.2 W/m.K and $dn/dT$=7.8×10$^{-6}$K$^{-1}$ [1]. The power dissipated as heat was calculated by assuming that the fraction of the absorbed pump power converted to heat is given by the quantum defect (i.e. $1-\frac{\nu_L}{\nu_p}$), such that for the pump source used $P_{hT}$=10W. It can be seen from the figure that for both situations, the laser mode size was <250$\mu m$ in the crystal, and that at the available pump power, thermal lensing will not significantly change the laser mode size.

The pump beam was aligned with the crystal axis using two beam steering mirrors shown in Figure 5.23. One of these mirrors had an ~10% transmission at 1932nm to enable the incident pump power to be determined. In order to obtain a good laser performance, the pump radius is required to be approximately the same as the laser mode. The launched pump beam waist was measured to be ~210$\mu m$, with a Rayleigh range of ~60mm at 1932nm. This implies that for the calculations in the next section, the pump beam size can be assumed to be approximately constant over the crystal length.

#### 5.4.3.2 Results and analysis

Initially, the Ho:YAG laser performance was characterised at room temperature in preparation for comparison with the expected performance enhancement due to reduced crystal temperature. Using a 10% Transmitting output coupler, the laser produced 8.3W of output for 29.8W of absorbed pump power, corresponding to a slope efficiency of ~31%, as seen in Figure 5.24. The threshold was measured to be 2.4W of absorbed pump power by observing the onset of relaxation oscillations. The laser emitted at 2097nm with a beam propaga-

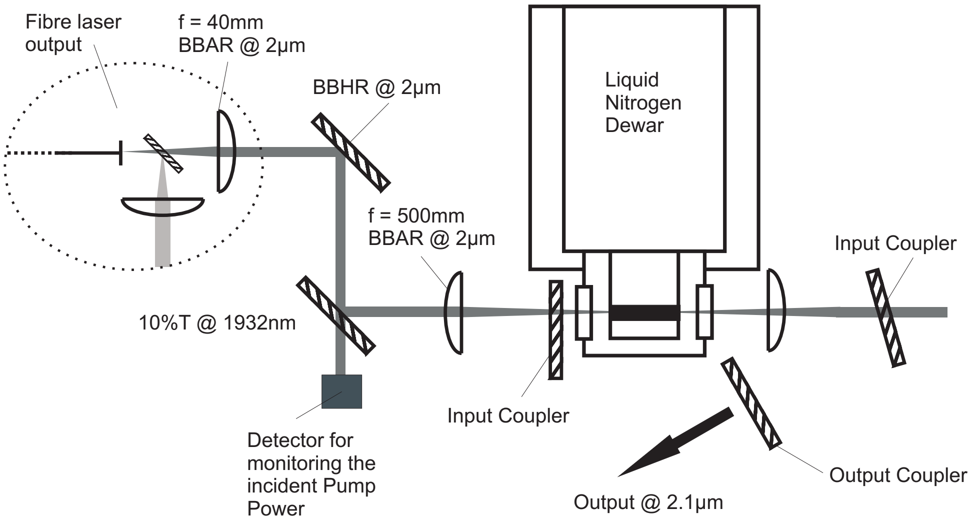

Figure 5.23: A schematic of the pump launching arrangement for the Ho:YAG laser cavity.

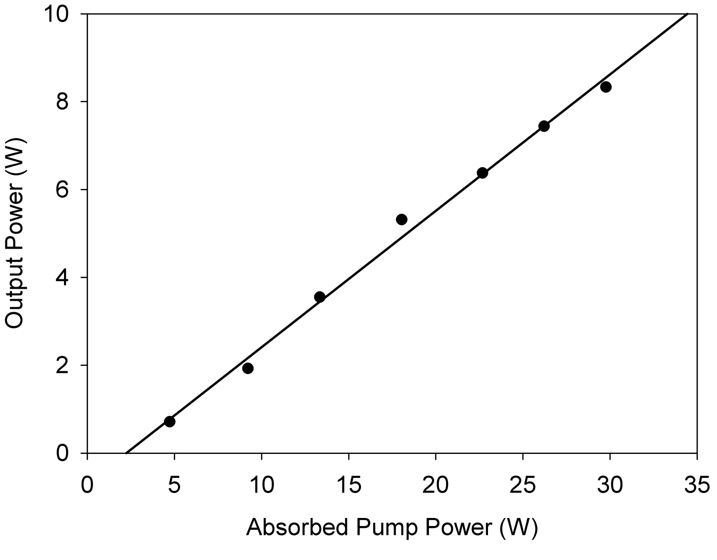

Figure 5.24: Output power as a function of absorbed pump power at room temperature, for a 10% transmitting output coupler.

tion factor of $M^2$ ~1.1. The reason for the poor slope efficiency is that the cavity losses are much higher than expected. To establish the source of these unexpected losses, the fibre laser pump source was tuned to ~2.1$\mu m$ and used to measure the transmission losses through each of the cavity optics. The findings were that the OC transmission was actually 8.2% and the losses from the IC were negligible. However, the loss due to the cryostat's windows and Ho:YAG crystal were measured to be ~8.5%. The crystal losses were measured at $LN_2$ temperature so there would be no absorption losses. Inspecting the Ho:YAG crystal's end faces, it became apparent that the coating had become degraded. It is therefore likely that the measured losses were due to scattering of the incident light from the coating surfaces. Considering these losses, the theoretical laser slope efficiency (from equation (2.3)) was calculated to be ~33% using $\eta_{abs}$ as 74% (measured as 81% but corrected for the scattering losses through the crystal), and $\eta_q$=1. It stands to reason that if the cavity losses were reduced to, for example a <0.1% reflection loss from each optical surface, such that the total loss was <2%, the slope efficiency would be >55%. This is still lower than some slope efficiencies quoted in the literature, due to the cavity losses still being too high because of the large number of optical surfaces in the cavity, combined with the fairly low absorption efficiency.

The absorbed threshold pump power for this laser configuration was measured to be 2.4W. The theoretical value is calculated to be 0.95W (using $w_L$ = 240$\mu m$, $w_P$ = 210$\mu m$, $N = 0.69 \times 10^{20} cm^{-3}$, $\sigma_a = 0.174 \times 10^{-20} cm^2$ [9], $\sigma_e = 1.14 \times 10^{-20} cm^2$ [9], $\tau_f = 8ms$). This difference between the measured and predicted threshold suggests that the laser is performing as expected.

Due to the unavailability of other Ho:YAG rods, this crystal had to be used to observe any enhancements in performance due to a reduction in the crystal temperature. However, by accounting for the known background losses due to the crystal surface, the results measured can still be used to estimate the performance that would be observed in the case where the crystal coatings were ideal and therefore the background losses were considerably reduced. Of particular interest was the laser threshold and the output beam quality. The dependence on the threshold condition due to temperature is shown in Figure 5.25. It can be seen that there is a significant decrease in the threshold with decreased temperature, such that at 296°K the threshold was 2.4W compared to 0.2W at 87°K. This is due to the laser moving from quasi-3-level to quasi-4-level operation. Plotted in the figure is the population of the low laser level as a function of temperature, calculated using the Boltzmann distribution

$$f = \frac{\exp\left(-\frac{\Delta E}{k_b T}\right)}{\sum_i \exp\left(-\frac{\Delta E_i}{k_b T}\right)} \tag{5.23}$$

where $\Delta E$ is the energy difference between the laser level and the lowest lying level within the Stark manifold, and $\Delta E_i$ is the energy separation of the $i^{th}$ level from the lowest energy level within the manifold. For the fractional population calculations, the energy levels used were given in Walsh et al [9], where for the 2097nm transition, the energy difference is 534.7cm$^{-1}$ from the ground state. This shows that the population of the lower laser level decreases with a decrease in the crystal temperature. This is significant as the energy level population factor governs the effective absorption cross-section (where $\sigma_a \propto f$) such that the signal re-absorption is reduced with a decrease in temperature. Given the definition of the absorbed threshold pump power in equation (2.1), it can be seen that reducing the signal re-absorption will also reduce the laser threshold condition. This reduction in the absorption cross section is shown spectroscopically by Walsh et al., where for $\lambda >$1980nm, the absorption cross-section becomes effectively zero below 125K [9]. Also shown in Figure 5.25 is the impact of the pump absorption efficiency plotted as $1/\eta_{abs}$ due to its inverse relationship with threshold. The significance of this is that the increase in the absorption cross-section with reduced temperature means that it is easier to reach a population inversion and thus the laser threshold. The increase in absorption is due to the beneficial changes in the pump energy level populations and the increase in the pump absorption cross-section, as shown in Figure 5.9.

The measurement of the beam propagation factor as a function of temperature showed no discernable change with decreased crystal temperature. It was expected that due to a reduction in thermal lensing, caused by the improvements in the thermo-optic properties with decreased temperature (as discussed in the

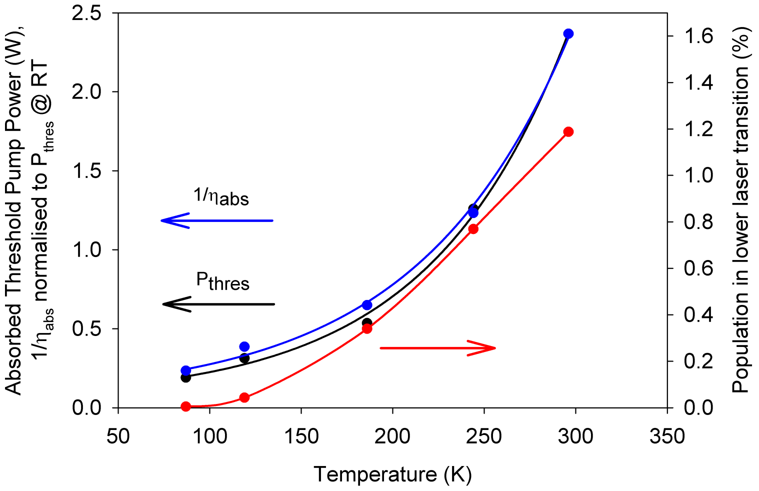

Figure 5.25: Threshold dependence on Ho:YAG crystal temperature for a 10% transmitting output coupler, with the population of the lower laser level and $1/\eta_{abs}$ normalised to the threshold power at room tempertaure.

introduction section), the beam quality would improve. However, the beam propagation factor at room temperature was already $M^2$ <1.1 and therefore was not thermally degraded. For these experiments, the operation power levels were low, suggesting that with an increased pump power the impact of thermal degradation to the beam will be increased and then the benefits of cryogenically cooling will become more apparent.

In addition to measuring the beam propagation factor and threshold as a function of temperature, the output power for a fixed incident pump power was measured. Figure 5.26 shows that the output power increases as the crystal temperature decreases due to the absorption efficiency increasing and the threshold pump power decreasing.

Given that the slope efficiency is proportional to $\frac{T\sqrt{1-L}}{T\sqrt{1-L}+L\sqrt{1-T}}$ [26], it follows that to achieve higher slope efficiencies at cryogenic temperatures with the current cavity losses, a higher output coupler would be required. The effect of the output coupler on the output power is shown in Figure 5.27 for the three suitable output couplers available. The slope efficiency obtained for each output

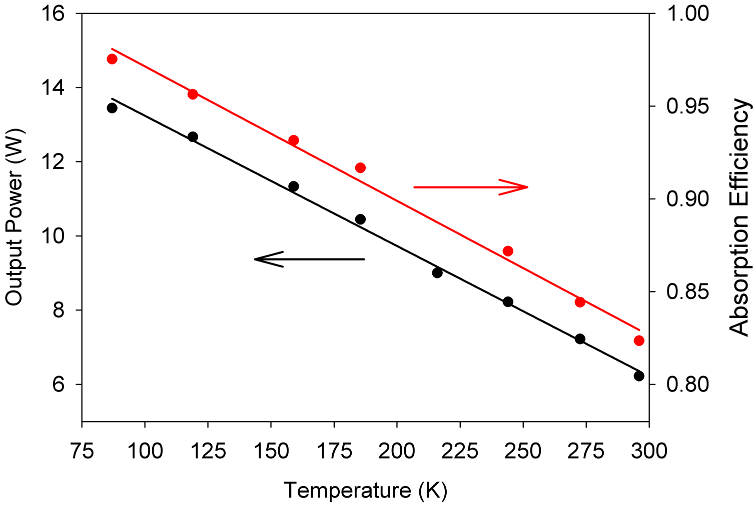

Figure 5.26: Output power as a function of temperature for 26.8W of incident pump power with a 10% transmitting output coupler.

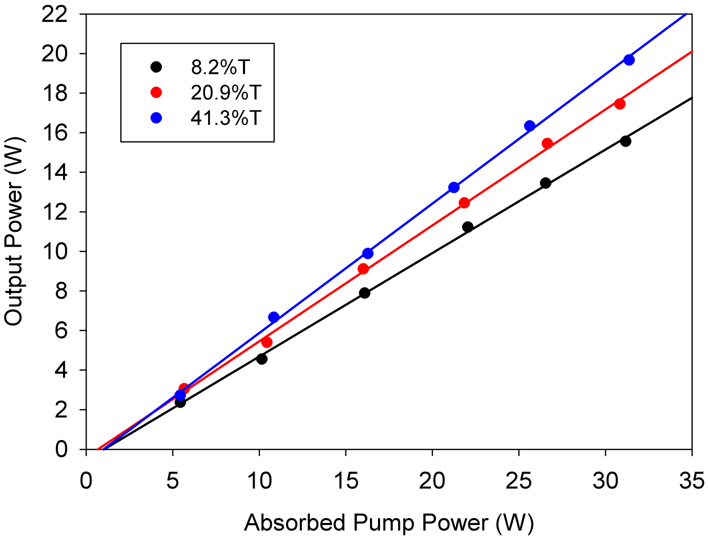

Figure 5.27: Showing the output power as a function of the absorbed pump power for different output coupler mirror transmissions at $LN_2$ Temperature.

coupler was 52.3%, 58.6%, and 65.4% for an output coupler transmission of 8.2%, 20.9% and 41.3%, respectively. As was the case at room temperature, the measured slope efficiency is very close to that predicted by the theory, such that the theoretical slope efficiency is ∼68% for the 41.3% OC mirror, assuming that $\eta_{abs}$=0.89 (corrected from the measured value of 97%). Furthermore, if the crystal losses were reduced to <2% again, at these cryogenic temperatures the slope efficiency should be >80%.

To further demonstrate the enhancement in the thermo-optic properties with reduced temperature, the cavity was operated in a polarised configuration. From this, the depolarisation loss can be determined as a function of crystal temperature. This was achieved by inserting a YAG plate at Brewster's angle ($\theta_B = \arctan{(n_2/n_1)}$, so in this case $\theta_B \approx 61°$) in between the focusing lens and the 8.2%T OC mirror in the original cavity design shown in Figure 5.20. The power reflected from the Brewster plate in the forward and backward beam directions was monitored to determine the total loss. The depolarisation loss was calculated as

$$L_{depol} = \frac{P_{depol}}{\frac{P_{out}}{T_{OC}} + P_{depol}} \tag{5.24}$$

where $T_{OC}$ is the output coupler transmission, $P_{out}$ is the laser output power, and $P_{depol}$ is the total power lost from the Brewster plate. The de-polarisation loss and output performance of the polarised cavity can be seen in Figure 5.28. It shows that above an absorbed pump power of around 15W, the output power begins to roll-over due to increased de-polarisation losses. When the measured value of the de-polarsiation is compared to other reported Ho:YAG lasers, it shows that our value is an order of magnitude larger [27]. This suggests that our crystal may have some residual stress caused by the mounting arrangement.

Equation (5.3) used in the chapter introduction to calculate the de-polarisation loss in a rod is only strictly valid for 'top-hat' pump beam profiles. That is not the case here as the pump beam has a Gaussian intensity beam profile.

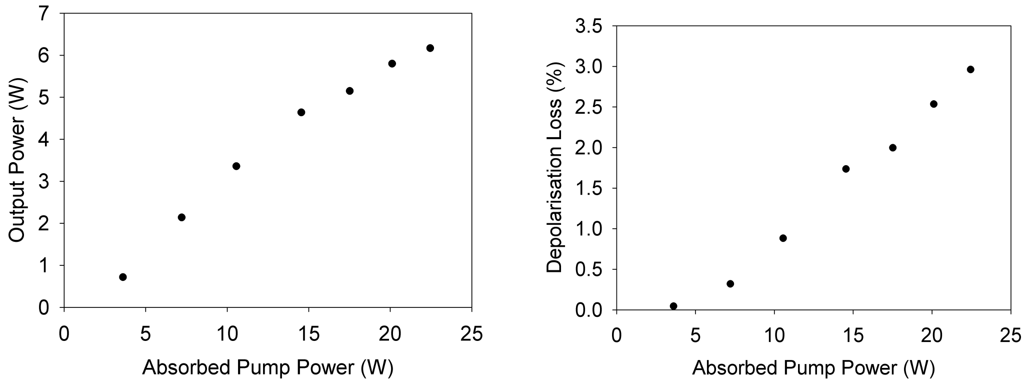

(a) (b)

Figure 5.28: Showing (a) the output performance in a polarised laser cavity configuration, and (b) the de-polarisation loss as a function of absorbed pump power, for room temperature operation.

Assuming that $w_l/w_p < 1$, the de-polarisation loss for a Gaussian pump beam can be approximated to [7]

$$L_d \approx \frac{1}{4}\left[1 - \frac{1}{C_T P_{hT}\left(\frac{w_l}{w_p}\right)^2}\right]^{-1} \tag{5.25}$$

Using this equation, the de-polarisation loss for this cavity can be estimated. At room temperature (300K), using the values for $\alpha = 6.14 \times 10^{-6}K^{-1}$ [1], $k = 8.6W/m.K$ (for 2at%Yb:YAG) [1], $n_0 = 1.833$, $C_B = -0.0099$ (for Nd:YAG) [8], $w_l = 240\mu m$, $w_p = 210\mu m$ and $P_{hT} = 22W$, the de-polarisation loss is approximately 15%. This is larger than our measured values due to the estimations for the values used in the calculations and that the approximation that $w_l/w_p < 1$ is not valid, although this should not have a significant impact as Fluck et. al. [7] show that equation (5.25) still serves as a reasonable approximation even for $w_l = w_p$. However, by using the values for 100K, the reduction in the de-polarisation loss can be approximated. Using the same values for $C_B$, $n_0$, $w_{l,p}$ and $P_{hT}$, and using the 100K values $\alpha = 1.95 \times 10^{-6}K^{-1}$ [1], $k = 33.8W/m.K$ (for 2at%Yb:YAG) [1] gives an approximate depolarisation loss of <0.25%. Therefore, it is reasonable to assume that the measured depolarisation losses will become negligible when the crystal temperature is reduced. However, in practice at $LN_2$ temperature, the depolarisation loss was approximately the same over the measured absorbed powers. This suggested that although the thermally induced de-polarisation losses are reduced, those caused by mechanical stress have increased. This mechanical stress is caused by the differential expansion and contraction coefficients for the crystal and crystal housing, with a result that the laser rod can be pinched by the mount, inducing high levels of stress and thus birefringence.

For improved performance, and to measure the thermally induced depolarisation losses, this mechanical stress needs to be removed. The easiest way to achieve this would be to change the crystal to a slab geometry which is mounted on the two large faces, so that the induced stress has only one component perpendicular to the mounted edge. Therefore, the mechanically induced birefringent axis can be aligned with the polariser removing its impact on the depolarisation losses.

### 5.4.4 Low quantum defect $Ho^{3+}$:YAG laser

An additional benefit to cryogenically cooled solid state lasers is that they allow for very low quantum defect operation. The benefits of operating in the low quantum defect regime are two-fold. Firstly, the slope efficiency is increased for lower quantum defects, therefore enhancing laser performance. Secondly, a low quantum defect means less pump power is converted to heat, therefore reducing detrimental thermal effects in the laser. However, the small separation in energy between the pump and signal photons and therefore the small difference in the ground state populations means that for low quantum defect operation, it is more difficult to achieve a population inversion. Therefore, as the quantum defect is reduced; the laser threshold is increased. As such, very low quantum defect operation can be difficult to achieve due to the correspondingly high threshold condition. In practice, it is often desirable to maximise the laser output efficiency, such that the quantum defect is selected to balance the enhancements due to a low quantum defect with the lower laser threshold for high quantum defects.

Low quantum defect operation has been documented for Er:$Sc_2O_3$ where at 77K, the laser operated at 1558nm when pumped at 1535nm with a quantum defect of 1.5% [28]. In this section, work conducted by Dr. Ji Won Kim will be briefly discussed to highlight the potential of low quantum defect operation in cryogenically cooled Ho:YAG lasers.

#### 5.4.4.1 Experimental procedure

The setup used in these experiments is shown in Figure 5.29. The fibre laser pump source used was the same as for the linear Ho:YAG laser cavity, with the astigmatic output corrected using a curved mirror to achieve a better signal to pump overlap inside the Ho:YAG crystal. The alignment of the cavity was conducted at $LN_2$ temperature, with the non-collinear cavity operated as both a free-running 2097nm laser and a low quantum defect laser at 1970nm. For low quantum defect operation, the 2097nm laser emission was suppressed using an intra-cavity mirror with high reflectance at 2097nm and a high transmission for 1970nm. A non-collinear cavity design was applied due to lack of suitably coated optics to allow a simple 2 mirror linear cavity to be used.

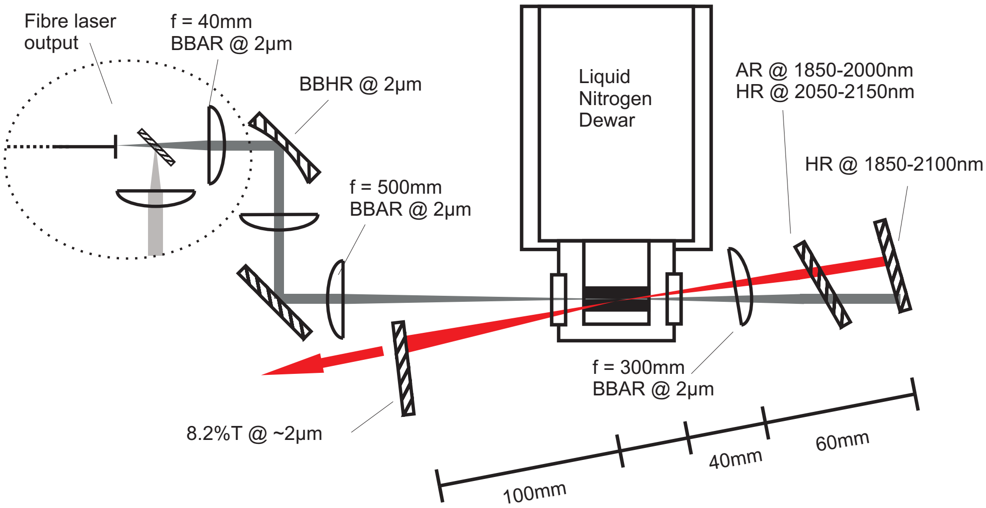

Figure 5.29: Experimental setup for the non-collinear Ho:YAG laser cavity.

#### 5.4.4.2 Results and analysis

The non-collinear laser cavity was initially operated without the intra-cavity mirror for removing the 2.1$\mu m$ emission. The output performance for this mode of operation can be seen in Figure 5.30. The slope efficiency obtained was 49% with respect to incident power. It can be assumed that the absorption efficiency for the single pass was >95% and thus the total absorbed power is similar to that achieved in the collinear cavity. The absorbed threshold pump power was measured by extrapolation to be ∼0.7W. Comparing this result to the collinear cavity, it can be seen that the slope efficiency is lower and the threshold higher than for the non-collinear cavity. However, given the degradation of the Ho:YAG crystals coatings, not much can be inferred from this, as the beam path through the crystal was changed, thus changing the potential coating losses.

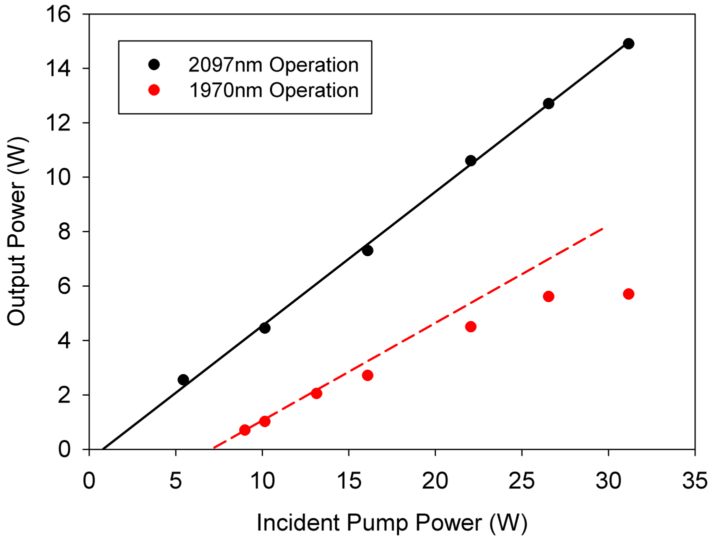

Figure 5.30: Showing the output performance for the non-collinear cavity operated in a free-running laser at 2097nm (black) and a low quantum defect laser operating at 1970nm (red).

For the low quantum defect operation, any oscillation at 2.1$\mu m$ was suppressed using the intra-cavity mirror as shown in Figure 5.29. In this configuration, lasing at 1970nm was obtained, corresponding to a quantum defect of only 1.9%.

As shown in Figure 5.30, the output power begins to roll-over for incident pump powers above 15W. This roll-over is due to signal absorption losses in the UV fused silica intra-cavity mirror. This absorption loss impacts the performance by increasing the cavity losses, thereby reducing the slope efficiency and increasing the threshold, as can be seen from equations (2.1) and (2.3). The slope before the roll-over was $\sim$33%. In order for the potential of this approach to be achieved, these cavity losses must be addressed, as was the case for the collinear cavity previously discussed. The most desirable approach for reducing the cavity losses would be to use a Brewster cut crystal combined with cavity windows that are also at Brewster's angle. This would effectively remove the coating losses on the crystal face, and limit the potential coating damage caused by the low temperatures and high vacuum for future crystals. In addition, suitably coated cavity mirrors need to be used to facilitate suppression of the 2.1$\mu m$ emission, without the use of an intra-cavity mirror. Additionally, the substrates used for all of the optical elements need to have a high transmission in the 2$\mu m$ region by using materials such as ZeSn, Infrasil, or $CaF_2$. This has the potential of making the total cavity losses $<$1%, with the slight limitation of requiring a polarised pump source.

If these cavity losses were reduced to more reasonable levels as suggested, then this approach has the potential for obtaining slope efficiencies in excess of 90%, with an absorbed threshold pump power of less than 0.3W, based on the results for the $LN_2$ collinear cavity shown in Figure 5.25. Considering the current maximum output power from Tm-doped fibre lasers of approximately 900W [29] unpolarised, the maximum output power in the low quantum defect laser could exceed $\sim$400W (assuming $P_{pump} \sim$ 450W polarised), assuming negligible degradation to the laser performance caused by thermal effects at these power levels.

### 5.4.5 Conclusions

The work described on Ho:YAG lasers shows the potential benefits from operating at cryogenic temperatures. Although the measured laser performance itself was poor, the gains demonstrated by cooling the laser crystal from room temperature to liquid nitrogen temperature demonstrate the laser's potential for power scaling.

In these experiments, the major limiting factor was scattering loss due to coating damage on the crystal's end faces. These were measured to be $\sim$8.5% at 2.1$\mu m$. The very high cavity loss caused a decrease in the slope efficiency and an increase in the threshold, thus significantly reducing the output performance. However, by accounting for these losses, the results can be used to predict the performance in a much lower cavity loss configuration. In the case where the total cavity loss was <2%, the output slope efficiency for a 10% output coupler would be >85% and >90% for a free running laser operating at 2097nm and a low quantum defect laser operating at 1970nm, respectively. This coupled with the absorbed threshold pump power reducing to less than a few hundred milliwatt at $LN_2$ temperatures, means that highly efficient laser sources should be produced.

Due to the high cavity losses, only relatively low pumping powers were used. As a result, the heat deposition density in the crystal remained small so that performance was not limited by thermal effects. Therefore, the temperature dependence of these effects could not be observed to test the performance enhancements predicted in the introduction. In order to fully appreciate the benefits of cryogenically cooled solid-state lasers, the pump power needs to be increased. With an increased pump power, the reduction in the thermal effects with temperature should be observed due to the higher thermal loading. Furthermore, at cryogenic temperatures, the impact of thermal effects should be greatly reduced, enabling the laser output to be potentially scaled to hundreds of watts of output power.

## 5.5 Summary

The main motivation for operating at cryogenic temperatures is the enhancement in the thermo-optic properties of the laser material, which reduce the thermal effects that have a detrimental impact on laser performance. The most significant of these thermal effects is thermal lensing, followed in polarised cavity configurations by depolarisation losses caused by stress induced birefringence. It was predicted using thermo-optic parameters from the literature [1–4], that by reducing the crystal temperature in YAG from 300K to 100K, the heat deposition density required to cause the same induced thermal lens or depolarisation loss is a factor of 13 times larger at 100K than the 300K thermal load. This means that the output power before these effects begin to limit the performance can also be scaled by at least the same factor. Another benefit of operating at cryogenic temperatures is that the populations of the energy levels in the upper and lower laser manifolds is changed according to the Boltzmann distribution. This allows for efficient in-band pumping and laser operation with a very low quantum defect. The benefits of this are two fold. The first is that the heat deposited into the material via quantum defect heating is reduced, further increasing the incident pump powers required for thermal effects to limit the performance. The second is that the output slope efficiency will be higher with a small quantum defect due to the $\nu_p/\nu_L$ dependence in the slope efficiency.

In this chapter, these performance enhancements with temperature were explored. The first part of the analysis was conducted in measuring the spectroscopic changes in Ho:YAG with temperature, as this would affect the required pump parameters. The literature [11, 12] showed that the transition linewidths and position were both temperature dependent. In order to measure these changes, the absorption spectrum in Ho:YAG was measured using an amplified spontaneous emission probe and monochromator with a resolution limit of 0.2nm. The results showed that the most suitable absorption peak was at 1932nm for low quantum defect operation, due to it being one of the longest wavelength absorption features that still had a relatively high absorption cross-section. At liquid nitrogen temperature, the bandwidth (FWHM) was ∼0.4nm. Therefore, the pump source for the Ho:YAG laser ideally needed an output linewidth of less than this for a good overlap and therefore, high absorption efficiency. The pump source used was a Tm-doped cladding pumped silica fibre laser with an external feedback cavity to control the laser linewidth and wavelength. The output had a linewidth of <0.2nm (as it was below the resolution limit of our monochromator).

This pump source was then used to in-band pump the Ho:YAG in two cavity configurations. The first was a simple 2-mirror collinear cavity operating at 2097nm, and the second was a low quantum defect 1.9% laser operating at 1970nm using a non-collinear cavity design. Experiments using the collinear cavity showed the enhancement in the output power with temperature for a fixed incident pump power. This was due to an increase in the pump absorption cross section and therefore the absorption efficiency, which increased the slope efficiency and decreased the threshold condition. Furthermore, the threshold was reduced due to the operating regime moving from a 3-level to quasi 4 level regime as a result of the changes in the population distribution in the laser manifolds, resulting in a reduction in the signal reabsorption losses and an increase in the emission cross section. However, the output performance was limited by high cavity losses, which were measured to be 8.5% at 2.1$\mu m$. This loss was due to damaged coatings on the rod's end faces. As a result, the maximum slope efficiency achieved was 65% for a 41% output coupler at liquid nitrogen temperature, corresponding to a maximum output power of 20W.

The collinear cavity was also used to highlight the improvement in the thermal lensing and stress induced birefringence with temperature. Due to the high cavity loss and subsequent poor performance, the pump powers used were limited to <30W. As a result, there was no measurable degradation in the beam propagation factor at room temperature, with the output beam propagation factor measured to be $M^2$ <1.1, and therefore, there was no change when the temperature was decreased. For observing any changes in the depolarisation loss, the cavity was operated in a polarised configuration with a brewster plate inserted. The results showed no change in depolarisation loss from room temperature to liquid nitrogen temperature. This is believed to be caused by the mechanical stress on the crystal from the mount increasing with decreased temperature due to differences in the expansion coefficients of the materials. The increased mechanical stress therefore counteracted any benefits that should be observed due to changes in the thermo-optic properties of the crystal.

In the non-collinear cavity, laser operation was achieved at 1970nm, corresponding to a quantum defect of 1.9%. As was the case with the collinear cavity, the high losses limited the measured performance of this system. These losses were exacerbated by absorption losses in the substrate of the cavity mirror inserted to suppress emission at 2097nm. Due to these losses, at higher powers the output began to roll-over. For low powers (<15W of output), the slope efficiency was measured to be only 33%.

In both cavity configurations, the main limitation on performance was the losses due to the crystal coatings. If these were reduced to acceptable levels, such that the total cavity losses were <2%, the predicted slope efficiency for both configurations with a 10% output coupler would be 85% and 90% for the linear and collinear cavities, respectively. Furthermore, with suitable optics, the low quantum defect operation would not require the more complicated non-collinear cavity design because emission at 2097nm could be suppressed by insertion of a suitable optic with negligible losses at 1970nm.

For future power scaling, the first requirement would be to use higher quality coatings on all cavity optics with suitably transparent substrates in the $2\mu m$ region. Furthermore, due to the neccessity of having the crystal mounting in a cryostat with optical ports, thus increasing the number of optical surfaces and the potential cavity losses, it would be advantageous to use a brewster cut crystal with the ports also at brewster's angle. This would reduce the losses from these surfaces to effectively zero in the correct polarisation and remove the requirement for durable coatings for the crystal that can withstand the extremes in temperature and pressure. The impact of using a brewster cut crystal is that the crystal geometry would need changing as the polarised signal would be affected by the depolarisation losses caused by the mechanical stresses in a rod geometry. Therefore, the more suitable geometry would be a slab mounted on the large faces such that any mechanical stress would occur in one direction and therefore the refractive index change can be selected to align with the cavity polarisation direction.

In order to explore the limits in the cryogenic laser, the pump power needs to be significantly increased. This would mean that for room temperature operation, thermal effects should limit the performance and the predicted changes with temperature should be observed. Given the current output power from Tm-doped silica fibres of ∼900W [29] of un-polarised light, it stands to reason that using the slope efficiencies calculated earlier, the output powers in cryogenically cooled Ho:YAG could potentially be scaled to >750W, depending on the impact of any thermal effects.

## 5.6 References

[1] **Aggarwal, R. L., Ripin, D. J., Ochoa, J. R.** and **Fan, T. Y.**, *Measurement of thermo-optic properties of* $Y_3Al_5O_12$, $Lu_3Al_5O_12$, $YAlO_3$, $LiYF_4$, $LiLuF_4$, $BaY_2F_8$, $KGd(WO_4)_2$, *and* $KY(WO_4)_2$ *laser crystals in the* 80-300*K temperature range*, Journal of Apllied Physics, Vol. 98, No. 10, pp. 103514–1–103514–14, Novemeber 2005.

[2] **Klein, P. H.** and **Croft, W. J.**, *Thermal conductivity, diffusivity, and expansion of* $Y_2O_3$, $Y_3Al_5O_12$, *and* $LaF_3$ *in the range 77°-300°K*, Journal of Applied Physics, Vol. 38, No. 4, pp. 1603–1607, March 1967.

[3] **Fan, T. Y.** and **Daneu, J. L.**, *Thermal coefficients of the optical path length and refractive index in YAG*, Applied Optics, Vol. 37, No. 9, pp. 1635–1637, March 1998.

[4] **Wynne, R., Daneu, J. L.** and **Fan, T. Y.**, *Thermal coefficients of expansion and refractive index in YAG*, Applied Optics, Vol. 38, No. 15, pp. 3282–3284, May 1999.

[5] **Siegman, A. E.**, *Analysis of laser beam quality degradation caused by quartic phase aberrations*, Applied Optics, Vol. 32, No. 30, pp. 5893–5901, October 1993.

[6] **Clarkson, W. A.**, *Thermal effects and their mitigation in end-pumped solid-state lasers*, Journal of Physics D: Applied Physics, Vol. 34, No. 16, pp. 2381, August 2001.

[7] **Fluck, R., Hermann, M. R.** and **Hackel, L. A.**, *Birefringence compensation in single solid-state rods*, Applied Physics Letters, Vol. 76, No. 12, pp. 1513–1515, March 2000.

[8] **Koechner, W.**, Solid-State Laser Engineering, Springer, New York, 6th edn., 2006.

[9] **Walsh, B. M., Grew, G. W.** and **Barnes, N. P.**, *Energy levels and intensity parameters of* $Ho^{3+}$ *ions in* $Y_3Al_5O_12$ *and* $Lu_3Al_5O_12$, Journal of Physics and Chemistry of Solids, Vol. 67, No. 7, pp. 1567–1582, July 2006.

[10] **McCumber, D. E.** and **Sturge, M. D.**, *Linewdith and temperature shift of the R lines in ruby*, Journal of Applied Physics, Vol. 34, No. 6, pp. 1682–1684, June 1963.

[11] **Kushida, T.**, *Linewidths and thermal shifts of spectral lines in Neodymium-doped Yttrium Aluminium Garnet and Calcium Fluorophosphate*, Physical Review, Vol. 185, No. 2, pp. 500–508, September 1969.

[12] **Beghi, M. G., Bottani, C. E.** and **Russo, V.**, *Debye temperature of Erbium-doped Yttrium Aluminium Garnet from luminescence and Brillouin Scattering data*, Journal of Applied Physics, Vol. 87, No. 4, pp. 1769–1774, February 2000.

[13] **Eichhorn, M., Fredrich-Thornton, S. T., Heumann, E.** and **Huber, G.**, *Spectroscopic properties of* $Er^{3+}$*:YAG at 300-550K and their effects on the 1.6μmlaser transitions*, Applied Physics B, Vol. 91, No. 2, pp. 249–256, May 2008.

[14] **Clarkson, W. A.**, **Barnes, N. P.**, **Turner, P. W.**, **Nilsson, J.** and **Hanna, D. C.**, *High-power cladding-pumped Tm-doped silica fiber laser with wavelength tuning from 1860 to 2090nm*, Optics Letters, Vol. 27, No. 22, pp. 1989–1991, November 2002.

[15] **Rothman, L. S.**, **Gordon, I. E.**, **Barbe, A.**, **Benner, D. C.**, **Bernath, P. F.**, **Birk, M.**, **Boudon, V.**, **Brown, L. R.**, **Campargue, A.**, **Champion, J. P.**, **Chance, K.**, **Coudert, L. H.**, **Danaj, V.**, **Devi, V. M.**, **Fally, S.**, **Flaud, J. M.**, **Gamache, R. R.**, **Goldmanm, A.**, **Jacquemart, D.**, **Kleiner, I.**, **Lacome, N.**, **Lafferty, W. J.**, **Mandin, J. Y.**, **Massie, S. T.**, **Mikhailenko, S. N.**, **Miller, C. E.**, **Moazzen-Ahmadi, N.**, **Naumenko, O. V.**, **Nikitin, A. V.**, **Orphal, J.**, **Perevalov, V. I.**, **Perrin, A.**, **Predoi-Cross, A.**, **Rinsland, C. P.**, **Rotger, M.**, **Šimečková, M.**, **Smith, M. A. H.**, **Sung, K.**, **Tashkun, S. A.**, **Tennyson, J.**, **Toth, R. A.**, **Vandaele, A. C.** and **VanderAuwera, J.**, *The HITRAN 2008 molecular spectroscopic database*, Journal of Quantitative Spectroscopy & Radiative Transfer, Vol. 110, No. 9-10, pp. 533–572, June-July 2009.

[16] **Jenssen, H. P.**, **Linz, A.**, **Leavitt, R. P.**, **Morrison, C. A.** and **Wortman, D. E.**, *Analysis of the optical spectrum of* $Tm^{3}+$ *in* $LiYF_4$, Physical Review B, Vol. 11, No. 1, pp. 92–101, January 1975.

[17] **Meschede, D.**, Optics, Light and Lasers, Wiley-VCH, 2004.

[18] **Pedrotti, F. L.** and **Pedrotti, L. S.**, Introduction to Optics, Prentice-Hall, 2nd edn., 1993.

[19] **Agger, S.**, **Povlsen, J. H.** and **Varming, P.**, *Single-frequency thulium-doped distributed-feedback fiber laser*, Optics Letters, Vol. 29, No. 13, pp. 1503–1505, July 2004.

[20] **Jackson, S. D.** and **King, T. A.**, *Theoretical modeling of tm-doped silica fiber lasers*, Journal of Lightwave Technology, Vol. 17, No. 5, pp. 948–956, May 1999.

[21] **Engelbrecht, M., Haxsen, F., Wandt, D.** and **Kracht, D.**, *Wavelength resolved intracavity measurement of the cross sections of a Tm-doped fiber*, Optics Express, Vol. 16, No. 3, pp. 1610–1615, February 2008.

[22] **Repasky, K. S., Brasseur, J. K., Wessel, J. G.** and **Carlsten, J. L.**, *Correcting an astigmatic, non-Gaussian beam*, Applied Optics, Vol. 36, No. 7, pp. 1536–1539, March 1997.

[23] **Ripin, D. J., Ochoa, J. R., Aggarwal, R. L.** and **Fan, T. Y.**, *300-W cryogenically cooled Yb:YAG laser*, IEEE Journal of Quantum Electronics, Vol. 41, No. 10, pp. 1274–1277, October 2005.

[24] **Kogelnik, H.** and **Li, T.**, *Laser beams and resonators*, Applied Optics, Vol. 5, No. 10, pp. 1550–1567, October 1966.

[25] **Metcalf, D., de Giovanni, P., Zachorowski, J.** and **Leduc, M.**, *Laser resonators containing self-focusing elements*, Applied Optics, Vol. 26, No. 21, pp. 4508–4517, November 1987.

[26] **Clarkson, W. A.**, *High power fiber lasers and amplifiers*, CLEO Short Course, 2008.

[27] **Shen, D. Y., Abdolvand, A., Cooper, L. J.** and **Clarkson, W. A.**, *Efficient Ho:YAG laser pumped by a cladding-pumped tunable Tm:silica-fibre laser*, Applied Physics B, Vol. 79, No. 5, pp. 559–561, 2004.

[28] **Ter-Gabrielyan, N., Merkle, L. D., Ikesue, A.** and **Dubinskii, M.**, *Ultralow quantum-defect eye-safe Er:*$Sc_2O_3$ *laser*, Optics Letters, Vol. 33, No. 13, pp. 1524–1526, July 2008.

[29] **Moulton, P. F., Rines, G. A., Slobodtchikov, E. V., Wall, K. F., Frith, G., Samson, B.** and **Carter, A. L. G.**, *Tm-doped fiber lasers: Fundamentals and power scaling*, IEEE Journal of Selected Topics in Quantum Electronics, Vol. 15, No. 1, pp. 85–92, January/February 2009.

# Chapter 6

# Conclusions and summary

## 6.1 Summary of thesis

This thesis has explored three architectures for power scaling. The first was for predominately single-ended operation using an all fibre approach for both an oscillator and amplified spontaneous emission source. Next, a fibre based master oscillator power amplifier was used to power scale the output from a single-frequency distributed feedback fibre laser. Lastly, cryogenic cooling of a Ho-doped Yttrium Aluminium Garnet (YAG) rod was used to combat detrimental thermal effects, allowing for further power scaling of the laser output. In each of the architectures, the emphasis was placed on demonstrating the potential of each approach, along with exploring any limitations, as opposed to obtaining record output powers.

### 6.1.1 Single-ended operation sources

Chapter 3 presented an all fibre geometry for obtaining predominantly single-ended operation of both a laser oscillator and amplified spontaneous emission source. This was achieved by controlling the feedback reflectivity of the end facets. A simple relation was derived, which showed that above the signal saturation intensity, the output power from each fibre end was given by $\frac{P_1}{P_2} = \frac{1-R_1}{1-R_2}\sqrt{\frac{R_2}{R_1}}$, where $P_{1,2}$ are the output powers from ends 1 and 2, respectively, and likewise $R_{1,2}$ are the feedback reflectivities of ends 1 and 2. From this it was shown that predominantly single-ended output from end 1 was achieved by selecting $R_1 \ll R_2$ and $R_{1,2} \ll 1$ in both a laser oscillator and Amplified Spontaneous Emission (ASE) source.

In the case of a laser oscillator, predominantly single-ended operation was obtained by selecting one fibre end to have a 3.5% Fresnel reflection from a perpendicularly cleaved facet and the other from a much lower reflectivity of $\sim 6 \times 10^{-3}$%, supplied by a twisted end facet [1]. The resulting laser oscillator based on Yb-doped silica had an output power of 29W for a launched pump power of 48W, corresponding to a slope efficiency with respect to launched pump power of 77%. However, this high loss cavity approach resulted in a high laser threshold of approximately 10W. As a result, there was significant ASE in the output. To determine the power content of the ASE, a diagnostic technique based on a Scanning Fabry Perot Interferometer (SFPI) was developed. With this technique, the SFPI mirror separation was carefully selected such that at certain mirror separations during the scanning cycle, only ASE frequency contributions were transmitted. This allowed a power dependent base line corresponding to the ASE to be calibrated, from which the incident ASE power could be determined. From this, the laser only signal power was calculated to be 24W for 48W of launched pump power. Furthermore, the ASE measurement showed that the ASE does not clamp at the laser threshold as commonly thought, but instead slowly rolled over with increased pump power. The significance of this is that as the pump power is further increased, the relative contributions to the output power from lasing to ASE will increase, such that for very high powers, the ASE can be considered negligible. Therefore, for high power operation, the high laser threshold and ASE content should not restrict the usefulness of this approach for selecting predominantly single-ended output from fibre lasers.

For the $2\mu m$ ASE source in Chapter 3, single-ended operation was achieved using a 3.5% Fresnel reflection from a perpendicularly cleaved facet at one end of the fibre, with the other angled polished to 14° for a much lower feedback reflectivity. With this arrangement, the fibre was pumped independently from both ends to explore the impact of pumping direction on the output power ratio. It was shown that the output power ratio was still governed by controlling the feedback reflectivity of the end facets, and was almost independent of the pumping direction. The pumping direction did however affect the maximum output power extracted from each end, where the counter propagating signal and pump yielded the highest output power as expected. When pumping both ends of the fibre equally, a maximum output of 11W was obtained for a total of 40W of launched pump power. The slope efficiency of the source was 38% with respect to launched pump power. This is comparable to the laser slope efficiency of 41% measured using the same length fibre but with an external feedback cavity to obtain single-ended operation. Further power scaling of the ASE output was limited by the onset of parasitic lasing. The limits imposed by the onset of lasing were explored by angle polishing both the fibre end facets to 14°. With this arrangement, a total output power of 15W was extracted for a launched pump power of 50W. At this highest available pump power, there was no evidence of parasitic lasing. This suggests that further scaling in the output power of this all fibre single-ended approach should be possible if the perpendicularly cleaved facet were angle polished slightly to reduce its feedback reflectivity (and therefore increase the laser threshold), whilst still maintaining $R_1 \ll R_2$ and thus predominantly single-ended output. It has been shown, since this work was conducted, that the ASE output in an Yb-doped fibre using the twisted end termination was scaled to 62W of single-ended output [2] before the onset of lasing. Furthermore, Chan et al. [3] showed that by applying a low reflectivity at both ends, the output could be scaled to ~110W of double ended ASE power. This shows a similar trend to our $2\mu m$ results, emphasising that additional pump power and a further reduction of the fibre end facet reflectivities will result in significant scaling in the output power.

Having said this, I proposed a theory that suggested that lasing will always occur in these high power ASE sources. This was based on a Fabry-Perot analysis where it was shown that certain frequencies will always resonate between the fibre end facets. Therefore, as the pump power is increased, these resonant frequencies begin to deplete more of the inversion than non-resonant ones. Eventually, as the pump power is further increased, the resonant frequencies will dominate the inversion such that the round-trip gain equals unity and they begin to lase. The significance of this is that although reducing the feedback reflectivity will extend the power scaling limit of an ASE source, the maximum output power will always eventually be limited by parasitic lasing. Furthermore, parasitic lasing can also be caused by feedback from Rayleigh scattering in the core. As a result, this may limit the benefit gained by reducing the fibre end facet reflectivities for increased ASE output power. Of course, the important point in terms of power scaling is whether the parasitic lasing threshold can be increased to the point that it cannot be reached using current commercially available laser diodes.

A limitation to both of these low feedback regimes is their susceptibility to external feedback. This can be a serious problem as, in the case of a laser, any feedback could increase the effective feedback reflectivity of the output coupler, causing the output power ratio to reduce and therefore reduce the effective laser efficiency. And, in the case of the ASE source, the impact of external feedback is even more pronounced as any feedback could cause parasitic lasing and potentially damage the fibre. Therefore, in both cases, controlling sources of feedback is a high priority and may require the use of a suitable high power optical isolator.

### 6.1.2 Single-frequency MOPA system

In Chapter 4, the output power from a low power distributed feedback laser based on Tm-doped silica was scaled using a three stage amplifier chain. The advantage of this approach was that the low power master oscillator, with excellent beam quality and single-frequency output, could be power scaled to output powers unobtainable in a single oscillator stage. The master oscillator used consisted of a UV written Bragg grating on a hydrogen sensitised Germanium Thulium co-doped fibre. The output was linearly polarised (with a PER>99%) with a linewidth of less than 240MHz and with a beam propagation factor of $M^2$=1.06 at 1943nm. The output power was measured to be 875mW due to limited pump absorption over the cavity length.

After amplification, the final amplifier stage produced 100W of single frequency output, with a beam propagation factor of $M^2$=1.25 and a PER>94%. The maximum output power was limited by thermal degradation of the outer polymer coating of the fibre. This should be able to be overcome by better thermal management along the entire fibre. Additionally, it would be beneficial to change the fibre's outer polymer coating to one with a higher thermal conductivity and/or a higher damage threshold.

Although the MOPA's performance was not limited by the optical isolators used between the amplifier stages, it is foreseen that this will become a future limitation. At present, the damage threshold is limited to ~200W/cm$^2$. As a result, this places a limit on the maximum signal power that can be used to seed the power amplifier stage and therefore also limits the maximum extraction efficiency from the amplifier. Furthermore, for most applications, the output from an amplifier system has to be isolated to prevent damage from feedback, and therefore the damage threshold of the available 2$\mu m$ isolators will ultimately limit the useable output power.

### 6.1.3 Cryogenically cooled Ho:YAG hybrid laser system

For solid-state laser sources, one of the main limitations for power scaling is detrimental thermal effects. The most significant of these thermal effects is thermal lensing, followed in polarised cavity configurations by de-polarisation losses caused by stress induced birefringence. It was predicted, using thermo-optic parameters from the literature [4–7], that by reducing the crystal temperature in YAG from 300K to 100K, the heat deposition density required to cause the same induced thermal lens or de-polarisation loss is a factor of 13 times larger at 100K than the 300K thermal load. This means that the output power before these effects begin to limit the performance can also be scaled by at least the same factor. Another benefit of operating at cryogenic temperatures is that the energy level populations in the upper and lower laser manifolds are changed according to the Boltzmann distribution. This allows for efficient in-band pumping and laser operation with a very low quantum defect. The benefits of this are two fold. The first is that the heat deposited into the material via quantum defect heating is reduced, further increasing the incident pump powers required for thermal effects to limit the performance. The second is that the output slope efficiency will be higher with a small quantum defect due to the $\nu_p/\nu_L$ dependence in the slope efficiency.

Of particular interest in this chapter were laser configurations based on Holmium doped YAG and YLF. In order to achieve good output performance from these lasers, a hybrid laser system was used that combined a fibre laser's good beam quality and high power scaling capability in a diode-cladding pumped configuration, with the benefits of cryogenically cooling the Holmium doped crystals. The work comprised of four areas: 1) Building an ASE source that was used in conjunction with a high resolution spectrophotometer to measure the temperature dependent absorption spectrum for the $^5I_8 \rightarrow ^5I_7$ transition (for in-band pumping) in Ho:YAG and Ho:YLF; 2) The construction of a Tm-doped silica fibre laser with wavelength tuning and good beam quality; 3) Measuring the performance enhancement of a Ho:YAG laser in a simple 2 mirror cavity configuration as a function of the crystal temperature; 4) To demonstrate low quantum defect operation in the Ho:YAG rod at liquid nitrogen temperature.

From the literature on temperature dependent spectroscopy [8,9], it was shown that a transition's linewidth and position were both temperature dependent. Therefore, it was important to understand how the absorption spectrum in Ho:YAG and Ho:YLF changed with temperature, so that the Tm-doped fibre laser wavelength could be appropriately adjusted for peak absorption in the crystals. These measurements were conducted using a Tm-doped fibre ASE source as a probe, and a monochromator with a resolution limit of 0.2nm. The benefits of using an ASE source over the more conventional white light source was that the ASE source had a higher spectral intensity in the $2\mu m$ region, so a less sensitive detector could be used. Furthermore, this approach benefits from the good overlap between the emission wavelength of Thulium and the absorption spectrum in Holmium. With this in mind, the ASE source was designed to emit from 1860nm to 1980nm, with a FWHM bandwidth of 50nm centred at 1920nm. Using this source, the absorption spectra within this wavelength range was taken as a function of temperature for both Ho:YAG and Ho:YLF (both axis). These showed absorption structure previously unreported in the literature [10].

From the temperature dependent absorption spectra, it was decided that the Ho:YAG laser should be pumped at 1932nm. This wavelength was chosen as it gave a good compromise between a lower quantum defect (resulting in a higher slope efficiency and lower thermal load in the crystal) and a high absorption cross-section for efficient pump absorption. At liquid nitrogen temperature, the FWHM bandwidth of the 1932nm absorption peak was ∼0.4nm. Therefore, the Tm-fibre laser output required a linewidth of less than this for a good overlap and thus a high absorption efficiency. The Tm-doped silica fibre laser used was diode pumped in a cladding pumped configuration with an external feedback cavity containing a diffraction grating for wavelength selection. The resulting laser had an output beam propagation factor of $M^2$ <1.6, an output linewidth at 1932nm of <0.2nm (as it was below the resolution limit of our monochromator) and a maximum output power of 50W.

The first of the two cavity configurations for the Ho:YAG was a simple two-mirror cavity operating at 2097nm. This configuration highlighted the improvements in the laser performance as a function of the crystal temperature. It was shown that decreasing the temperature from 300-77K resulted in a factor of 10 decrease in the threshold, and for a fixed incident pump power the output power doubled over the same temperature change. The output power change with decreased temperature was attributed to the increased absorption cross-section at 1932nm and therefore an increased absorption efficiency, which decreased the threshold pump power and increased the slope efficiency. Furthermore, the threshold was further decreased with reduced temperature due to changes in the population distribution in the laser manifolds moving from a 3-level to quasi 4 level regime, which reduced the signal reabsorption losses and increased the emission cross section. The highest slope efficiency at $LN_2$ was measured to be 65% with respect to absorbed pump power for a 41% transmission output coupler. This is much lower than would be expected from the theory due to high cavity losses caused by coating damage on the crystal end facets. However, the result was used to predict the expected performance if these losses were reduced. It showed that with the same cavity configuration but with a round trip loss of 2%, the slope efficiency should be >85%.

In addition to output power considerations, this cavity configuration was also used to highlight improvements in thermal lensing and stress induced birefringence with temperature. However, due to the high cavity losses, the laser was not operated at sufficiently high power levels for a temperature dependent change in the output beam propagation factor to be determined. To measure the de-polarisation loss with temperature, a Brewster plate was inserted into the cavity for polarised operation. The results showed no change in depolarisation loss from room temperature to liquid nitrogen temperature. This was believed to be caused by the mechanical stress on the crystal from the mount increasing with decreased temperature due to differences in the expansion coefficients of the materials. The increased mechanical stress therefore counteracted any benefits that should be observed due to changes in the thermo-optic properties of the crystal.

For the second cavity configuration, laser operation was selected for emission at 1970nm, corresponding to a quantum defect of 1.9%. The laser wavelength was selected by inserting a cavity mirror to suppress lasing at 2097nm. However, the laser performance in this cavity configuration was worse than expected, due to the high cavity losses caused by the coatings on the crystal end faces and absorption losses in the substrate of the cavity mirror inserted to suppress lasing at 2097nm. As a result, at high pump powers the laser output began to roll-over, and at low powers (<15W of output), the slope efficiency was measured to be only 33%. If these cavity losses were reduced to less than

2%, the laser slope efficiency would be in excess of 90%.

## 6.2 Future prospects

For all the sources discussed in this thesis, the availability of higher power diode sources will either directly or indirectly lead to a scaling in the various source's output power. If the example of a single stage Tm-doped fibre oscillators is taken, it has been shown that the output power can be scaled to 300W for a 25$\mu m$ core, 400$\mu m$ cladding fibre similar to that used in Chapter 5 [11]. Furthermore, by increasing the cladding size and keeping the core to cladding ratio approximately the same, high power lower brightness pump sources were used to obtain 900W of output for 1.8kW of pump power at 793nm [11]. However, as was discussed in Chapter 2, the increase in core size and NA resulted in the larger fibre having an increased V-value and thus reduced beam quality. Ideally, any high power sources desire diffraction limited or near diffraction limited performance, which still poses a problem for fibre sources.

In addition to increasing the diode pump power, the future prospects of each laser architecture and their possible applications are discussed below.

### 6.2.1 Single-ended operation sources

For this high loss cavity approach for obtaining single-ended laser emission the initial prospects will be to scale the output power using higher power diodes. The interest in this will be to confirm that the ASE background will roll-over entirely, and that for much higher powers the ASE becomes effectively negligible. Another avenue of interest would be to adapt the fibre and twisted-end-facet design to yield diffraction limited performance which would greatly improve the usefulness of the laser.

For single-ended operation of the ASE source, the limiting factor was the onset of parasitic lasing. Therefore, the first avenue of interest in the future will be to investigate how the feedback reflectivity at both ends needs to be reduced so that the reflectivity ratio still yields single-ended output, but significantly increases the laser threshold. This will enable the useful ASE output power to be initially scaled. Moving on from this, the next avenue for investigation would be to further explore the relationship between the fibre end facet reflectivities and the onset of lasing at much higher pump powers. This would be done with the aim of supporting the proposed theory that lasing threshold will always eventually be reached if there is sufficient pump power. Similarly, it would be interesting if the fibre end facet reflectivities can be selected so that the laser threshold is not reached when using the maximum currently available laser diode power. Of course, at these power levels, thermal degradation of the fibre may limit the performance, but this would need to be confirmed.

An alternative approach for scaling the ASE output power could be to use an amplifier system. This has the advantage over a single gain element, as the output from a lower power ASE source can be power scaled using a series of fibre amplifiers, without the drawback of parasitic lasing. This approach has been demonstrated to good effect at $1\mu m$ by Wang et al. [2] using a Yb-doped fibre ASE source and amplifier. They showed that in the single gain element, the ASE power was limited to 40W of output before the onset of parasitic lasing, whilst when using two gain elements (an ASE seed and amplifier), they produced >120W of ASE output limited only by the available pump power. It therefore stands to reason that an ASE seed and amplifier system based on Tm-doped silica should yield a similar increase in the maximum ASE power.

### 6.2.2 Single-frequency MOPA

In the single-frequency MOPA, one of the main prospects for the future is to increase the pump power in the power amplifier stage and therefore increase the output power. In conjunction with increased pump power, further power scaling will also require better thermal management of the power amplifier fibre, and also optical isolators with higher damage thresholds. Of these, the optical isolators pose the biggest problem due to the present lack of commercially available high power handling low loss isolators in the $2\mu m$ spectral region.

Therefore, in order for the power scaling potential of any $2\mu m$ MOPA system to be realised, more research and development is required into isolators in the $2\mu m$ spectral region.

Once the current output power limits due to thermally induced fibre damage and the availability of suitable optical isolators are resolved, it is foreseen that SBS will limit further power scaling. However, there are many ways to increase the SBS threshold. These include: increasing the effective area by increasing the core size [12]; controlling the optical and acoustic properties of the core and cladding by changing the fibre's refractive index profile [13–15]; and reducing the Brillouin gain coefficient by creating a non-uniform Brillouin spectrum along the fibre, by changing the dopant level, applying distributed stress, or using a temperature gradient along the fibre. Therefore, by resolving the current issues and implementing some of these techniques for increasing the SBS threshold, the maximum output power should be considerably increased.

In addition to direct power scaling, the single-frequency amplified output can be used for frequency conversion to the mid-infrared or visible region of the spectrum. The interest here would be to access wavelengths outside of the operational wavelength regions of other rare-earth doped materials. In conjunction with this, the single-frequency DFB master oscillator can be modified to provide other operational wavelengths, providing an even wider range of wavelengths via frequency conversion.

### 6.2.3 Cryogenic lasers operating around $2\mu m$

For the cavity configurations discussed in Chapter 5, the major limitation on performance was caused by high cavity losses due to poor optical coatings on the crystal end faces. In order to obtain efficient laser operation, the cavity losses will need to be minimised. This can be more challenging for a cryogenic laser cavity due to the high number of optical surfaces created by the necessity of housing the crystal in a cryostat. One potential approach is to use a Brewster cut crystal in conjunction with the chamber windows being at Brewster's angle in relation to the beam direction. If correctly aligned, this should significantly reduce the reflection losses in the cavity and allow for much better performance. However, to obtain efficient pump launch into the crystal, the pump source will need to be polarised, increasing its complexity. This should not prove too challenging given the availability of polarisation maintaining fibres like that used in the Chapters 4 and 5. With the pump source used the external feedback cavity would only require the addition of a polarising element and a half-wave plate to optimise the polarisation to the slow/fast axis of the fibre.

It was shown in Chapter 5 that the current mounting arrangement for the crystal induced high mechanical stress, especially as the temperature was decreased. In the polarised cavity, this resulted in significant depolarisation losses. If the cavity design was to use the brewster cut crystal approach, then these stresses need to be removed. A simple approach for this would be to change the crystal to a slab geometry, which can then be mounted for good thermal contact of the large faces only. Therefore, any mechanical or thermal stress should be induced in only one direction (i.e. perpendicular to the slab's large faces). Therefore, as long as the polarised beam is orthogonal to the axis between the large faces, it should experience no depolarisation losses.

Another future direction is to further scale the output power by increasing the pump power from the Tm-doped fibre. As was mentioned earlier, this can be achieved by increasing the diode-pump power available for the Tm-doped fibre. As was discussed in Chapter 5, if the pump power was increased and the Tm fibres output power was increased to a level similar to that reported in the literature [11], then it would be possible, using the low loss cavity described above, to scale the CW power to in excess of 400W. Furthermore, using a higher pump power source would also enable the limits of low quantum defect operation to be explored. Although reducing the quantum defect has the advantage of increasing the laser slope efficiency and reducing the thermal load on the crystal, it has the disadvantage of increasing the threshold pump power. Using a higher pump power source would allow the higher threshold pump power to be easily reached and still allow the laser to operate many times above threshold.

The potential for cryogenic lasers is not limited to CW mode of operation. For pulsed operation it is desirable to use a large beam diameter and small interaction length to reduce the signal intensity and therefore any non-linear effects. This is one of the main attractions for using solid-state lasers instead of fibre lasers for pulsed operation. Q-switched operation presents the ideal method for pulsed operation, with the current pump arrangement as it is compatible with CW pumping. In a continuously pumped, repetitively Q-switched system, when the cavity quality factor is low (i.e. the cavity losses are high), the inversion build-up, $n(t)$, is given by [16]

$$n(t) = W_p \tau_f N \left(1 - \exp\left(\frac{-t}{\tau_f}\right)\right) \tag{6.1}$$

where $W_p$ is the pump rate, $\tau_f$ is the fluorescence lifetime, $N$ is the total ion density in the crystal, and $t$ is the pump time in the low Q cavity condition. It is assumed in equation (6.1) that the inversion is completely depleted by the pulse and that the inversion density is much less than the total ion density. From the equation, it can be seen that a long fluorescence lifetime is advantageous as it results in a higher maximum inversion density and therefore a higher pulse energy. Therefore, for Q-switched operation, Ho:YLF should yield higher energy pulses than Ho:YAG given that their respective lifetimes are 14ms for YLF [17] and 8.5ms for YAG [18]. Furthermore, Q-switched operation has some of the same limitations as CW-mode in terms of thermal effects and de-polarisation losses. Naturally, cryogenic cooling will improve the laser performance, as was the case for CW operation. However, for active Q-switched operation, the laser has to be polarised, so it is again advantageous to use Ho:YLF as it is birefringent and therefore not affected by de-polarisation losses, as is the case with YAG. It was with these potential future experiments in mind that the spectroscopic measurements in Chapter 5 for Ho:YLF at liquid nitrogen temperature were conducted. It is expected that the benefits of cryogenic cooling will greatly increase the Q-switched performance in Holmium doped crystals, as has been demonstrated for other rare-earth doped crystals [19,20].

## 6.3 References

[1] **Clarkson, W. A.** and **Wang, P.**, *UK Patent Application "Optical fiber device", Application Number 0600179.6*, Jan 2006.

[2] **Wang, P., Sahu, J. K.** and **Clarkson, W. A.**, *Power scaling of ytterbium-doped fiber superfluorescent sources*, IEEE Journal of Selected Topics in Quantum Electronics, Vol. 13, No. 3, pp. 580–587, 2007.

[3] **Chan, J. S. P., Wang, P., Sahu, J. K.** and **Clarkson, W. A.**, *Ultra-low feedback fibre end termination geometry for high power fibre source applications*, CLEOE-IQEC, 2007.

[4] **Aggarwal, R. L., Ripin, D. J., Ochoa, J. R.** and **Fan, T. Y.**, *Measurement of thermo-optic properties of $Y_3Al_5O_12$, $Lu_3Al_5O_12$, $YAlO_3$, $LiYF_4$, $LiLuF_4$, $BaY_2F_8$, $KGd(WO_4)_2$, and $KY(WO_4)_2$ laser crystals in the 80-300K temperature range*, Journal of Apllied Physics, Vol. 98, No. 10, pp. 103514–1–103514–14, Novemeber 2005.

[5] **Klein, P. H.** and **Croft, W. J.**, *Thermal conductivity, diffusivity, and expansion of $Y_2O_3$, $Y_3Al_5O_12$, and $LaF_3$ in the range 77°-300°K*, Journal of Applied Physics, Vol. 38, No. 4, pp. 1603–1607, March 1967.

[6] **Fan, T. Y.** and **Daneu, J. L.**, *Thermal coefficients of the optical path length and refractive index in YAG*, Applied Optics, Vol. 37, No. 9, pp. 1635–1637, March 1998.

[7] **Wynne, R., Daneu, J. L.** and **Fan, T. Y.**, *Thermal coefficients of expansion and refractive index in YAG*, Applied Optics, Vol. 38, No. 15, pp. 3282–3284, May 1999.

[8] **Kushida, T.**, *Linewidths and thermal shifts of spectral lines in Neodymium-doped Yttrium Aluminium Garnet and Calcium Fluorophosphate*, Physical Review, Vol. 185, No. 2, pp. 500–508, September 1969.

[9] **Beghi, M. G., Bottani, C. E.** and **Russo, V.**, *Debye temperature of Erbium-doped Yttrium Aluminium Garnet from luminescence and Brillouin Scattering data*, Journal of Applied Physics, Vol. 87, No. 4, pp. 1769–1774, February 2000.

[10] **Walsh, B. M., Grew, G. W.** and **Barnes, N. P.**, *Energy levels and intensity parameters of* $Ho^{3+}$ *ions in* $Y_3Al_5O_12$ *and* $Lu_3Al_5O_12$, Journal of Physics and Chemistry of Solids, Vol. 67, No. 7, pp. 1567–1582, July 2006.

[11] **Moulton, P. F., Rines, G. A., Slobodtchikov, E. V., Wall, K. F., Frith, G., Samson, B.** and **Carter, A. L. G.**, *Tm-doped fiber lasers: Fundamentals and power scaling*, IEEE Journal of Selected Topics in Quantum Electronics, Vol. 15, No. 1, pp. 85–92, January/February 2009.

[12] **Broderick, N. G. R., Offerhaus, H. L., Richardson, D. J., Sammut, R. A., Caplen, J.** and **Dong, L.**, *Large mode area fibers for high power applications*, Optical Fiber Technology, Vol. 5, No. 2, pp. 185–196, April 1999.

[13] **Kobyakov, A., Kumar, S., Chowdhury, D. Q., Ruffin, A. B., Sauer, M.** and **Bickham, S. R.**, *Design concept for optical fibers with enhanced SBS threshold*, Optics Express, Vol. 13, No. 14, pp. 5338–5346, July 2005.

[14] **Koyamada, Y., Sato, S., Nakamura, S., Sotobayashi, H.** and **Chujo, W.**, *Simulating and designing Brillouin gain spectrum in single-mode fibers*, Journal of Lightwave Technology, Vol. 22, No. 2, pp. 631–639, February 2004.

[15] **Ruffin, A. B., Li, M., Chen, X., Kobyakov, A.** and **Annunziata, F.**, *Brillouin gain analysis for fibers with different refractive indices*, Optics Letters, Vol. 30, No. 23, pp. 3123–3125, December 2005.

[16] **Koechner, W.**, Solid-State Laser Engineering, Springer, New York, 6th edn., 2006.

[17] **Walsh, B. M., Barnes, N. P.** and **Bartolo, B. D.**, *Branching ratios, cross sections, and radiative lifetimes of rare earth ions in solids: Applications to* $Tm^{3+}$ *and* $Ho^{3+}$ *ions in* $YLiF_4$, Journal of Applied Physics, Vol. 83, No. 5, pp. 2772–2787, March 1998.

[18] **Schellhorn, M.** and **Hirth, A.**, *Modeling of intracavity-pumped quasi-three-level lasers*, IEEE Journal of Quantum Electronics, Vol. 38, No. 11, pp. 1455–1464, November 2002.

[19] **Tokita, S., Kawanaka, J., Fujita, M., Kawashima, T.** and **Izawa, Y.**, *Efficient high-average-power operation of Q-switched cryogenic Yb:YAG laser oscillator*, Japanesse Journal of Applied Physics, Vol. 44, No. 50, pp. 1529–1531, 2005.

[20] **Manni, J. G., Hybl, J. D., Rand, D., Ripin, D. J., Ochoa, J. R.** and **Fan, T. Y.**, *100W Q-switched cryogenically cooled Yb:YAG laser*, IEEE Journal of Quantum Electronics, Vol. 46, No. 1, pp. 95–98, January 2010.

# Appendix A

# List of publications

### Journal articles

L. Pearson, J. W. Kim, Z. Zhang, M. Ibsen J. K. Sahu, W. A. Clarkson, *"High-power linearly-polarized single-frequency thulium-doped fiber master-oscillator power-amplifier"*, Optics Express (2010), Vol 18(2), pp1607-1612.

D. Y. Shen, L. Pearson, P. Wang, J. K. Sahu, W. A. Clarkson, *"Broadband Tm-doped superfluorescent fiber source with 11W single-ended output power"*, Optics Express (2008), Vol 16(15), pp11021-11026.

L. Pearson, J. S. P. Chan, P. Wang, J. K. Sahu, W. A. Clarkson, *"Novel approach for single-ended operation of a cladding pumped fibre laser"*, Applied Physics B (2007), Vol 87(1), pp75-78.

### Conference papers

J. W. Kim, J. I. Mackenzie, W. O. S. Bailey, L. Pearson, D. Y. Shen, Y. Yang, W. A. Clarkson, *"Cryogenically-cooled Ho:YAG laser in-band pumped by a Tm fibre laser"*, Contributed Paper CA10.5, CLEO Europe, Munich, June 2009.

L. Pearson, J. W. Kim, Z. Zhang, J. K. Sahu, M. Ibsen, W. A. Clarkson, *"High-power single-frequency thulium-doped fiber master oscillator power amplifier at 1943nm"*, Contributed Paper CThN1, CLEO US, Baltimore, June 2009.

W. A. Clarkson, L. Pearson, Z. Zhang, J. W. Kim, D. Y. Shen, A. J. Boyland, J. K.

Sahu, M. Ibsen, *"High Power Thulium Doped Fiber Lasers"*, Invited Paper, OFC, San Diego, March 2009.

J. I. Mackenzie, W. O. S. Bailey, D. Y. Shen, L. Pearson, Y. Yang, W. A. Clarkson, *"Tm:fibre laser in-band pumping cryogenically-cooled Ho:YAG laser"*,LASE 2009 at Photonics West, San Jose, January 2009.

D. Y. Shen, L. Pearson, J. K. Sahu, W. A. Clarkson, *"11W Broadband Amplified Spontaneous Emission fibre source at 2 microns"*, Contributed Paper WC5, ASSP 2007, Vancouver, January 2007.

L. Pearson, J. S. P. Chan, P. Wang, W. A. Clarkson, *"Simple Scheme for single-ended operation of a cladding pumped fibre laser"*, 2nd EPS-QEOD Europhoton, Pisa, September 2006.